



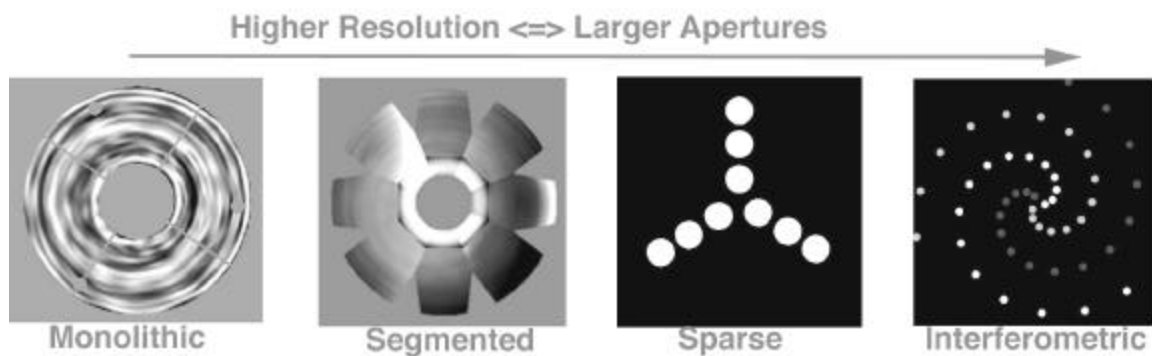
Universities
Space
Research
Association



Workshop on *Computational Optics and Imaging for Space Applications*

Richard G. Lyon
Chair/Editor

May 10, 11, 12, 2000
NASA/Goddard Space Flight Center
Greenbelt, MD 20771



Foreward

The first NASA workshop on *Computational Optics and Imaging for Space Applications* was held during May 10, 11 and 12, 2000 at the NASA/Goddard Space Flight Center in Greenbelt, Maryland. NASA Goddard Space Flight Center, Universities Space Research Association's Center of Excellence in Space Data and Information Sciences and the Optical Society of America jointly sponsored the workshop.

The general purpose of the workshop was to bring together researchers in all aspects of computational optics, imaging, wavefront sensing, optical control systems as well as on-board and ground processing and advanced computer architectures whose primary emphasis has been on space based applications. The primary focus of the workshop was to address computational methods and techniques in the areas of:

1. Modeling and simulation of space optical systems.
2. Wavefront sensing and optical control.
3. Phase retrieval and phase diversity.
4. Image restoration, deconvolution and super-resolution.
5. Sparse and interferometric imaging techniques.
6. Computer architectures for on-board and ground processing.

The opening remarks, given by Alphonso Diaz - director of NASA/GSFC, discussed the increased reliance on information theoretic methods for spacecraft design, analysis, control, pipeline and post-processing of data. The banquet speaker, Milton Halem - Chief Information Officer NASA/GSFC, discussed the increased use of software, algorithms, parallel computing, and large scale data database required for the future of NASA. All told there were 24 presented papers, of which 2 were invited this was the first workshop of its kind at NASA/GSFC and it is hoped that others will follow.

On behalf of the Program Committee members, I wish to thank all of the authors for their contribution and for producing the manuscripts in the requested time and for their presentations. I wish to thank Michele Barton (USRA) for putting together these proceedings.

Richard G. Lyon (NASA/GSFC)

Workshop Committee

Conference Chair/Editor

Richard Lyon, NASA/Goddard Space Flight Center

OSA Technical Representative

James Fienup Veridian/ERIM International

Program Committee

Dennis Andrucyk	NASA/Goddard Space Flight Center
Paul Atcheson	Ball Aerospace and Tech. Corp.
Charles Bowers	NASA/Goddard Space Flight Center
Scott Dixon	Photon Research Associates
John Dorband	NASA/Goddard Space Flight Center
Lee Feinberg	NASA/Goddard Space Flight Center
James Fienup	Veridian/ERIM International
Milton Halem	NASA/Goddard Space Flight Center
William Hayden	NASA/Goddard Space Flight Center
Edward Howard	National Oceanic and Atmospheric Administration
Dave Leisawitz	NASA/Goddard Space Flight Center
Jacqueline Lemoigne	NASA/Goddard Space Flight Center
Timothy Murphy	University of Maryland, Baltimore County
Richard Paxman	Veridian/ERIM International
John Wood	NASA/Goddard Space Flight Center
Eric Young	NASA/Goddard Space Flight Center

Opening Remarks

Alphonso Diaz NASA/Goddard Space Flight Center

Invited Speakers

Dennis Chesters	NASA/Goddard Space Flight Center
Robert Fugate	Air Force Research Laboratory
Milton Halem	NASA/Goddard Space Flight Center

Workshop Attendees

Name	Affiliation
Atcheson, Paul	Ball Aerospace & Tech. Corp.
Bartlett, Chanda	University of Arizona
Basinger, Scott	NASA/JPL
Bronez, Thom	Ball Aerospace & Tech. Corp.
Burke, James	Univ. of Washington
Carpenter, Kenneth	NASA/GSFC
Chesters, Dennis	NASA/GSFC
Content, David	NASA/GSFC
Diaz, Alphonso	NASA/GSFC
Dean, Bruce	NASA/GSFC
Dorband, John	NASA/GSFC
Feinberg, Lee	NASA/GSFC
Fienup, James	Veridian/ERIM International
Fisher, Shalom	NRL
Friedman, Scott	Johns Hopkins University
Fugate, Robert	Air Force Research Lab/Starfire Optical Range
Gong, Qian	Swales and Assoc.
Gonsalves, Robert	Tufts University
Halem, Milton	NASA/GSFC
J. Mike Hollis	NASA/GSFC
Jenstrom, Del	NASA/GSFC
Katz, Daniel	JPL
Krist, John	STScI
Laher, Russ	CalTech/SIRTF Science Center
Loew, M.	George Washington University
Luke, D. Russell	Univ. of Washington
Lyon, Richard	NASA/GSFC
Maker, David	Teledyne Brown Engineering
Meinel, Ed	The Aerospace Corp.
Moos, W.	Johns Hopkins University
Moshir, Mehrdad	CalTech/SIRTF Science Center
Mundy, Lee	University of Maryland, College Park
Murphy, Tim	CESDIS/UMBC
Noll, Robert	Raytheon Optical Systems
Ohl, Raymond	NASA/GSFC
Paxman, Rick	Veridian/ERIM International
Ranawake, Udaya	NASA/GSFC
Redding, David	NASA/JPL
Saha, Timo	NASA/GSFC
Shiri, Shahram	George Washington University
Solyar, Greg	CESDIS/UMBC
Springer, Paul	NASA/JPL
Tasker, Fred	Swales and Assoc.
Teuben, P.	University of Maryland, College Park
Thelen, Brian	Veridian/ERIM International
Waluschka, Eugene	NASA/GSFC
Wasyliwskyj, W.	George Washington University
Young, Eric	NASA/GSFC
Zhang, Xiaolei	NASA/GSFC

Table of Contents

Foreward	i
Workshop Committee	ii
Workshop Attendees	iii
Overview: Computational Complexity and Space Based Optical Systems R. Lyon, J. Dorband, (NASA/GSFC), T. Murphy, G. Solyar (USRA/CESDIS).....	1
HORIZON - A Proposal for Large-Aperture, Active Optics in Geosynchronous Orbit D. Chesters and D. Jenstrom - Invited Paper (NASA/GSFC).....	10
A Spaceborne Embedded COTS Cluster for Computational Optics D. Katz, and P. Springer (NASA/JPL).....	28
Adventures in Phase Retrieval: Lessons Learned from HST & SIRTf J. Krist (Space Telescope Science Institute).....	29
Pipeline Processing of Infrared-Array-Camera Images from the Space Infrared Telescope Facility (SIRTf) R. Laher and M. Moshir (SIRTf Science Center/CalTech).....	30
Optical Performance Modeling of FUSE Telescope Mirror Using METDAT and OSAC Software T. Saha, R. Ohl, (NASA/GSFC), S. Friedman, and W. Moos (JHU).....	38
LISA Far Field Phase Patterns E. Waluschka (NASA/GSFC).....	47
Large Aperture Sparse Array Space Telescope D. Maker (Teledyne Brown Engineering).....	60
Trading Mirror Mass for Megaflops R. Paxman and B. Thelen (Veridian/ERIM International).....	72
Scaling Laws for Sparse-Aperture Imaging J. Fienup (Veridian/ERIM International).....	76
Wavefront Sensing for Sparse Apertures by Phase Diversity R. Gonsalves (Tufts University).....	79
A Phase Diversity Solution to the Small-Phase Retrieval Problem R. Gonsalves (Tufts University).....	80
Overcoming Dynamic Disturbances in Imaging Systems E. Young, R. Lyon, D. Chesters, (NASA/GSFC), G. Dente (GDA) and Q. Gong (Swales).....	81
Speculation on Future Adaptive Optics Technology R. Fugate - Invited Speaker (AFRL-Starfire Optical Range).....	90
Wavefront Control Testbed Results D. Redding, S. Basinger, A. Lowman, F. Shi, C. Bowers, R. Burg, L. Burns, P. Bely, D. Cohen, P. Davila, B. Dean, T. Norton, P. Petrone, B., Perkins, M. Wilson (JPL, NASA/GSFC).....	91
Benchtop Phase Diverse Imaging Testbed G. Solyar, R. Lyon, J. Dorband, and U. Ranawake (NASA/GSFC and USRA/CESDIS).....	92

Preliminary Phase Diverse Imaging Testbed Algorithms and Results	
R. Lyon, G. Solyar, J. Dorband, and U. Ranawake (NASA/GSFC and USRA/CESDIS).....	102
A Performance Study of a Phase Diversity Program on NASA GSFC Hive Test Bed	
U. Ranawake, R. Lyon, and J. Dorband (NASA/GSFC and CESDIS/USRA).....	116
Cramer-Rao Bounds for Focus Diverse Wavefront Sensing with Deformable Mirror "print-through" and Control Noise	
B. Dean and R. Lyon (NASA/GSFC).....	121
A Limited Memory Algorithm with Trust Regions for Phase Retrieval	
R. Luke, J. Burke, and R. Lyon (U. of Washington and NASA/GSFC).....	137
Sparse Matrix Approximation Method for Phase Retrieval Based Active Optical Control System	
T. Murphy, R. Lyon, J. Dorband, and J.M. Hollis (NASA/GSFC and USRA/CESDIS).....	158
The Application of Radio Astronomy Algorithms to Imaging Interferometry for SPECS, SPIRIT, and WIIT	
X. Zhang, L. Mundy, and P. Teuben (ITSS/NASA /GSFC and U. of Maryland).....	167
A Mathematical Model of Electromagnetic Wave Propagation in the Volume Holographic Recording Using Photorefractive Polymer	
S. Shiri, M. Loew, W. Wasylkiwskyj, and R. Lyon (GWU, NASA/GSFC).....	170
Superresolution Using Laplacian Filter on Isophote Ridges	
D. Maker (Teledyne Brown Engineering).....	179

Overview: Computational Complexity and Space Based Optical Systems

Richard Lyon
NASA - Goddard Space Flight Center
Greenbelt, MD 20771
lyon@jansky.gsfc.nasa.gov

John Dorband,
NASA - Goddard Space Flight Center
Greenbelt, MD 20771

Timothy Murphy
University of Maryland Baltimore County, Center of Excellence in Space Data And Information Sciences,
NASA/Goddard Space Flight Center, Code 900.1,
Greenbelt, MD 20771

Greg Solyar
University of Maryland Baltimore County, Center of Excellence in Space Data And Information Sciences,
NASA/Goddard Space Flight Center, Code 900.1,
Greenbelt, MD 20771

ABSTRACT

Future space based imaging systems require increasingly larger aperture sizes to keep pace with the demand for higher spatial resolution for both Earth and Space sciences missions. The cost and weight becomes increasingly prohibitive for telescopes and instruments with apertures greater than 1 meter. A number of solutions are possible and are under investigation; these include: deployable segmented aperture systems, sparse aperture systems, interferometric imaging systems, computational deconvolution and super-resolution techniques. The commonality of these techniques lies in increased reliance on sophisticated computational and information theoretic techniques. We give an overview of the complex optical and image processing techniques required for such systems to become operational.

1. INTRODUCTION

NASA's Origins [1] and New Millennium [2] programs require large space based imaging systems. Many of these imaging systems will need to be interferometric imaging systems (Submillimeter Probe of Evolutionary Cosmic Background - SPECS), segmented aperture telescopes (Next Generation Space Telescope - NGST), sparse aperture systems (Terrestrial Planet Finder - TPF). Many of these systems will require wavefront sensing (WFS) and optical control systems (OCS) because of weight, deployment, thermal, structural and dynamics, and may require substantial post-processing to obtain the desired image quality. Each of these requires complex algorithms and computer processing. Imaging interferometers in order to convert from the observed visibility function to the "dirty" image and subsequent deconvolution/enhancement to the "cleaned" image. Segmented aperture systems for WFS methods such as phase retrieval and/or phase diversity and an active optical control system for initial alignment and to maintain alignment. Sparse aperture systems may also require WFS methods and an active optical system with enhancement/deconvolution to clean the resultant image. NASA/Goddard Space Flight Center's Optical Systems Characterization and Analysis Research (OSCAR) project has been actively researching these methods from an analytic and computational points of view and has also developed a phase diversity testbed.

Most of NASA's previous space based imaging systems have relied on a "monolithic" telescope design examples of which are the Hubble Space Telescope (HST) and the Space Infrared Telescope Facility (SIRTF). Monolithic, as defined here, means a telescope with a single piece primary mirror. This has the advantage that the mirror is generally ground, polished, integrated, aligned, tested and deployed as a single piece of material, and in flight, the mirror is generally thermally and structurally stable. The mirror

size is determined, ideally, by the desired science return, however, it is also severely constrained by cost, weight, size and ability to manufacture, test and must be able to fit into available launch vehicles. However it has become increasingly obvious that we must quantitatively evaluate the aforementioned alternative telescope configurations for high resolution images. We develop a generalized imaging model and develop each of these telescope configurations within the model. Shown will be a simulation of each as well as wavefront sensing, optical control and deconvolution methods.

2. GENERALIZED IMAGING MODEL

An observed noisy image, $d(x,y)$, can be represented by:

$$d(x,y) = PSF(x,y; A, \mathbf{f}) * O(x,y) + \mathbf{h}(x,y) \quad (1)$$

where $PSF(x,y)$ is the optical point spread function, $O(x,y)$ is the object, $\mathbf{h}(x,y)$ is the noise and (x,y) represent the image plane coordinates.

The PSF can be calculated as the two dimensional Fourier transform of the complex pupil function [3]. Let $A(u,v)$ represent the aperture mask of the pupil function. $A(u,v)$ is the amplitude within the aperture and zero outside. $\mathbf{f}(u,v)$ is the phase delay at each point in the system exit pupil. (u,v) are the spatial coordinates in the system exit pupil and λ and F represent the wavelength and system focal length respectively. With these definitions the PSF is given by:

$$PSF(x,y,A,\mathbf{f}) = \left| \frac{1}{IF} \iint A(u,v) e^{i\mathbf{f}(u,v)} e^{-i2\pi\left(\frac{xu}{IF} + \frac{yv}{IF}\right)} dudv \right|^2 \quad (2)$$

We see that the PSF is the modulus squared of the 2D Fourier transform of the complex pupil function defined as $P(u,v) = A(u,v) e^{i\mathbf{f}(u,v)}$. If we define $u = IFf_x$ and $v = IFf_y$ then the optical transfer function (OTF) is given by the Fourier transform of equation (2):

$$OTF(f_x, f_y) = \frac{P(f_x, f_y) \otimes P(f_x, f_y)}{P(f_x, f_y) \otimes P(f_x, f_y) \Big|_{f_x=f_y=0}} \quad (3)$$

and the observed monochromatic image in the Fourier domain by:

$$\tilde{d}(f_x, f_y) = OTF(f_x, f_y) \tilde{O}(f_x, f_y) + \tilde{\mathbf{h}}(f_x, f_y) \quad (4)$$

The imaging operation is a low pass filter. For a given aperture it can be shown that the highest frequency response filter is given when the phase, $\mathbf{f}(u,v)$, is equal to zero. In a well designed optical system the rms of the phase is less than $\lambda/20$ and represents a "diffraction limited" system. Even with zero phase the OTF is compactly supported, since the autocorrelation in equation (3) is non-zero over only a finite region. Thus any optical system is, at best, a low-pass spatial filter. Image restoration methods a.k.a. deconvolution, are an attempt to boost the response of the spatial filter below the cutoff frequency implicitly defined by equation (3). Super-resolution is an attempt to analytically continue the spatial frequency content beyond the optical cutoff frequency, a much harder proposition and attained in only in a limited number of cases to date.

The above imaging model is the same for a monolithic, segmented, sparse or an interferometric imaging system. What changes, in each of these cases, is the point spread function and hence the optical transfer function. For a given aperture size the OTF has the same optical cutoff frequency for the monolithic, segmented, sparse and interferometric systems. However, how the filter rolls off to the cutoff frequency is different, resulting in very different image quality.

Residual design errors, misalignments, deformations and temporal dynamics caused by thermal and structural effects cause the phase function, $f(u,v)$, to be non-zero, and possibly time dependent resulting in lower fidelity imaging. If the phase function can be determined then it may be possible to correct these sources of errors. Wavefront sensing is the method by which one determines the phase and an optical control system is what uses the phase function to correct the system by moving and/or deforming the optics and ideally driving the phase function to zero.

The telescopes angular resolution scales as λ/D , where D is the diameter of the primary mirror and λ is the wavelength. High resolution implies a large diameter mirror, however, did does not necessary imply that we use a filled aperture. The segmented, sparse and interferometric imaging systems are methods to overcome having a large aperture without using a single large optic, however, more post-processing may be required.

In the following sections we will show the PSFs, OTFs and a simulated image for the monolithic, segmented, sparse and interferometric imaging cases and discuss their differences as well as discuss wavefront sensing and optical control and deconvolution.

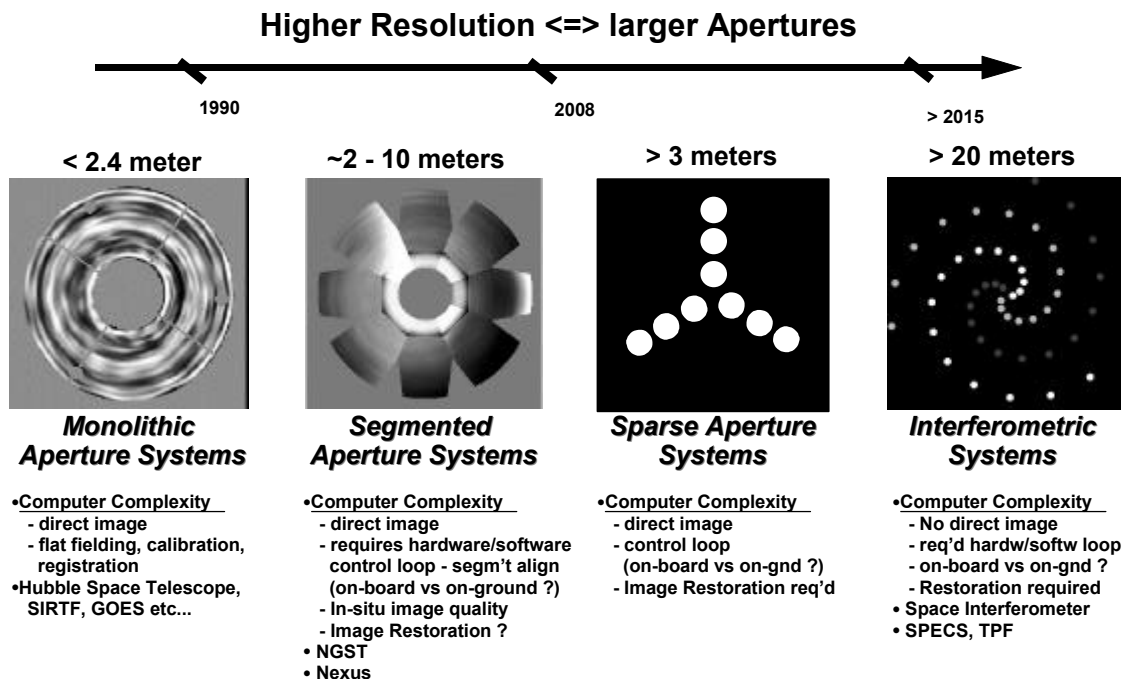


Figure 1
Alternative Telescope Mirror Configurations

3. MONOLITHIC, SEGMENTED, AND SPARSE APERTURE IMAGING

Monolithic Imaging Systems

The leftmost image of Figure 1 shows the Hubble Space Telescope primary mirror [4] as an example of a monolithic mirror. The residual polish marks are shown as light and dark regions, where white is too high and black too low. In space it is possible to reach apertures for space 2-3 meters with this type of configuration, however the cost and weight is high. Little post-processing must be performed on the image for useable science. Typical processing would include flat-fielding, i.e. correcting for radiometric errors over image plane, calibration, i.e. conversion to radiometric units and possibly image registration.

Segmented Imaging Systems

The 2nd picture from the left of Figure 1 shows a simulation of one possible design for the Next Generation Space Telescope (NGST). It shows a simulation of an 8 meter segmented deployable telescope primary mirror [5]. Segmented since each of the 9 petals (1 center and 8 edge) are actually manufactured as separate mirrors. Deployed implies that the segments fold up to fit in the launch vehicle and are unfurled (deployed) after launch, and locked into position. This configuration has the advantage that a larger telescope can be built. However the segments must be first deployed, then aligned and the alignment must be maintained throughout the mission life. Furthermore the configuration is generally less structurally and thermally stable than the monolith. This generally requires an active optical control system [5][6] requiring much more computational complexity.

Sparse Aperture Imaging Systems

The 3rd picture from the left of Figure 1 is a sparse aperture configuration. It may be realized a number of different ways in hardware. Each of the white circles can represent a piece of the same mirror, or separate telescopes mounted on the same structure, or, they could be entirely separate telescopes which are tethered together or as “free flyers”, i.e. a constellation of telescopes. If the apertures are not part of the same rigid, thermally stable structure then an active control loop may be required to maintain alignment of the sub-apertures [7][8]. In a sparse aperture configuration, the aperture locations are fixed both in number and position. Sparse aperture configurations typically give a lower quality image than both the monolith and segmented cases however the overall aperture can be much larger. The image quality increases with increasing number of sub-apertures. Note that the total area of the sub-apertures is smaller than a full aperture case, thereby decreasing the light gathering ability, i.e. the sensitivity. The typical low image quality generally requires some post-processing such as image restoration and/or enhancement [9].

Interferometric Imaging Systems

The rightmost picture of Figure 1 shows a simulated interferometric imaging system. Each of the 3 different gray scales corresponds to a separate telescope system. In this simulation there are 3 separate telescope systems which are spatially moving in time. At each temporal position a separate image is collected in its Fourier domain. These sub-images are mosaiced together in the Fourier domain and inverse Fourier transformed to obtain the synthesized image. These type of systems can in principle be very large, 100's of meter, since each of the telescopes could be separately launched and subsequently aligned, i.e. “phased” together in space [10][11]. This type of system may also require an active metrology system and/or an active control loop. This active metrology system would determine the relative aperture locations, since this knowledge is required to create an image. Furthermore an active optical system may be required to maintain alignment of each individual telescope during the collection time. Although the image resolution can be extremely high, the image quality can still be relatively poor. It also generally has a small field of view. Post processing of the resultant image is usually required.

The top row of Figure 2 shows a monolithic, a segmented and a sparse aperture PSFs, on a logarithmic scale, all for a 1 meter full aperture size. The monolithic PSF is circularly symmetric (some aliasing is evident due to the printing process – not the modeling). The segmented PSF shows large diffraction flares, diffracting energy out of the core. The sparse PSF is relatively large with much less relative energy in the core. The bottom row shows their respective optical transfer functions on a linear scale. The monolithic PSF falls off from the core and shows much more modulation away from the center. The segmented falls off faster than the monolithic case and has a cutoff frequency which is a weak function of direction. The sparse OTF falls off quickly and is strongly dependent on direction. Note that all the OTFs have approximately the same area over which they are non-zero, i.e. the support.

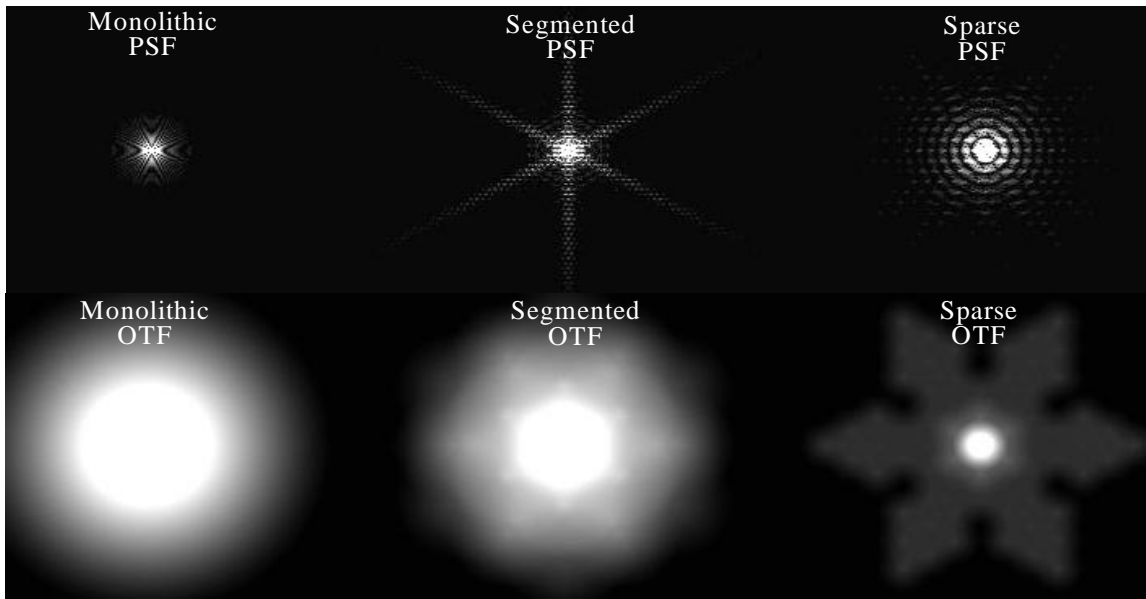


Figure 2
Simulated PSFs and OTFs for Each Configuration

Figure 3 shows a simulated image of Saturn with a monolithic, segmented and sparse aperture system. The monolithic is the sharpest, the segmented is slightly less sharp and the sparse is noticeably more blurry. Figure 4 shows slices through the power spectral densities, on a log-linear scale, for the raw image and the monolithic, segmented and sparse imaging cases. The cutoff frequency is easily seen where the power drops sharply and is nearly the same for all the imaging cases except the raw (true) image. However below the cutoff the modulation varies by 2 orders of magnitude with the lowest for the sparse case and the best for the monolithic.

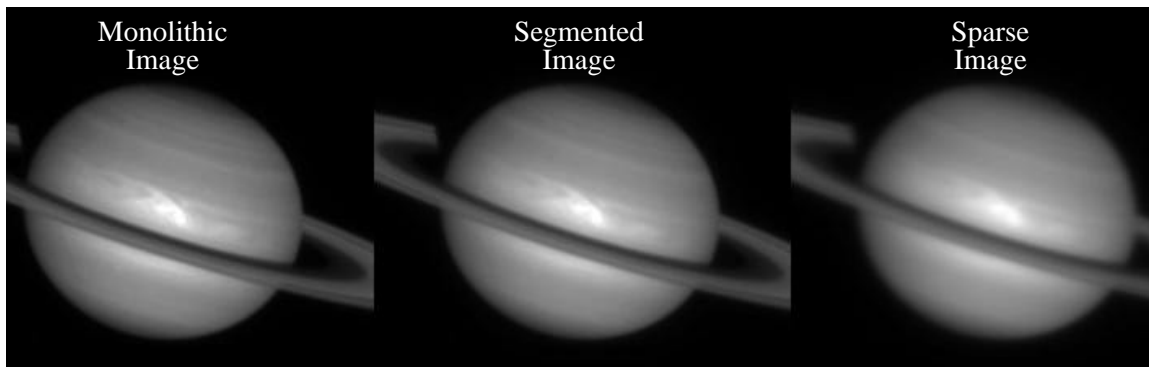


Figure 3
Simulated Images for Each Configuration

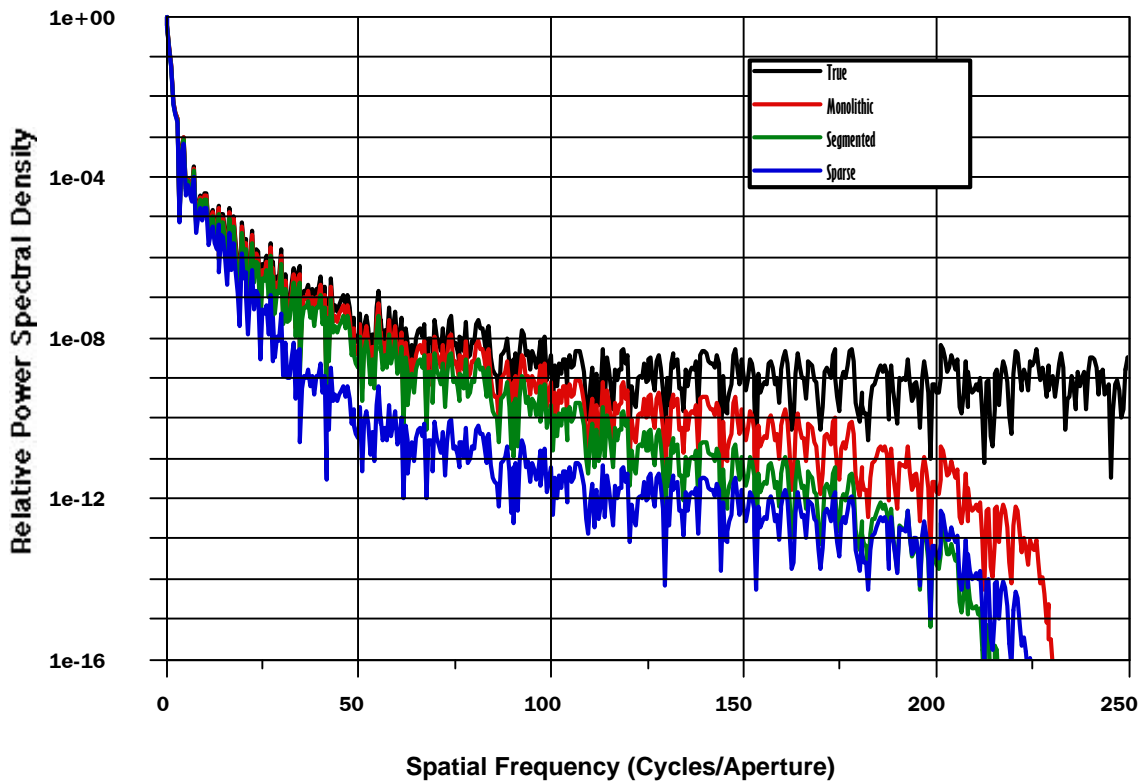


Figure 4
Saturn Image Power Spectral Densities

4. PHASE DIVERSITY

Phase diversity is a method which uses multiple observed imagery, Earth or extended astronomical objects, with a high fidelity computer model of an optical system. These are coupled to an inverse wave propagation algorithm, based on nonlinear optimization theory, to determine the phase function and hence the mirror shapes and misalignments, and, estimate the object, i.e. boost the spatial frequency response. Phase diversity will work with all the aforementioned mirror configurations and is still an active area of study. Shape determination allows for an adaptive optical control system to reshape the mirrors. This is directly useful to determine the on-orbit design as well as thermal/structural deformations, misalignments and potential rapidly varying dynamic errors of space based imaging systems. This would allow for the use of larger and lower cost mirrors than current monolithic mirror technology.

Model based image processing methods can be used to deconvolve, or reconstruct imagery, and phase retrieval methods can be used to determine the wavefront error in an optical system. At first glance these might seem mutually exclusive, however, they are tightly coupled. Image deconvolution requires the systems optical response, i.e. the point spread function (PSF), and generally this is not accurately known due to incomplete knowledge of the phase function. Thus, one desires to determine the object signature without completely knowing the system that created it. Determination of the phase function (phase retrieval) and deconvolution (object estimation) problem can be cast into a symbiotic hardware/software relation requiring the use of only one methodology, known as Phase Diversity. Thus one can recast the imaging problem as a tightly coupled phase retrieval and image deconvolution problem inherently coupled to the optical system either via phase retrieval or the use of active optics. It is this *Phase Diversity* which will be discussed with regards to the aforementioned optical configurations.

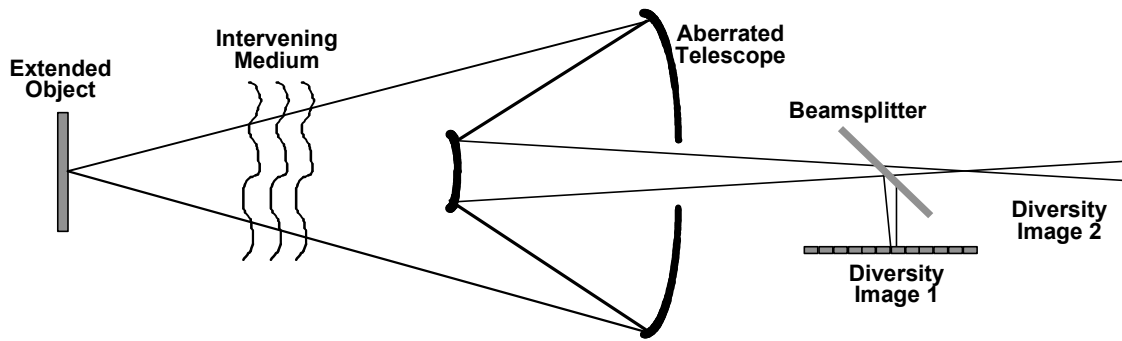


Figure 5
Conceptual Phase Diversity Imaging System

Figure 5 shows a conceptual optical schematic of a phase diversity system; both the telescope and the intervening medium contribute to the phase function of the entire system. The telescope by deterministic design residuals, and the unknown, but fixed, misalignments, fabrication errors, surface scatter and thermal/mechanical drift; the atmosphere by thermally induced, multi-layer, density changes contributing to stochastic phase fluctuations. In figure 5 the phase diversity is introduced via a beamsplitter to split the beam into 2 (or more) separate channels, each of which sees a large, known, phase aberration such as focus. The telescope and atmospheric aberrations occur in both channels (common mode) while the diversity is dissimilar each channel. Note that although focus is used in this simplified schematic it is not the only choice, just the simplest. The phase diversity method has not been shown to be either unique, convergent nor the results accurate, but, yet, it does appear to qualitatively work in practice, why, how well and what is the optimal approach? The optimal phase function introduced is currently unknown.. Thus the phase diversity problem is a rich research problem with potential applications in future NASA missions. Towards this end OSCAR has been researching, developing and enhancing different methods and attempting to quantify their accuracy, precision and range for each of the aperture configurations. Furthermore we are developing an experimental prototype benchtop system to research the problem in a controlled fashion. The goal being introduce a multitude of real world effects, at first, in an open loop fashion and to ultimately develop a closed loop optical control system. The primary limitations for closed loop control are a trade between accuracy/precision and computational horsepower. We have also been applying massively parallel and fault tolerant processing techniques to these methods.

Figure 6 shows a simulation of phase diversity for the monolithic aperture case. We introduced focus into a 2 channel imaging system. The top image shows the “true” extended object followed by images through channels 1 and 2 of a phase diverse imaging system. These 2 images are input, along with an optical systems model, to a phase diversity algorithm. This algorithm estimates both the phase function and the object. If we use an active optical control loop we can minimize this phase function giving an even higher quality image.

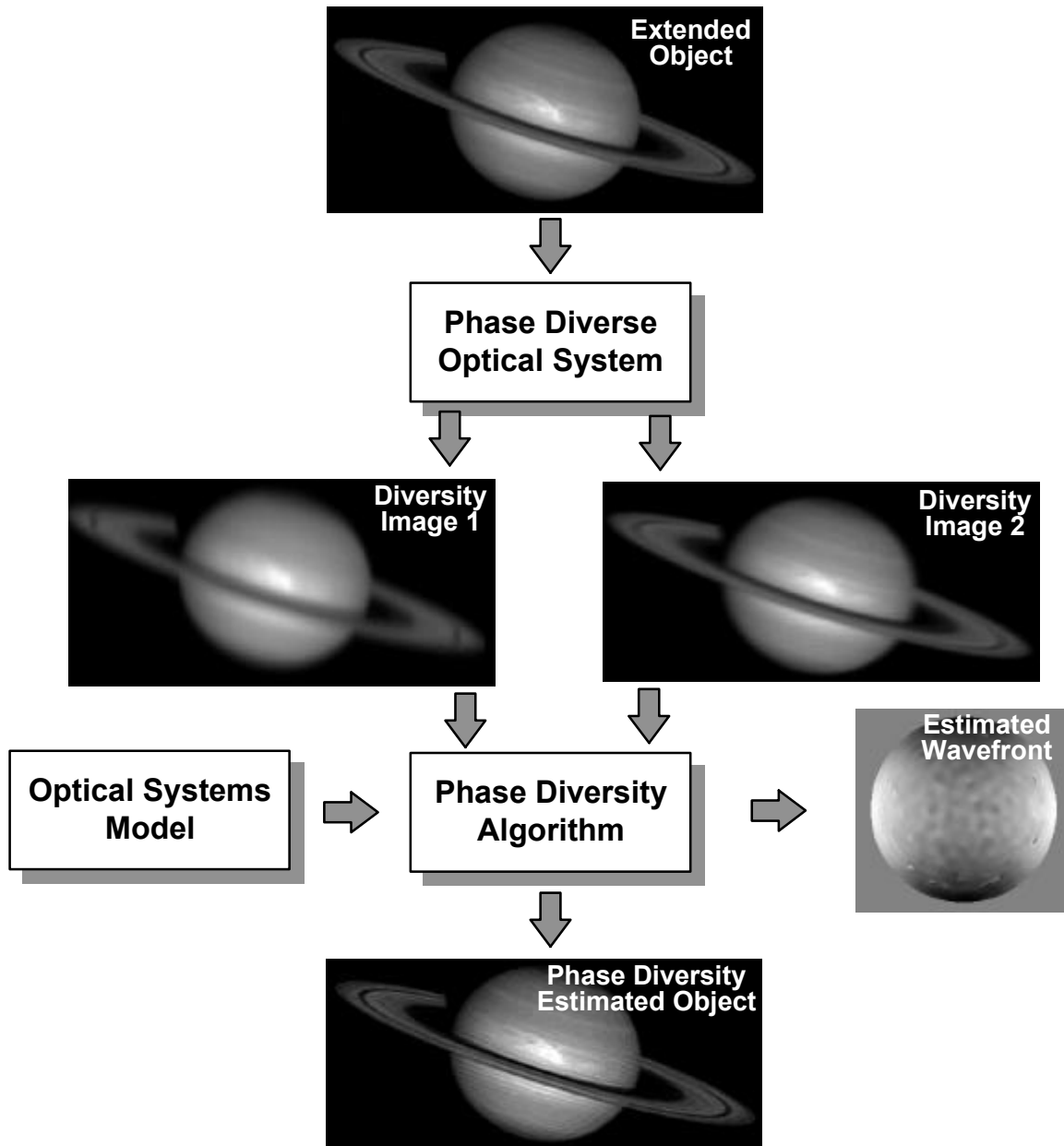


Figure 6
Phase Diverse Imaging Simulation

5. SUMMARY AND FUTURE WORK

In summary, we have given an overview of the different types of imaging systems potentially applicable to future NASA space imaging systems for both Earth and Space sciences missions. We have developed a comprehensive modeling package to model these systems and have the capability to include, diffraction, phase aberrations, scattering, sampling, finite detector size, photon and gaussian noise as well as model wavefront sensing including phase retrieval and phase diversity and optical control techniques for both open and closed loop. We have shown a simulations for the monolithic, segmented, and sparse apertures imaging systems and have shown a phase diversity simulation. In this overview paper we have forgone the quantitative results but are currently in the process of documenting and preparing them for publication.

6. REFERENCES

- (1) See <http://origins.jpl.nasa.gov>
- (2) See http://nmp.jpl.nasa.gov/index_menu.html
- (3) J. W. Goodman, " *Introduction to Fourier Optics* ", McGraw-Hill Inc., 1986
- (4) Lyon, R. G., Dorband, J. E., Hollis, J. M., "Hubble Space Telescope Faint Object Camera Calculated Point Spread Functions", *Applied Optics*, 36, No. 8 (1997).
- (5) Lyon, R. G., Hollis, J. M., Dorband, J., Murphy, T.P., "Extrapolating HST Lessons to NGST", Invited Paper, *Optics and Photonics News*, Vol. 9, No. 7 (1998)
- (6) Redding, D., Basinger, S., Bely, P., Burg, R. Lyon, R. G., Mosier, G., Femiano, M., "Phasing of a Segmented Aperture Telescope in Space", Proceedings of SPIE (Poster Paper), Vol. 3356, Kona Hawaii, March 1998
- (7) Deyoung, D.B., Dillow, J., Corcoran, S., Andrews, E.V., Yellowhair, J., Devries, K., "Ground Demonstration of an Optical Control System for a Space-Based Sparse Aperture Telescope", Proc. SPIE Vol. 3381, p. 181-192, Airborne Laser Advanced Technology, 09/1998
- (8) Deyoung, D.B., Deshetler, D.B., Kvasnack, M.A., "Low-cost space structure experiment optical phasing control system", Proc. SPIE Vol. 2478, p. 117-127, 06/1995
- (9) Lyon, R. G., Hollis, J. M., Dorband, J. E., "A Maximum Entropy Method with A Priori Maximum Likelihood Constraints", *Ap.J.*, 478, 658-662 (1997).
- (10) Leisawitz, D.; Mather, J. C.; Moseley, S. H. Jr.; Danchi, W.; Dwek, E.; Gezari, D.; Pedelty, J. Silverberg, R.; Staguhn, J.; Yorke, H.; Zhang, X., "The Uniqueness Space for SPIRIT and SPECS", American Astronomical Society Meeting 195, #88.07, 12/1999
- (11) Leisawitz, David; Mather, John C.; Moseley, S. Harvey, Jr.; Dwek, Eli; Feinberg, Lee; Hacking, Perry; Harwit, Martin; Mundy, Lee G.; Mushotzky, Richard F.; Neufeld, David; Spergel, David; Wright, Edward L., "The Submillimeter Probe of the Evolution of Cosmic Structure (SPECS)", The Physics and Chemistry of the Interstellar Medium, Proceedings of the 3rd Cologne-Zermatt Symposium, held in Zermatt, September 22-25, 1998

HORIZON

A Proposal for Large Aperture, Active Optics in Geosynchronous Orbit

Dennis Chesters and Del Jenstrom
NASA Goddard Space Flight Center, Greenbelt MD 20771

In 1999, NASA's New Millennium Program called for proposals to validate new technology in high-earth orbit for the Earth Observing-3 (NMP EO3) mission to fly in 2003. In response, we proposed to test a large aperture, active optics telescope in geosynchronous orbit, partnering with a corresponding technology demonstration in astronomy. This would flight-qualify new technologies for both Earth and Space science: 1) a future instrument with LANDSAT image resolution and radiometric quality watching continuously from geosynchronous station, and 2) the Next Generation Space Telescope (NGST) for deep space imaging. Six enabling technologies were to be flight-qualified: 1) a 3-meter, lightweight segmented primary mirror, 2) mirror actuators and mechanisms, 3) a deformable mirror, 4) coarse phasing techniques, 5) phase retrieval for wavefront control during stellar viewing, and 6) phase diversity for wavefront control during Earth viewing. Three enhancing technologies were to be flight-validated: 1) mirror deployment and latching mechanisms, 2) an advanced microcontroller, and 3) GPS at GEO. In particular, two wavefront sensing algorithms, phase retrieval by JPL and phase diversity by ERIM International, were to sense optical system alignment and focus errors, and to correct them using high-precision mirror mechanisms. Active corrections based on Earth scenes are challenging because phase diversity images must be collected from extended, dynamically changing scenes. In addition, an Earth-facing telescope in GEO orbit is subject to a powerful diurnal thermal and radiometric cycle not experienced by deep-space astronomy. The Horizon proposal was a bare-bones design for a lightweight large-aperture, active optical system that is a practical blend of science requirements, emerging technologies, budget constraints, launch vehicle considerations, orbital mechanics, optical hardware, phase-determination algorithms, communication strategy, computational burdens, and first-rate cooperation among earth and space scientists, engineers and managers. This manuscript presents excerpts from the Horizon proposal's sections that describe the Earth science requirements, the structural-thermal-optical design, the wave-front sensing and control, and the on-orbit validation.

1.0 MEASUREMENT CONCEPT/SCIENCE RETURN

The Horizon mission was proposed to the NMP EO-3 flight mission solicitation to be a partnership between NMP EO-3, funded through NASA's Earth Science Enterprise, and NGST, funded through NASA's Space Science Enterprise. The purpose of the joint mission was to validate in space large aperture telescope technologies critical to the future of both earth and space science programs. Horizon was designed to heavily leverage key technologies already under development for the NGST project.

The Horizon technology validation mission would enable continuous, real-time, Landsat-quality imagery to observe highly dynamic events on Earth. This would offer a revolutionary new view of Earth with real-time observations that are an order of magnitude improvement in spatial resolution over current geosynchronous orbit (GEO) measurements and three orders of magnitude improvement in temporal resolution over current low Earth orbit (LEO) capabilities.

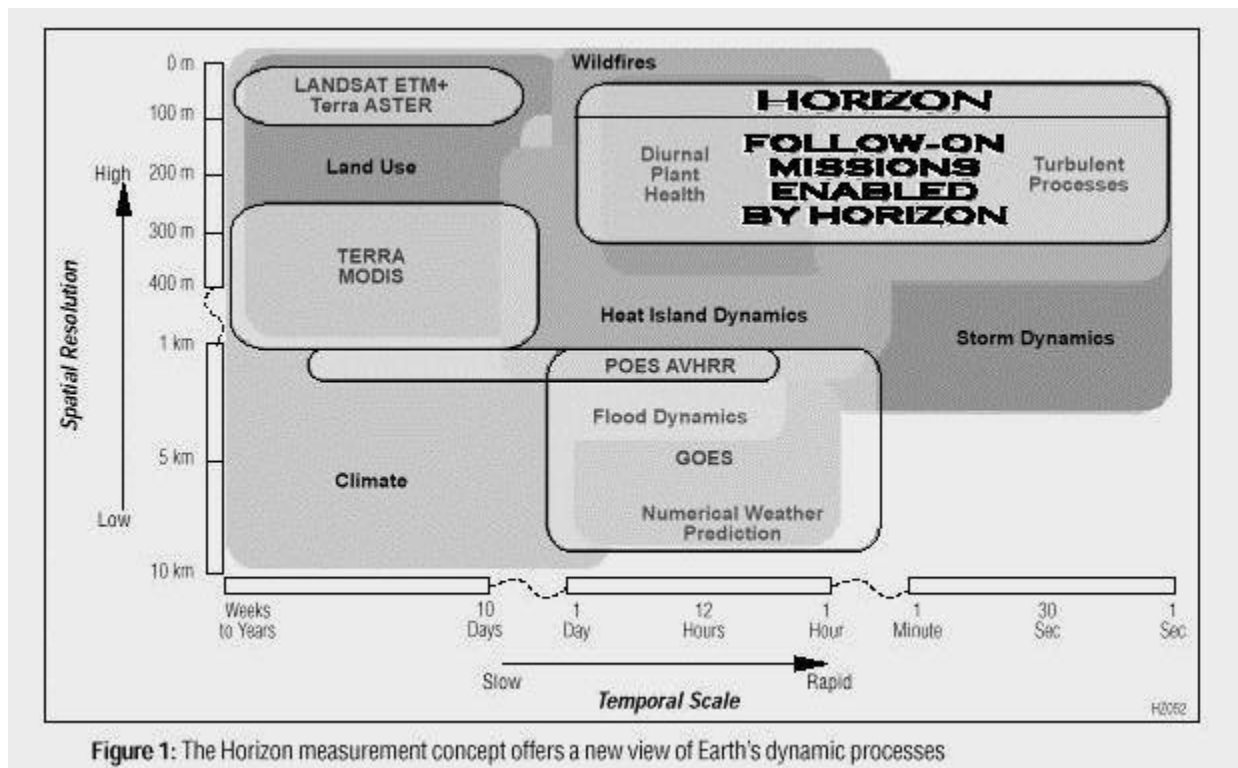
Current remote sensing systems provide either moderate resolution continuous coverage (GOES) or high-resolution periodic snapshots (Landsat) of the Earth's environment. Neither of these is sufficient to understand and monitor the development of dynamic land, water, and atmospheric processes. Wildfires, hurricane eyewall changes, and convective outbursts are on the scale of hundreds of meters and develop in minutes to hours. In order to achieve the temporal resolution required, the sensing system must be at GEO, which is the closest point to the Earth that allows continuous observation. However, the required spatial resolution is currently unachievable at GEO distances from Earth.

To meet this need, Horizon would flight validate breakthrough advances in lightweight segmented telescopes and wavefront sensing (WFS) and control technologies. The Horizon New Millennium demonstration of these innovative technologies and techniques would be not only the first application of

segmented aperture control for Earth remote sensing, but also the largest optical telescope ever launched for Earth-science-related activities.

1.1 Future Earth Science Return

There is ever-increasing demand in the research and operational communities for finer spatial and temporal resolution imagery of Earth. Horizon meets this demand by space validating imaging technology that can provide continuous coverage with spatial resolutions of 30 meters or better. For the first time, scientists would be able to observe environmental events at full resolution as they occur: convective outbreaks in hurricanes and tornadic storms, life cycle of wildfires, diurnal cycle of urban heat islands, and the chaotic thermal variations of oceans, rivers, valleys, snow fields and soil (Figure 1).



Among the priorities identified, there is a select set of measurements that drive the technology requirements to enable future science:

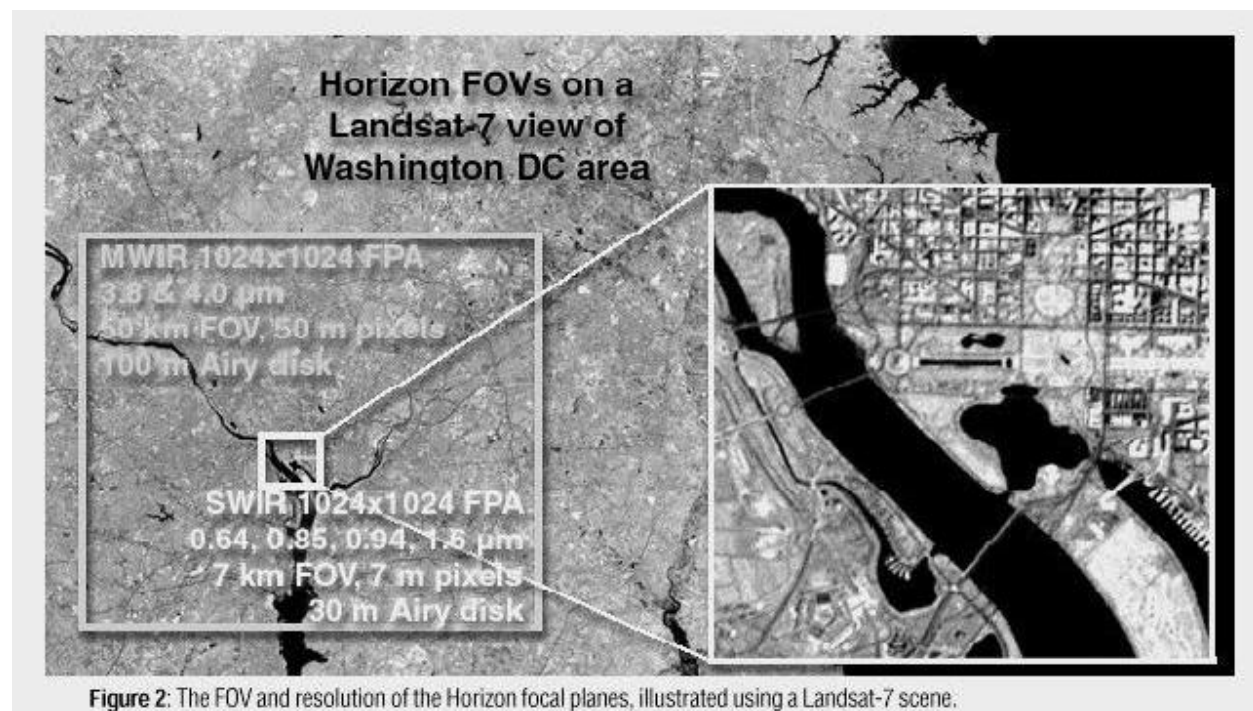
Intense Convective Storms: Severe thunderstorm initiation and growth processes occur on spatial/temporal scales much smaller than current satellite observing systems can detect (on the order of minutes and seconds). These processes must be properly resolved if scientific knowledge, public warnings, and forecast models are to be improved.

Life Cycle and Scale of Wildfires: Although most fires (both natural and man made) have time and space scales of minutes to hours and meters to kilometers, their impact on vegetation cover and aerosol generation is global. Additionally, fires are a localized natural hazard to human activity and natural ecosystems.

Diurnal Cycle of Surface Heating: Some land processes (e.g., the urban heat island heating/cooling cycle) require hours of monitoring with frequent image updates. Diurnal changes in surface temperature arise due to heat-capacity differences in landscapes, heterogeneity of soil moisture, and other urban effects. Such variability in surface temperature affects surface energy budget and local microclimates. Heating and cooling rates derived from continuous observations also provide a useful mechanism to infer soil moisture, a critical link in the atmospheric, hydrologic, and terrestrial cycles of the Earth.

Vegetation Classification: Vegetation is a constantly changing patchwork of small regions with different color, shading, health and hydrology. Decades of Landsat observations and ground truth measurements have resulted in thematic maps that document these properties. However, these remote surveys are taken by LEO satellites that pass over at a fixed local time-of-day. The apparent color, shading, and moisture of plant surfaces actually depend upon the solar illumination angle and angle of observation. For example, vegetative canopy under stress has a different appearance at different times of day. The color, shading, and temperature are all significantly different. Resolving small patches (~ tens to hundreds of meters) of stressed vegetation within larger regions under varying solar conditions is a breakthrough science measurement.

Applications: Horizon would enable detailed, continuous monitoring of conditions that are hazardous to human life or that have significant public interest or economic impact. For example, Horizon would provide an unprecedented vantage point for observing and tracking in real time the growth of active wildfires, enabling efficient application of fire fighting resources and other emergency response strategies. In addition, by measuring the diurnal cycle of apparent surface temperature and color of vegetation, Horizon can contribute to a flood or fire hazard index, particularly in large sparsely inhabited regions where remote sensing is cost-effective.



1.2 Measurement Concept

The Horizon concept is based on a set of key parameters for a future observing system that can provide multispectral imagery with spatial resolutions ranging from better than 30 meters (visible and near infrared) to 300 meters (long-wave infrared), image update rates as fast as 5 seconds, fields of view of 10 to 50 km or larger, and the ability to stare at an Earth target for 18 hours or more at a time. Figure 2 illustrates the field-of-view (FOV) and over-sampled, diffraction-limited spatial resolution proposed for the Horizon mission.

The need for continuous observation can be met only from GEO, and the need for rapid high-resolution imaging of local areas from great distances (36,000 km) from Earth requires a 3-meter-class or larger telescope with large detector arrays. The need to stare for long periods of time requires stable pointing and an ability to over-come the diurnal and seasonal solar environment of GEO. And, of course, the measurement concept must be affordable, both in a developmental sense and in the cost to reach GEO, if it is to be applied for research and applications. Affordability has been the greatest obstacle to realizing the desired measurements due to the cost of building and launching conventional large-aperture systems.

System Architecture : The proposed optical concept (Figure 3) includes a segmented-mirror optical telescope assembly (OTA) derived from the Next Generation Space Telescope (NGST). Each segment of the primary mirror is approximately one meter across. By applying NGST lightweight mirror technology, Horizon's primary mirror mass can be reduced by a factor of five or more over conventional approaches. In addition, each primary segment, or petal, can be made to be deformable to assist in on-orbit correction of aberrations. Each petal is movable by high-precision fine and coarse tip, tilt, and piston mechanisms to correct for post-launch misalignments. The secondary and tertiary mirrors of the OTA reimage the entrance pupil onto a small deformable mirror (DM) which may have as many as 350 actuators. Such a DM, also being developed under NGST, would be used to actively correct for thermally induced optical distortions, which the primary mirrors cannot correct and which otherwise degrade the imaging performance of the solar reflective channels. Following the DM in the optical path is a fast steering mirror (FSM), which can be used to compensate for spacecraft pointing jitter and can also quickly reposition the detector field-of-view (FOV) to create image mosaics of larger areas of the Earth within the telescope FOV. One or more simple staring focal plane array (FPA) cameras capture the imagery, and dichroic beam splitters might be used for simultaneously imaging thermal- and solar-reflective spectral regions.

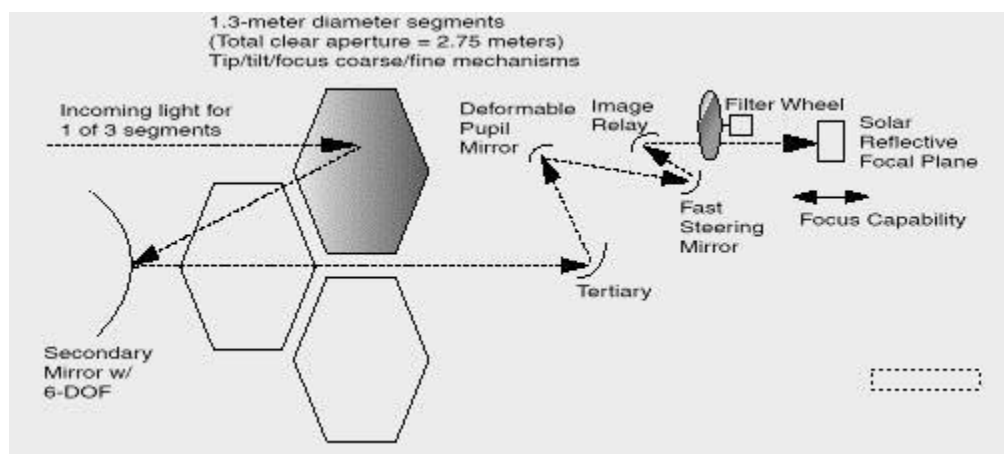


Figure 3: The Horizon concept for segmentation, active op-tics and wavefront control

A critical aspect of segmented imaging systems is that they require WFS and control techniques to establish phasing after launch and to maintain optical focus and phase between the segments, especially if visible or other shortwave imagery is to be produced. In large light-weight systems like Horizon's, the need for WFS and control is further amplified by the semi-rigid nature of large lightweight mirrors. NGST plans to solve this problem through the use of coarse phasing algorithms for initial system tuning and then phase retrieval algorithms for fine wavefront control (WFC). Both require star point sources imaged on a detector array to extract wavefront information. However, during Earth viewing, point sources would not be available, and regular slewing of the spacecraft to point to stars for phasing would greatly interfere with Earth observations. Therefore, Horizon would implement an innovative phase diversity algorithm for fine WFC using extended sources, such as clouds or ground features. This algorithm, to be space validated as an NMP technology, is key to enabling Earth observation using large aperture telescopes.

Physical Measurement and Conversion to Earth Science Data: Solid-state FPAs measure a voltage that is proportional to the incident radiative flux. Modern photovoltaic FPAs have slow drift rates and very little $1/f$ noise; regular views to an internal cold/dark target or cold space provide a solid voltage floor for such arrays. Fullaperture calibration is not practical for large aperture systems. A dark field can be viewed regularly in a filter wheel to determine zero-point radiance and to null slow drifts in baseline voltage. Detector gain can be determined by using occasional views of the moon and Earth, using deliberately out-of-focus and motion-blurred images. The digital counts from the individual pixels on the FPA can be converted on board the spacecraft using the "flat field" observations. Cross-correlation of physical values at Earth validation sites with well calibrated MODIS and Landsat radiometers can augment calibration if the instruments have similar spectral bands.

Once in the form of Earth-located brightness temperatures and albedos, satellite data products can be calculated using correlation with ground-truth sites and well-established algorithms

1.3 Space Validation

Horizon would be the first civilian demonstration of large-aperture optics for Earth remote sensing. Horizon requires the space environment to perform engineering and operational tests of the technologies and the overall system. The earth science validation measurements required for this mission cannot be obtained from a vantage point other than geosynchronous orbit.

Engineering and Operational Experiments: The segmented telescope architecture with its large, lightweight, deformable primary mirror segments would be subject to zero-g unloading and residual strain effects that are not well understood. Space flight is required to validate the ability to recover mirror figure and alignment after launch using the coarse and fine phasing algorithms and the many precision mechanisms.

Microdynamical snaps, which are rarely seen in gravity loaded, seismically disturbed laboratory tests, occur as structural loads change in nearly unloaded structures, for instance as the temperature changes. This provokes load relief in joints and materials, seen as a sudden local transient displacement, followed by a long ring- down period. The magnitude of the displacement can be optically significant, as proven by Hubble Space Telescope thermal ringing problems. Frequencies of the snaps are quite high and can change within single events. Experiments, including deliberately changing structural temperatures would help define conditions for onset of microdynamical snaps.

On-orbit experiments are also required to demonstrate and optimize phase control using real, variable Earth scenes. Measurements from space would determine the speed and frequency of re-phasing needed to maintain image quality as well as the true availability of scenes of sufficient contrast for phase diversity processing. Also, on-orbit data are required to validate and improve models that predict the impact of diurnal variations on thermal/structural/wavefront interactions. These models are essential for optimizing WFC and, hence, reducing costs for future Earth science missions.

Science Measurements: Finally, space-flight validation is required to characterize the new data sets that this measurement concept would provide. By collecting real-time, continuous Landsat-quality imagery from GEO, Horizon would validate for the science community an entirely new set of climate and land-use research tools. It is necessary to provide this precursor data set to begin the development of algorithms and data products to define science requirements for future missions. Figure 4 presents simulated multispectral scenes scaled to the Horizon FOV and resolution.

1.4 Science and Technology Validation

The mission requires geosynchronous orbit to validate the ability to achieve Landsat-quality imagery from that altitude and to accumulate the GEO solar loading environment to enable long duration imaging. The required 3-meter segmented telescope must be light-weight and of a deployable architecture to minimize future launch costs. Three mirror petals are the minimum to fully explore segmented aperture WFC, but a minimum validation can be performed with only two. Fine phase control of the telescope must be validated using real Earth scenes from GEO such that Landsat-class imagery can be obtained in the solar-reflective spectral region. These shorter solar reflective wave-lengths are more sensitive to variations in optical wave-front quality than are longer thermal wavelengths, thereby providing a more stringent validation of the measurement concept's ability to meet future science imaging needs. In addition, this enhanced wavefront sensitivity requires precise temperature stability within the optical path, just as thermal imaging requires temperature stability for thermal calibration. Hence, if solar reflective imaging can be validated, so then is the ability to do thermal imaging.

A minimal set of science validation measurements has been defined to compare Horizon data to other well-characterized data sets and to validate the ability to capture select environmental events and processes related to the driving science requirements discussed earlier. Horizon's high resolution

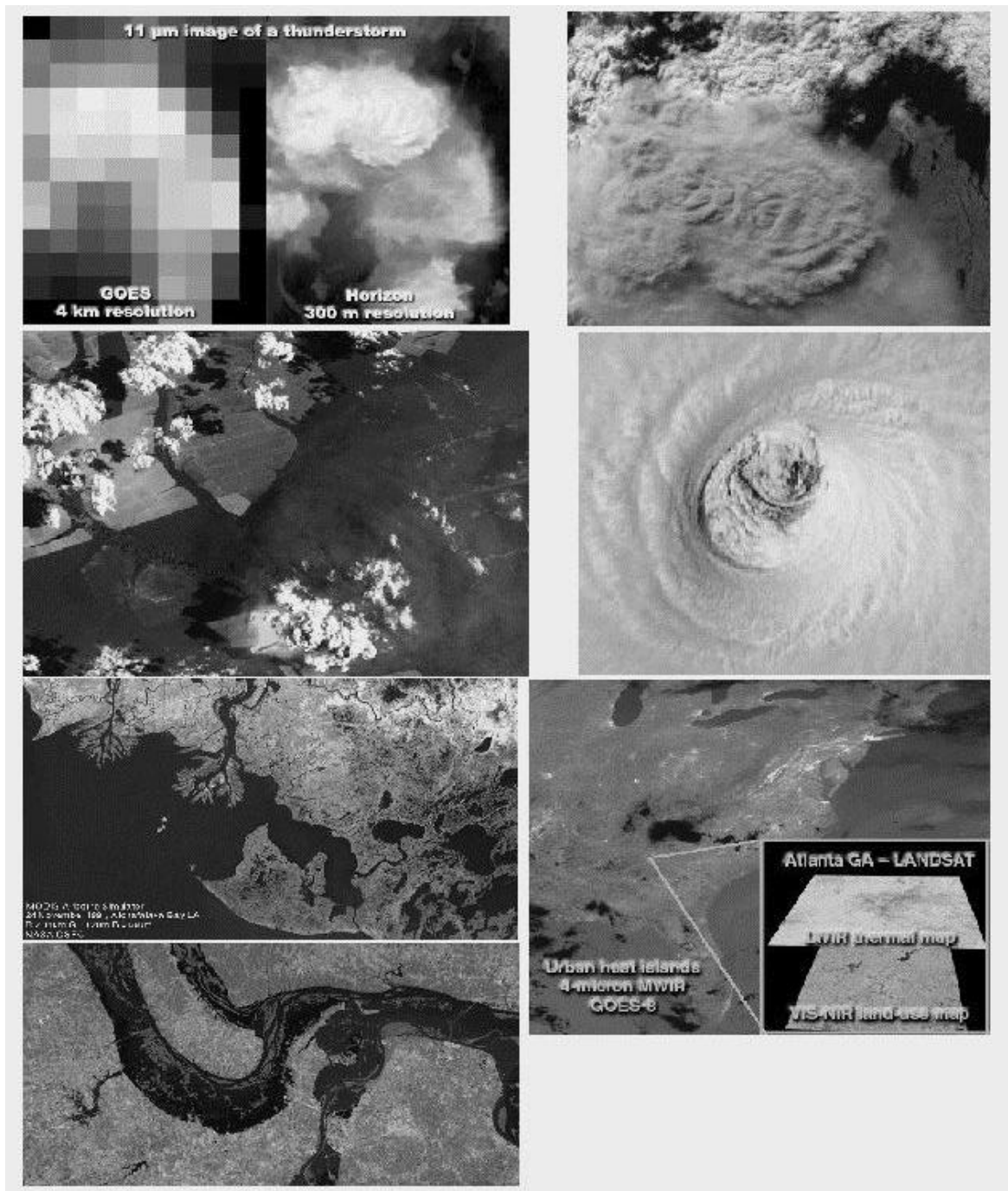


Figure 4: Examples of dynamic terrestrial processes at Horizon's FOV and spatial resolution, simulated using multispectral images from MAS, Landsat and the Space Shuttle. Clockwise from the top left: thunderstorm development (unresolved by GOES); cloud types and phase during convection; the dynamics of a hurricane eye wall; urban heat islands (one of many unresolved by GOES); flooding and effects on agriculture; coastal zone interactions between land, water and biota; the effect of land use and the role of fire and smoke in local climatology.

radiometric measurements must be validated using the coincident observations by LEO instruments with similar characteristics: ETM+ on Landsat and MODIS on Terra. Further, the study of such data from Horizon would greatly benefit trade studies conducted to select spectral bands for follow-on Landsat missions.

Horizon would validate the ability to observe selected dynamic environmental events and processes. The first three of these observations involve measurement of specific cloud features within convective storm and hurricane eyewall events that require rapid, high resolution imagery. The last two observations validate the ability to make longer duration measurements of land processes. The solar-reflective spectral region is ideal for validating the ability to extract plant heat and water content measurements as a function of solar illumination angle. Wildfire observations in the short-wave infrared would validate the ability to continuously monitor this rapidly changing and often small scale process, evaluating its diurnal behavior and determining the value of such observations for emergency response planning.

The design of the measurement payload is directly responsive to the measurement concept requirements. The telescope has an aperture diameter of 2.75 meters to validate the ability to achieve the required diffraction-limited performance. Deformable optics and WFC algorithms optimize the image quality and compensate for thermal-induced distortions due to seasonal and diurnal solar loading that plague Earth viewing telescopes in GEO. One spectral region will be used to validate the measurement concept: 0.8 - 2.4 μm . The N/SWIR band is needed to meet validation requirements for WFS and control while viewing Earth scenes and it serves the same function during stellar viewing. The large focal plane array (FPA) camera captures the multispectral data required to validate the measurement techniques.

The measurement payload is made up of an optical telescope assembly (OTA), infrared instruments, phase control algorithms, and the necessary control and calibration systems. Each is described in the following subsections.

1.4.1 Payload Leverages NGST Development

1.4.1.1 Optical Telescope Assembly

Horizon's OTA design reflects that this is a technology demonstration mission. Only requirements traceable to the technology and science validation are implemented. This is a major part of the cost and risk containment strategy. The OTA requirements are set to optimize the WFC experiments while ensuring the success of the science validation. In addition to these requirements, there are specific programmatic goals set by the NGST project. These include low temperature, 175 K, operation of the OTA in order to test the design and I&T concepts applicable to NGST and the use of lightweight mirror technologies being developed by the NGST project.

The Horizon OTA consists of three components: the optics, the structure, and the WFC system. The optical system is a three-mirror anastigmat. A three-mirror system can be designed to have a wide field-of-view (FOV) since spherical, coma and astigmatism can all be corrected. The optical design of the OTA was scaled from the yardstick design for NGST, which has been modeled extensively. The telescope is designed as an on-axis system but used off-axis to allow the light to travel between the petals to the aft optics on the back side of the optical bench. It has an accessible pupil for the deformable mirror (DM) and sufficient working distance to accommodate the fast steering mirror (FSM).

The light path, after reflecting off the primary and secondary mirrors, passes between the primary mirror segments and through a hole in the OTA optical bench. The light path in the aft optics is illustrated in Figure 3. Between the secondary mirror and tertiary mirror, the optics are folded out of the plane of the telescope. The fold mirror, the tertiary mirror, DM, FSM and another fold flat are all mounted together on an "OTA mini-bench". The OTA prescription was optimized over a curved focal surface, with a radius of curvature equal to the distance from the FSM to the focus, in order to minimize defocus as the FSM is scanned (Figure 5).

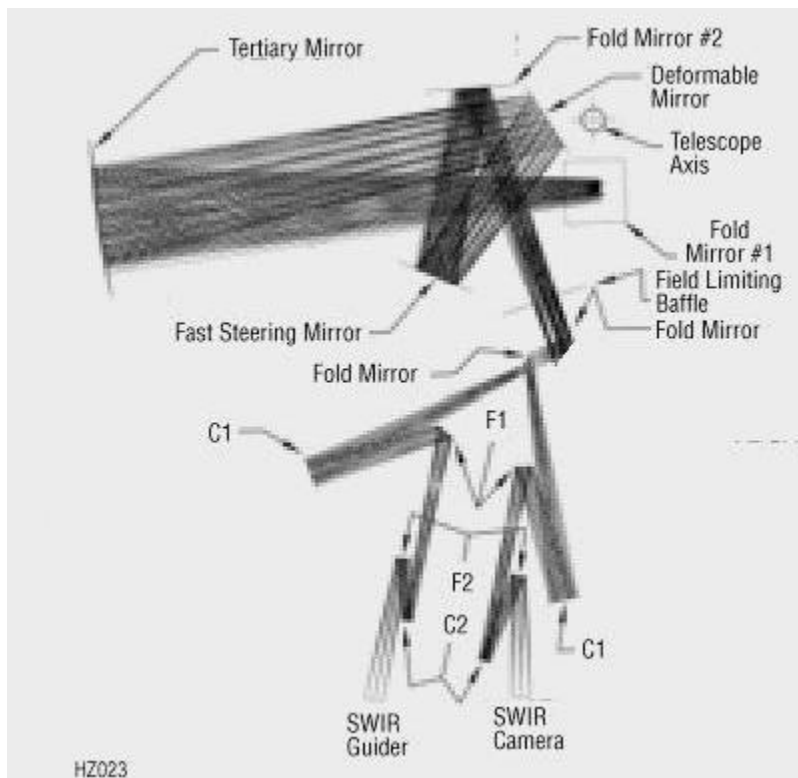


Figure 5: Horizon's optical design, shown in this ray trace diagram, meets image quality requirements.

The $f/1.25$ primary mirror is segmented into three identical hexagons, each 1.3 meters in diameter arranged in an axisymmetric geometry. Only one of the segments is deployable; this enables flight validation of the deployment and latching technologies without the cost and risk of deploying all of the segments. Concept study analysis shows that, because of stiffness considerations as well as manufacturing processes, the Horizon mirror segments must be larger than 1 meter in diameter. To fully validate lightweight mirror performance for both gravity release and figure control (in particular radius of curvature control), the mirrors must be large enough to be scalable to larger mirror segments for future missions. The secondary and tertiary mirrors are 0.635 meters and 0.356 meters in diameter respectively. The overall OTA has an f /number of 12. This is convenient when feeding the $f/24$ N/SWIR camera.

Detailed modeling shows that three-DOF active mirror mounts are needed for the primary mirror segments and that a six-DOF active mount is needed for the secondary mirror. Actuators with both coarse and fine stages are needed to enable both the large range of 1 cm needed for initial capture and the precision of 10 nm needed for diffraction-limited WFC.

The key component of the line-of-sight (LOS) orthogonal control system for stellar viewing is the FSM mechanism. It will also be used in Earth-observing mode to quickly reposition the FOV of the N/SWIR. The mechanism is simple – it uses voice coil actuators – and there are no significant problems for 175 K operation. The FSM will be momentum compensated in order not to excite the structure.

Segmented optics require a very high level of optical alignment stability in order to achieve diffraction-limited performance. This drives both mechanical and thermo-mechanical performance and tolerances. Non-segmented optics have alignment requirements of approximately $1\ \mu\text{m}$. With segmented optics the primary mirror segments must be aligned to a tolerance of about 10 nm, an increase in stability of two orders of magnitude. Active control with edge sensors can be used to relax alignment stability requirements (as in the Keck telescope). Passive alignment stability in the presence of small disturbances and temperature drifts is the preferred approach to minimize cost, mass, complexity, and failure modes.

At GEO the only external disturbance is due to solar loading, which is constant for stellar observing and has a 24-hour period for Earth observing. To compensate, the attitude control system (ACS) bandwidth will be set at 0.01 Hz. Using standard gyroscopes and star trackers, the LOS disturbance will be roughly 1 arcsec (rms). This residual disturbance is removed with the FSM for stellar pointing and by using fast snapshots (1/4 second or faster) in Earth-pointing mode. The error sensor for the FSM disturbance rejection loop comes from the guider camera when stellar pointed. This loop has a bandwidth of 1 Hz and produces the 10 milliarcsec stability needed for diffraction limited imaging. Above 1 Hz there is no disturbance rejection either for the stellar or Earth-observing modes. The only disturbance source is the reaction wheel assembly and Horizon modeling has demonstrated that off-the-shelf components along with a passive 1 Hz vibration isolation will meet the requirements of this mission. Furthermore, the first mode of the structure is designed to be 10 Hz or greater.

Horizon selected materials to meet stability and mass requirements. Horizon used coefficients of thermal expansion (CTE), mass, ease of fabrication as the criteria for evaluating Beryllium, SiC, Glass/CFRP and ULE glass options. Horizon's baseline architecture is a thin meniscus Zerodur™ glass mirror coupled to a CFRP reaction structure through an array of figure control actuators. Analysis shows that this design has a CTE of 0.06 ppm/K at 175 K and a low cumulative strain from room temperature to 175 K. With this architecture, the primary is fully deformable with coarse and fine corrections, and all WFC corrections can be made on the primary. Validation of this approach enables a much larger FOV than achievable with deformable mirrors only at the pupil. This is particularly important for Earth-observing missions where large fields are needed. Since Horizon will also have a deformable pupil mirror, both systems of WFC can be tested in flight. Furthermore, this allows for redundancy in the WFC system, which is the leading technology to demonstrate in this mission.

The primary mirror figure-control actuators developed by NGST are simple impact-driven nuts on precision lead screws. This actuator design is simple, has a low parts count, can be manufactured at a low cost, and is light-weight. It utilizes electromagnetic solenoids; thus performance is largely independent of temperature.

The thermal control system provides as stable an environment as possible in order to achieve diffraction-limited imaging throughout the orbit. The WFC system must remain stable for at least 24 hours without re-phasing when stellar viewing. This is possible in this mode due to the platform's inertial pointing which provides essentially constant solar loading resulting in a stable, lateral thermal gradient. When observing the Earth, the sun apparently revolves around the spacecraft causing the temperature field on the sunshade to change and resulting in a less stable WFC system. This drives the need for the ability to re-phase the telescope periodically while observing the Earth using the phase diversity (PD) algorithm.

The OTA is too large to meet the zero-thermal gradient requirement of an athermal design. Required stability in thermal gradients needs to be better than 0.01 K. Furthermore, an athermal design is not compatible with NGST or other envisioned follow-on missions. Consequently, Horizon will use low CTE components in the OTA, and a thermal control system to maintain temperature to the desired stability. The greatest sensitivity is due to distortion of the OTA optical bench causing primary-mirror segment piston errors. Simple thermo-mechanical distortion analysis shows that to meet the required 10 nm optical bench stability, the $CTE \cdot \Delta T$ product must be in the range of $1E-7$ to $1E-8$. Implementation requires combination of material CTE of approximately 0.1 ppm/K and thermal control to ± 0.1 K.

The optical bench is fully protected with multilayer insulation (MLI) to shield from the variable heat input over the orbit. Approximately 50 proportionally controlled heaters maintain the temperature to within ± 0.1 K of the set point. Without heaters, the peak warm case temperature seen during an orbit is roughly 145 K. The set point is placed at 175 K in order to have sufficient margin. Our analysis shows 25 to 50 W of heat input is required to maintain the OTA at 175 K.

The optical bench and secondary mirror tower will be made from CFRP which has a long history of use as an optical bench material. Near-zero CTE at the selected operating temperature is achievable through proper selection of fiber and resin, fiber orientation, and control of fiber fraction. It has a high specific stiffness and specific strength and is compatible with Invar.8 and titanium metal attachment fittings. The only drawback to CFRP is that it is susceptible to absorbing moisture and then subsequently out-gassing

on orbit. Horizon study analysis shows that this will not be a problem if proper handling techniques are used. Small, slow change on orbit can be compensated by the secondary mirror focus mechanism and the primary mirror actuators. The selected composite is M55J/954-3. It is cryo-compatible to 20 K and is often used in cryo applications. Furthermore, it has high fracture toughness and provides a CTE of <0.1 ppm/K at both 175 K operating temperature and at room temperature.

The optical bench structure consists of a planar structure for supporting all instruments and optics except the secondary mirror. The options for the secondary mirror support structure were a central tower or a tripod design. The tripod design was selected because of the excellent stiffness and strength-to-weight ratio. This design allows for a low-mass structure that has a first mode of approximately 20 Hz. It allows for lower cost and simpler design and construction. The tripod design has a better structural load path to the outer edge of optical bench and from there directly through bipods to the spacecraft primary structure. The optical bench planar structure is out of the load path of the secondary mirror assembly.

1.4.1.2 Wavefront Sensing and Control

Space telescopes have traditionally relied on massive, stable structures to preserve optical alignments through launch and on-orbit operation. This approach is extremely costly for large apertures. It is also cruelly vulnerable to fabrication errors—witness HST. WFC provides a means of recovering from alignment and figure errors induced by launch loads, space environment effects, and fabrication errors. WFC enables order-of-magnitude lighter optics and support structures, reducing mission cost proportionately. It also enables much larger apertures than can otherwise be considered through the use of deployable, segmented primary optics. Horizon would be the first mission to implement this new technology on orbit, providing a pathfinder for future Earth and space science missions.

Phase control begins at first light with millimetric wavefront errors and concludes with nanometer errors and a diffraction-limited telescope. The first steps are Coarse Adjustment (CA) and Coarse Phasing (CP), illustrated in Figure 6.

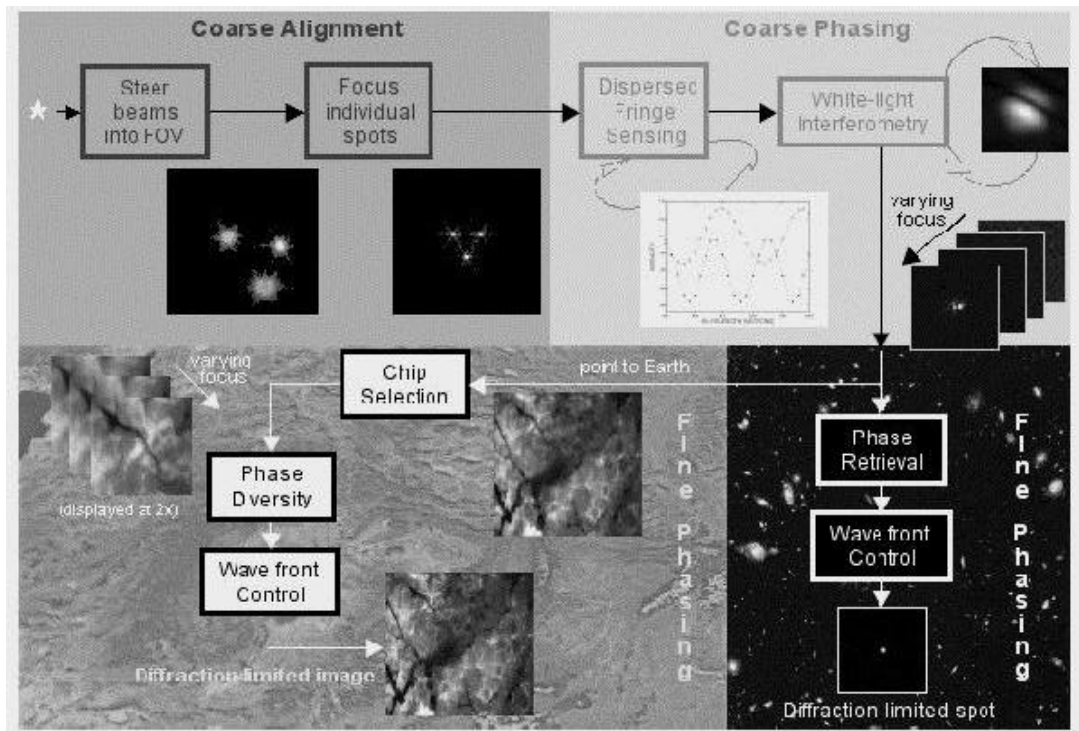


Figure 6: Horizon proposes a 3-step phasing strategy for Horizon WFC, with the final step being either phase retrieval for stellar observations or phase diversity for extended earth scenes.

CA manipulates segments singly using tip-tilt position actuators, scanning them to put their images on the N/SWIR detector. The spots are then driven into alignment and focused separately, to within approximately 10 μm of wavefront error.

CP works with segments in combination, using broad-band light to achieve coherent piston phasing to within a wave. The first step, dispersed fringe sensing (DFS), utilizes a grism in the N/SWIR filter wheel to disperse the light from two overlaid segment spots. The effect is to modulate the fixed segment path-length difference by wavelength, creating an interference fringe pattern with frequency proportional to the path-length difference. The DFS provides a large capture range (mm), but not exceptional accuracy (0.2 mm). To achieve sub-wavelength phasing, a white-light interferometry (WLI) step is also performed. One segment is moved in piston with respect to the other, and the peak intensity is recorded. The peak values map out an interference fringe, the brightest point of which indicates the best phasing. WLI phasing accuracy is limited by the figure error and the precision of the actuators, and will lead to less than 1 wave of error.

The next step is Fine Phasing (FP). FP consists of two parts: Wave Front Sensing and Wave Front Control (WFS and WFC). WFS utilizes focus-diverse images from the science camera, processed with either of two algorithms: phase retrieval or phase diversity. For the purpose of this mission, Phase Retrieval (PR) refers to wavefront estimation from point sources (stars) and Phase Diversity (PD) refers to Earth-science WFS from extended scenes. Both methods use a series of focus-diverse images formed by moving the focus mechanism in the N/SWIR camera. Each method produces a wavefront estimate that is processed by the WFC algorithm to correct not only the relative alignment of the segments, but also higher-order deformations of the segments and other optics. These corrections are imparted to the optical system using primary mirror-segment-deforming actuators and/or the DM. By taking into account the modes and the dynamic range of correction for each adjustable optic, an optimal apportionment of the wavefront correction amongst the actuators can be derived.

PR uses a modified Gerchberg-Saxton algorithm with four defocused star images to estimate the wave-front at high resolution (1 cm at the PM). Piston ambiguities are resolved by using wavelength-diverse data.

PD-based FP uses imagery from the N/SWIR cameras during daylight operations. The large-format N/SWIR images are analyzed for scene content and contrast to select sub-images that optimize WFS performance. Both PD and PR have comparable computational requirements on the order of a Mflop per image, requiring seconds to minutes of processing. Ground-based WFC can be repeated as often as every few minutes.

During observations, the segment alignments and figure settings are held without active WFC through careful suppression of disturbances. The chief causes of misalignment or deformation when on orbit are thermal deformation of the structure, vibrations due to on-board machinery, microdynamical "snaps" induced by load relief in the structure, and outgassing and other long-term effects. Vibration from the reaction wheels is the largest disturbance source for Horizon. Its effects will be minimized by passive isolation, which analysis shows is adequate to keep jitter and wavefront error below required levels.

From the standpoint of operations, FP will be repeated throughout the mission as needed. During astronomical observations, the observatory will be inertially pointed, and GEO automatically provides a benign environment for inertially pointed systems. Hence, thermal induced optical distortions are expected to be very low in this mode of operation, reducing the frequency at which FP must be performed. However, during Earth observations, the diurnal solar heating cycle will result in some amount of structural deformation due to thermal variation, especially if sunlight is allowed to shine into the optical aperture on internal baffle structures or optical elements. Thermal loading of the optical structures will be minimized by careful passive and active thermal control, including shielding of the optics from direct illumination by the sun, and use of heaters to precisely maintain a high bias temperature. Actual flight data are needed to determine how often and to what degree WFC can be optimized for future Earth and space science missions.

1.5 New Technology

The component-level technology suite selected for this mission provides high value for the measurement concept and for future Earth science missions. All of the technologies considered to be enabling are key elements within the measurement payload. Additional enhancing technologies either improve the performance of the observatory or promise to reduce the cost of future space systems.

The enabling component technologies are:

- Lightweight meter-class deformable primary mirror segments
- Primary/secondary mirror three- and six-degree of freedom (DOF) mechanisms
- Deformable pupil mirror
- Coarse Phasing (CP) using dispersed-fringe sensing and white-light interferometry
- Phase Retrieval Wavefront Control (PR WFC)
- Phase Diversity Wavefront Control (PD WFC)

The first three of the enabling technologies are fundamental to the operation of the large segmented telescope. The last three are technologies that enable the segmented telescope to be properly phased for sharp imagery during Earth viewing. CP is a technique used to initially align the telescope after launch using stellar sources. PR finely phases the telescope on star point sources, and PD does the same while looking at extended Earth scenes. Due to the dynamic thermal environment when looking at the Earth from GEO, it is anticipated that PD will be critical to enabling long duration Earth observation without large outages to slew off to look at stars. Flight validation of the ability to continuously observe the Earth while performing WFC using extended scenes is essential to prove the feasibility of large aperture Earth imaging systems.

The enhancing component technologies included in the baseline mission are:

- Deployment and latching mechanisms,
- Global Positioning System (GPS) at GEO,
- An advanced microcontroller.

The following subsections describe the details of the key technologies, the development roadmap, validation objectives and plans, and the future benefits to Earth science.

1.5.1 Enabling Technologies for Measurement Concept

1.5.1.1 Lightweight Meter-Class Deformable Primary Mirrors

Horizon's primary mirror technology is key to enabling future large telescope missions. With lightweight, deployable, controllable optics, future missions will no longer be limited to apertures that fit in a launch vehicle shroud. Lower mirror areal density equates to lower mirror, structure, and spacecraft mass, which in turn equates to lower launch vehicle costs and greater access to space. The primary mirror's areal density (15-25 kg/m²) is an order of magnitude lower than that of any current telescope.

Horizon will have a segmented primary, with three 1.3-meter segments providing the overall 2.75-meter aperture. The Horizon primary mirrors will have active figure control, using high-performance actuators to position the mirror in tip, tilt and piston and to control the relative radius of curvature (ROC) of the mirror segments within ~20 μ m. Absolute ROC control, feasible to within 2 mm, is not necessary, since it is only the difference that contributes to wavefront error. Additional figure control actuators may be used to compensate for on-orbit aberration sources and fabrication uncertainties.

The Horizon mirror candidates range from semi-rigid to fully deformable, and the degree of rigidity will be a selection factor in the Horizon downselect. A fully deformable primary allows the greatest range of on-orbit experiments, optimizing the roles of the primary and a deformable pupil mirror in providing wavefront error correction. However, these experiments are not required to validate the technology, so cost and technology maturity will be greater factors in the selection process. A partial list of the mirror developers is shown in Table 1.

Table 1: NGST mirror developers will supply Horizon mirrors

Developer	Program	Architecture	Deg. of Rigidity
U. of AZ	NMSD	Glass meniscus	Fully deformable
Composite Optics	NMSD	Glass/CFRP hybrid	Semi-rigid
Raytheon	AMSD	Glass meniscus	Fully deformable
Kodak	AMSD	Glass/CFRP hybrid	Semi-rigid

Horizon's baseline design has a goal of three primary mirror segments to best validate multi-segment phasing techniques. However, the validation of the WFS and control can be accomplished with only two segments. This descope option allows for one of the three flight petals to be used for space qualification through environmental testing, thus avoiding the added time and expense of manufacture of a dedicated qualification unit. It also allows for unforeseen damage to one of the mirror segments late in the Horizon development schedule, while still ensuring a viable validation mission. Mirror cost scales with diameter, so a final descope option is to reduce the diameter of the mirror segments.

1.5.1.2 Primary/Secondary Mirror: Three- and Six-DOF Mechanisms

All telescope designs that use lightweight, segmented optics require precision actuators to enable deformation for wavefront error correction. In order to provide coarse- and fine-stage deformation, these actuators must have repeatable performance, long enough stroke to bring the petals in and out for interferometry, and fine enough resolution for PR and PD. The stroke must be ± 0.5 cm and the resolution within ± 10 nm. This dual requirement can be met with either a single actuator or by a compound actuator with coarse and fine stages. Typically, actuators must also be stiff enough to withstand launch loads.

Horizon requires precision actuators for three DOF (tip, tilt, and piston) correction on the primary and six-DOF correction on the secondary mirror. The Horizon design incorporates the compound approach, with coarse actuators (± 0.5 cm stroke and ± 1 – 2 μ m resolution) used for identification. Fine-resolution actuators (± 30 – 50 μ m range and ± 10 nm resolution) are used for FP. Both sets of actuators must operate at 175 K.

1.5.1.3 Deformable Mirror

One planned Horizon experiment is to determine the extent to which phase control can be optimized using a deformable pupil mirror in addition to the deformable primary and secondary mirrors. Some researchers contend that fully deformable primary mirrors are required to obtain high quality imagery, while others contend that less expensive semi-rigid primary mirrors are optimal if a smaller deformable pupil mirror (DM) is used in the back optics for the fine phase correction. Depending on the final primary mirror selection and its degree of rigidity, Horizon would be able to validate in the GEO environment the relative performance of both approaches. With a fully deformable primary, Horizon can simulate each operating condition: deformable primary/rigid pupil, semi-rigid primary/deformable pupil, and both deformable, to varying degrees.

The Horizon design calls for a high density of DM actuators (>300 on the mirror) to provide fine phase control. This would be the first time a DM with this density of actuators, and hence fineness of phase control, has been put into space for imaging applications.

Desclope options include falling back to a smaller DM with approximately 97 actuators or eliminating the DM from the mission if fully deformable primary mirrors are used.

1.5.1.4 Coarse Phasing Using Dispersed-Fringe Sensing and White-Light Interferometry

There are three phases of Horizon WFC: capture, CP, and FP. All three phases of Horizon WFC take images of stars or Earth using science cameras, process those images to determine controls, and then implement those controls using primary segment actuators and the DM. They differ in dynamic range, accuracy, and processing techniques.

Horizon CP utilizes two white-light-detection schemes to provide segment phasing signals. Dispersed-fringe sensing (DFS) is a novel technique, utilizing a grated prism, a “grism,” in the N/SWIR filter wheel to detect phase errors. The grism has a large dynamic range to capture large errors. WLI scans segments to determine the best-phase condition with excellent accuracy, but it has a limited dynamic range. Combining both techniques results in a coarse-phasing capability that has high dynamic range and excellent accuracy. Total dynamic range is about 10^6 ; final accuracy is limited by segment actuator accuracy and segment figure error.

Horizon coarse-phasing functions are being developed and refined by NGST using the NGST DCATT and LMMS Multi-Ap testbeds. DFS performance has been demonstrated to be very good, with up to 0.5-mm phase errors accurately detected and corrected using Multi-Ap. DCATT results with up to 10- μ m phase errors have been repeatable to <100 nm. WLI is a well-established technique used in Fourier transform spec-trometers. A backup design using more conventional but less accurate edge sensors will be considered during the definition phase as a risk mitigation step.

CP will be validated by on-orbit experimentation. This testing will systematically misalign and then recover the optics. PR and PD will establish final accuracy.

1.5.1.5 Phase Retrieval Wavefront Control

In stellar-observing mode, WFC using PR picks up where CP leaves off, with 1-3 waves wavefront error (peak-to-valley). PR takes 4 defocused star images and 1 pupil image and processes them to estimate wave-front errors with high spatial resolution and accuracy. It then computes optimized primary segment actuator and DM controls to eliminate the residual effects of misalignments and figure errors. Final wavefront errors are dependent on actuator accuracy and figure errors beyond the spatial-frequency cut-off of the DM and will be well below the diffraction limit for the N/SWIR camera [Figure 7].

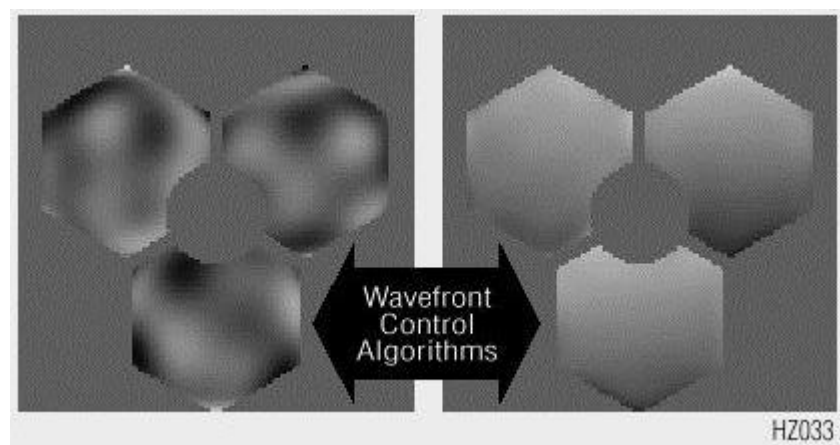


Figure 7: Comparison of mirror with phase error vs. phased mirror without error.

Horizon PR utilizes a novel algorithm to estimate the wavefront. It processes multiple defocused images in separate Gerchberg-Saxton inner iterations modified to use pupil images as a constraint. Phase unwrapping is done separately for each image's estimate and cross-checked with the others to prevent unwrap errors. Resolution is about 1 cm; higher resolution is easily achievable, but not necessary for diffraction-limited performance. Execution, which currently requires four minutes on a four-processor workstation, is speeded by using multi-processing and multi-threading techniques. New actuator settings are determined using sensitivity matrices comprised of the partials of wavefront error.

DCATT testing shows this PR algorithm is highly robust with respect to noise, jitter, bandwidth and other effects. The DCATT has demonstrated robust, accurate performance for the CP DFS and FP using PR (<1/100 wave at 0.63 mm for the latter). DCATT is running reliably using software and operational procedures that are directly traceable to those needed for Horizon. Analysis shows it should be better for Horizon, due to better point spread function sampling. DCATT DM actuation performance leaves residuals of better than 1/33 wave, currently limited by the DM actuator spatial resolution.

FP will be validated by on-orbit experimentation. This testing will systematically misalign and then recover the optics. Performance will be verified by calibration of in-focus point spread functions. Similar to CP, a more conventional backup design will be considered during the definition period as a risk mitigation step.

1.5.1.6 Phase Diversity Wavefront Control

The space-flight demonstration of PD WFS represents an important milestone enabling future lightweight mirror telescopes to operate adaptively, without the aid of a known beacon, thus supporting stated New Millennium goals of reducing cost through mass reduction and relaxed-tolerance fabrication. In Earth observing mode, PD provides fine phase control by estimating and correcting aberrations from both compact (point) signal sources and from extended scenes such as clouds or the Earth itself. The ability to perform WFC in an Earth-science mission without the need for a point-like source is critical to achieving the goals of continuous, fine-resolution imaging from GEO.

An additional benefit of PD for WFS is that it does not require a dedicated WFS device, but rather can use the science arrays. Many wavefront sensors have difficulties detecting discontinuities in the phase, such as inter-segment piston errors, but this is not the case for image-based wavefront sensors. PD data are theoretically more informative than are data from competing wavefront sensors. A survey of candidate wavefront sensors (including Shack-Hartmann, shearing interferometer, curvature, and PR) suggests that PD is the only wavefront sensor that can sense both inter-segment (piston and tilt misalignments) and intra-segment (segment misfigure) aberrations using low-contrast extended imagery.

PD WFS will be interspersed with Horizon Earth observations at a frequency dictated by aberration dynamics. Determining the optimal re-phasing frequency will be one of the Horizon validation experiments. PD utilizes multiple images from the N/SWIR at varying focal depths, collected while the scene and aberrations are unchanged. The PD algorithm uses these images to jointly estimate the aberrations and an undegraded image of the scene. Filters of varying thicknesses (implemented with filter wheels) will create differing amounts of defocus and regulate optical bandwidth of the images. The wavefront estimate error was 0.03 waves rms, which is well within the error bud-get for a diffraction-limited system.

Although PD is less mature in wavefront-sensing applications, PD has transitioned to operational capability for certain image-recovery applications. The PD WFS development plan for use on the Horizon mission identifies risks, retires risks with validation efforts and contingency options, and meets schedule requirements. Under this plan, the PD algorithm will be tailored to the Horizon mission by identifying the optimal wavefront parameterization, determining the preferred objective function (Gaussian or Poisson), and refining the chip-selection stage. A risk of encountering unanticipated modes of aberration on orbit will be managed by diagnostics using high-contrast scenes and incorporating new modes into ground-station code. The risk of algorithm stagnation at sub-optimal wavefront estimates will be evaluated with Monte-Carlo simulations that characterize performance as a function of SNR, scene content and dynamics, degree of aberration, and number of image channels. This risk will be retired by developing robustness strategies including more frequent corrections, use of chip-selection confidence metrics for data censoring, use of multiple initial wave-front estimates, and collecting additional image channels.

1.5.2 Enhancing Technologies Reduce Costs for Future Missions

Due to the aggressive nature of this mission, Horizon was very selective in choosing only three enhancing technologies for the baseline mission.

1.5.2.1 High Stability Deployment and Latch Mechanisms

A reliable deployment and latching system is a key technology for future large-aperture, segmented tele-scopes. The largest monolithic telescope that can fit within present and planned rocket shrouds is no larger than about four meters. High-stability latch mechanisms allow folding segmented mirrors to reduce stowed launch volume. On orbit, these mechanisms enable deploying the segments into a stable mirror with sufficient precision for the wavefront alignment system to capture the shape needed for a diffraction-

limited mirror. Coupled with low arealdensity mirrors, this deployable lightweight architecture enables the use of smaller launch vehicles to lower mission cost. The new technology is not the deployment function, but the precision of the deployment, about 1 μm , and the high-stability of the latching, about 10 nm.

1.5.2.2 GPS at GEO

This non-payload technology promises to reduce orbit-tracking costs on this and future GEO missions by making use of the GPS. The GPS satellite constellation was designed to provide accurate position knowledge to users on or near the ground but not to very-high-altitude users like Horizon. Study results show that when Horizon is in the Earth-viewing orientation, GPS may be able to provide 100-meter accurate orbital position knowledge on board the satellite. Conventional tracking from ground stations using the S-band transponders will validate this performance.

1.5.2.3 Advanced Microcontroller

The Advanced Instrument Controller (AIC), currently being developed by JPL through the NMP, is a small (2 cm x 3 cm), low power (0.05 W), self-contained computer with analog interface capability. The AIC provides, in a single chip, an 8051 microcontroller with 128 x 8 SRAM, 128 x 8 EEPROM, three 16-bit timers, an 24-bit bi-directional parallel port, an 8-bit parallel output port, four RS-422 ports, and 32 Analog-to-Digital converter (ADC) channels with 12-bit resolution.

1.5.3 Validating Science and Technical Performance

Horizon technology validation would consist of two phases. One would be the engineering evaluation of the technology while on orbit though analysis of specific image-quality parameters and component-level tests. Many of these tests would be done in conjunction with NGST through both stellar and Earth observations. This phase would also include radiometric comparison of Earth imaging data to data taken by underflying LEO instruments such as MODIS, ETM+, and ASTER. The second phase would consist of demonstrations of the ability of Horizon to capture dynamic environmental events.

Horizon would conduct a series of on-orbit experiments to enable optimization of telescope design parameters and control systems for future missions. For example, coarse and fine WFC would be validated by systematically misaligning and then recovering the optics. Statistics on accuracy, time-to-complete, etc., would be accumulated vs. initial misalignment and actuator error. Testing would characterize how often rephasing must be done in both Earth pointing and stellar pointing modes and would measure the impact of cloud motion and other scene dynamics on phase diversity retrieval accuracy. If the primary mirror is fully deform-able, then WFC experiments would be performed using both the primary mirrors and the deformable pupil mirror independently and together. Subsequent comparison of WFC performance would determine if either technique is superior or whether both technologies would be required to maximize performance of future large aperture missions.

Wavefront sensing algorithms like phase retrieval and phase diversity typically rely on Nyquist-sampled imagery. This is oversampled in comparison to sampling typically used for Earth science imagery. Horizon would experiment to determine the degree to which less-than-Nyquist- sampled imagery can be used for phase diversity WFC. The results of this experiment would enable future large aperture systems to maximize their achievable FOV for a given detector array size. The primary purpose of the Horizon mission is to demonstrate that a large lightweight segmented telescope can be built and flown to observe selected environmental events and processes from GEO—that is, to retire the risks associated with such measurements. Minimum technology and science validation requirements have been defined in Table 2.

1.6 Acknowledgements

The Horizon proposal was the result of teamwork between many, many people at Goddard, JPL, and industry. The Goddard proposal preparation office and Lisa May/Jackson-May Assoc. created an excellent document. Jim Adams/GSFC was project formulation manager. Richard Burg/GSFC defined the technologies for the astronomical mission, and Joe Burt/GSFC was the OTA manager. Dave Redding/JPL defined the astronomical phasing strategies, and Rick Paxman/ERIM International defined the phase diversity strategy. Dennis Evans/Evans Engineering designed the optics, and Jim Bremmer/Swales Assoc. engineered radiometric performance. Mission and instrument design were formulated by Goddard's Integrated Mission Design Center (IMDC) and Instrument Synthesis and Analysis Lab ISAL), respectively. The authors of this summary are Dennis Chesters/GSFC, earth scientist, and Del Jenstrom/GSFC, the Principal Investigator and Chief Technologist for the Horizon proposal.

Table 2: On-orbit validation requirements ensure value to future missions (technologies shown in bold)

Technology Validation Objective	Required Data / Measurements	Validation Approach	Minimum Performance Requirement	Expected Performance
Launch and Deploy 3-m class Segmented Primary Mirror (PM)	Telemetry will verify segment deployment and locking in place	Launch 2- or 3-segment PM with one segment stowed. Deploy stowed segment and lock it in place.	Launch 2-segment PM, each segment 1 m diameter. Val. stowing, deploying & precision locking of 1 segment to 3 mm	Launch 3, 1.3 m segment PM. Achieve precision locking of one segment to 1.5 mm
Mirror Mechanisms and Coars phasing	Measure motion of PM and Secondary Mirror actuators and observe star images	Wait for telescope to reach operating temperature. Using ground test data and analysis, set actuators to nominal best focus positions. Vary these positions	Val. predictions of cold, zero-g telescope alignments. Achieve 1 wave RMS @2 μ m	Achieve I/20 RMS @ 2 μ m
			Temperature is 293K	Temperature is 175K
Phase Retrieval (PR)	Images of stars will be processed on the ground giving telescope performance. Calculate corrective actions for actuator	Using star image data, command PM figure correction. Repeat process until no further improvement possible	Telescope corrected to I/20 RMS @ 2 μ m	Telescope corrected to I/20 RMS @ 1 μ m
		Using star image data, command needed Deformable Mirror (DM) correction. Repeat process until no further improvement possible	Telescope corrected to I/20 RMS @ 2 μ m	Telescope corrected to I/20 RMS @ 1 μ m
		Command temperature excursions around temperature setpoint and readjust PM or DM	Val. materials properties and structural modeling	
		Create calibrated mechanical shocks and determine performance change	Val. Microdynamic structural models	
Phase Diversity (PD)	Images of Earth scenes will be processed on the ground giving telescope performance. Calculate corrective actions for actuator	Using Earth image data, command PM figure correction. Repeat process until no further improvement possible	Telescope corrected to I/20 RMS @ 2 μ m	Telescope corrected to I/20 RMS @ 0.8 μ m
		Using Earth image data, command DM correction. Repeat process until no further improvement possible	Telescope corrected to I/20 RMS @ 2 μ m	Telescope corrected to I/120 RMS @ 0.8 μ m
		Slew off Earth, image nearby star	Val. PD=PR performance	
	Run PD algorithm at lower resolution	Combine pixels to change effective image resolution	Val. image resolution vs. telescope correction model	
	Process moon images	Image moon's edge	Val. predicted MTF	
Earth Imaging Quality	Acquire images from known Earth scenes Acquire moon scenes	Image ground path under ETM+ on Landsat and MODIS on Terra and PM1 in 3 or more spectral bands Image calibrated test sites Image moon	Val. pointing to 2 arcsec	Pointing to 1 arcsec
			Val. pointing stability of 16 milli-arcsecs over 5 seconds	10 milli-arcsec over 5 seconds stability
			Val. 30 m resolution	20 m resolution with image enhancement
			Val. 10% radiometry	5 % radiometry
	Acquire Earth images over 18 hrs and measure pointing shifts	Image 50X50 km Earth scene with FSM	Val. 5 arcmin telescope FOV	
		View site with a well-defined landmark. Run PD algorithm every hour	Val. <1 km image shift Val. 12 hour without need for PD correction	<0.5 km image shift Do PD correction once per day
Stellar Imaging Quality	Acquire star images	Point to designated star	Val. pointing to 2 arcsec	Pointing to 1 arcsec
		Control LOS with FSM	Val. pointing stability of 16 milli-arcsecs for 900 seconds	
		Image star pairs	Val. Image resolution: 120 milli-arcsec full width half max	
Earth Science Validation	Acquire Earth images of scientifically interesting events	Determine scientific value of continuous Landsat quality images anywhere in the Americas. See Foldout 1 for typical targets.	Val. ability to do new kinds of Earth Science	
Space Science Validation	Acquire "deep field" stellar image	Point to star field with low Zodiacal background for 12 days	Val. ability to see very dim stellar objects	
Solar intrusion into Telescope Baffle	After 11 months operation, allow sun to shine into telescope	On 4 successive days, start and stop sun avoidance maneuver 15 minutes later and earlier respectively than the previous day	Val. thermal control & PD performance with up to two hours of sunshine into baffle	
GPS at GEO	Compute orbit from conventional tracking	Compare GPS and ground track orbits (Earth observation mode)	Val. 200 m GPS orbit accuracy	100 GPS orbit accuracy
Advanced Microcontroller	Engineering performance data	Exercise control functions	Val. perf. upgrades since NMP DS-2 version	Meets engineering requirements

A Spaceborne Embedded COTS Cluster for Computational Optics

Daniel S. Katz and Paul L. Springer
Jet Propulsion Laboratory

ABSTRACT

Over the last decade and continuing into the foreseeable future, a trend has developed in the spacecraft industry of both number of missions and the amount of data taken by each mission increasing faster than bandwidth capabilities to send these data to Earth. The result of this trend is a bottleneck between data gathering (on-board) and data analysis (on the ground), which many missions try to avoid by running instruments at a low duty cycle. Another alternative is to overcome this bottleneck by performing data analysis on-board and only transferring the results of this analysis to the ground, rather than the raw data. However, this demands a dramatic leap in capability of on-board computing. One attempt to do this is being made by the NASA HPCC Remote Exploration and Experimentation (REE) Project, which is developing spaceborne embedded COTS clusters. These clusters, while originally intended to solve one problem (of limited bandwidth causing low duty cycles,) may also provide answers to many other questions, such as how to ensure segmented mirror systems maintain a flat phase front and how to use traditional CCDs to take long images in a relatively high radiation environment. These questions are now being examined by the NGST Supercomputing Study Group working with REE, as one part of the REE's vision is to enable new science that had not previously been considered feasible. We expect spaceborne embedded clusters will share many characteristics of the growing community of traditional, ground-based clusters (i.e.; Beowulfs) such as POSIX-compliant operating systems and message-passing applications, but they will also have significant differences, including packaging and the need for fault-tolerance and real-time scheduling in software. The similarities will allow software to be developed on standard workstations and ground-based clusters, and then ported with limited changes to the spacecraft. REE's intent is that as many of the differences as possible be hidden from the application developer by middleware. However, some of the differences, such as the fault rates that will occur when using commodity components in space will have some impact. This paper discusses both the similarities and the differences, and how they impact application development and application performance.

Adventures in Phase Retrieval: Lessons Learned from HST & SIRTf

John Krist
Space Telescope Science Institute

ABSTRACT

(Oral) Phase retrieval has been used at STScI since the days when spherical aberration was first discovered in HST. The primary tool we use is FITPSF, a program that iteratively compares model PSFs to observed ones using a nonlinear least-squares algorithm. The software can solve for aberrations, obscuration sizes and positions, and pupil illumination. A particularly useful feature is the ability to fit PSFs from multiple focus positions simultaneously, which significantly helps constrain a number of parameters, especially when PSFs are obtained on both sides of focus. When necessary, results from FITPSF can be used as starting guesses for a Gerchberg-Saxton phase retrieval algorithm, which is used to determine unknown obscuration patterns and non-parametric aberrations (such as zonal polishing errors). The FITPSF software has been used to characterize all of the HST cameras, either in pre-launch tests or on-orbit. It was applied to the verification of the corrective optics in WFPC2 and COSTAR. Detailed maps of the HST zonal errors were derived from out-of-focus PSFs taken with WFPC2 and have been used to improve PSF models generated by the Tiny Tim simulation program. FITPSF is currently being used to measure focus offsets and aberrations in the SIRTf IRAC cameras during ground tests, and it is in routine use for monitoring the HST focus. Lessons learned from experiences using phase retrieval will be described, including the utility of through-focus image sequences, the importance of avoiding vignetting when defocused, and how astigmatism is your friend when measuring nearly-in-focus images.

Pipeline Processing of Infrared-Array-Camera Images from the Space Infrared Telescope Facility (SIRTF)

Russ Laher
SIRTF Science Center
Laher@ipac.caltech.edu

Mehrdad Moshir
SIRTF Science Center

ABSTRACT

The Space Infrared Telescope Facility (SIRTF), the fourth and final element of NASA's Great Observatory program, is scheduled for launch into an Earth-trailing solar orbit in December 2001. Its Infrared Array Camera (IRAC) will provide 5.12×5.12 arcminute images of the celestial sky in four infrared bands centered at 3.6, 4.5, 6.3 and 8.0 microns simultaneously. Two InSb and two Si:As focal-plane-array (FPA) systems, each with 256×256 pixels, are used for raw image acquisition in the two shortest and two longest wavelength bands, respectively. The pixels are read out in four multiplexed channels, opening up the possibility of four separate bias drifts in the image data. Prior to distribution of the data to the relevant observers, the raw images will undergo several stages of automated processing at Caltech's SIRTF Science Center (SSC) to remove instrument artifacts and transform them into basic calibrated data (BCD) products. The image-data processing will be done for each band independently, and will include the following steps: 1) transformation of InSb data into the positive "sense"; 2) conversion of the integer image data to real numbers; 3) truncation correction; 4) detection and correction of wrapped-around negative data; 5) barrel-shift and Fowler-sampling number normalization; 6) electronic bandwidth correction; 7) latent-image detection; 8) dark-current subtraction; 9) dark-current channel-offset normalization; 10) linearity correction; 11) non-uniformity correction; 12) cosmic-ray/radiation-hit detection; 13) engineering-to-astronomical units conversion; and 14) quality-assurance characterization. The "science data-processing" thread will require several calibration products generated by at least five calibration threads of the pipeline. There are separate calibration threads for estimating the dark current, detector linearity, and image non-uniformity (field-flatness). There is also an ancillary thread that uses a Kalman filter for noise-mitigated estimates of the image non-uniformity measurements in time. A fifth calibration thread will provide gain and read-noise estimates for the images on a pixel-by-pixel basis. The scale factor that is required for the final step of converting data numbers (DN) into absolute flux densities will be determined by non-automated analysis. A "calibration server" will determine the latest and/or most-suitable calibration products to use in pipeline-reduction of a given data set. The pipeline design calls for modular software elements written in the UNIX-style of command-line inputs and outputs, with namelist capability for parameters that change infrequently. Higher-level scripts written in either Perl or C-shell will chain the relevant software elements into the various processing threads. Other scripts running under the automated pipeline processing with little operator intervention. All raw and processed images will be stored in FITS (Flexible Image Transport System) format, and will be archived at the SSC. Both raw and processed images and intermediate data products, as well as the calibration data used in the processing, will be made available to the appropriate SIRTF observers. Following a proprietary period, all SIRTF data will be made publicly available.

1.0 INTRODUCTION

As the scheduled launch date of December 2001 for the Space Infrared Telescope Facility¹ (SIRTF) fast approaches, the level of activity associated with SIRTF data-processing software design and development is ramping up at the SIRTF Science Center (SSC). In particular, several key software elements for processing data from SIRTF's onboard Infrared Array Camera (IRAC) have been implemented and unit-tested in the past year. Furthermore, the architectures of the various processing chains, or threads, needed to estimate the calibration data and reduce raw images, or Data-Collection Events (DCEs), into Basic Calibrated Data (BCD) have matured. High-level thread scripts have been written to direct the data flow through the software elements of the threads. Integrated software testing using both instrument test data and simulated data is now under way.

The SIRTF data flows along a circuitous route before finally reaching the SSC. Starting at the spacecraft, the data will be transmitted via telemetry to a ground receiving station where it will be sent to Jet Propulsion Laboratory (JPL) for processing by the Flight Operations System (FOS). The data will be separated into FITS (Flexible Image Transport System) images, housekeeping, pointing, and spacecraft-engineering data. The FITS image format is preferred by astronomers, who are the ultimate consumers of SIRTF data. The data will then be shipped to the SSC for processing into a calibrated form, that is, the BCD, which will be readily useable by the astronomy science community. The BCDs will be archived at the SSC, and will be eventually made available to the public.

This paper describes the architectures of the SSC's IRAC-data processing threads and the algorithms of its associated software elements that have been or are planned to be implemented in support of this aspect of the SIRTF mission.

2.0 IRAC DATA-PROCESSING PIPELINE

The pipeline threads described in this section process one or more raw FITS images of the same infrared (IR) band at a time. The production thread takes a single raw image and generates a calibrated image. A major requirement is that the processing of data for a given IR band must be independent of the other bands, even though the fields of view of the 3.6 and 5.8 μm bands, and the 4.5 and 8.0 μm bands are directly overlapping. The calibration threads typically process several images of a given type for good statistical results. The processing is done for the data associated with each pixel in the image.

In its most basic form, a FITS image of IRAC data consists of an ASCII-text header and a binary image-data portion. The header contains useful ancillary information about the image, such as where the telescope was pointing when the image was acquired and to which IR band the image data correspond. The binary portion consists of a single plane of 256 \times 256 pixels of 16-bit unsigned integer data. Both FITS header information and the image data itself are used in the pipeline processing.

2.1 Production Thread

The production thread is used for routine processing of science data. Other data taken for deriving calibration constants are processed by the calibration threads described in the next section. The calibration threads must be executed at least once prior to production thread operation, in order to generate the needed calibration quantities. Figure 1 depicts the data flow through the production thread. Generally, each box in the processing chain of Figure 1 represents a stand-alone software program, written in either C or FORTRAN, which is suitable for testing separately as a unit.

The first or TRANHEAD step translates the numerous FOS-encoded keywords in the FITS-file header, such as "A0123D00", into human readable keywords, such as "INSTRUME". It also averages groups of similar keywords to reduce the size of the header where possible, and derives quantities needed for the processing, such as the date/time of image acquisition, image exposure time, etc., which are then written to the output FITS header.

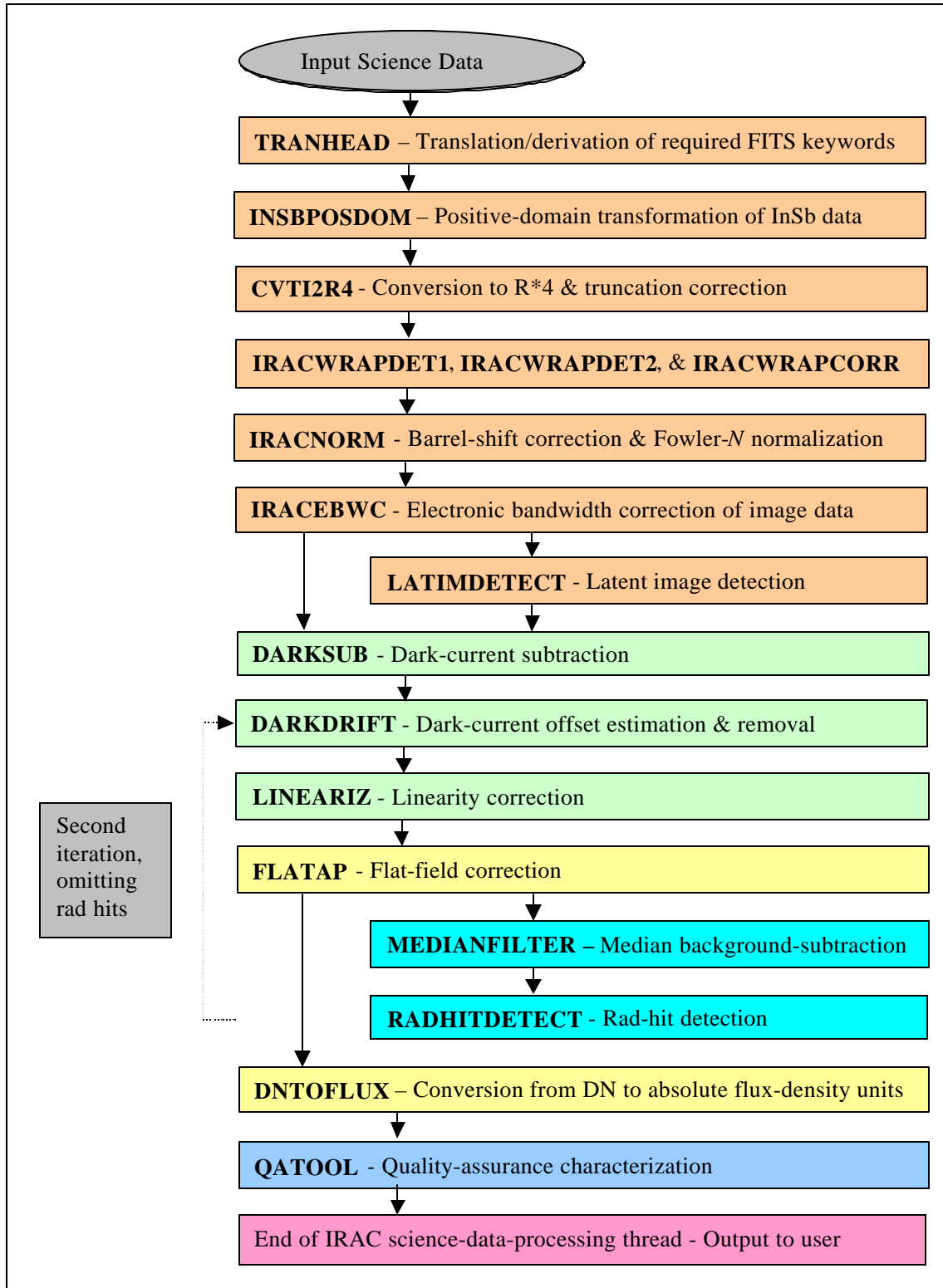


Figure 1. IRAC Science-Data-Processing Thread

The INSBPOSDOM step is executed only for band-1 (3.6 μm) and band-2 (4.5 μm) IRAC data. This is due to the conditioning of the data by readout electronics for these bands, which cause the data to decrease with increasing irradiance on the associated InSb focal plane arrays (FPAs). The purpose of this step is to transform the data so that it increases with increasing irradiance like the Si:As data from the two longer wavelength bands.

The CVTI2R4 step converts the 16-bit unsigned integer data into 32-bit floating data. It also optionally removes the bias in the data caused by truncation of the data's precision, which amounts to adding 0.5 DN (data numbers) to the data if it was right-bit-shifted on the spacecraft. This condition is determined by examination of the appropriate FITS keyword by the pipeline script, which then loads either 0.0 or 0.5 into CVTI2R4's command line.

The IRACWRAPDET1, IRACWRAPDET2, and IRACWRAPCORR steps transform data values in the high end of the unsigned 16-bit range, which has been reserved for the negative data values expected due to noise or bias drift, into small negative values. Generally, values greater than M , nominally 50000, will be "wrapped around" in the 2's complement sense by this software. The four multiplexed readout channels for each IR band are handled with separate M -value settings. IRACWRAPDET2 is currently just a stub, but it will eventually employ a more sophisticated algorithm than the simple thresholding used by IRACWRAPDET1, in order to distinguish radiation hits from wrapped-around values.

The IRACNORM step normalizes the data. It divides the data by the number of Fowler samples that were accumulated onboard the spacecraft during the data integration period. It also multiplies the data by 2^N , where N is the number of bits the data were right-shifted prior to transmission to the ground.

The IRACEBWC step performs electronic bandwidth correction, which is basically a time-domain deconvolution to remove the relatively slower response of the readout electronics from the underlying signal. This correction has been characterized separately on the ground for each of the four IR bands.

The LATIMDETECT step thresholds the data to determine the locations of bright pixels that may cause ghosting, or latent images, in subsequent data frames. A mask image of bright pixel locations is produced to facilitate image analysis and mitigation of this effect. This software element's companion reporting process, which combines LATIMDETECT results for relevant prior data frames into a latent-image map for the current frame, will be implemented within the next couple of months.

The DARKSUB step subtracts from the data the dark-current, which is determined via the DARKCAL calibration thread (see next section).

The DARKDRIFT step corrects the data for drifts in readout-channel biases since the last dark-current calibration, which can occur independently in each of the four multiplexed readout channels. DARKDRIFT has flexible operating modes, which allow the drift corrections either to be interpolated from "local" dark-current images (taken near the time of science-data acquisition), or estimated from the science data itself. The software also has in place a stub for temperature compensation of the drift corrections, which allows for variations in temperature between times of acquisition of the dark-current and science data. If deemed necessary, the IRAC instrument team will provide the correct temperature-compensation transfer function for this software.

The LINEARIZ step converts the data from observed values into linear values. That is, it linearizes the data over its entire dynamic range according to the linear portion of the response of each pixel, which tends to go nonlinear at high DN values. The linearity correction coefficients used by LINEARIZ are determined via the LINCAL calibration thread (see next section).

The FLATAP step performs the nonuniformity correction (also known as field flattening) to the data. This step requires a "flat" from prior execution of the FLATFIELD calibration thread (see subsection 2.2.3). The flattening is done by dividing the input image by the flat on a pixel-by-pixel basis. If the flat was determined from data acquired by flooding the FPA with the transmission-calibrator (TC) lamp (with the shutter closed), then an additional correction to make the TC illumination uniform is required. This is made by comparing a flat determined from sky data ("sky flat") and a flat determined from TC data ("TC flat") taken at nearly the same time.

The MEDIANFILTER step produces a local-median-filtered image using a nominal, 5×5-pixel, sliding input window, where the local median value is computed at a given pixel by centering the window on that pixel and using data values in the window. The local-median image is subtracted from the original image to produce a background-subtracted image. Note that this is an ancillary product used only in the next step (RADHITDETECT); the final output of this thread is a BCD that includes the celestial background.

The RADHITDETECT step detects radiation (cosmic-ray) hits in the background-subtracted image by application of an artificial neural network (ANN). The ANN is a standard hidden-layer type with sigmoidal nonlinearities, a 5×5-pixel input grid, 20 hidden nodes, and one output node². The ANN output is a value in the range [0, 1], and corresponds to the posterior probability of rad-hit presence. The ANN weights and biases are computed via off-line backpropagation training on ten workstations in parallel, in order to speed-up the training to three days per IR band. Data acquired during in-orbit check-out (IOC) will be used for ANN training and testing. Simpler filters, which have adequate but lower performance, will be used in place of RADHITDETECT until the ANN weights and biases are available. Testing at the SSC using simulation and cyclotron data has shown that this method of rad-hit detection has a false-detection probability of 4×10^{-4} at a threshold setting corresponding to a probability of true detection of 0.80. This performance is five times better than that of the conventional local-median spike filter. The products generated by RADHITDETECT include an image of rad-hit-presence probabilities, and a table of locations and strengths of rad-hit presence probabilities that exceed the rad-hit detection threshold.

The DNTOFLUX step converts the data values in DN units to some absolute units that have yet to be determined, such as Janskys ($=10^{-26}$ W/m²/sec). The conversion factor will be determined from analysis of suitable IOC data by an astronomer specializing in photometric calibration. Optionally, this software generates an additional BCD image with Not-a-Number (NaN) markers at the locations of bad pixels identified prior to and during the processing.

The QATOOL step performs various statistical calculations on the output BCD image for the purpose of providing a quantitative measurement of the data quality. Among the many statistics computed are the median, trimmed mean and standard deviation, and datascale³, which is a very robust estimator of distribution width that is relatively insensitive to outliers. The statistics are computed over the entire image, separately over the image quadrants, separately over the four readout channels, and also over a user-definable box in the image.

Although a final decision has yet to be made, there is the possibility that a second iteration through some of the software elements in the production thread will be done with the detected rad-hits excluded, in order to improve the final BCD product.

2.2 Calibration Threads

The calibration processes described in this section will produce an output mask image to indicate the problematic pixels of various types that may be encountered, in addition to their regular calibration products.

2.2.1 Dark-Current Estimation

The dark-current-estimation thread includes pre-processing by the orange blocks in Figure 1, followed by the DARKCAL process, which robustly averages a number of dark images (acquired with the shutter closed and stimulator lamps off) to produce an estimate of the dark current for a given IR band and integration time. Included in this processing is an outlier-rejection scheme, and uncertainty estimation. Prior to the averaging at each pixel across input images, the bias is computed for each readout channel separately and subtracted off. This yields an estimate of the dark-current on relatively long time scales, which is used in subsequent processing by the DARKSUB step of the pipeline.

2.2.2 Linearity Estimation

The linearity-estimation thread includes pre-processing by the orange blocks in Figure 1, followed by the LINCAL process, which analyzes a number of images taken for different integration times with the stimulator lamp(s) on and the shutter closed. The integration times must produce data that span its dynamic range to an extent suitable for determining the linear response of each pixel, and characterizing the nonlinear response range and saturation threshold level. After rejecting outliers, the remaining data are processed via a least-squares fit of linear values versus observed values. The fit coefficients are used in subsequent processing by the LINEARIZ step of the pipeline.

2.2.3 Nonuniformity Estimation

The thread for nonuniformity estimation, or field flattening, includes pre-processing by the orange and green blocks in Figure 1. It then executes the FLATFIELD process, which analyzes a set of equal-integration-time images of a sky region with a uniform background (with telescope dithering between image acquisition for point-source rejection in the median calculations). Alternatively, it can also analyze a set of TC images taken with the shutter closed, but in this case, it needs to apply a correction for nonuniformities in the TC illumination. Outlier rejection is included in this processing. At each pixel, a normalization factor, also known as a flat-field correction factor, is computed for equalizing the response of the associated detector to all others in the FPA. The flat-field correction factors for all detectors in the FPA are assembled into a FITS image, known as a “flat”. As an option, pixel-by-pixel statistics of the stacked images are computed and outputted for use by the gain/read-noise estimation thread (see subsection 2.2.5). A flat produced by this thread is used in subsequent processing by the FLATAP step of the pipeline.

2.2.4 Nonuniformity Tracking

This thread deals with the possibility of noisy flat-field estimates by implementing a separate Kalman filter⁴ at each image pixel to make improved state estimates of flat-field correction factors propagating in time. This form of filtering assumes independent, Gaussian-distributed process and measurement noise. The inputs to the FLATTRACK process used in this thread include the noise-mitigated flat-field state estimates at the previous time and the current flat-field estimates at the current time from the FLATFIELD process. FLATTRACK outputs a noise-mitigated flat-field state estimate at the current time. This thread is executed separately for flats associated with each different integration time of interest. A filtered flat produced by this thread can be used in place of a non-filtered flat in production processing.

2.2.5 Gain/Read-Noise Estimation

The GAINREAD process is executed in this thread after pre-processing by several runs of the FLATFIELD thread for data sets with different integration times, where the range of integration times result in good coverage of the data’s dynamic range at every image pixel. The GAINREAD process employs the conventional signal-versus-variance technique⁵ to estimate the gain and read noise at each image pixel. This involves least-squares fitting a line to the input data at each pixel. The gain, in units of electrons per DN, corresponds to the inverse of the line’s slope, and the read noise, in units of electrons, is derived from

3.0 CALIBRATION SERVER

A “calibration server” will be implemented for the purpose of providing the appropriate calibration data to the science-data processing thread. For example, production processing of a raw image will require, among other things, subtraction of a dark current image taken with the *same* integration time. Thus, the calibration server must be capable of searching a “library” of dark-current images for the correct one to apply.

The calibration server’s “brain” will be programmed with sets of rules specific to the various types of observations possible, many of which will dedicate a certain amount of observing time for acquisition of new raw calibration data, which are processed by the calibration threads and used to update the calibration data base. The development of this vital component of the SIRTf software subsystem is currently in an early stage; however, significant progress in this area is expected to occur over the next six months.

4.0 DISCUSSION AND CONCLUSIONS

The data-processing pipeline, with its various threads for generating BCDs and calibration products, has a modular design. Each software element in the pipeline is a stand-alone program with well-defined inputs and outputs. Software control is provided by parameter passing via command-line and/or namelist. This design facilitates upgrading the methods employed in the software elements as the development progresses. It also allows the software elements to be easily reconfigured as the processing requirements evolve and the interplay among the processes becomes better understood. This design philosophy has served the development effort very well so far.

The software elements have been developed to be as general and flexible as possible. For example, data memory is allocated dynamically by reading the image size from the FITS header. This allows many of the IRAC software elements to be used in pipelines for the Infrared Spectrograph (IRS) and the Multiband Imaging Photometer for SIRTf (MIPS), which are the other science instruments onboard SIRTf. These instruments produce images of different sizes than the IRAC, so it is important that the software be flexible enough to handle this without having to re-compile. It is noteworthy that the pipeline for the MIPS 24- μ m data is in many ways similar to that for the IRAC data; some differences are that the MIPS 24- μ m images are smaller (128 \times 128 pixels), and require an additional correction for the “droop” effect.

For initial non-automated pipeline-thread testing, Perl-wrapper scripts have been written to chain the software elements together such that the output of one process becomes the input to the next process. Either these scripts, or translated C-shell versions of these scripts will be implemented for the final testing under an automated-processing executive.

Pipeline-thread testing is now under way. In late March, several test images from the IRAC instrument were processed by FOS and made available for testing at the SSC. Exercises were conducted with the dark-current, linearity, and flat-field calibration threads, as well as the science-data processing thread. Here are some preliminary results of the testing. The flat-field results using a small 8.0- μ m image set indicate a preliminary image flattening to within 1.2% (1- σ). The dark-current results for the 3.6- μ m data show a pseudo-mux-bleed artifact in the data, which is not present in the 4.5- μ m data, even though the same FPA technology is utilized. For removal of this effect from the 3.6- μ m data, another software element (not shown in Figure 1) will be required.

The success realized thus far has proven the robustness of the pipeline design. Between now and launch the additional software that is required will be developed and software refinements will be made. Much more testing with simulated and instrument data is planned.

5.0 ACKNOWLEDGEMENTS

The support of the National Aeronautics and Space Administration (NASA) is gratefully acknowledged.

6.0 NOMENCLATURE

ANN	Artificial Neural Network
BCD	Basic Calibrated Data
DCE	Data Collection Event
FPA	Focal Plane Array
FOS	Flight Operations Software
IOC	In-Orbit Check-Out
IR	Infrared
IRS	Infrared Spectrograph
IRAC	Infrared Array Camera
JPL	Jet Propulsion Laboratory
MIPS	Multiband Imaging Photometer for SIRTf
NaN	Not a Number
NASA	National Aeronautics and Space Administration
SIRTf	Space Infrared Telescope Facility
SSC	SIRTf Science Center
TC	Transmission Calibrator

7.0 REFERENCES

1. Fanston, J., G. Fazio, J. Houck, T. Kelly, G. Rieke, D. Tenerelli, and M. Whitten, The space infrared telescope facility (SIRTf), Proc. SPIE, Vol. 3356, pp. 478-91, August 1998. Further and more up-to-date information on the SIRTf mission can be found at <http://sirtf.jpl.nasa.gov/sirtf>.
2. Pao, Y.-H., *Adaptive Pattern Recognition and Neural Networks*, Addison-Wesley, Reading, Mass., 1989.
3. Rousseeuw, P. J. and C. Croux, Alternatives to the median absolute deviation, Journal of the American Statistical Association, Vol. 88, pp. 1273-83, 1993.
4. Bar-Shalom, Y. and T. E. Fortmann, *Tracking and Data Association*, Academic Press, Boston, 1988.
5. McLean, I., *Electronic Imaging in Astronomy: Detectors and Instrumentation*, ISBN 0-471-96972-9, Wiley and Sons, 1997.

Optical performance modeling of a FUSE telescope mirror using METDAT and OSAC software

Timo T. Saha and Raymond G. Ohl
NASA/Goddard Space Flight Center, Greenbelt, MD 20771

Scott D. Friedman and H. Warren Moos
Center for Astrophysical Sciences, Department of Physics and Astronomy, The Johns Hopkins University,
Baltimore, MD 21218

We describe the Metrology Data Processor (METDAT), the Optical Surface Analysis Code (OSAC), and their application to the image evaluation of the *Far Ultraviolet Spectroscopic Explorer (FUSE)* mirrors. We found an excellent correlation between experimentally measured and theoretically predicted encircled energy at UV wavelengths and conclude that the FUSE telescope mirror meets its encircled energy requirement of 90% of the energy within 1.5 arcseconds at 100 nm.

1. INTRODUCTION

The *Far Ultraviolet Spectroscopic Explorer (FUSE)* instrument – designed and developed by the Johns Hopkins University and launched on 24 June 1999 – is an astrophysics satellite which provides high resolution spectra ($\lambda/\Delta\lambda=20,000$ -25,000) in the wavelength region from 90.5 to 118.7 nm.¹⁻³ The *FUSE* instrument is composed of four co-aligned, normal incidence, off-axis parabolic mirrors, four Rowland circle spectrograph channels with holographic gratings, and delay line microchannel plate detectors.

The Metrology Data Processor (METDAT)⁴ program is used in conjunction with the Optical Surface Analysis Code (OSAC)⁵ program. METDAT is designed for the analysis of mirror surface metrology data. The program reads in laboratory metrology data, e.g., optical path difference maps in a normalized format. The code then fits the data using annular Zernike polynomials for normal incidence systems or Legendre-Fourier polynomials for grazing incidence systems. It removes low-order polynomial terms from the metrology data, calculates statistical autocovariance (ACV) or power spectral density (PSD) functions, and fits these data in the analytical models for the OSAC scatter analysis. The details of the METDAT program are discussed in Section 2

The OSAC program⁵⁻⁸ is designed to evaluate the optical performance of optical systems including system fabrication and alignment errors. The program provides full analysis of the system performance, including, geometric ray trace calculation, optical surface scatter, and aperture diffraction analyses. The program can model near normal incidence mirror systems intended for infrared, visible, and ultraviolet wavelength regions and grazing incidence mirror systems intended for x-ray applications. The code also properly accounts for reflectance losses on the mirror surfaces. Low frequency surface errors for the ray trace analysis are described in OSAC by using annular Zernike polynomials for normal incidence mirrors and Legendre-Fourier polynomials for grazing incidence mirrors. The scatter analysis of the mirror is based on scalar scatter theory.⁹ The program accepts simple, analytical ACV or PSD models fit to mirror surface metrology data as input to the scatter calculations. The end product is a user-defined pixel array containing the system point spread function (PSF). In Section 3 the overall flow and major features of the program are discussed.

In Section 4 and 5 we briefly describe the FUSE mirror design and the laboratory image testing of the FUSE spare mirror performed in the near and vacuum ultraviolet at Johns Hopkins University (JHU)^{10,11} and OSAC modeling of the test setup performed at Goddard Space Flight Center (GSFC). The test setup is a typical double-pass configuration. The modeling is based on Zernike fitting and PSD analysis of surface metrology data measured by both the mirror vendor (SVG Tinsley, Inc.) and JHU. The results of our models agree well with the laboratory imaging data, thus validating our theoretical model. Finally, we predict the imaging performance of this mirror in the flight configuration at far-ultraviolet wavelengths.

2. METROLOGY DATA PROCESSOR (METDAT)

METDAT⁴ program analyzes surface metrology data and produces all of the required polynomial coefficient and scatter parameters to describe the surface error for subsequent OSAC performance analysis. The program flow and major functions are shown in Figure 1. The program divides the metrology data into two components: figure error and a statistical description of residual roughness. The program is written in FORTRAN IV and has been implemented on the DEC/VAX platform.

The INPUT routine of the program reads in the surface error data set in a specific normalized format for normal incidence mirrors or grazing incidence mirrors. Several data sets can be combined using the COMBO routine. The FITPOLY routine fits the data to annular Zernike polynomials for normal incidence mirror geometries and Legendre-Fourier polynomials for grazing incidence mirror geometries. There are a maximum of 325 Zernike polynomials and 101 Legendre polynomials available for fitting. METDAT outputs the annular Zernike or Legendre-Fourier coefficients that can then be read by the DRAT routine of OSAC program for ray trace analysis. The RMVPOLY routine removes the annular Zernike or Legendre-Fourier 'figure error' terms from the data.

The residual surface error is then analyzed using statistical ACV or PSD routines. These parameterized functions can be input to OSACs scatter routine for mirror scatter analysis. The ACV is determined from the surface height error function $\delta(r)$ by calculating the expectation value $\langle \delta(r)\delta(r-r') \rangle$ using standard methods for a discrete set of data points. Nine ACV models are available for use in the program. These include exponential, Gaussian, modified Bessel function $K_0(r)$, a product of exponential and cosine, a product of Gaussian and cosine, a product of exponential and inverse of the lag length, and combinations of the above ACV models. The PSD is defined in METDAT as:

$$\text{PSD}(f) = \text{FT}(\delta(r)) \text{FT}(\delta(r))^* / (P(r)) dr^2, \quad (1)$$

where FT denotes a Fourier transform and $P(r)$ is a pupil function which is unity inside the aperture and zero outside it. For normal incidence systems the PSD is calculated from a discrete set of data points using the above equation. In the case of a grazing incidence surface the PSD is calculated from the surface ACV through the Hankel transform. In this case the PSD is based on the axial surface data alone. The PSD models available are an inverse power function that can be defined in several segments and a modified Lorentzian model. If requested, the program fits the calculated ACV and PSD functions to analytic functions available in OSAC.

The purpose of the GRATING routine is to allow the user to analyze the PSD of residual surface error sets as an additive pair of sinusoidal errors that are perpendicular to each other. This is useful, for example, for analyzing a surface primarily influenced by an underlying grid structure.

The METDAT optionally returns the polynomial coefficients (annular Zernike or Legendre-Fourier) and PSD or ACV fit parameters for subsequent OSAC analysis. The program will also output processed surface error sets or calculated PSD and ACV files.

3. OPTICAL SURFACE ANALYSIS CODE (OSAC)

The OSAC code was originally developed by the Perkin-Elmer Corporation about 20 years ago.⁵⁻⁷ Since then, Bauer Associates, Inc. has improved and added several new features to the program⁵. Most significant additions include the implementation of high amplitude scatter theory (no limitation on the magnitude of Strehl ratio), the addition of the PSD models as an input to the program, and the addition of wavefront tolerancing capabilities. The wavefront tolerancing option is not covered in this paper. The program is written in FORTRAN IV and has been implemented on the DEC/VAX platform. Bauer Associates is currently implementing new version of OSAC program designed to run under Microsoft Windows on a PC. This version will also include the METDAT program.

OSAC is composed of a set of twelve compatible programs that are executed in a user-defined sequence. The flow of routines used in the analysis of the *FUSE* telescope mirror is shown in Figure 2. The wavefront tolerancing routines are not shown in the figure.

The first routine, GEOSAC, simply sets up the geometry of the optical system. The base surfaces currently allowed by the program are: on-axis conic, off-axis conic, fold flat, grazing incidence conic, toroidal surface, and obscuration surface. In practice any surface shape can be analyzed by using the surface fitting routines described later. The real part and imaginary part of the dielectric constant of the surface or coating are required input parameters to model the reflectivities of the surfaces and the efficiency of the system.

Geometric ray trace is accomplished by using the NABRAT and DRAT routines. NABRAT traces an input bundle of collimated rays through an optical system that consists of two (conic) elements. No other surfaces are allowed. DRAT traces a bundle of rays through multiple elements with arbitrary distortion from their ideal prescriptions as specified in the GOESAC routine. The DRAT module uses the annular Zernike polynomial coefficients (normal incidence mirror) or Legendre-Fourier polynomial coefficients (grazing incidence mirror) calculated by METDAT to trace a system with non-zero figure error.

SUSEQ and DEDRIQ programs are used to analyze system scatter properties. The purpose of SUSEQ is to provide a mapping from scatter angles at optical surfaces to ray displacements at the focal plane. DEDRIQ calculates the amount and distribution of scattered light for each ray and transfers this scatter pattern to the focal plane with the help of scale factors calculated by SUSEQ. DEDRIQ utilizes scalar scatter theory.⁹ The program can directly solve the scatter integral^{5,9} using Fourier transform techniques. However, if the optical system Strehl ratio is 0.8 or higher, approximated scatter integral is used to simplify calculations and speed up program run time.⁵ The evaluation of scatter integral implemented in DEDRIQ requires the knowledge of the surface ACV or PSD. The METDAT program can calculate these parameters for all of the models and send them to DEDRIQ. In the past, exponential ACV model has been often used. However, quite often this model is not realistic since it leads to f^{-3} falloff of the PSD spatial frequency f at high frequencies. The modified Lorentzian PSD model implemented recently in OSAC is more practical. This model is expressed as:

$$\text{PSD}(f) = A D / (C^2 + f^2)^{B/2}, \quad (2)$$

where A is square of RMS surface roughness (σ^2), $D = (B-2)f_0^{B-2} / 2\pi$, C is a breakpoint in the spatial frequency f at which the PSD tends to change from constant to a power falloff, and B is the power law falloff.

The OPD and PSF routines calculate the system pupil function and its Fourier transform to give the system point spread function at the focal plane.

Finally, the FPLOOK program is used to combine the information from the DRAT, DEDRIQ, and PSF modules. The output of this routine is a user defined focal plane pixel array describing the system point spread function.

4. FUSE TELESCOPE MIRRORS

The FUSE instrument consists of 4 independent Rowland circle spectrographs fed by 4 telescope mirrors. Detailed descriptions of mirrors optical design, mounting scheme, surface error measurement, and optical performance testing are given elsewhere.^{10,11} Five mirrors were fabricated, one of which is a spare. The spare mirror is very similar to the others in terms of surface error. In this paper, we concentrate on the modeling of the *FUSE* spare telescope mirror using METDAT and OSAC.

The mirrors are rectangular off-axis paraboloids with aperture dimensions of 352x387 mm, focal length 2245 mm, and off-axis angle about 5.5 degrees. The figure error, mid-frequency error, and microroughness were measured by the mirror manufacturer (SVG Tinsley). After the delivery to JHU, figure error measurements using a different interferometric technique were performed during assembly and qualification.

The figure error, mid-frequency error and microroughness measurements at Tinsley covered roughly the spatial periods 350 – 3 mm, 10 – 0.1 mm, and 100 – 2 μm , respectively. Figure 3a displays the METDAT fit to the figure error derived from one of the interferometric data sets taken after the mirror was attached to its

mounting hardware. The figure error shown is a fit of 37 Zernike terms to the figure data. This number of terms is a good representation of the surface error spatial frequency below the breakpoint between scatter and geometric ray trace for mirrors of this surface quality. The strong Y-shaped figure error is the result of distortions attributable to the mirror mounting structure.¹² The RMS figure error is 0.049 waves at 633 nm. Figure 3b shows the residual surface error after removing the content of 37 Zernike terms. 'High' frequency content of the residual error is dominating. A low order error (few cycles over the length) is also seen at front and back edge of the mirror. The RMS for this residual error is 5.6 nm.

Figure 4 shows the radially averaged 'figure' PSD calculated from the interferometric data after removing the content of 37 Zernike polynomials. We call this error low mid-frequency error as opposed to high mid-frequency error measured by Tinsley in 10-0.1 mm⁻¹ frequency band. The high mid-frequency PSD is also calculated using METDAT by averaging the PSDs of several 10-cm diameter spots on the mirror surface. The average high mid-frequency RMS error is about 1.2 nm. As-delivered mirror low mid-frequency PSD (Tinsley data) is clearly below the post assembly PSD's (measured independently by Tinsley and JHU) at low frequencies (up to 0.03 mm⁻¹) indicating the figure change during mirror assembly. The post-assembly PSD measured by JHU falls below Tinsley data due to low sensitivity of their setup in this frequency band. Unfortunately, the microroughness PSD is not shown in the figure since it was not readily available to us. Tinsley measurements indicated an average microroughness of about 0.37 nm.

The composite PSD model shown in Figure 4 consists of two models of the type shown in Eq.(2). The low mid-frequency model corresponds to the PSD calculated from the figure error files and the high mid-frequency PSD was forced to match the high mid-frequency data and the microroughness data. Numerical values of the parameters that were entered into OSAC are given in Table I.

5. LABORATORY IMAGING TEST OF FUSE TELESCOPE MIRROR

The JHU imaging tests of the *FUSE* spare mirror were performed using a double-pass setup (Figure 5).¹⁰⁻¹² The tests were run at two wavelengths (436 nm and 254 nm) in the ambient laboratory atmosphere and at one wavelength in a nitrogen-purged environment (185 nm). The test setup consists of a Hg discharge source, the *FUSE* off-axis parabolic mirror under test, an autocollimating flat mirror, and a tomographic imaging detector. Two additional, small fold flats (#1 and #2) are used in the optical train to accommodate the light source and the detector.

Interferometric testing of the autocollimating flat and fold flats #1 and #2⁹ indicated that they are much smoother than the *FUSE* mirror in terms of the figure error and comparable in terms of surface roughness. Thus, we ignore the scatter effects of the flats in the model. The ~45 degree angle of incidence and the location of the flats close to the source and detector also change the effects of scatter for a given spatial frequency, since the scatter angles viewed from the detector are much larger for the fold flats than for the *FUSE* mirror. Also, the experimental setup was limited by high background outside of the central core of the image where the microroughness would contribute significantly to the image.

The imaging test and associated modeling were further complicated by an unstable test setup.^{11, 12} The *FUSE* mirror drifted out of alignment over the course of an imaging test. This caused the image to become slightly defocused and comatic.

Figure 6 a and b display the measured and modeled encircled energy at 436 nm and 185 nm. In both cases the model closely resembles the measured encircled energy curve. The dashed curve in Figure 6 a shows also the encircled energy curve assuming only the effects of the light source and estimated mirror tilt errors but no figure error on the *FUSE* mirror and no scatter from the surface. This curve clearly indicates that the tested system is sensitive to figure variations across the mirror surface. Good agreement between the testing and modeling validated our figure error and scatter models for the *FUSE* mirrors and demonstrates that we can use this model to predict the optical performance of the mirrors in their intended wavelength range of 90 – 120 nm.

6. FUSE MIRROR PERFORMANCE AT 90 - 120 NM

We created a new OSAC model for single-pass setup closely resembling the flight configuration. Figure 7 shows the encircled energy curves at 90, 100, and 120 nm. As can be seen, the curves are not strong functions of wavelength in this narrow wavelength range, figure error is dominating the energy content inside the central core, and the high mid-frequency/microroughness errors scatter a very small amount of the energy out from the core. Figure 7 also shows the encircled energy resulting from aperture diffraction alone at 100 nm assuming no other errors in the system. One can conclude that the *FUSE* mirror is not diffraction limited in the FUV. The encircled energy curve for the figure error alone clearly indicates that this error dominates the central core and is the cause of image broadening. In spite of these surface imperfections, the *FUSE* spare mirror meets the imaging requirement of 90% in 1.5 arcseconds at 100 nm.

7. ACKNOWLEDGEMENTS

We gratefully acknowledge the *FUSE* team at SVG Tinsley for providing mirror metrology data.

8. REFERENCES

1. H. W. Moos, et. al., ApJ, in press (2000).
2. D. J. Sahnou, et. a., ApJ, in press (2000).
3. D. J. Sahnou, S. D. Friedman, H. W. Moos, J. Green, O. Siegmund, SPIE Proceedings, **3356**, 552-556 (1998).
4. P. Glenn, Metrology Data Processor (METDAT) Version 2.0 User's Manual, NASA/GSFC, (1994).
5. T. T. Saha, Optical Surface Analysis Code (OSAC) Version 7.0 User's Manual, NASA/GSFC, (1993).
6. P. Glenn, Opt. Eng. **25**, 1026-1033 (1986).
7. R. J. Noll, P. Glenn, and J.F. Osantowski,, SPIE Proceedings, **62**, 78-82 (1983).
8. T. T. Saha, D. B. Leviton, and P. Glenn, Appl. Opt., **35**, 1742-1750 (1996).
9. P. Beckman and A. Spizzichino, *The Scattering of Electromagnetic Waves from Rough Surfaces*, (Pergamon Press, New York, 1963).
10. R. G. Ohi, S. D. Friedman, T. T. Saha, R. H. Barkhouser, and H. W. Moos, SPIE Proceedings, **3765**, 482-494 (1999).
11. R. G. Ohi, T. T. Saha, S. D. Friedman, R. H. Barkhouser, H. W. Moos, Appl. Opt., in press (2000).
12. R. G. Ohi, *Experimental and Observational Studies in Ultraviolet Space Astronomy*, (Ph.D. Dissertation, University of Virginia, May 2000).

Table I. Input parameters for the PSD models used in the OSAC scatter calculations.

	A(mm ²)	B	C (mm ⁻¹)	
Low mid-frequency model		4.94×10^{-11}	3.55	6.67×10^{-03}
High mid-frequency model		2.19×10^{-12}	2.52	8.60×10^{-02}

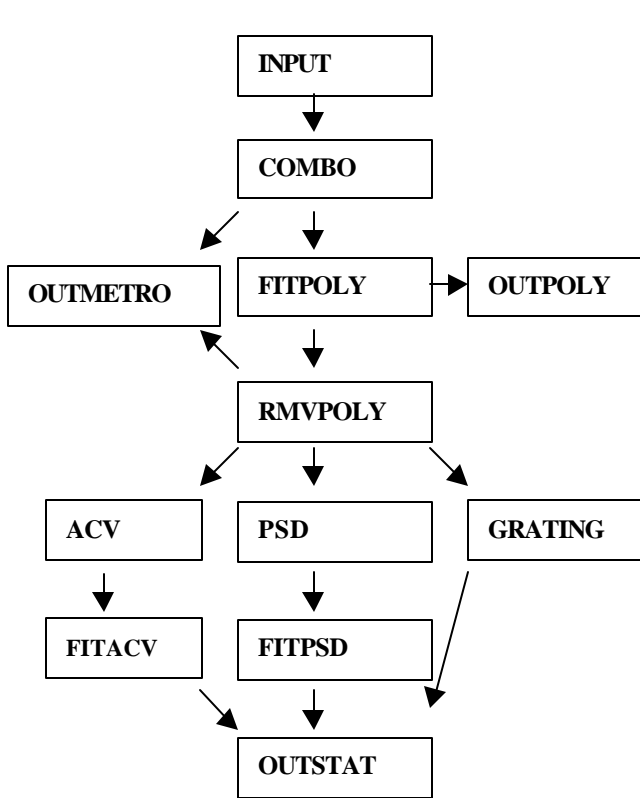


Figure 1. Main routines and flow of METDAT.

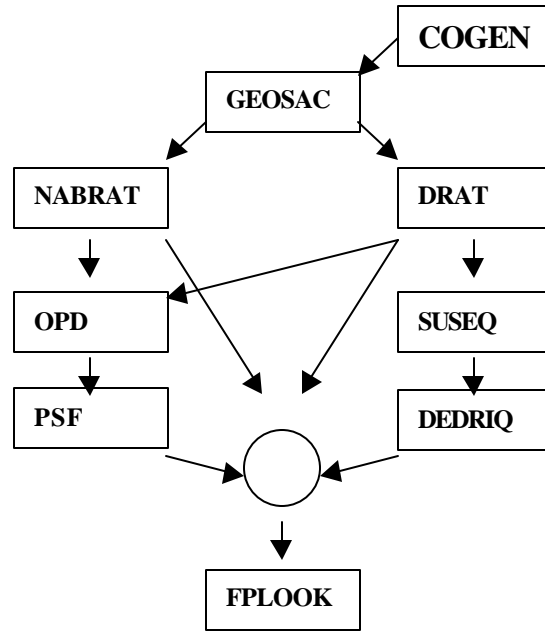


Figure 2. Main routines and flow of OSAC.

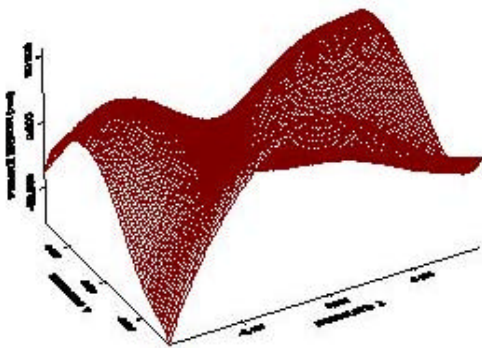


Figure 3a. Figure error of *FUSE* spare mirror. The figure error is a result of fitting 37 Zernike terms to measured figure error data. The RMS error is 0.049 waves at 633.

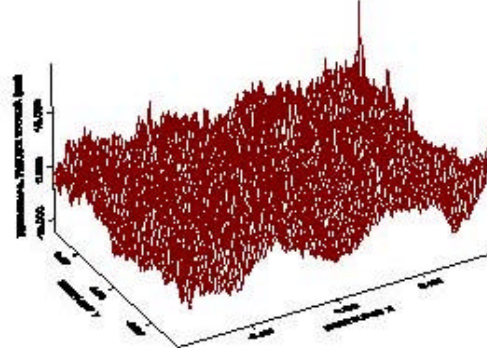


Figure 3b. Residual surface error of *FUSE* spare mirror after removing the 37 Zernike FIT. The RMS residual error is 5.6 nm.

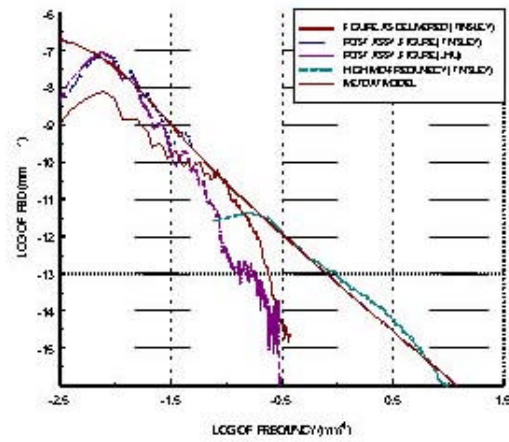
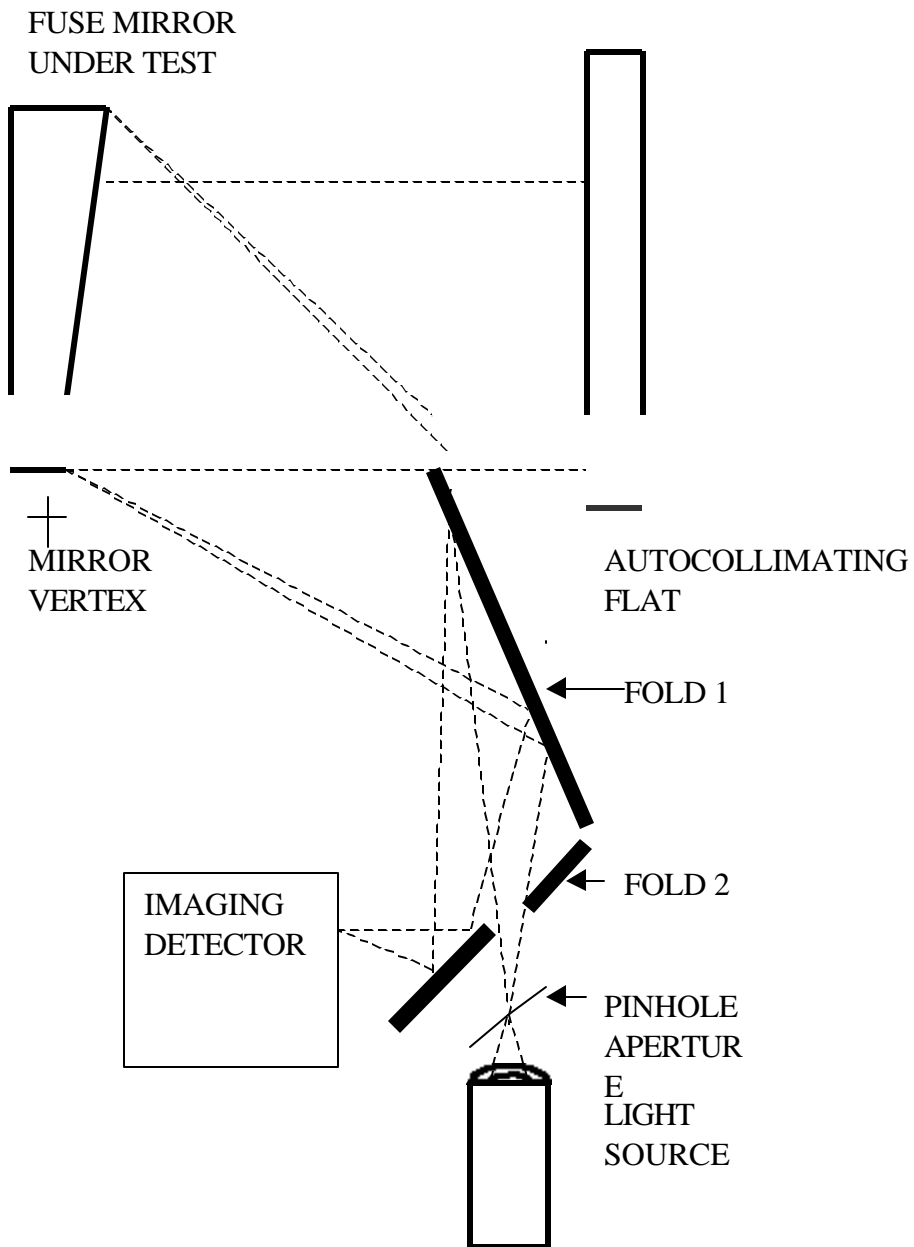


Figure 4. PSD of *FUSE* spare mirror before and after the assembly of the mirror into its housing. The PSD curves are calculated from the residual figure error (Fig. 3a) and the measurements of the mid-frequency error. Derived PSD model is also shown.

Figure 5. Schematic of the image test setup for *FUSE* spare mirror.



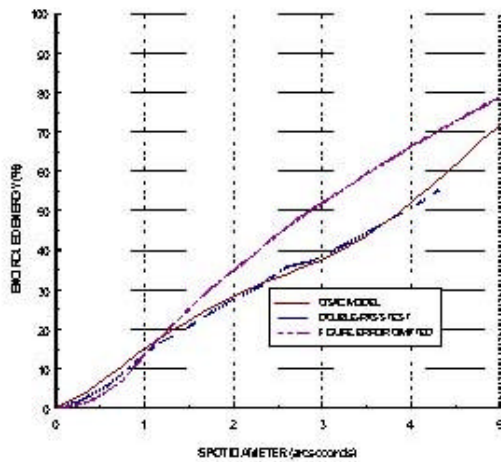


Figure 6a. Encircled energy for double-pass test setup of *FUSE* spare mirror calculated from the laboratory test and OSAC model at 436 nm.

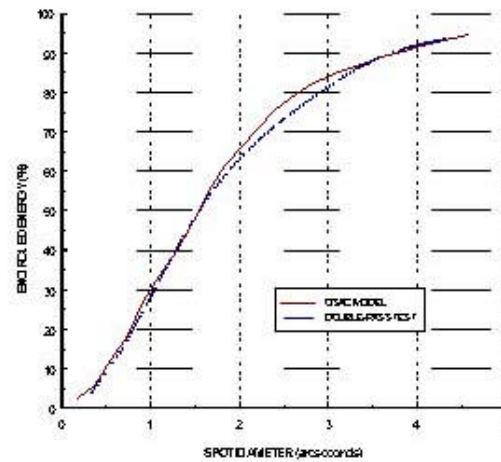


Figure 6b. Encircled energy for double-pass test setup of *FUSE* spare mirror calculated from the laboratory test and OSAC model at 185 nm.

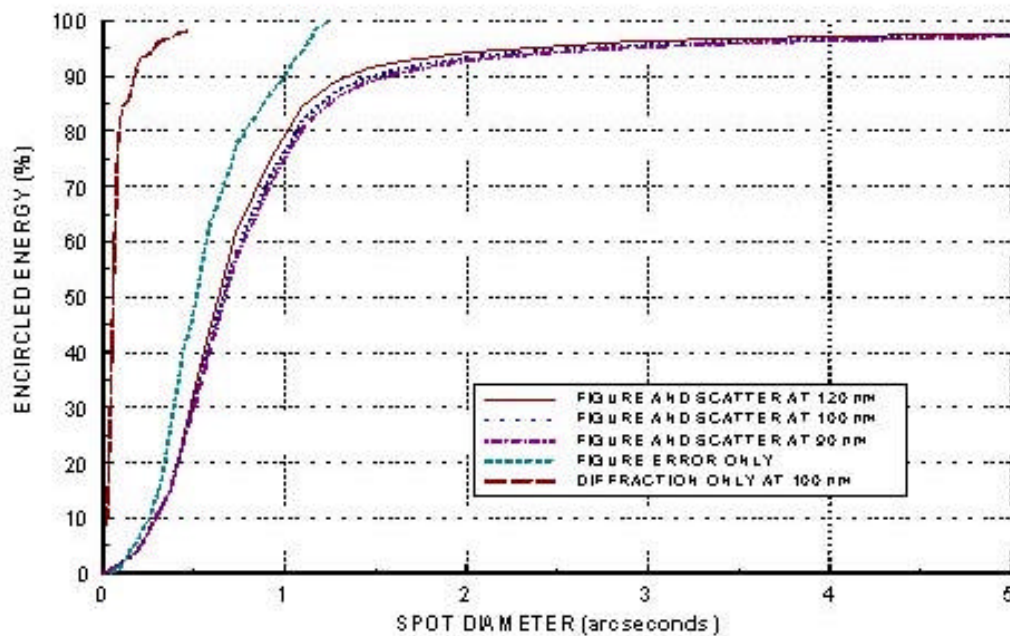


Figure 7. Predicted encircled energy of *FUSE* spare mirror in 90-120 nm wavelength range including the figure error model and scatter model. Also shown are encircled energies due to the aperture diffraction alone and figure error alone.

LISA far field phase patterns

Eugene Waluschka
NASA/Goddard Space Flight Center/551.0
Greenbelt, Maryland 20771

ABSTRACT

The Laser Interferometer Space Antenna (LISA) for the detection of Gravitational Waves is a very long baseline interferometer that will measure the changes in the distance of a 5 million kilometer arm to pico meter accuracies. Knowledge of the phase deviations from a spherical wave and what causes these deviations are needed considerations in (as a minimum) the design of the telescope and in determining pointing requirements. Here we present the far-field phase deviations from a spherical wave for given Zernike aberrations and obscurations of the exit pupil.

Keywords: Gravitational Waves, interferometry, space, optics, Zernike

1. INTRODUCTION

The Laser Interferometer Space Antenna (LISA) consists of three spacecraft in orbit about the sun. The orbits are chosen such that the three spacecraft are always at (roughly) the vertices of an equilateral triangle with 5 million kilometer leg lengths. Even though the distances between the three spacecraft are 5 million kilometers, the expected phase shifts between any two beams, due to a gravitational wave, only correspond to a distance change of about 10 pico meters, which is about 10 waves for a laser wavelength of 1064 nm.

To obtain the best signal-to-noise ratio, noise sources such as changes in the apparent distances due to pointing jitter must be controlled carefully. This is the main reason for determining the far-field phase patterns of a LISA type telescope. Because of torque on the LISA spacecraft and other disturbances, continuous adjustments to the pointing of the telescopes are required. These pointing adjustments will be a "jitter" source. If the transmitted wave is perfectly spherical then rotations (jitter) about its geometric center will not produce any effect at the receiving spacecraft. However, if the outgoing wave is not perfectly spherical, then pointing jitter will produce a phase variation at the receiving spacecraft.

The following sections describe the "brute force" computational approach used to determine the scalar wave front as a function of exit pupil (Zernike) aberrations and to show the results (mostly graphically) of the computations. The approach is straightforward and produces believable phase variations to sub-pico meter accuracy over distances on the order of 5 million kilometers.

2. DIFFRACTION INTEGRAL

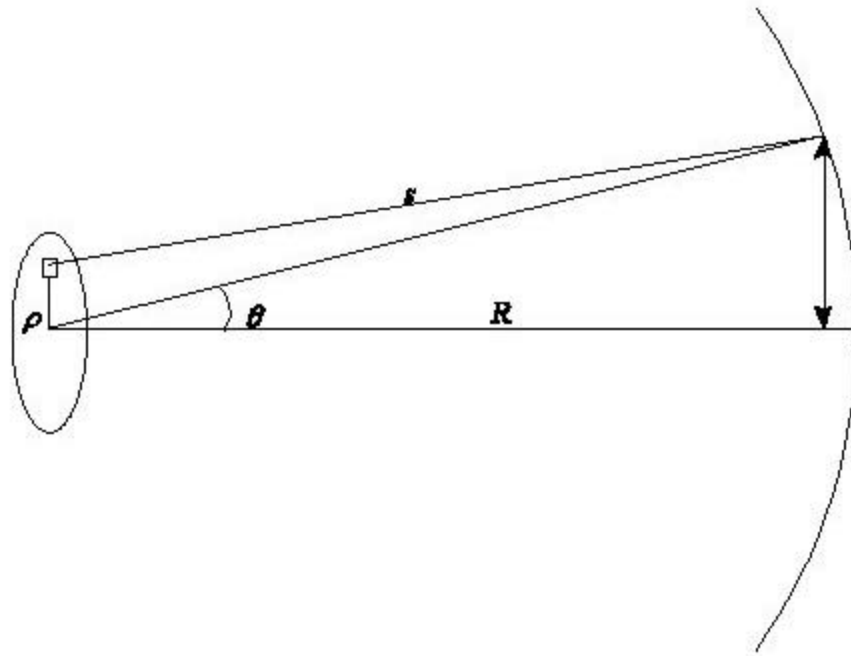
The (scalar) far field is described by ²

$$A(X, Y, Z) e^{i \frac{2\pi}{\lambda} R} e^{i \frac{2\pi}{\lambda} f(X, Y, Z)} = \iint E(x, y, z) \frac{e^{i \frac{2\pi}{\lambda} (Z_n + S)}}{S} dx dy$$

where (X,Y,Z) are the far field variables that lie on a sphere of radius, R, of 5 million kilometers and centered on the center of the exit pupil as shown. The integration is over the exit pupil and Z_n is the exit pupil aberration.

The quantity of interest is ϕ , the deviation of the phase from a spherical wave. Determining ϕ is not a new quest. Nijboer's 1947³ paper derives a formula for ϕ in terms of Bessel functions for given aberrations. However the problem with just using the formula is that complex variations in the amplitude and phase are difficult to handle. A straightforward numerical integration of the above integral is easy to implement and creates a general purpose capability that can handle central obscurations and "spiders" and non-uniform

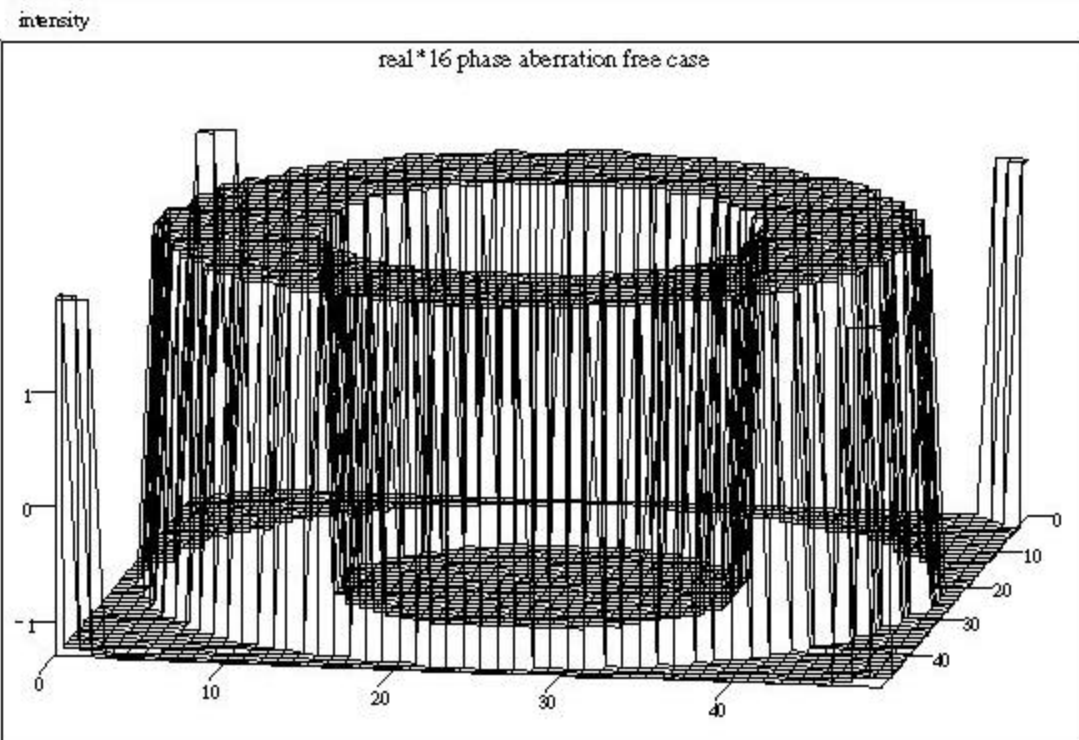
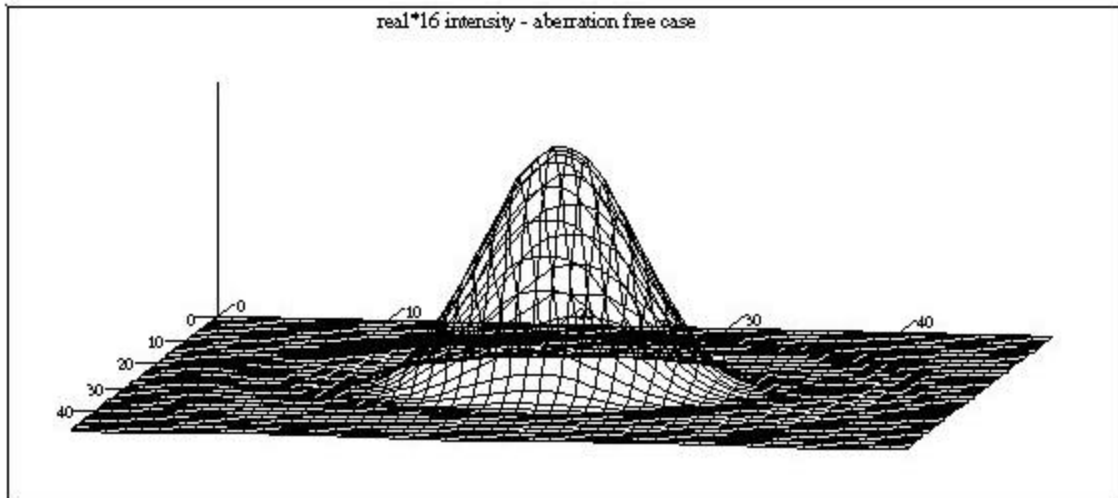
pupil functions $E(x,y,z)$. It should be noted that the speed of today's computers makes this approach very attractive.



The numerical approximation of the diffraction integral, in this case, requires the addition of very large numbers, s , measured in millions of kilometers and very small numbers, Z_n , measured in fractions of a wavelength. This mismatch cannot be handled by "double precision" (eight byte) computer arithmetic. However, an easy solution is to simply use quadruple precision (16 byte) available on Digital Alpha computers and supported by their FORTRAN compilers. This "quad" precision distinguishes between 5 million kilometers and 5 million kilometers plus one pico meter, easily. With quad precision the "machine epsilon" is about $9.6 \cdot 10^{-35}$.

3. NO ABERRATIONS

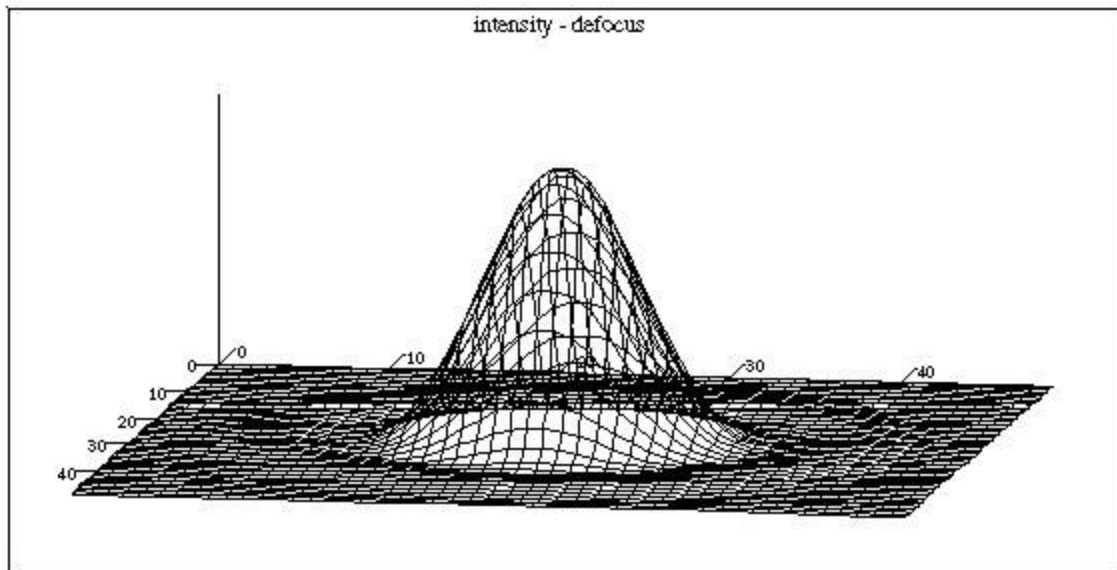
As a check on the numerical integration procedure, the next two plots show the far field intensity and phase out to the second dark ring for the case of an aberration-free uniformly illuminated unobstructed 30 cm exit pupil. As can be seen, the intensity, on the 5 million kilometer sphere, is the Airy diffraction pattern and the phase, in radians, shows the appropriate, π , discontinuity at the zero intensity points.



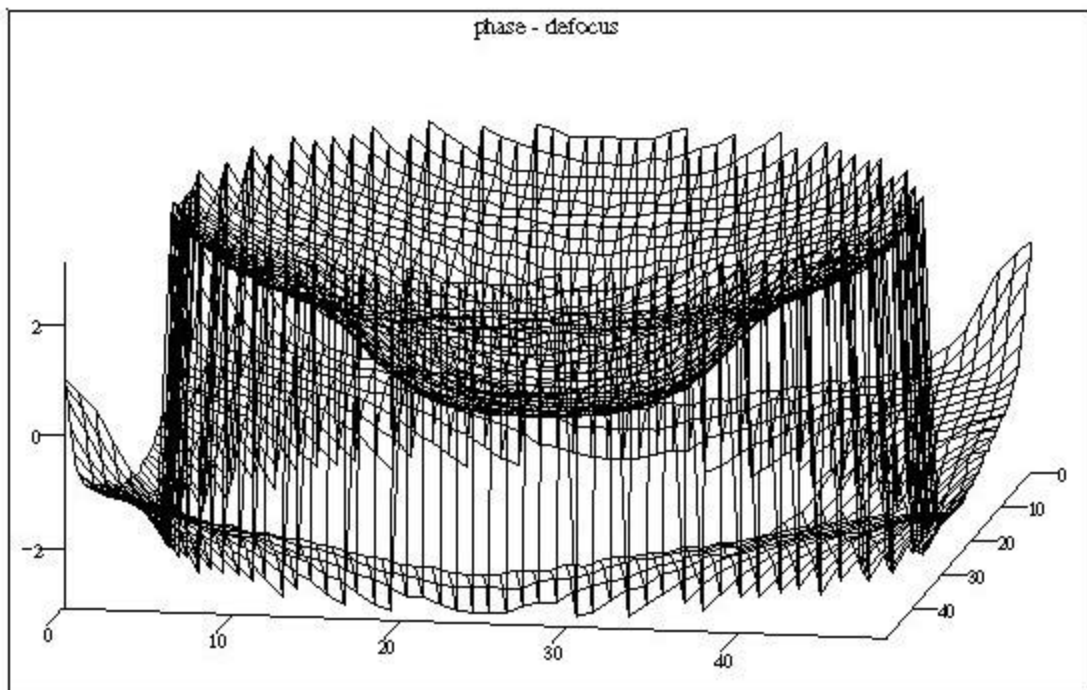
phase

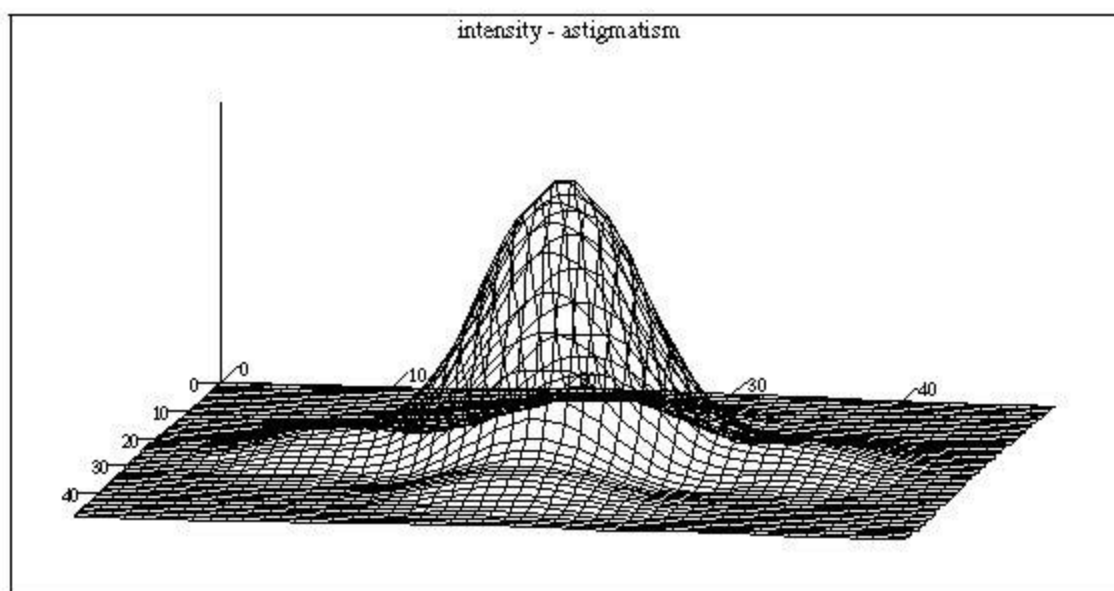
4. DEFOCUS AND ASTIGMATISM

If we introduce a $1/10 \lambda$ rms wave front aberration in the exit pupil and perform exactly the same numerical integration, we get the following results for the intensity and phase distributions on the 5 million kilometer sphere.

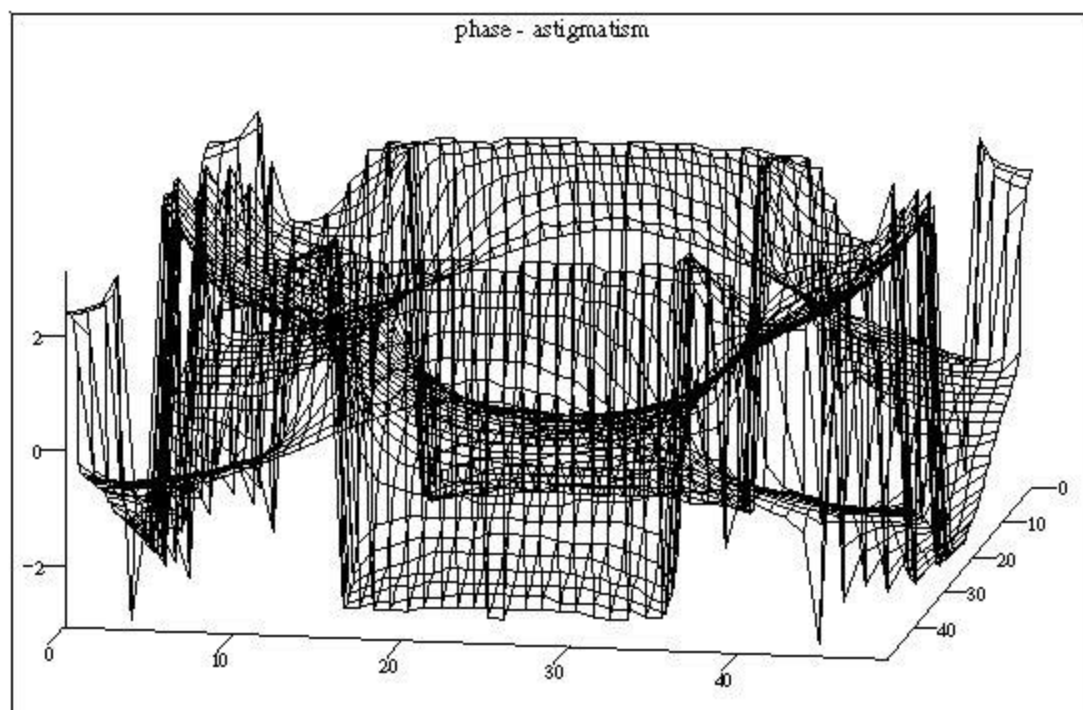


intensity





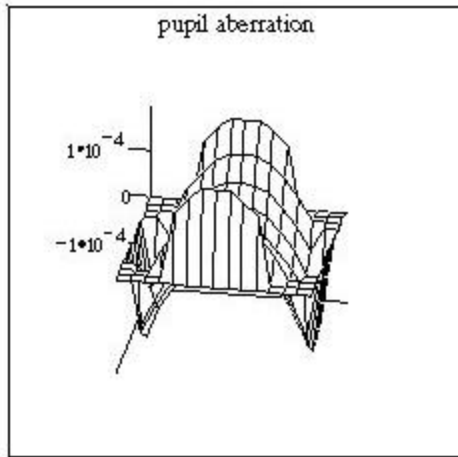
intensity



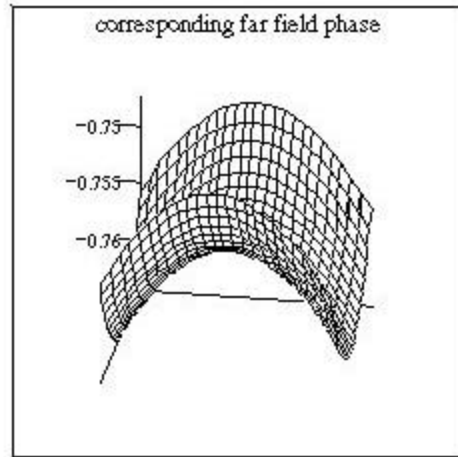
phase

5. REDUCED FIELD OF VIEW

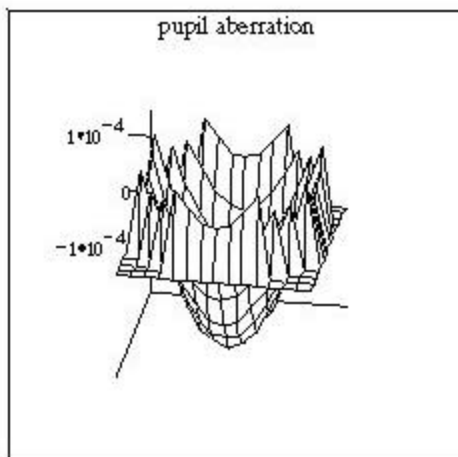
The field of view in the above plots is out to the second Airy dark ring. The above plots are presented primarily to show the reader the "large" scale phase variations. However, in order to maximize the signal and avoid phase discontinuities the central portion, out to the 95% of peak intensity, points are of particular interest. The first dark ring subtends an angle of $4.3 \cdot 10^{-6}$ radians and the 95% points subtend an angle of $0.53 \cdot 10^{-6}$ radians. The plots below show only the behavior of the phase, on the 5 million kilometer sphere, within this smaller field of view. The spatial extent is from -2.64 to +2.64 kilometers for both x and y, and the vertical axis is the phase in radians. The pupil aberrations are $1/10 \lambda$ rms of the indicated Zernike functions for Z4 to Z15 (in the CODE-V™ numbering scheme). Both the pupil aberration and the far-field phase distribution are shown to emphasize the similarities.



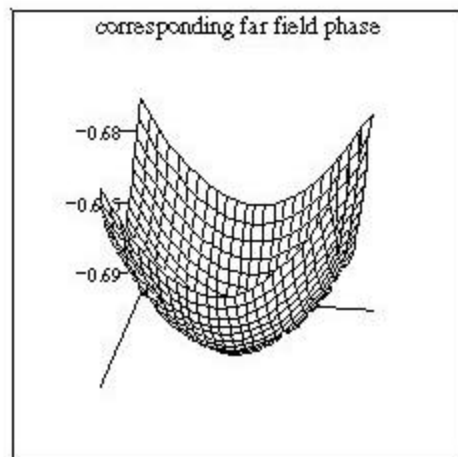
z4



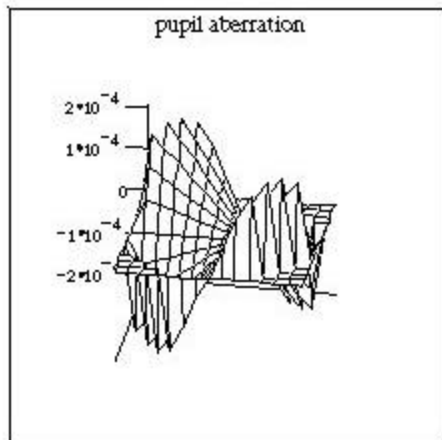
p4



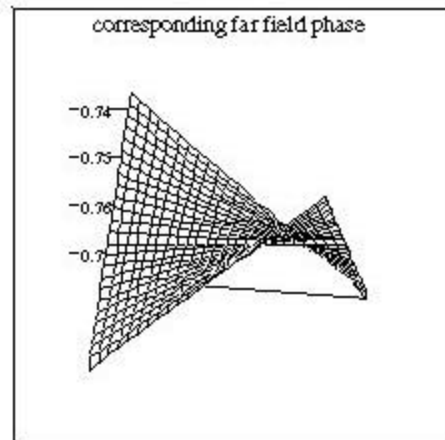
z5



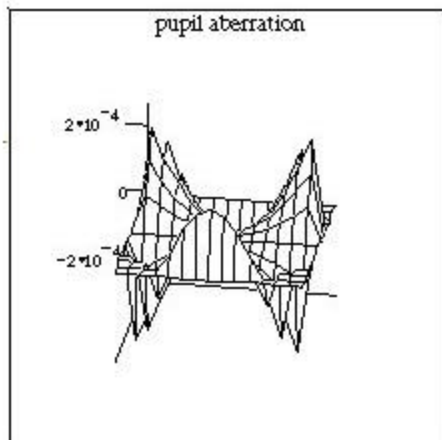
p5



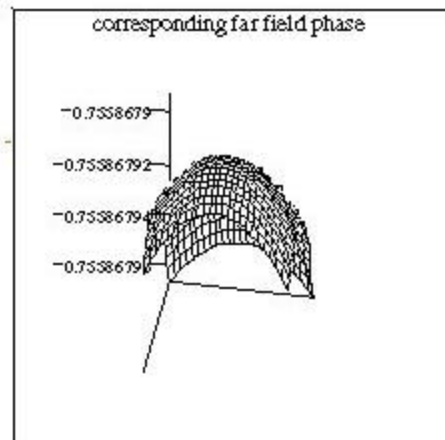
z6



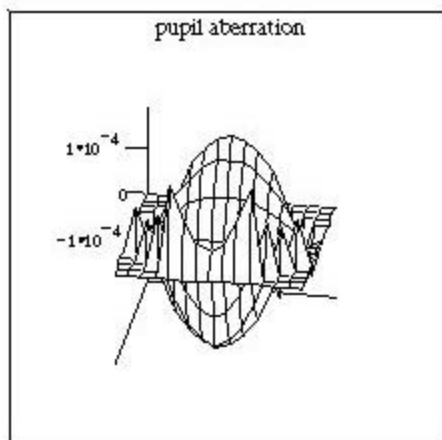
p6



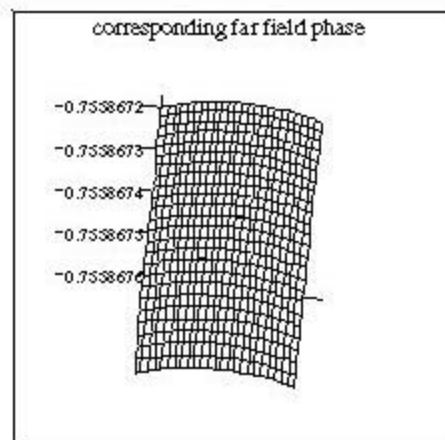
z7



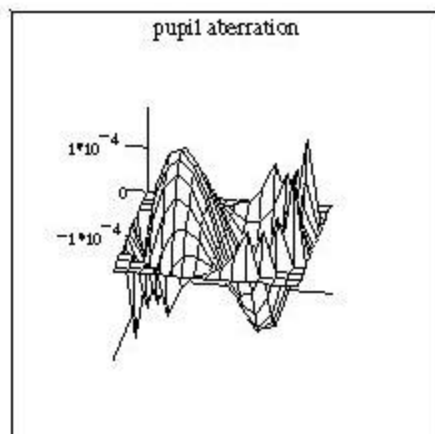
p7



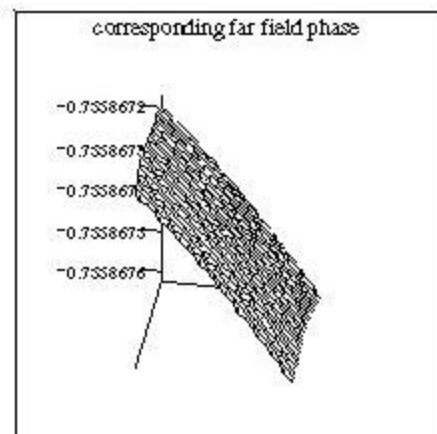
z8



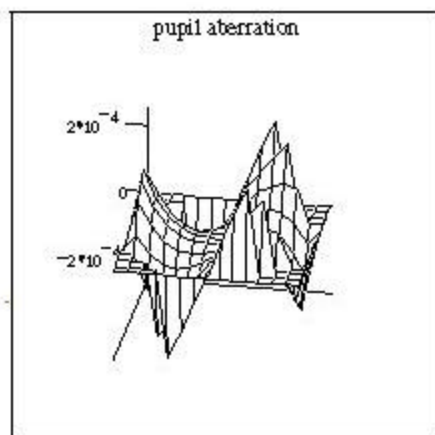
p8



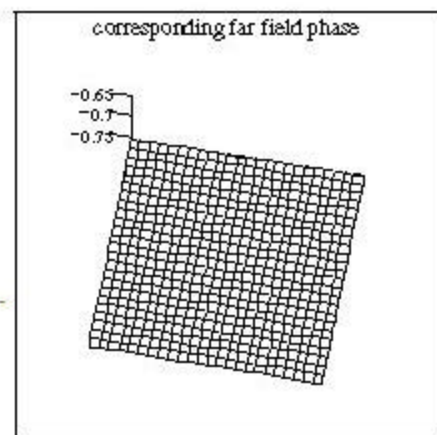
z9



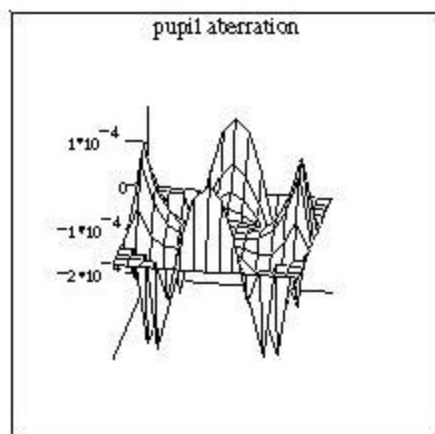
p9



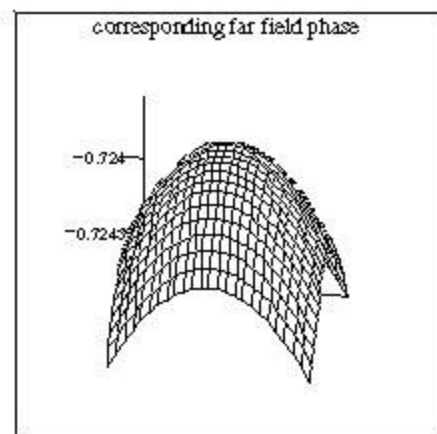
z10



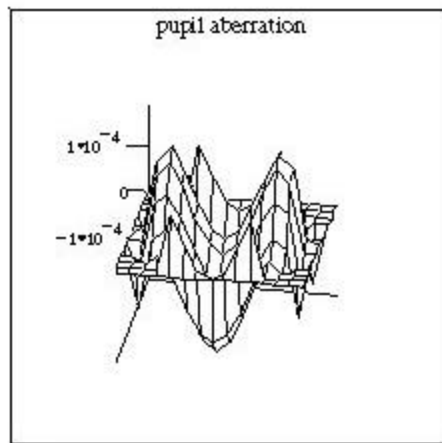
p10



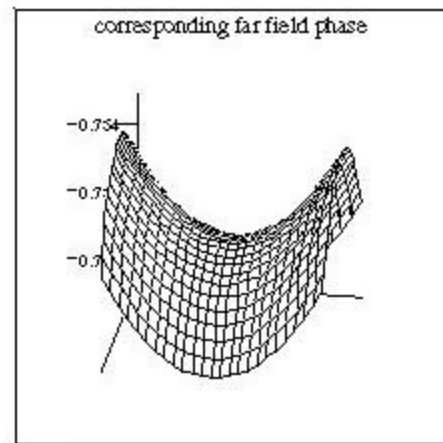
z11



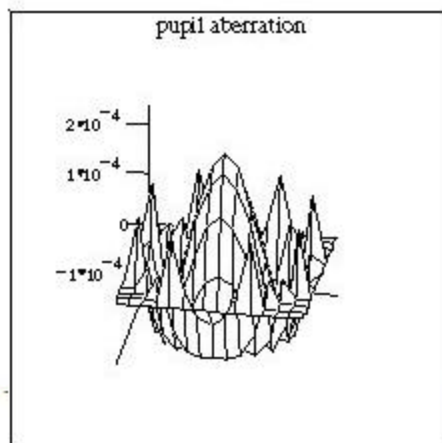
p11



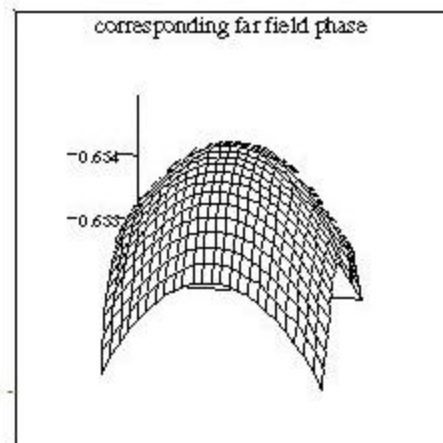
z12



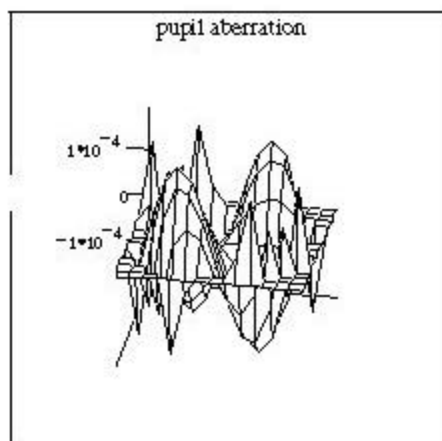
p12



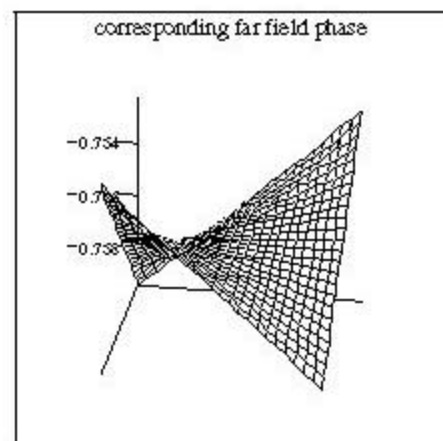
z13



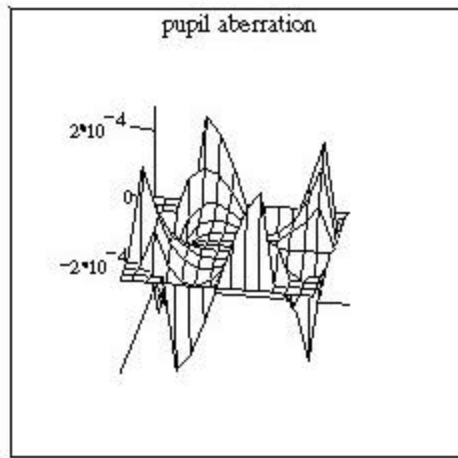
p13



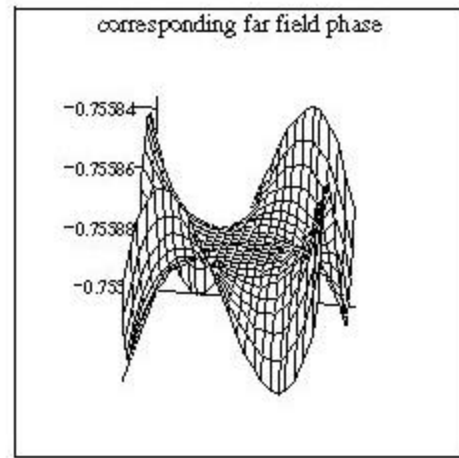
z14



p14



z15



p15

6. ANALYTIC EXPRESSIONS

Fitting Zernike polynomials to these far field phase variations (on a suitable circle) produces the following (to a suitable approximation) analytic expressions, where X and Y are the far field distances measured (in kilometers) from -2.64 to +2.64 kilometers. (When using the formula use $x=X/2.64$ and $y=Y/2.64$, the scaled to a unit circle coordinates.) The phase (in radians) variation, for a given $1/10 \lambda$ rms Zernike aberration on the 5 million kilometer sphere, is then given by the following formula along with the names of the exit pupil aberrations.

$$P4(x,y) := -1.34 \frac{1}{\sqrt{\pi}} + 6.21 \cdot 10^{-3} \cdot \left[-\sqrt{6} \cdot \frac{(-x^2 + y^2)}{\sqrt{\pi}} \right] \quad \text{Astigmatism 1st order 0°}$$

$$P5(x,y) := -1.22 \frac{1}{\sqrt{\pi}} + 3.47 \cdot 10^{-3} \cdot \left[\sqrt{3} \cdot \frac{(-1 + 2 \cdot x^2 + 2 \cdot y^2)}{\sqrt{\pi}} \right] \quad \text{Defocus}$$

$$P6(x,y) := -1.34 \frac{1}{\sqrt{\pi}} + 7.04 \cdot 10^{-3} \cdot \left(2 \cdot \frac{\sqrt{6}}{\sqrt{\pi}} \cdot y \cdot x \right) \quad \text{Astigmatism 1st order 0°}$$

$$P7(x,y) := -1.34 \frac{1}{\sqrt{\pi}} \quad \text{Trifoil 0°}$$

$$P8(x,y) := -1.34 \frac{1}{\sqrt{\pi}} \quad \text{Coma X}$$

$$P9(x,y) := -1.34 \frac{1}{\sqrt{\pi}} \quad \text{Coma Y}$$

$$P10(x, y) := -1.34 \frac{1}{\sqrt{\pi}}$$

Trifoil 30°

$$P11(x, y) := -1.28 \frac{1}{\sqrt{\pi}} - 3.35 \cdot 10^{-4} \left[\sqrt{3} \frac{(-1 + 2x^2 + 2y^2)}{\sqrt{\pi}} \right]$$

Tetrafoil 0°

$$P12(x, y) := -1.34 \frac{1}{\sqrt{\pi}} - 2.1 \cdot 10^{-3} \left[-\sqrt{6} \frac{(x^2 + y^2)}{\sqrt{\pi}} \right]$$

Astigmatism 2nd order 0°

$$P13(x, y) := -1.16 \frac{1}{\sqrt{\pi}} - 7.25 \cdot 10^{-4} \left[\sqrt{3} \frac{(-1 + 2x^2 + 2y^2)}{\sqrt{\pi}} \right]$$

Spherical

$$P14(x, y) := -1.34 \frac{1}{\sqrt{\pi}} - 1.23 \cdot 10^{-3} \cdot \left(2 \cdot \frac{\sqrt{6}}{\sqrt{\pi}} \cdot y \cdot x \right)$$

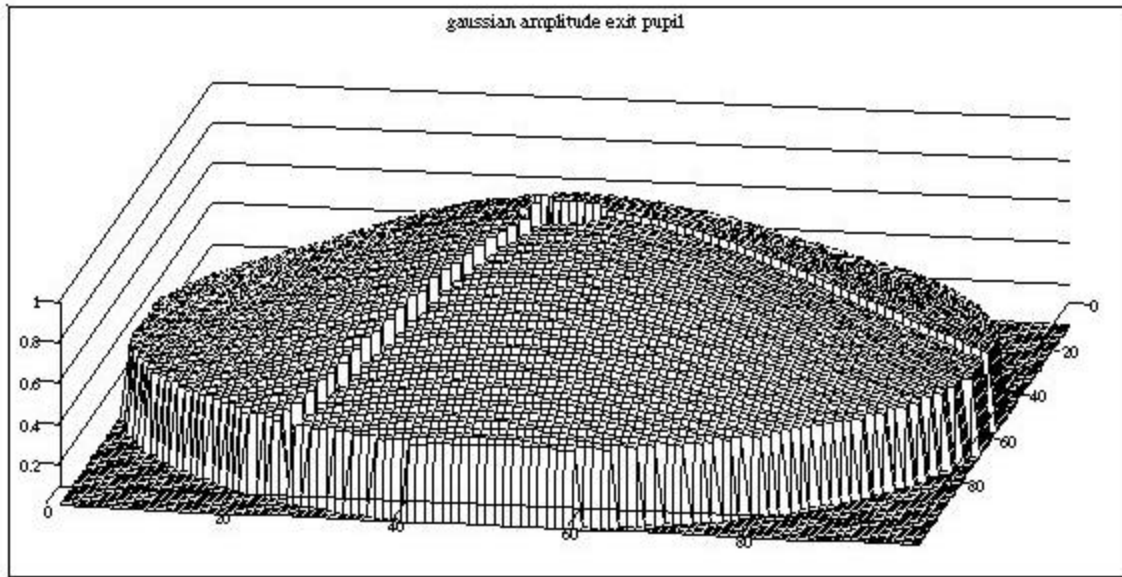
Astigmatism 2nd order 45°

$$P15(x, y) := -1.34 \frac{1}{\sqrt{\pi}} - 1.19 \cdot 10^{-5} \left[-4 \sqrt{10} \cdot y \cdot x \frac{(x^2 + y^2)}{\sqrt{\pi}} \right]$$

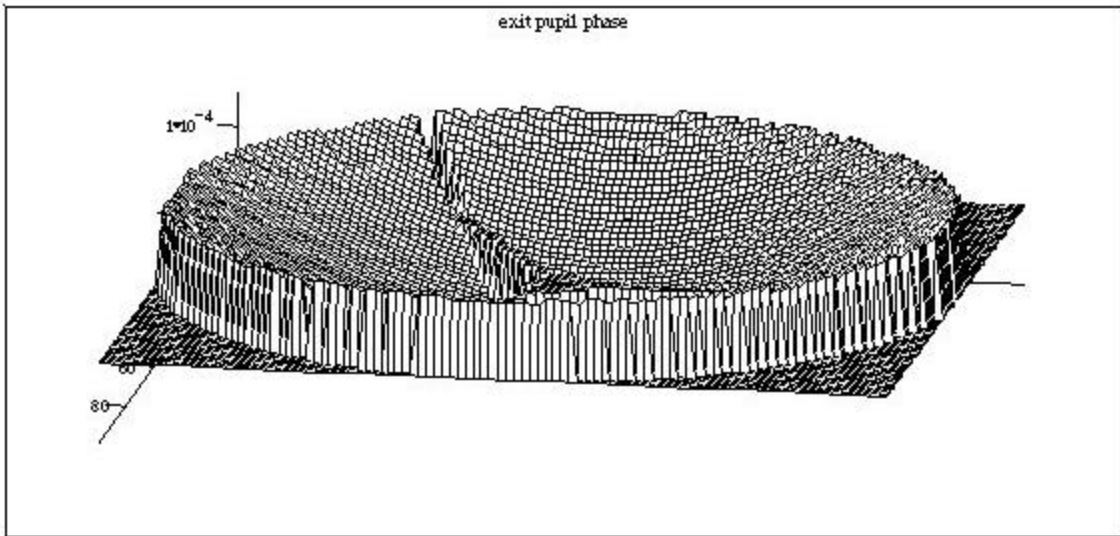
Tetrafoil 22.5°

7. GAUSSIAN BEAM, CENTRAL OBSCURATION, AND SUPPORTING STRUTS

The above results all assumed a uniformly illuminated exit pupil with no obscuration. This is a good starting point, however the real telescope may have obscurations and a Gaussian beam profile, in which case the exit pupil will appear as the following plots (with 1/10 λ defocus added for better visualization). The diameter of the pupil is 254 mm.



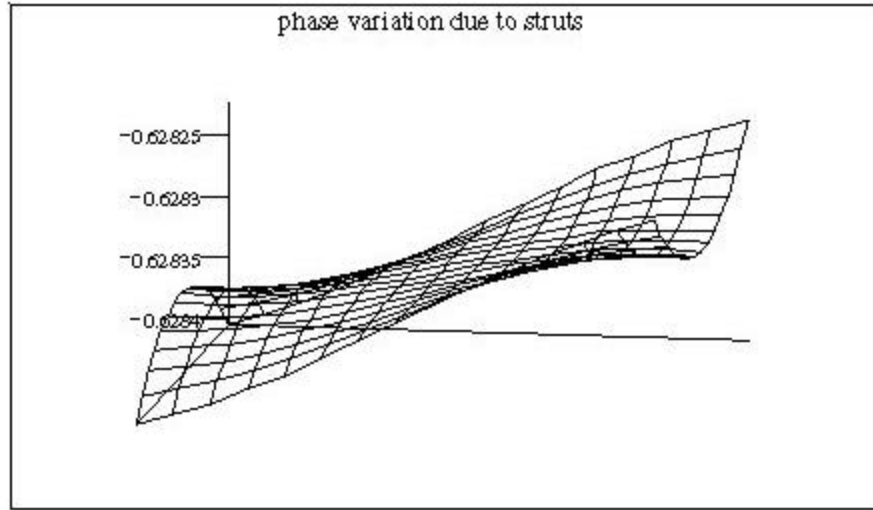
23



z4

The diameter of the central obscuration is 24 mm and the strut thickness is 10 mm.

For the unaberrated beam there is no phase variation on the 5 million kilometer sphere within the central peak as seen in the earlier plot. Now, adding only the obscurations and Gaussian beam profile but leaving the exit pupil phase "flat" (constant) does produce a variation in far field as is shown in the plot below.



P_z

The phase in this plot exhibits an asymmetry. This is due to the fact that there are only three struts with two of them on one side and only one on the other side (loosely speaking). This is what breaks the symmetry. The phase variation is very small, but present. As can be seen the predominant effect of the struts is to introduce tilt. An analytic expression for this curve (obtained by fitting Zernike polynomials within a appropriate circle) is.

$$Phase(x,y) = \frac{1.11}{\sqrt{\pi}} + 4.13 \cdot 10^{-5} \cdot \frac{2}{\sqrt{\pi}} \frac{y}{2.64} + 1.37 \cdot 10^{-5} \sqrt{\frac{8}{\pi}} y \left(\frac{3x^2 - y^2}{2.64^3} \right).$$

Where, as before x and y are the far-field distances measured (in kilometers) from -2.64 to +2.64 kilometers (hence the factor in the denominator) and the phase variation, on the 5 million kilometer sphere, is in radius

8. CONCLUSION

As optical systems grow in size, and LISA is a example of a particularly long optical system, it is reassuring that analyzing them can still be performed with slightly modified existing analysis tools. All of the ray tracing was performed with QRAYPKS, a FORTRAN ray trace code written by the author. The code was modified to perform REAL*16 arithmetic, hence the leading "Q". A large portion of the analysis shown here only requires quadruple precision for the numerical sum that approximates the diffraction integral. It is possible to approach the problem analytically. However, "brute force" ray tracing has a distinct advantage in that the only question that arises is "did we fire enough rays?" For example, I would be hard pressed to generate the above "phase variation due to struts" plot using an analytical approach. But numerically it is straightforward. We have also shown some of the large scale (out to the second Airy dark ring) phase behavior and some of the phase behavior right around the central peak. All of the plots and analysis not requiring quad precision were performed using MATHCAD™.

ACKNOWLEDGMENTS

This work was performed at JILA, a joint institute of the National Institute of Standards and Technology and the University of Colorado at Boulder and supported by a Goddard Space Flight Center's Fellowship.

REFERENCES

1. *Laser Interferometer Space Antenna for the detection and observation of gravitational waves*, Pre -Phase A Report, Second Edition, July 1998.
2. M. Born and E. Wolf, *Principles of Optics*, Pergamon Press, 1980.
3. B.R.A. Nijboer, *Physica*, 10 (1943), 679; *ibid.*, 13 (1947), 605.

Large Aperture Sparse Array Space Telescope

David Maker
Teledyne Brown Engineering
david.maker@tbe.com

ABSTRACT

This proposal that I would like to introduce at this workshop is a golay 6 sparse f/2 sparse array with freeflying mirrors giving us >1 kilometer effective aperture. These mirrors (each with ~3meter aperture) are be distributed over a hemispherical region in space, with a module placed at the common focal point. In this focal point module would be several small refracting telescopes (~10cm aperture, one for each of the mirrors) that focus the light from these various distributed (distant) mirrors to a common imaging device. Because of the long >1km focal lengths used here wobble-tip tilt control (NGST research has found it to be the most difficult problem) can be done using the same sensors that control the beam pointing! No extra work is required to control the most difficult problem! So a seemingly intractable 6 DOF problem is reduced to a manageable 1 DOF piston phasing problem! But simple laser ranging can be used here to fix the mirror position to within about a millimeter. Strehl ratio maximization on the star accompanying the planet can further fix the position which can then be phase locked (two frequency carrier wave) using an unequal arm interferometer. Some of the maneuvering technology (magnetic field angular momentum dumping) required for this accurate of pointing is already aboard the Hubble space telescope. If one sensor is used for both the interferometer and laser ranger then the 1 DOF problem is further reduced to systems management(computer code) solution for the output of just one sensor! Contrast writing these few lines of computer code (for this free flyer) with the massive (tethered or otherwise) millions or billion dollar structure required to hold together a space based interferometer of comparable effective aperture! We could use thin flat mirrors (probably glass) with actuation and so we could get all this up there with just one shuttle launch. The circular thin mirrors (with some small amount of ribbed backing) could be stacked in the shuttle cargo bay like pancakes. Each mirror would be deployed to its position using its own small maneuvering rockets. Also this method is versatile enough to give you kilometer or more effective apertures with no added structure. The tethered interferometers give you a hundred meters. Also when you do the standard calculation for calculating the effective aperture($1.22 \lambda/D = \text{diam}/4\text{ly}$) for resolving an earth sized planet(=diam)at the distance of alpha centauri (nearest star=4ly)in the visible($\lambda=.5\text{M}$) into a 5 pixel width you get an aperture of 1 km (=D), not that 50m baseline value used by the Gossamer literature. So our kilometer effective aperture method will actually be only the only proposal that will do it! Also it is possible to estimate the magnitude sensitive at from 29 to 30 for this telescope, enough to image (and because of the effective aperture size) and resolve the disk of earthlike extrasolar planets.

Space Based Large Effective Aperture Golay 6 Array

In this talk I would like to make the case for long focal length (~km) space based sparse arrays. We use a Golay 6 as an example. Advantages due to long (~km) focal lengths:

1. 6 DOF wobble control done by sensors that also control pointing errors. Motion along reflected ray optical axis becomes most critical. So problem reduced to 1 DOF piston phasing.
2. Flat mirrors (with actuators). All put up with one shuttle launch.
3. For 1 DOF piston phasing get close with laser ranging ± 1 mm. Then possible use of phase lock unequal arm interferometry with augmentation by Strehl ratio maximization on the companion star. Note the interfereferometry problem is much smaller here than lets say for Lisa or LIGO.
4. Micrometeroid degradation less of a problem because of $1/r^2$ light intensity from nicks on mirror surface. Can use orbit within magnetic field of earth.

ARRAY CONFIGURATION

The general trend is that a larger number of smaller elements can provide a required resolution limit⁷ with a minimum of aperture area. A golay 6 or circle 9 configuration are optimal.

Interestingly the family of Golay 6 two dimensional nonredundant subaperture arrays⁸ results in nonredundant MTF passbands that are equally spaced, and it thus provides the most uniform spatial frequency coverage within the cutoff spatial frequency aperture area. So we recommend here a Golay 6 array. Apparently this also the choice for the Darwin sparse array.

SPARSE ARRAY DECONVOLUTION ALGORITHMS

Here we use a generic Fourier Deconvolution as an example where $H(x)$ is the optical transfer function (OPT) of the sparse array. We use well known golay6 sparse array psf s to create the H functions.

$H(\mathbf{w}) = \int_{-\infty}^{\infty} e^{-i\mathbf{x}\mathbf{w}} H(x) dx$, which is the Fourier transform of the OPT. We also can get the Fourier transform

of the intensity distribution $G(x)$ which is:

$G(\mathbf{w}) = \int_{-\infty}^{\infty} e^{-i\mathbf{x}\mathbf{w}} G(x) dx$ then using the theorem about the Fourier transform of a convolution integral:

$\frac{1}{2\pi} \int_{-\infty}^{\infty} \left(\frac{G(\mathbf{w})}{H(\mathbf{w})} \right) e^{i\mathbf{w}\mathbf{x}} d\mathbf{w} = f(x)$ which is the image (restoration) distribution. Thus we can use deconvolution

algorithms and the optical transfer function for the sparse array to create an image even for a unfilled aperture. In practice a massively parallel Lucy-Richardson algorithm has already been invented and tested for these purposes. Post Factum Image Processing restores MTF and enhances image quality⁷.

F-NUMBER

Fast F ratio here for array. About F/3 to take advantage of the long focal lengths for *each* mirror element (since effective aperture size is what we are after) with an effective focal ratio of perhaps f/8 due to the beam combiner. The amplifying power of the beam combiner (acting like a secondary mirror in a Schmidt Cassegrain) produces the long effective focal length and small effective focal ratio. In terms of standard telescope optics typically the positioning tolerance of an f/8 Newtonian's rack and pinion is about .002 inch while the position tolerance of the Schmidt-Cassegrain's primary f/2 must be to approximately .0001 inch, about 1/20 the Newtonian, which is still tolerable focusing. The effective "motion" of this primary (the large mirrors in our case) in the Schmidt Cassegrain situation fixes this position tolerance.

Large Effective Aperture Sparse Array

I INTRODUCTION 6DOF→1DOF

This proposal is a golay 6 f/3 sparse array with free flying mirrors giving us >1 kilometer effective aperture. These mirrors (each with ~3meter aperture) are be distributed over a hemispherical region in space, with a module placed at the common focal point. In this focal point module would be several small refracting or reflecting telescopes (~10cm aperture, one for each of the mirrors) that focus the light from these various distributed (distant) mirrors to a common imaging device. Because of the long >1km focal lengths used here wobble-tip tilt control (NGST research has found it to be the most difficult problem) can be done using the same sensors that control the beam pointing! No extra work is required to control the most difficult problem! So a seemingly intractable **6 DOF problem is reduced to a manageable 1 DOF** piston phasing problem.

FLAT MIRRORS

We could use thin flat mirrors (probably glass) with actuation and we could get all this up there *with just one shuttle launch*. The circular thin mirrors (with some small amount of ribbed backing) could be stacked in the shuttle cargo bay like pancakes.

MICROMETEOROID PROBLEM

Micrometeoroid nicks create light **scattering that goes as $1/r^2$** . But the specular reflection decreases at much lower rate. So distant mirrors also allow low orbit where micrometeoroid impacts are far more frequent.

Thus the angular momentum dumping into the earth's magnetic field perhaps can be used for control but not to low an orbit to prevent significant differential rotation relative motion

RESOLUTION

Also when you do the standard calculation of the effective aperture ($1.22\lambda/D = \text{diam}/4\text{ly}$) for resolving an earth sized planet(=diam) at the distance of alpha centauri (nearest star=4ly)in the visible($\lambda=.05\mu$)into a 1 pixel width you get an aperture of 1 km (=D), not that 50m baseline value I have seen.

Additional Notes For Reference:

I WAVEFRONT SHAPE CONTROL

A Introduction

The fine tuning needed here to get 1/10 wavefront control is actually about the same complexity of control as that needed for radio controlled model airplanes (ie.,4 controls: the throttle, rudder, elevator, and aileron; over 6 AM channels.). There are only 4 controls needed (in addition to the usual coarse controls used on imaging satellites such as inertial guidance). For 1/10 wave we only need 3 thruster wobble (two dimensional, 2DOF) control and that is easily accomplished by doing continuous collimation using the signals from sensors at the focal point module. And we need the much less demanding radial control (1DOF) along the line connecting the mirror to the focal point for a total of 4 controls (vs the 4 controls for the radio controlled model airplane).

B 1/10 Wave Control: Wobble Control and Piston Control

The core concept in understanding wavefront control using a telescope is that of imaging a point source. Thus mirror motion perpendicular to the wavefront direction (toward the focal point) is not nearly as critical as that caused by a mirror element wobble, which strongly redirects the light away from the focus point for the point source. And piston motion must be accurate to 1/10 wave.

For coarse control we use the familiar inertial guidance attitude controls (and also laser ranging for distances between the mirror and the focal point apparatus, with the side lobes of the laser beam used for coarse θ and ϕ control,) that space telescopes such as the Hubble, SOHO, etc., use.

A1 Control along Axis to Focal Point

David Redding's figure 17 shows the NGST telescope WFE s are over 10 times LESS sensitive to radial missalignments (along the line between the mirror and the focal point apparatus) than for individual segment errors which are dealt with by beam misalignment detection near the focal point in this proposal. And this all makes sense in terms of spot diagram arguments. And it makes sense in terms of what the Zernike polynomials are measuring (wave front directional propagation distortion, which is not affected much by slight mirror motion along the beam axis).

Also motions along the beam axis require radial phasing and that is discussed below. But motions of the one mirror edge relative to another on the same mirror do require the 1/10 wave accuracy and do cause a large degradation in the image of our point source. But to have this kind of control just requires the usual pointing methodology used to create an image in any case. One way of doing pointing is to use the image of the star near the planet. Off axis (along the optical axis of the eyepiece telescope located at the focal point region) there is a mirror that diverts the light from the star and three sensors next to this diverted beam (120° apart) are used to actively point the beam of each mirror. The thrusters adjusting the radial position of the mirror are now controlled by these three (collimation) sensors NOT the inertial guidance system. Fast /ratio primary mirrors are very sensitive to collimation errors.

Here are details of the 6DOF® 1DOF

Solution

To find the minimum diameter of a point stellar source for a 3 meter mirror at 1 kilometer we use $\frac{1.22\lambda}{D} = q$, So $\frac{1.22\lambda}{D} = \frac{1.22 \times 5 \times 10^{-7}}{3} = q = 2 \times 10^{-7} = \frac{x}{1000}$ so $x \approx 2\text{mm}$ minimum diameter at focal point.

Now if one side of the mirror has moved 1/10 wave radially relative to the other side 3 meters away then at the focal point 1000 meters distant the beam will have moved about 1/25 of a millimeter. We see this by using similar triangles and the fact that the law of reflection implies that the angle of light path deviation change be twice the mirror angle change:

$$\frac{x}{1000} = 2 \frac{(1/10)5 \times 10^{-7}}{3} \text{ so } x \approx 1/30 \text{ millimeter.}$$

If, lets say, the beam decreased uniformly in intensity from the center out to .1 mm then beam intensity changes of 1 part in 3 is required. These beam intensity changes are to be measured (and normalized) relative to the other two sensors (separated by 120°) so fluctuating beam intensities will not alter this result. Detection of light intensities to 1 part in a 3 is easily done (Limb darkening on resolved stellar images slightly complicates this picture). In any case this kind of pointing error is required for imaging purposes so no additional control is required!

NOTES: 1DOF PISTON CONTROL

Also by controlling the lateral pupil geometry, a multiple telescope array can be simultaneously phased across a wide field⁹. Even so it will probably still turn out that the mirror distance must be measured with an unequal path interferometer such as Kocher's with phase lock on the correct Strehl ratio distance and compensation with the lateral pupil geometry. Unequal path interferometers require frequency stabilized lasers¹⁰. A phase lock (within lets say 1mm) can be obtained by using two frequencies on the interferometer of about 20 A wavelength separation. There would then be one point where the peaks themselves are at a true minimum within that millimeter (which itself is gotten from laser ranging). The question here is how much SNR is lost in the time taken to maintain the correct mirror 1 DOF phasing (there will be less time for image integration because of the nearly continuous phasing activity using the Strehl ratio).

More Miscellaneous Notes:

So the interferometry wobble problem (e.g.,SAMI, other GOLAY projects) that has been the bane of sparse arrays can be overcome in this particular situation by *doing nothing extra*. The irony is that this solution wouldn't be possible with much shorter focal length arrays since "x" (in the above equation) would be proportionally smaller and thereby measurement that much more difficult. It is no wonder that this method of mirror control has not been contemplated before: it works best on a planet imager!

C Piston Radial Distance Phasing

For radial distance phasing the crude position controls (laser ranging or unequal arm interferometer) put the radial position within a couple of wavelengths accuracy. The final part is done by maximising the Strehl ratio. In this procedure we use one mirror as a reference and maximize the Strehl ratio for all the other mirrors with this reference. This accuracy is close to 1/10 wave. Finally all the mirror beams are combined and the position is maintained for a few seconds (and perhaps phased locked using unequal path interferometer) and then the process is repeated. The image is much less dependent on this radial positioning (along a line to the focal point) than on the angle positioning using the long focal length so this is not nearly as critical a control as is the angular correction which can be done continuously. This Strehl ratio maximization can also be used to control imperfections in the individual mirrors via the actuators. And the Strehl ratio optimization procedure has been worked out for the NGST. In any case in practice such control would be periodic and automatic. Also by controlling the lateral pupil geometry, a multiple telescope array can be simultaneously phased across a wide field⁹. And it was learned from NGST that the initial radial position must be within 1 mm, which in this case laser metrology on an elbow mirror at the focal point apparatus (laser ranging used in surveying) can already do. "The DISTO pro has a standard accuracy tolerance of plus/minus 1.5mm over its entire working distance which is in most cases limited to

100M"(Jack Wolf, Leica systems). In a vacuum the tolerance promises to be much greater (fraction of a millimeter). Finally this distance can be measured to higher precision with an unequal path interferometer such as Kocher's with phase lock on the correct Strehle ratio distance. Unequal path interferometers require frequency stabilized lasers¹⁰. A phase lock (within lets say 1mm) can be obtained by using two frequencies on the interferometer of about 20 A wavelength separation. There would then be one point where even the peaks are at a true minimum within that millimeter (which itself is gotten from laser ranging).

There is the important question here of how much time this Strehl ratio maximization procedure has to take for radial phasing. But the brighter the source the more easily and rapidly is the Strehl ratio maximization. So one trick for doing this could make use of the fact that for earthlike planets a bright star is very near the field of view (e.g., the maximum elongation of earth's orbit as viewed from α centauri is about 1 arc second) so that rapid Strehl ratio optimization would be done for that star with actual (very slightly) off axis imaging being done of the planet itself. In our case the star image will probably show a disc and a variant on the Strehl ratio maximization procedure used. In any case the phase lock would keep us at this distance once we found it using Strehl ratio maximisation.

II FLAT MIRRORS

Here we calculate the mirror displacements (given by the actuators) needed to give us our long focal length and use these displacements (plus the shear modulus for glass) also to find an approximation for the actuator force required to create this sag. There is slope continuity at the center of the mirror so the shear modulus is required to calculate actuator forces. Actuator forces that create stretching are much smaller.

To get the actual mirror sag (displacement=sag) from optical considerations we use the sagitta equation, focal length ($\approx 10\text{km} = \frac{1}{2}R$) and mirror aperture ($\approx 3\text{m} = 2r$). Thus:

$$\frac{r^2}{2R} \approx .05\text{mm} \equiv \text{sag} \quad \text{recall for the shear modulus } G$$

$$\frac{\frac{F}{A}}{\frac{\Delta L}{L}} = G \quad \text{so} \quad F = GA \frac{\Delta L}{L}$$

Here $\Delta L = x = .05 \text{ mm}$, $L = 1.5\text{m} = r$, and for a narrow glass beam (radial segment of mirror) of width ds and height $w = .0001\text{m}$ (for our mirror thickness¹ $\approx .1\text{mm} = w$) we have that $A = w \times ds$. The shear modulus for zerodur Glass is $92 \times 10^{10} \text{ N/m}^2 = G$. In our integration we divide the distance ds (along the circumference) by 2 since the actual beam (which is a triangle as opposed to our rectangular model) is half as wide. So integrating over all these thin beams to get the total actuator force:

$$F = \oint \Delta F = \oint \frac{Gx}{2L} w ds = 10^3 \text{ Newton} = \text{actuator force which is tolerable (50 newtons on each of 20$$

actuators) and gives us the high stress needed to keep the ribbed backing rigid and *makes the flat mirror concept technically possible*. Of course simply grinding a 1/10 wave hyperbolic curve on a 1cm thick glass plate eliminates the need for these high forces and also the need for most of the actuator control and thick ribbing support.

III THICKNESS OF RIBBED SUPPORT STRUCTURE

If the mirror is on the order of 2 cm thick it has large shear damping and little in the way of active controls are needed. With very little generated mechanical motion (such as torsional motion, no seismic motion sources here) in each of these mirrors a relatively small support rib backing ($\frac{1}{2}$ meter) is all that is necessary. In the 1mm mirror scenario some backing is needed to absorb the large reaction forces from the actuators. Silicon carbide has a high specific stiffness (E/ρ) and appears to be best here for weight reduction purposes. There would be a photovoltaic shield just outside the ribbed structure of each mirror.

IV SHUTTLE CARGO BAY PACKAGING

Each mirror itself (at most) is 2cm thick. And each mirror plus its ribbing cross supports needn't be more than a half meter in thickness. Six mirrors then would be approximately 3 meters thick. The focal point module adds about 3 more meters. Thus the space shuttle cargo bay could contain this 6 meter long object. There is still the option of the inflatable thermal shield on each mirror. Mark Gerry MSFC has already explored this option for the NGST. The weight of 6 three meter aperture mirror flats is about 1500 kg, which is not prohibitive for a shuttle payload (which could be as large as 20,000 kg).

A Self Organizing Deployment

One method for easily deploying the mirrors from the shuttle cargo bay is to use individual microwave transmitters (set at a different frequency for each mirror) at the focal point apparatus. Each mirror would simply move to the position of maximum microwave power, the center of the beam. Thereafter the laser ranging would be used to get an approximate radial position. This methodology would require a minimum of software writing and so in a sense would be a self organizing deployment.

V FOCAL POINT MODULE

At the focal point is an array of refractors for combining the light from the respective mirrors. There is one refracting telescope for each mirror. We use refractors since obstructions in reflecting telescope optical paths (e.g., secondary mirror supports) cause many complications in the deconvolution process.

The field of view of each refracting telescope is just a circular projection on the telescope mirror. The beams from the refracting telescopes are combined in a beam combining element to form one beam and recorded as an image. This process must be done in such a way that the beams have only residual phase decoherence (are phase matched) in the plane. The only beam interference must be due to the source wavefront itself. If the ccd focal plane is lets an 5mm wide, with lets say the beam from one of the mirrors being a $1/6$ 5mm we can determine the distance needed to combine the beam to get the correct exit pupil geometry $\lambda/0.005 = 0.001/5 \times 10^{-8}$. So 100 meters is required for beam recombination. This can be done in a multiple (25) reflections inside a 4 meter cylinder with $\lambda/100$ flat mirrors. So a long tube is required for these beams to gradually merge. This tube must be stored cross wise in the cargo bay.

A chopper is put into each beam just after it leaves the refracting telescopes. Each chopper has a mirror that reflects a light from the companion star (from the mirrors) along a tube. In that tube are the sensors required for pointing control.

This idea is remotely similar to the ground demonstration GOLAY 6 conceptual design done at Phillips lab in Albuquerque NM. Except here we eliminate the secondary hyperboloid and replace it with a focal point module. This combines the focal point and secondary modules into one and allows for the relatively large volume needed for mirror pointing control. Note that the technical requirements are very different for GOLAY 6 ground deployment then for this space based deployment. Another similar design is the TRIOS-SAMSI approach researched in the 1980s (See Max Nien's discussion in NGST literature). Construction of the SAMSI interferometer apparatus apparently proved to be too large a technical challenge. Hope this isn't the case here.

III METEORIC DEGRADATION

At the L2 point meteoric degradation is not a problem. It was concluded that at the L2 lagrangian point that only .18% surface was degraded over 10 years. This issue has been studied extensively by J.Robinson, MSFC.

It is to be noted that <1mm meteoric impact regions mostly would give diffuse reflection and so $1/r^2$ intensity falloff. For example a mirror at 100 meters would have 100 times more image degradation than a mirror at 1 km. And so the effect on the imaging a kilometer distant mirror (with these impacts on it) would be negligible (as opposed to the much smaller NGST distance effects). So it is conceivable that the telescope could be put in low earth orbit since it is easy to show that it would take many such impacts to

degrade the image appreciably. Thus the tried and true magnetic angular momentum transfer used in the Hubble space telescope (since it is in the earth's magnetic field) could be used here so that using up of thruster gas would not be a problem. In any case studies need to be done of what kind of glass would allow high velocity impacts to give diffuse reflecting impact regions (instead of specular).

A Magnitude and Resolution Requirements

By comparison the sun has an apparent magnitude of $-26 \frac{1}{2}$ and Venus (an earthsize planet) at it's brightest -4 at a distant comparable to the earth's distance from the sun (at approximately maximum elongation). So conservatively there is about 23 magnitude difference. Now one can image 27th magnitude objects with Hubble. Here there are 6 such mirrors in this golya 6 array raising that to about 29 (if the phase heterodyning time is not considered). So there is a wiggle room here of about $29-23=6$ magnitudes, or about a 200 times difference in brightness. This is about the brightness difference between the dimmest visible naked eye stars and a star such as Rigel. So this telescope does have enough collecting area to image earthsize extra solar planets. Matched Filters (are very effective at filtering out images from noise) and detector cooling can be used to assist in solving the problem of low contrast using sparse arrays because of noise integration. In regard to resolution requirements: In one light year there are 5.8×10^{12} miles $= 5.8 \times 10^{12} \times 1600$ meters. So 1.3 parsecs equals about $4 \text{ ly} = 4.5 \times 10^{16} \text{ m}$ = distance to alpha centauri. So equating the diffraction limited resolution angle (in the visible) for a 50 meter aperture to the actual (radian) angle subtended by the planet at the distance of the nearest star (alpha centauri $= 1.3 \text{ parsecs} = 4 \text{ ly}$) $1.22 \lambda / D = x / (1.3 \text{ parsec})$ For visible $\lambda = .5 \mu = 5 \times 10^{-7} \text{ m}$, $D = 50 \text{ m}$, $1.3 \text{ parsec} = 3.7 \times 10^{16} \text{ m}$, so $x = 283,000 \text{ miles}$, about the diameter of the sun! So 50m (the Gossamer program baseline) is hardly the aperture required to resolve extrasolar planets. If you replace D with $1 \text{ km} = 1000 \text{ m}$ you get $x = 14,200 \text{ miles}$, about 2 times the diameter of the earth. So at least a kilometer effective aperture is required to resolve an earthsize planet. A kilometer effective aperture then becomes a good baseline for designing an extrasolar planet imager. If all you want is effectively a radiometer measurement of the planet then 50 meters will do. And if you don't use this large effective aperture then you simply are not going to resolve extrasolar planets! (but why use 50 meters when kilometers effective aperture are easier anyway, the main point of this talk).

Also, a 4 meter diameter sun shade with solar panels (thermally separated from the mirrors) could be used to block sun light so that enough natural focal plane cooling could occur to allow infrared imaging.

More miscellaneous Notes:

E Orientation and Linear position Control

The Hubble must keep a $\pm 10 \times 10^{-7}$ radian directional control just to keep it's psf's on pixel and so within the diffraction limit. By the way this translates into a positional tolerance of one end (of that telescope) relative to the other of about 2 microns. But in the above sparse array situation $5 \times 10^{-2} \text{ mm} / 10^6 \text{ mm} = 2 \times 10^{-7}$ radians or 50 times better pointing accuracy. And radially we require here a $\pm .5 / 10 = .05 \mu$ tolerance. Again our sparse array must be about 50 times more accurate in linear positioning as well! Note that linear positioning tolerances don't change for even much larger sparse arrays while the angular tolerances decrease.

For submicron control can use liquid crystal change in reflectivity to move mirror. Can show this just by plugging into Newton's second law. 6 newtons per km^2 for solar sails at 1 AU. So $6 \times 10^{-6} \text{ N}$ for 1 m^2 . $F = ma$, so $6 \times 10^{-6} \text{ N} = 1000 \text{ kg} \times a$, $a = 6 \times 10^{-9} \text{ m/s}^2$. $.05 \times 10^{-6} \text{ m} = D = \frac{1}{2} a t^2 = \frac{1}{2} 6 \times 10^{-9} t^2$. So $t = 4 \text{ sec}$ a reasonable time. So gas jets not needed for submicron control. Also can use in near earth orbit to be able to use earth's magnetic field for angular momentum dumping as the Hubble does. And so there would be no need for gas jet thrusting (cold gas jets run out of gas within months). But in that case micrometeoroid degradation is large and mirrors would have to be replaced periodically (~2 years).

F Exit Pupil vs Entrance Pupil Geometry

The bottom line in sparse arrays⁹ is the need for exact matching of exit pupil geometry to entrance pupil geometry which was first recognized by Mienel in 1970. As with the NGST, maximizing the Strehl ratio is the bottom line for accomplishing this. Also our beam combination tube is needed to create the correct exit

pupil. Note the OPT must here be the combination of the OPTs for the sparse golay6 array and the focal point module optics such as the refracting telescopes.

"i" is the angle of incidence. $1/t' + 1/t = 2/\cos i$ is the formula for the tangential fan. For $t = \infty$ then $t' = (r \cos i)/2$ where r is the radius of curvature, t' image distance and t object distance. The Petzval surface radius is $r/2$. Coma arises from offense against the sign condition. The offense against the sign condition gives $f(y^2/4f^2) = \Delta M$ for coma magnification. y is transverse distance from the paraxial ray to the mirror, f is the focal point of the mirror.

The bottom line for this idea is that we have taken the sparse array problem from the hardware realm to the systems analysis realm (i.e., its a computer software problem!). The real complexities here for example are when to transfer control let's say from coarse to fine adjustments. But that is a far cry from the hardware and materials problems that plague the other Gossamer proposals.

Summary:

- 1) 6DOF problem goes to 1DOF phasing problem since tip-tilt easier to detect for large mirror distances.
- 2) Nearly flat mirrors only needed (for distant mirrors), easier to fabricate
- 3) Mirrors can get nicked a lot by micrometeoroid impact with small resultant scattering for distant mirrors
- 4) Uses glass instead of membranes, more practical for getting $(1/10) \lambda$ accuracy in the visible and therefore high resolution.

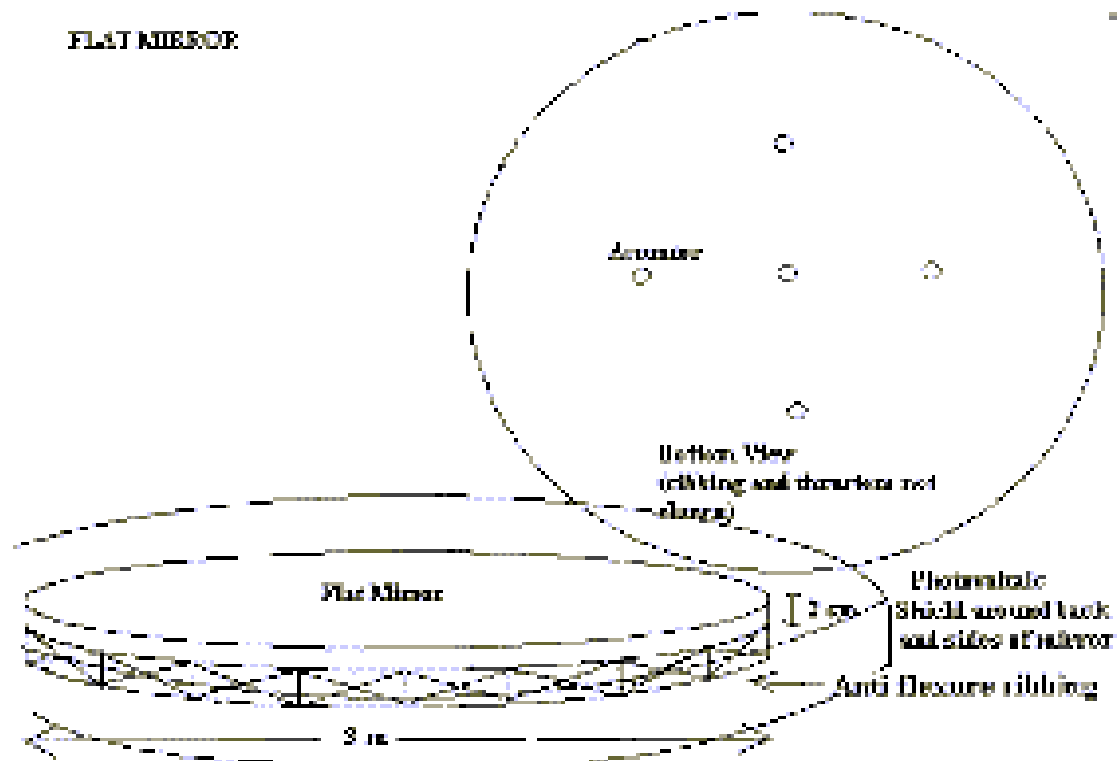
Things get easier in many ways with 1 km effective aperture (giving extrasolar earthlike planet imaging) than with 100 meter effective aperture.

So why bother with low resolution when high resolution is easier in many ways? Go for the gold and do high resolution since it's easier anyway. It would be nuts to do low resolution under these circumstances.

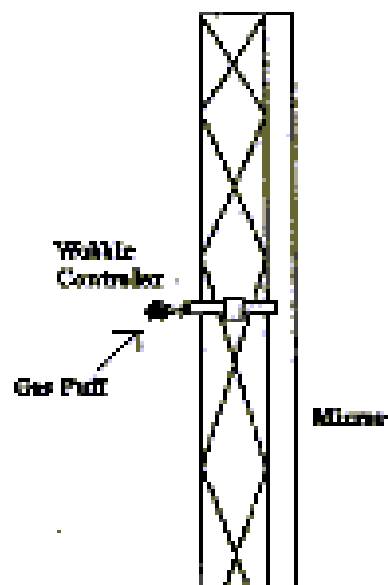
Notes and Bibliography

- 1) Excellent figure achieved on millimeter thick substrates at MSFC. We could use a 1 cm mirror thickness to eliminate the need for complicated active optic elements.
- 2) Can use electroformed Ni. Pyrex has low specific stiffness and thermal distortion
- 3) Replicated optics can make it cheaper to build these mirrors.. See electroformed cassegrain mirror of D. Engelhaupt, UAH, UAH-CAO, W. Jones MSFC
- 4) Thermotex corporation has demonstrated 2 mm thin shell mirror with actuator control
- 5) Could use Schaeffer type 5 actuator
- 6) Wavefront Control for the Next Generation Space Telescope , David Redding, et al.
- 7) M.Krim and R.Rockwell, "Delivery,Deployment, and design strategies for giant astronomical telescopes in the 2000 to 2025 era "presented at the SPIE conference Reflective Optics (Los Angeles), Jan15-16, 1987
- 8) M.J.Golay, "Point arrays having compact non-redundant autocorrelations" J.Optical Society of America"61,272(1971)
- 9) Weaver Lawrence, "Design considerations for multiple telescope imaging arrays" Optical Engineering, vol.27,No.9
- 10) Malacara, Daniel, Optical Shop Testing 2nd ed, Wiley

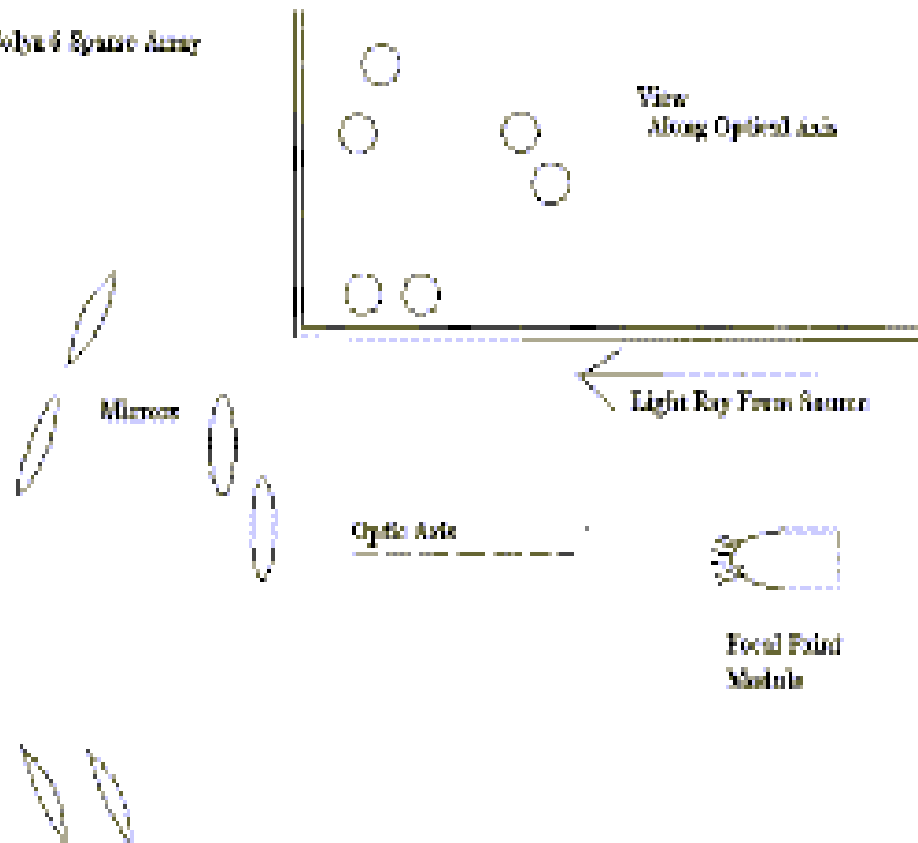
FLAT MIRROR



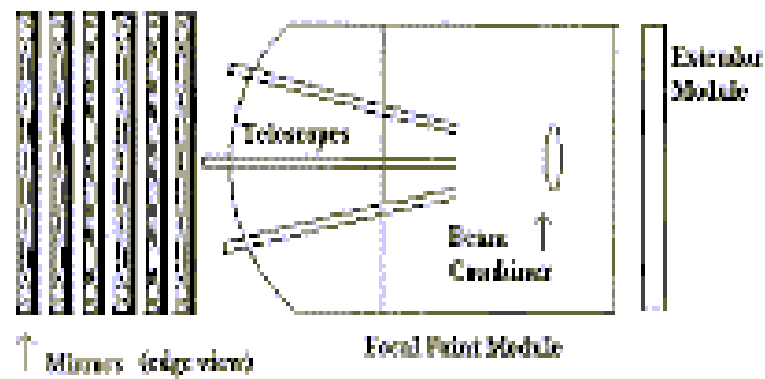
MIRROR POSITION STABILIZATION ELEMENTS OF TELESCOPE SPACER ARRAY ACTIVE BEAM DIRECTION CONTROL



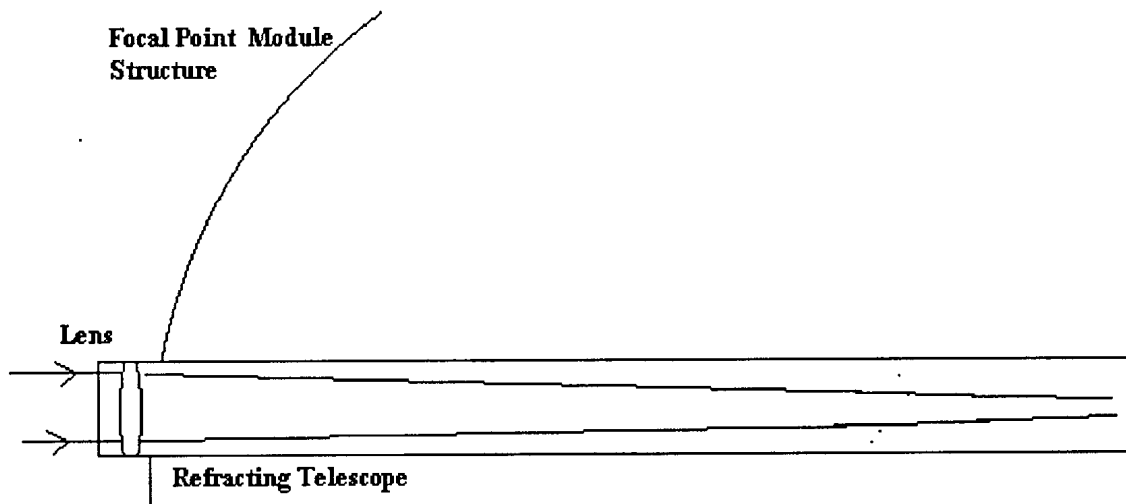
Column & Sparse Array



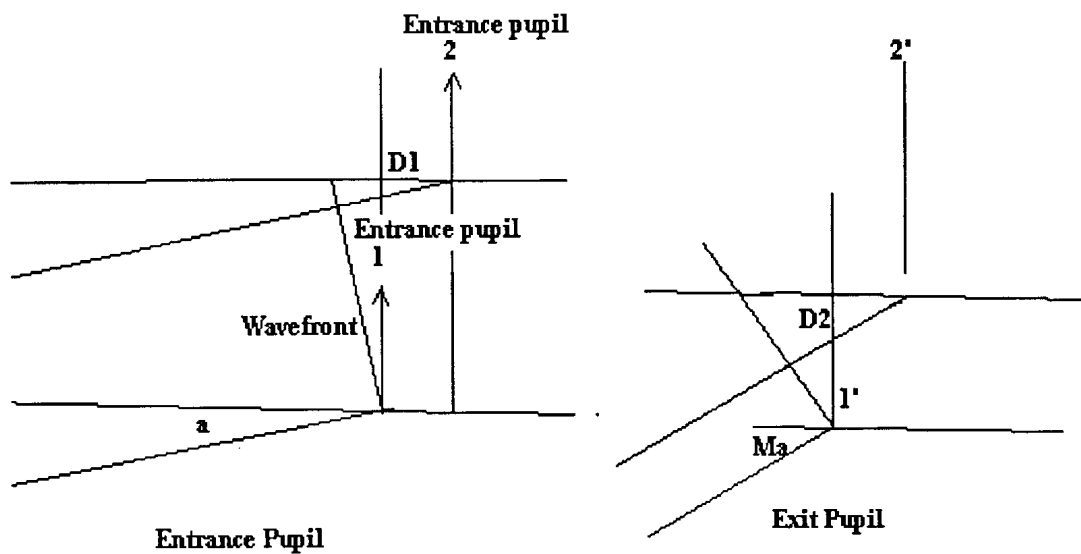
CARGO BAY PACKING



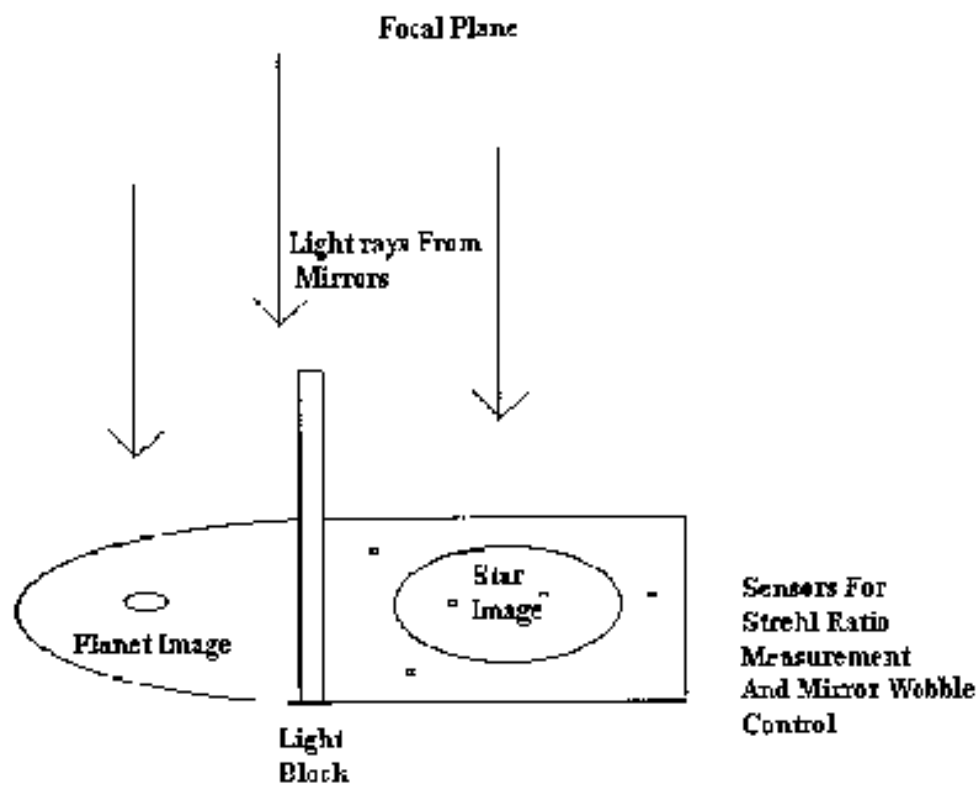
Individual Refracting Telescope Element In Focal Point Module



Pupil Geometry



Net Piston error = $D1 - D2$ Need small piston error in sparse arrays



Trading Mirror Mass for Megaflops

Richard G. Paxman^{and} Brian J. Thelen
Veridian ERIM International
P.O. Box 134008
Ann Arbor, MI 48113

ABSTRACT

There is an ever-increasing need for fine-resolution imaging for both astronomical and earth-observing space telescopes. The unquenchable desire for improved resolution will continue to drive technologists to develop larger apertures. Accordingly, there is currently a significant effort to advance lightweight mirror technology. However, the optical tolerances imposed on this technology development significantly limit projected areal densities. Consequently, weight, fabrication time, and cost are also constrained. The distributed correction of imaging errors represents a novel concept for use in overcoming these technology constraints. Whereas a primary mirror is traditionally designed to meet strict optical tolerances, under the distributed-correction paradigm, we relax the optical tolerances on the primary and seek to distribute the correction over various subsystems down stream, including multi-conjugate corrective elements, adaptive correction with phase-diverse wavefront sensing, and post-detection processing. The relaxed-optical-tolerance concept has the effect of "trading mirror mass for megaflops".

Relaxed-optical-tolerance imaging, phase diversity, wavefront sensing, segmented mirror, areal density, adaptive optics

1. INTRODUCTION

The insatiable desire for improved image resolution is driving the development of increasingly large, space telescopes, both for astronomical and earth-observing applications. Because large monolithic primary mirrors are difficult or impossible to deploy in space, alternative designs are being developed. Deployable-optic systems, such as segmented-aperture designs employing light-weight mirrors, seek to achieve a large primary-mirror effective diameter while allowing stowage and deployment of the system. Accordingly, there is currently a significant effort to advance light-weight mirror technology to accommodate this need. However, the optical tolerances imposed on this technology development significantly limit projected areal densities for light-weight mirrors. It follows that weight, fabrication time, and cost are also constrained.

A candidate solution to this technology shortfall is to relax optical tolerances on the primary mirror and maintain overall system performance through pre-detection (active optical) correction and post-detection (processing) correction. We are investigating a unified system-design approach in which the functional blocks shown in Figure 1 are jointly designed, in contrast to historical methods of optimizing each function independently.

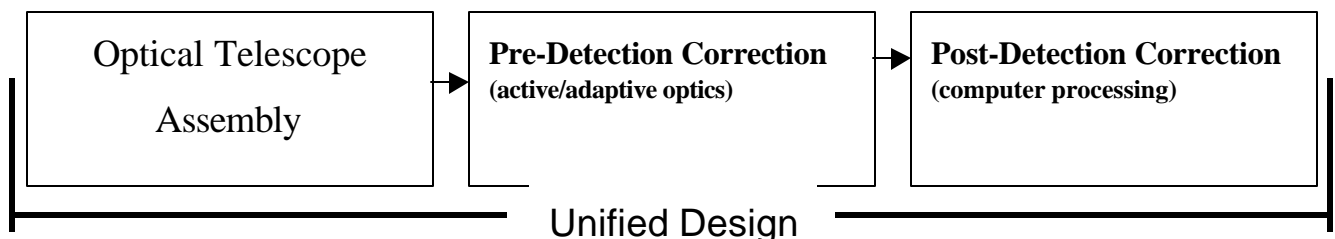


Figure 1: Unified system design for distributed correction of relaxed optical tolerances in the primary mirror.

The driving principle is to reduce the mass of the primary *for* mirror at a modest increase in computational complexity -- a concept we refer to as trading *mirror mass megaflops*. This appears to be a favorable

tradeoff, given the cost and performance trends in computing technology. By relaxing optical tolerances, we seek:

- a significant reduction in weight implying reduced launch costs,
- simplified deployment of segmented-aperture designs, and
- reduced fabrication, integration, and testing costs associated with the development of complex, low-volume production-run space systems.

In addition, a unified design approach provides greater design freedom by introducing the new trade space of computer processing for pre- and post-detection correction. Relaxing optical tolerances also accelerates the light-weight mirror technology development effort.

2. TRADING MIRROR MASS

The concept of trading mirror mass for megaflops has an historical precedent in sparse-aperture telescopes. The goal of sparse-aperture systems is to achieve a resolution equivalent to that of a filled-aperture system while using significantly less mirror surface. Post-detection processing in the form of MTF boosting is an essential component of the image-formation process for such systems. The cost of adopting a sparse-aperture strategy is the need for post-detection computations and a decrease in SNR. Thus, sparse-aperture systems trade mirror mass for megaflops.

In sparse-aperture systems, mirror mass is reduced by eliminating mirror surface area from a filled primary mirror, in cookie-cutter fashion. By contrast, under the relaxed-optical-tolerance concept, mirror mass is reduced by thinning the mirror (reducing areal density) while retaining a filled aperture. Aberrations incurred with thinned mirrors will need to be sensed and corrected down stream with both pre- and post-detection processing. We are investigating this trade. The SNR trends with relaxed-optical-tolerance systems may be more favorable than with sparse apertures since aperture fill is maintained and more photons are collected.

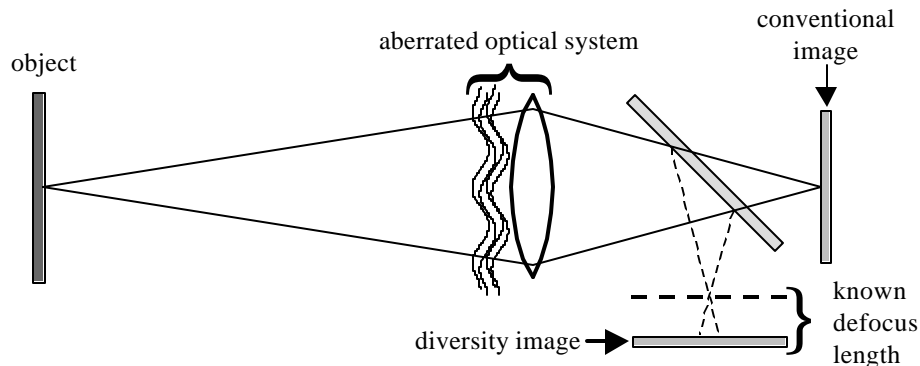


Figure 2: Typical phase-diversity data collection setup

3. WAVEFRONT SENSING

Wavefront sensing is an essential component of a relaxed-optical-tolerance system. In order to achieve the imaging performance desired, light-weight segments must be figured, aligned, and phased to within a small fraction of a wavelength of light. When a segmented-aperture system is deployed, a series of steps is undertaken to capture the phasing and alignment of the system, following which maintenance of the phasing is initiated. Methods that utilize image-plane data have been shown to be useful in many of these steps. Such methods have the additional advantage that they use the science camera rather than introducing auxiliary sensors. In the case of astronomical telescopes, such as the Next Generation Space Telescope (NGST), images of a known unresolved star can be used with phase-retrieval algorithms to estimate fine

phase errors, including inter-segment piston and tilt errors and intra-segment figure errors^{1,0}. In this context, phase-retrieval algorithms rely on the validity of the known-object assumption. However, when the object is not known *a priori*, such as with unknown binary stars or when earth observing, then other methods must be employed. The method of phase diversity (PD) is a strong candidate in this case. PD has been shown to be useful for sensing aberrations when observing unknown objects, including objects that extend beyond the field of view.

4. PHASE DIVERSITY

Phase diversity (PD) is a combined collection and post-processing technique used to infer unknown phase aberrations from image data^{0,0,0}. PD requires the collection of two or more images of the same object. One of these images is typically the conventional focal-plane image that has been degraded by the unknown aberrations. Additional images are formed by perturbing these unknown aberrations in some known fashion. For example, a simple translation of the detector array along the optical axis further degrades the imagery with a known amount of defocus. The quadratic phase introduced by this intentional defocus is a common choice for the phase-diversity function, owing to its relatively simple implementation. This traditional phase-diverse data collection approach is illustrated in Figure 2. Statistical estimation techniques are employed to identify a combination of object and aberrations that is consistent with all of the collected images, given the known phase diversities. The phase-error estimate is of primary interest for wavefront-sensing applications, but the object must be estimated as well when an unknown extended scene is imaged. This object estimate is a fine-resolution representation of the unaberrated scene, which can be used for post-detection correction of the degraded imagery when

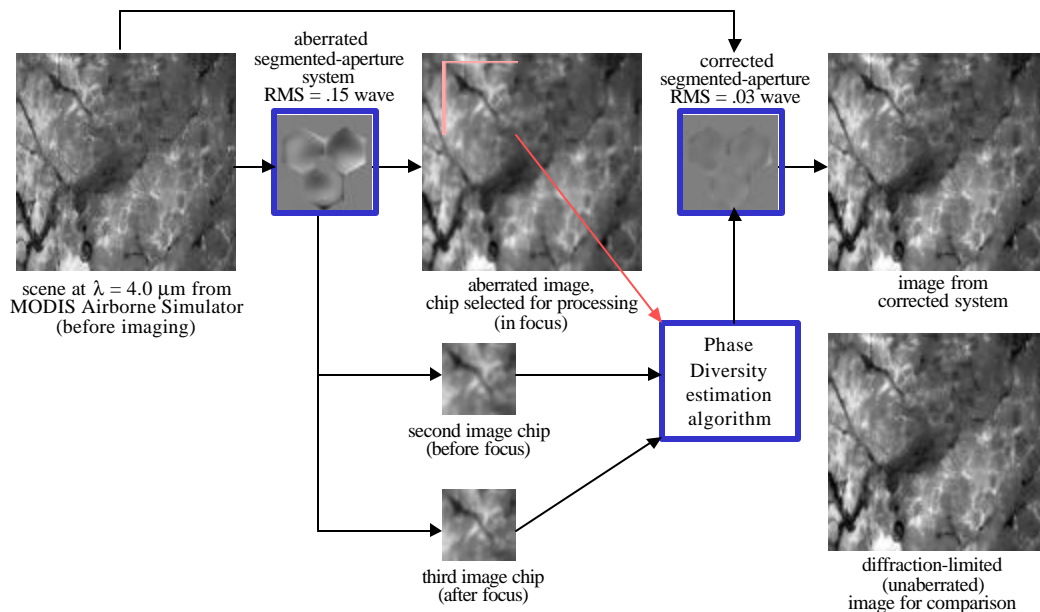


Figure 3: Phase diversity is able to estimate wavefronts from low-contrast scenes to well within the Marechal criterion. Moderate Resolution Imaging Spectrometer (MODIS) data were used to simulate imagery aberrated with piston, tilt, and low-order segment-figure error (20 Zernike polynomials per segment) and having realistic SNR. The PD algorithm estimates the aberrations to within .03 waves RMS and imagery from the corresponding corrected system is essentially diffraction limited.

required. If the object is known *a priori*, such as when imaging an unresolved star, only the aberrations must be estimated, resulting in a much easier problem, referred to as Phase-Diverse Phase Retrieval (PDPR)⁰.

Researchers at ERIM International have pioneered the use of PD and have extensive experience in applying PD to both pre-detection correction and post-detection processing. We have demonstrated the use of PD as a wavefront sensor in simulation⁰ and in the laboratory⁷. A simulation result for a 3-segment telescope, having both inter-segment piston and tilt misalignments and intra-segment figure error, is shown in Figure 3. This simulation corresponds to the down-looking function of NASA/Goddard's proposed Nexus/Horizon system. Even with low-contrast images of clouds, the wavefront estimate error is seen to be

0.03 waves RMS -- well within the error budget designed to meet the Marechal condition (.07 waves RMS) for a well corrected system. In this simulation, it was assumed that one could correct the primary mirror perfectly according to the wavefront estimate generated from PD. But PD also can be used for post-detection processing, thus relaxing these pre-detection requirements as well.

The phase-diversity technique offers several advantages over other aberration-sensing methods. The optical hardware required is modest. For example, a simple beam splitter and a second detector array allow the simultaneous collection of two phase-diverse images. Like phase retrieval, PD uses image-plane data from the science camera, thus obviating the need for auxiliary sensors. In addition, the method relies heavily on an external reference (the object being imaged), making PD less susceptible to systematic errors introduced by optical hardware. The technique accommodates discontinuous wavefronts, such as a piston error between two adjacent segments. Finally, PD works well for unknown extended objects, including those extending beyond the field of view.

CONCLUSION

Relaxed-optical-tolerance imaging is a concept that seeks to enable the technology trend of increasingly large space telescopes. Like sparse-aperture imaging, relaxed-optical-tolerance imaging trades mirror mass for megaflops. However, with relaxed-optical-tolerance imaging, this trade is accomplished by reducing the primary-mirror areal density while maintaining aperture fill, thus preserving photon flux. Aberrations resulting from reduced areal density must be sensed and corrected downstream with pre- and post-detection correction. Phase diversity is a strong candidate wavefront sensor for this application, particularly in earth-observing scenarios where an unknown object extends beyond the field of view. We are investigating the cost-performance trends as a function of primary mirror areal density.

REFERENCES

1. J.R. Fienup, "Phase retrieval for undersampled broadband images", *J. Opt. Soc. Am. A* 16, pp.1831-1837, 1999.
2. D. Redding, S. Basinger, A.E. Lowman, A.Kissil, P. Bely, R. Burg, R. Lyon, G. Mosier, M. Femiano, M. Wilson, G. Schunk, L. Craig, D. Jacobson, J. Rakoczy, and J. Hadaway, "Wavefront sensing and control for a Next Generation Space Telescope," in *Space Telescopes and Instruments V*, Piere Y. Bely and James B. Breckinridge, eds., Proc. SPIE 3356-47, pp. 758-772, Kona HI, 1998.
3. R. A. Gonsalves and R. Chidlaw, "Wavefront sensing by phase retrieval," In *Applications of Digital Image Processing III*, A. G. Tescher, ed., Proc. SPIE 207, pp. 32-39, San Diego, CA, 1979.
4. R. G. Paxman and J. R. Fienup, "Optical misalignment sensing and image reconstruction using phase", *J. Opt. Soc. Am. A* 5, pp. 914-923, 1988.
5. R. G. Paxman, T. J. Schulz, and J. R. Fienup, "Joint estimation of object and aberrations by using", *J. Opt. Soc. Am. A* 9, pp. 1072-1085, 1992.
6. B. L. Ellerbroek, B. J. Thelen, D. J. Lee, D. A. Carrara, R. G. Paxman, "Comparison of Shack-Hartmann wavefront sensing and phase-diverse phase retrieval," In *Adaptive Optics and Applications*, R. K. Tyson and R. Q. Fugate, eds., Proc SPIE 3126-38, San Diego, CA, 1997.
7. J. H. Seldin, R. G. Paxman, V.G. Zarafis, L. Benson, and R.E. Stone "Closed-loop wavefront sensing for a sparse-aperture multiple-telescope array using broadband phase diversity" in *Imaging Technology and Telescopes*, J.B.Breckinridge, ed., Proc. SPIE 4901-07, San Diego, CA, July 30, 2000.

Scaling Laws for Sparse-Aperture Imaging

James R. Fienup
Veridian ERIM International
1975 Green Rd., Ann Arbor, MI 48105
fienup@erim-int.com

ABSTRACT

Scaling laws for sparse-aperture telescopes are derived. Included are both fixed-aperture and synthetic-aperture telescopes, and a variety of noise sources.

Sparse-aperture incoherent imaging systems produce low-contrast, reduced-resolution images because the modulation transfer function (MTF) is suppressed at the higher spatial frequencies relative to that of a filled-aperture telescope. If the signal-to-noise ratio (SNR) is sufficiently high, then the deleterious effects of the MTF can be compensated by post-detection processing, for example by Wiener-Helstrom filtering. However, the frequency-domain SNR is reduced not only by increased photon noise, since the smaller total aperture area collects fewer photons, but also because of the reduced MTF. As apertures become sparser, one would like to know what scaling laws hold: how do the SNR, MTF, and integration (exposure) time to get a desired image quality vary with array sparsity [1]. In this paper we give the scaling laws and show how they vary for different sources of noise. The analysis here holds for sparse-aperture telescopes, multiple-telescope telescopes, and imaging interferometers.

We begin with a model for the imaging process:

$$g(x, y) = \text{Poisson} [f(x, y) * s(x, y) + n_b(x, y) + n_{dc}(x, y)] + \mathbf{S}_r n_3(x, y) - n_b - n_{dc}$$

$$\approx f(x, y) * s(x, y) + \sqrt{f(x, y) * s(x, y)} n_1(x, y) + \sqrt{n_b} n_2(x, y) + \sqrt{n_{dc}} n_3(x, y) + \mathbf{S}_r n_4(x, y)$$

where f = object brightness (in photons), s = PSF, \mathbf{S}_r = rms readout noise

n_b = additive bias (path radiance, haze), n_{dc} = dark current,

$n_k(x, y)$ = independent zero-mean Gaussian noises (unit variance)

From it we can derive the SNR of the complex Fourier transform of the image, as a function of spatial frequency, (u, v) :

$$SNR_1(u, v) = \frac{(P/M)S(u, v)\mathbf{m}(u, v)}{\left[\left(P/M^2\right) + n_b + n_{dc} + \mathbf{S}_r^2\right]^{1/2}} \quad (1)$$

where

P = total number of photons in $M \times M$ image

$\mathbf{m}(u, v) = F(u, v)/F(0, 0)$ = normalized scene Fourier transform

Note that for the complex Fourier data, the noise is uniformly distributed in the Fourier domain; however, the SNR is a strong function of spatial frequency because typically both $\mathbf{m}(u, v)$ and $S(u, v)$ vary greatly with spatial frequency. One can also consider the SNR of the power spectrum of the image, but ultimately this will lead to the same conclusions for the scaling laws.

We put the SNR expression in terms of the telescope's fill factor, a , the ratio of the area of the sparse aperture to the area of an equivalent-diameter filled aperture. The total number of detected photons in an $M \times M$ image is

$$P = \Phi_o a A_f \mathbf{h}_t T \quad (2)$$

where

Φ_o = image photons per unit aperture - area per unit time

a = fill factor

A_f = area of filled aperture giving same resolution

\mathbf{h}_t = total efficiency (system throughput)x(detector q.e.)

Figure 1 shows the case of two apertures, a filled circular aperture and a sparse

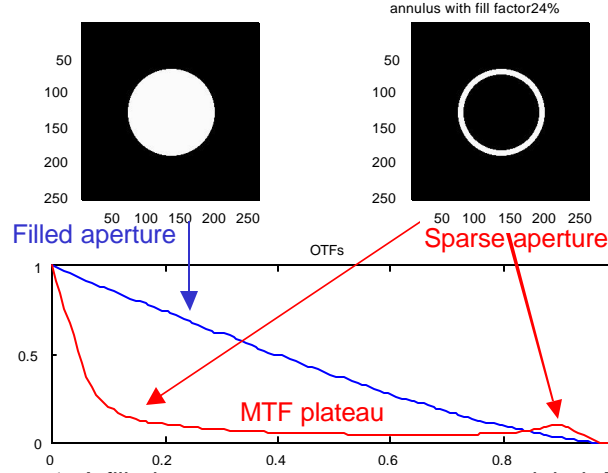


Figure 1. A filled aperture, a sparse aperture, and their MTFs.

annular aperture. The former has an MTF that decrease almost linearly with spatial frequency, whereas the later has an MTF that has a large plateau region where it is almost constant. We can show that the MTFs of most well designed sparse apertures have this same characteristic: the MTF is approximately constant for a wide range of spatial frequencies, and value of the MTF in that plateau region is proportional to the fill factor:

$$MTF \approx \mathbf{h}_A a, \mathbf{h}_A = \text{constant} \quad (3)$$

where \mathbf{h}_A depends on the aperture type.

Using the relations

$$S(u_{mid}, v_{mid}) = \mathbf{h}_A a$$

$$M^2 n_b = \Phi_o a A_f \mathbf{h}_t T$$

$$n_d = r_{dc} T \quad [\text{(dark current rate) x T}]$$

we find that at the middle spatial frequencies in the plateau region,

$$SNR_1(u_{mid}, v_{mid}) = \frac{(\Phi_o A_f \mathbf{h}_t \mathbf{h}_A a^2 T / M) \mathbf{m}(u, v)}{[(\Phi_o + \Phi_b) A_f \mathbf{h}_t a T / M^2 + r_{dc} T + s_r^2]^{1/2}} \quad (4)$$

From this we see that there is a complicated relationship between the SNR and the fill factor, a . However, if we take one noise source at a time (setting the others to zero), the expression simplifies, and we can solve for the integration time, T , needed to achieve a desired SNR threshold, SNR_t . For example, for photon and background noise combined, we have

$$T = \frac{SNR_t^2}{A_f \mathbf{h}_t a^3 (\mathbf{h}_A \mathbf{m}(u, v))^2} \frac{\Phi_o + \Phi_b}{\Phi_o^2}, \quad (5)$$

and we see that the required integration time is proportional to the inverse cube of the fill factor. The reason for this strong dependency on the fill factor is that the SNR increases only as the square root of T , and it increases (i) as the square root of a as sparser apertures transmit fewer photons to the detector and (ii) as a as the MTF is proportional to a . Hence, the reduced MTF plays a much larger role in the need for longer

integration times than does the fact that fewer photons are being detected. Similar analysis shows that the integration time is proportional to the inverse fourth power of the fill factor for dark-current noise and to the inverse square of the fill factor for readout noise.

The analysis above is for sparse apertures that are fixed during the integration time. Another possibility is to have a sparse aperture that moves during the integration time, having only partial (u, v) -plane coverage at any one instant, but temporally synthesizing the (u, v) -plane MTF during the integration time. This would be the case, for example, if NASA's Space Interferometer Mission (SIM) were used in an imaging mode. For such temporal synthesis imaging systems, different scaling laws hold. For such systems the total integration time is proportional to the inverse square of the fill factor for photon noise, background noise, and readout noise, and to the inverse cube of the fill factor for dark-current noise. The reason that the scaling laws are more favorable for synthetic-aperture systems is as follows. If the photons are detected in a focal plane, then the photon noise is spread all over the (u, v) (Fourier) plane. However, at any given instant only a small portion of the (u, v) plane has any signal in it. Consequently, for a frame of data taken at any instant, we can just keep the part with the signal, and filter out most of the noise. This reduction in noise by filtering individual frames is what gives the more favorable scaling laws. If, on the other hand, the focal plane images were simply summed over time as the complete aperture is synthesized, and filtered after the summation, then this advantage would be lost.

In conclusion, we have derived scaling laws for incoherent sparse-aperture imaging systems and predicted SNR, MTF, and required integration time as a function of fill factor. We found substantially different scaling laws depending on the source of noise and on whether the telescope aperture is fixed or the MTF is synthesized over time.

Reference

1. J.R. Fienup, "Integration Time versus Fractional Fill for Sparse-Aperture Telescopes," Annual Meeting of the O.S.A., Santa Clara, CA, September 1999, paper TuM2.

Wavefront Sensing for Sparse Apertures by Phase Diversity

Robert A. Gonsalves
Tufts University

ABSTRACT

The advantage of a sparse aperture is that the optical system is lightweight when compared to a large, solid-aperture system but it retains the same high resolution of a large aperture. To get the benefit of the large spatial extent of the aperture, the subapertures must be properly phased to each other; and the subapertures, themselves, may have phase aberrations, which must be removed. In this paper we show how the overall phase can be estimated by recording two phase diversity images. We use an iterative algorithm, which modifies the input point spread functions in a controlled, non-linear way. We calculate performance based on computer simulations.

A Phase Diversity Solution to the Small-Phase Retrieval Problem

Robert A. Gonsalves
Tufts University

ABSTRACT

We present a non-iterative solution to the phase retrieval problem when the unknown phase, T , is small and when the observable is a pair of diversity images. The solution specifies the even and odd parts of T in two separate equations. In this talk we provide details of the derivation and show computer simulations of the technique.

Overcoming Dynamic Disturbances in Imaging Systems

Eric W. Young

NASA Goddard Space Flight Center, Greenbelt, MD 20771

Gregory C. Dente,

GCD Assoc., 2100 Alvarado NE, Albuquerque, NM 87110

Richard G. Lyon

NASA Goddard Space Flight Center, Greenbelt, MD 20771

Dennis Chesters

NASA Goddard Space Flight Center, Greenbelt, MD 20771

Qian Gong^c

Swales Aerospace, 5050 Powder Mill Rd., Beltsville, MD 20705

ABSTRACT

We develop and discuss a methodology with the potential to yield a significant reduction in complexity, cost, and risk of space-borne optical systems in the presence of dynamic disturbances. More robust systems almost certainly will be a result as well.

Many future space-based and ground-based optical systems will employ optical control systems to enhance imaging performance. The goal of the optical control subsystem is to determine the wavefront aberrations and remove them. Ideally reducing an aberrated image of the object under investigation to a sufficiently clear (usually diffraction-limited) image. Control will likely be distributed over several elements. These elements may include telescope primary segments, telescope secondary, telescope tertiary, deformable mirror(s), fine steering mirror(s), etc. The last two elements, in particular, may have to provide dynamic control. These control subsystems may become elaborate indeed. But robust system performance will require evaluation of the image quality over a substantial range and in a dynamic environment. Candidate systems for improvement in the Earth Sciences Enterprise could include next generation Landsat systems or atmospheric sensors for dynamic imaging of individual, severe storms. The technology developed here could have a substantial impact on the development of new systems in the Space Science Enterprise; such as the Next Generation Space Telescope(NGST) and its follow-on the Next NGST. Large Interferometric Systems of non-zero field, such as Planet Finder and Submillimeter Probe of the Evolution of Cosmic Structure, could benefit. These systems most likely will contain large, flexible optomechanical structures subject to dynamic disturbance. Furthermore, large systems for high resolution imaging of planets or the sun from space may also benefit. Tactical and Strategic Defense systems will need to image very small targets as well and could benefit from the technology developed here.

We discuss a novel speckle imaging technique with the potential to separate dynamic aberrations from static aberrations. Post-processing of a set of image data, using an algorithm based on this technique, should work for all but the lowest light levels and highest frequency dynamic environments. This technique may serve to reduce the complexity of the control system and provide for robust, fault-tolerant, reduced risk operation. For a given object, a short exposure image is "frozen" on the focal plane in the presence of the environmental disturbance (turbulence, jitter, etc.). A key factor is that this imaging data exhibits frame-to-frame linear shift invariance. Therefore, although the Point Spread Function is varying from frame to frame, the source is fixed; and each short exposure contains object spectrum data out to the diffraction limit of the imaging system. This novel speckle imaging technique uses the Knox-Thompson method. The magnitude of the complex object spectrum is straightforward to determine by well-established approaches. The phase of the complex object spectrum is decomposed into two parts. One is a single-valued function determined by the divergence of the optical phase gradient. The other is a multi-valued function determined by the circulation of the optical phase gradient-"hidden phase." Finite difference equations are developed for the phase. The novelty of this approach is captured in the inclusion of this "hidden phase." This technique

allows the diffraction-limited reconstruction of the object from the ensemble of short exposure frames while simultaneously estimating the phase as a function of time from a set of exposures.

The following subsections of the paper are included: Introduction, Technical Approach, Plans, Preliminary Results of earlier work and a Conclusion.

1. INTRODUCTION

The desired result of this new algorithm is the development and verification in a laboratory setting of a technique to reduce the sensitivity and improve performance of NASA and DOD optical systems in dynamic environments. On the ground and in the laboratory such systems are sensitive to and the performance is degraded by atmospheric turbulence, laboratory seeing, and motion/jitter of key optical elements. In space the sensitivity of such optical systems is primarily to jitter; however some effects of downward looking through an atmosphere may still be present. Of course, seeing effects may still be present if the system is sealed and operating at non-zero pressure. In any event the development envisioned here will be able to improve algorithms that compute system performance. A key feature of the improvement lies in the inclusion of the "hidden phase" component in this algorithm.

We intend to investigate the improvement, our technique offers, in the context of various system architectures. For large, space systems with flexible structures various control architectures will be applied. Control will most likely be distributed over several elements. These elements can include primary mirror segments, secondary, tertiary, deformable mirror(s)-DM(s), Fast Steering Mirror(s)-FSM(s), etc. The control subsystem goal is to improve a system with substantially aberrated imaging to diffraction-limited imaging. Further the control subsystem will have to ameliorate the effects of temporally and spatially varying disturbances. It is in the realm of the temporally varying disturbances that this algorithm will be most effective. Indeed it is the hope that it can eliminate the need for any higher order aberration correction in the temporal domain and leave perhaps just a simple two-axis FSM. Post-processing using this algorithm will work at all but the lowest light levels. Realistic estimates of light-level limits on performance will be investigated.

Space systems of the future will be driven to lighter weight and lower areal densities for the optics. Such systems tend to be flexible and therefore prone to dynamic/jitter effects. For all NASA and DOD systems, sources of dynamical disturbances/jitter are certainly reaction wheels (as well as other stabilization devices), detector coolers, as well as other sources.

The Severe Storm type of mission may be particularly exciting and challenging, since the object of study (a single storm cell) is time evolving. The nature of the temporal disturbances onboard the satellite and those in the object will have to be studied and separated. Other geostationary systems may also benefit, such as Fourier transform spectrometers and other advanced meteorological satellites. Low earth orbiting systems such as Landsat may benefit as well.

The technology developed here could have a substantial impact on the development of new space telescopes; such as the Next Generation Space Telescope (NGST) and its follow-on the Next NGST. Large Interferometric Systems of non-zero field, such as Planet Finder and Submillimeter Probe of the Evolution of Cosmic Structure, could benefit. These systems most likely will contain large, flexible optomechanical structures subject to dynamic disturbance. Furthermore, large systems for high resolution imaging of planets and the sun would like benefit from this technology.

Positive results from this approach could lead directly to a high accuracy (near diffraction-limited) system for imaging in the presence of various disturbances, including vibration. Further, our approach has the potential to reduce cost and risk for large, light-weight systems in many potential applications. This approach is innovative and requires development to enhance its technology readiness. But it is believed to hold great promise for improvements.

For high power level systems, mainly DOD tactical and strategic systems, coolant flow induced jitter may be a significant source of disturbance. We have enumerated some specific types of systems that may be candidates for improvement.

Flowing from this development may be significant reduction in the complexity of space-borne optical systems. Consequent significant reductions in cost may also accrue from such a reduction in complexity. More robust systems may be a result as well. The output from this development quite likely would be a quantitative and qualitative reduction in risk for such space missions.

2. TECHNICAL APPROACH

This section of the proposal is divided into three sections. In the first section we present an overview of the speckle imaging technique to be used in this investigation. Secondly we elaborate the specifics of the Knox-Thompson approach used here and explain the enhanced feature; the development of the hidden phase. In the last section we discuss the particular plan to be followed in the future.

2.1 Overview

Speckle imaging techniques have been evolving since the fundamental idea was presented almost 30 years ago.¹ Labeyrie's key observation was that the speckles in short exposure images contain richer spatial frequency information than long exposures. The speckle imaging technique can be described as follows.² Two data sets are required to perform this imaging; one set of RO short exposures images of the object under study and one set RR of similar images of a bright, nearby reference. Normally, values of RO and RR are on the order of tens or hundreds, driven by signal-to-noise ratio considerations. Exposure times are typically a few to tens of milliseconds.

The first step in the process is to compute the fourier transform of the images. Next one computes the modulus squared and the cross spectrum or bispectrum. We use the cross spectrum obtained by the Knox-Thompson method. Statistics are then accumulated and the process is repeated either RO or RR times as appropriate. Then one computes the average modulus squared and the average cross spectrum or bispectrum. Continuing, one deconvolves the image modulus squared and computes the phase spectrum. Finally the fourier modulus and phase data are combined; the inverse transform is computed; and the image estimate is obtained.

Many methods exist to find the modulus and we will not elaborate them here. We will explain our approach below. Iterative methods start with the modulus and proceed along the following lines. First the inverse FFT is computed. Next the constraints are imposed. Finally the FFT is computed to obtain the phase and the process is iterated. We use a method to directly compute the phase using difference equations.

2.2 Detailed Approach

Here, we will concentrate on the particular implementation called the Knox-Thompson, or cross-spectrum, method and, in particular, deal with the object spectrum phase reconstruction.³

We label the arrays of short-exposure data as:

$$d(l; i, j). \quad (1)$$

The index $l = 1, 2, \dots, R$ labels the frame, while the next two indices, (i, j) , label the pixel in the array. We take a two-dimensional Finite-Fourier-Transform (FFT) on the pixel indices as:

$$\tilde{d}(l; m, n) = FFT\{d(l; i, j)\}. \quad (2)$$

The array indices, m and n , label the elements of the two-dimensional FFT. The zero spatial frequency point is labeled (\bar{m}, \bar{n}) . We then form the unbiased cross-spectra as⁴

$$C_x(m, n) = \frac{1}{R} \sum_{l=1}^R \left\{ \tilde{d}(l; m, n) \tilde{d}^*(l; m+1, n) - \tilde{d}^*(l; \bar{m}+1, \bar{n}) \right\} \quad (3)$$

$$C_y(m, n) = \frac{1}{R} \sum_{l=1}^R \left\{ \tilde{d}(l; m, n) \tilde{d}^*(l; m, n+1) - \tilde{d}^*(l; \bar{m}, \bar{n}+1) \right\}.$$

in which we have picked one unit offset in each direction in the FFT; other offsets can easily be analyzed, however, the unit offset choice gives the best accuracy on the high-spatial-frequency phase. The ensemble averaging over many realizations of the turbulence-induced phase screens makes the cross-spectrum transfer functions real-valued.³ Therefore, the turbulence-induced phase errors are averaged away and the phase of the cross-spectrum can be directly related to phase differences in the object spectrum.⁴ The remaining phases of these two cross-spectra lead to two two-dimensional difference equations for the phase of the object spectrum as:

$$C_x(m, n) = |C_x(m, n)| \exp(i V_x) \quad (4a)$$

$$C_y(m, n) = |C_y(m, n)| \exp(i V_y),$$

in which the cross-spectrum phases, V_x, V_y , are related to the object spectrum phase, W , as:

$$V_x(m, n) \equiv W(m, n) - W(m+1, n) \quad (4b)$$

$$V_y(m, n) \equiv W(m, n) - W(m, n+1).$$

In a new paper⁴ these equations for the object spectrum phase are solved⁴; we will refer to these equations as “phase flow” equations. In the derivation⁴ we first define discrete gradient, divergence and curl operations, followed by our proof that the phase flow on the FFT-grid can be decomposed into an irrotational part with zero curl and a rotational part with zero divergence. Next in the derivation⁴ we will demonstrate that in a similar fashion, the object spectrum phase can be decomposed into a regular single-valued function determined by the divergence of the phase gradient, as well as a multi-valued function determined by the circulation of the phase gradient; this second function has been called the “hidden phase”.⁵ We will present a solution method that gives both the regular and hidden parts of the object spectrum phase. Elsewhere it is also demonstrated⁵ that the standard least-squares solution to the two-dimensional difference equations will only generate the regular part of the phase, while always missing the hidden part. In the preliminary results section, we will give several examples of imaging through turbulence and post-processing, augmenting the Knox-Thompson method with a hidden phase algorithm. In particular, we will compare reconstructions with and without the hidden phase component included in the reconstruction algorithm. Finally, in the conclusion we discuss prospects for the method, as well as ongoing problem areas.

The solution difficulties associated with the cross-spectrum phases are reasonably well-known. In 1986, Fontanella, et. al. provided a discussion of the effects of phase dislocations on the phase reconstruction.⁶ In 1987, Takajo, et. al. acknowledged the difficulty of phase reconstruction near isolated zeroes in the object spectrum and proposed a solution.⁷ More recently, several authors have presented branch-point tolerant phase reconstructors.^{8,9,10} The present paper⁴ adds to these results by emphasizing a unique decomposition

of the phase flow into an irrotational and a rotational part. We feel that this approach lends considerable clarity to the phase reconstruction problem. Furthermore, we specifically treat phase reconstruction in the Knox-Thompson speckle imaging method, providing a post-processing algorithm that appears to be very effective for ground-based astronomy applications.

We have mentioned above that we can decompose the vector phase flow into a piece with zero divergence, and a piece with zero circulation. That a continuous vector field can be decomposed into rotational and irrotational parts has proved quite useful in hydrodynamics for nearly 150 years.¹¹ Our results are a discrete analog of those well-known results.

2.3 PLANS

We now present the future direction for conducting this development. It can be decomposed into four phases. These phases are enumerated below:

- (1) Complete application of the method to the atmospheric turbulence case
- (2) Develop disturbance model for the space environment
- (3) Obtain calculated results for this environment
- (4) Develop designs and plans for laboratory demonstrations of the technique.

The first phase will entail expanding on results already obtained for atmospheric compensation and to be briefly described below. This work will include assessing precision of the method and developing light level/dynamic range models. Other source objects including distributed ones will be investigated. The modeling of laboratory (horizontal) seeing effects will commence.

The second phase will cover the development of the jitter model for two candidate prototype systems; one a two element telescope system and the other a large observatory with three or four main telescope elements. Jitter sources on spaceborne systems will be investigated such as gyros, stabilization subsystems, cryogenic subsystems, cooling subsystems, etc. Disturbance sensitivities of the optical subsystem will be explored, such as motion of key optical elements (secondary, tertiary, etc.) and the detector. The impact of the statistical distribution functions (Gaussian, Poisson, etc.) will be incorporated. Lab seeing effects will be fully incorporated. Development of typical system transfer models will start. In these models we will determine the attenuation of the disturbances expected with candidate control systems and the resulting residual after control.

In the third phase we will fully exercise the baseline algorithm on typical source objects with known jitter disturbances present. Image reconstruction performance of the algorithm will be thoroughly evaluated. Again we will assess precision of the method and develop light level/dynamic range models. Other source objects including distributed ones will be investigated as before for atmospheric compensation. System transfer performance will be fully evaluated for the two specific candidate systems mentioned in the paragraph above. Comparison of this speckle-imaging algorithm to other such approaches will be started. The relationship of speckle approaches to phase retrieval and phase diversity reconstruction approaches will be addressed.

In the final phase, a laboratory demonstration concept will be developed. A simple, probably two element, telescope system will be designed and analyzed. A surrogate source will be imaged on a CCD detector. Stingers will be identified for the telescope secondary and the detector to introduce jitter. The performance of the image reconstruction process in the presence of known disturbances and Known sensitivities will be analyzed. The comparison of this speckle imaging algorithm to other such approaches will be finished. The relationship of speckle approaches to phase retrieval and phase diversity reconstruction approaches will be further addressed. Avenues to obtain actual hardware and lab space will be pursued.

3. PRELIMINARY RESULTS

In this section, we will demonstrate image reconstructions, using the Knox-Thompson Method augmented by our complete solution for both the regular and hidden parts of object spectrum phase. Figure (1a) plots a diffraction-limited image of a four-star group, in which one of the stars is twice the intensity of the other three. (We show all figures on a gray scale on which the original 32 x 32 intensity data is bilinearly interpolated to a 256 x 256 grid. The specific bilinear interpolation method is in Ref. 12.) Figure (1b) shows a turbulence-degraded, long-time exposure of the identical asterism. Here, we have averaged 640 short exposures, using aberrated point-spread functions. In addition, we have added shot noise to each pixel (32 x 32 array) in each short-exposure frame, while assuming 10,000 photons per frame.

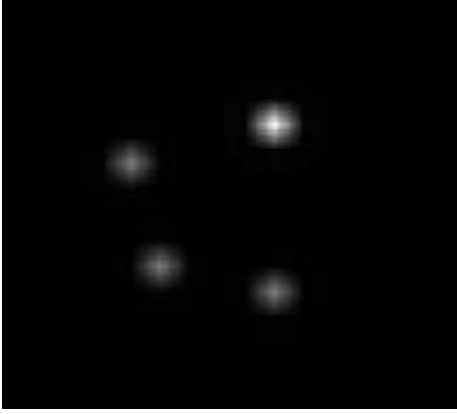


Figure 1a.) Diffraction-limited



Figure 1b.) Long-time average with $D/r_0 = 10$.

We use standard speckle methods, as described in reference 1, to determine the modulus of the object FFT. In this step, we use an independent set of reference star short exposures, in order to deconvolve the speckle transfer function from the modulus of the object FFT. We then use the Knox-Thompson method to generate difference equations for the phase, and to solve for both the regular, W^S , and multi-valued, W^H , components of the object FFT phase.

Prior to taking the inverse FFT, we multiply by the optical transfer function, $H_{DL}(m,n)$, of the diffraction-limited telescope. The final diffraction-limited object reconstruction is then given as

$$I(i, j) = FFT^{-1} \left\{ \left| \tilde{I}(m, n) \right| e^{i \left(W^S(m, n) + W^H(m, n) \right)} H_{DL}(m, n) \right\}.$$

This reconstruction is plotted in Fig. (1c); the reconstruction accuracy is excellent. If we affect the identical reconstruction procedure, but use a minimum least-squares phase estimator, then the hidden phase is not included in the object FFT estimate. The reconstruction results with the hidden phase neglected are shown in Fig. (1d). Obviously, the hidden phase plays a critical role in the reconstruction process.



Figure 1c.) Reconstruction with hidden phase.



Figure 1d.) Reconstruction without hidden phase.

As a second example, Fig. (2a) shows a contour plot of a diffraction-limited image of a binary star in which one star is twice the intensity of the other. Figure (2b) shows the turbulence-degraded, long-time average of 640 short exposures with 10,000 photons per frame. Using the augmented Knox-Thompson procedure, we obtain the results in Fig. (2c). In this simpler object case, there are no zeroes in the original object spectrum, and the hidden phase is essentially zero. Figure (2d) shows the reconstruction when the hidden phase is set exactly to zero. The results are excellent in either case.

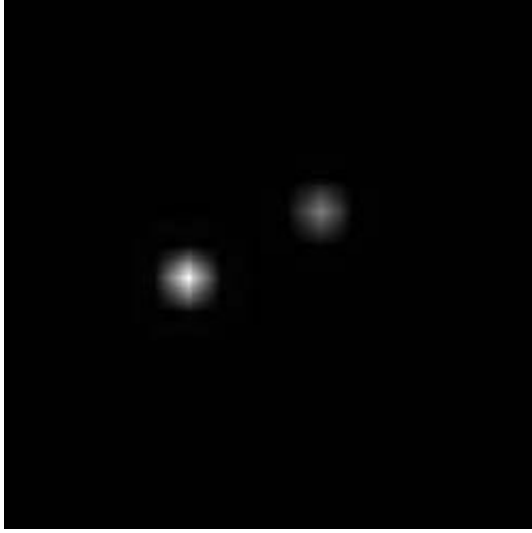


Figure 2a.) Diffraction-limited binary image.

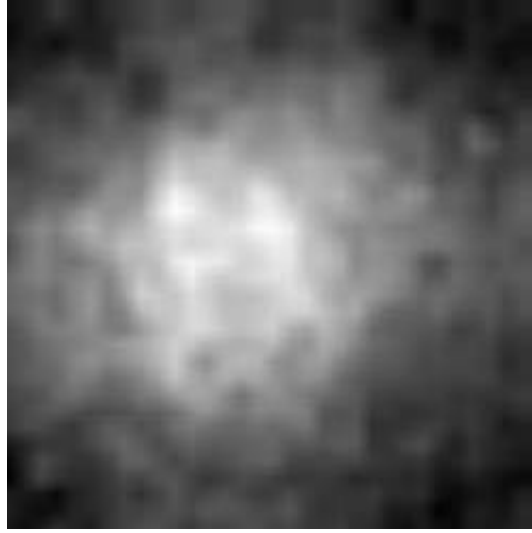


Figure 2b.) Long-time average with $D/r_0 = 10$.

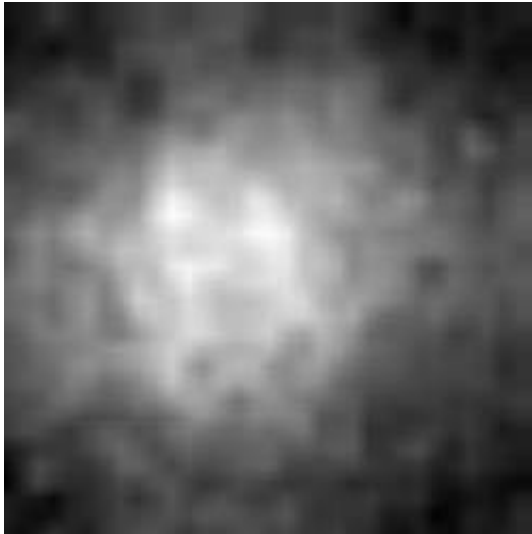


Figure 2c.) Reconstruction with hidden phase.

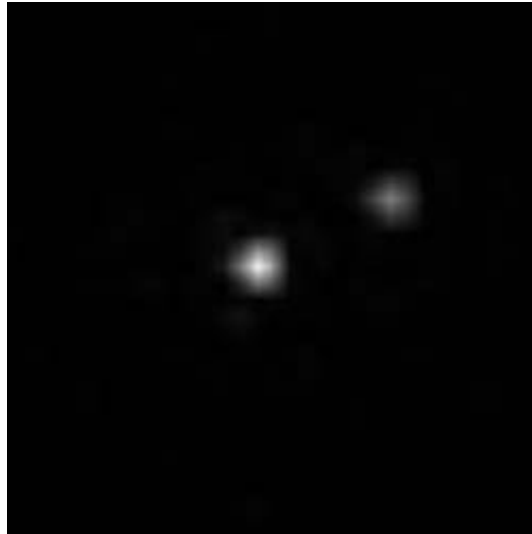


Figure 2d.) Reconstruction without hidden phase.

4. CONCLUSION

The Knox-Thompson, or cross-spectrum, method provides two two-dimensional difference equations for the phase of the object spectrum. A complete solution to these difference equations can be decomposed into a regular single-valued function, W^S , determined by the divergence of the phase gradient, as well as a multi-valued function, W^H , determined by the circulation of the phase gradient. Furthermore, this phase decomposition is unique and complete. An accurate object spectrum reconstruction then requires a modulus estimate, as well as both parts of the phase. For almost any object on the celestial sphere more complicated than an unequal magnitude binary, both components of the object spectrum phase are needed for an accurate reconstruction. Knox-Thompson reconstructions based on a minimum-least-squares phase estimator will usually be of limited value.

The examples in Section 3 demonstrated reconstructions on 640 short-exposure frames in the presence of significant turbulence and shot noise. In addition, we have tested the method with realistic shot and read noise corrupting the short-exposure data. Although our augmented Knox-Thompson method worked well in these examples, as well as in many other test problems, several questions remain: Is the method an optimum method in the presence of noise? Is there a better way to motivate or derive our method for filtering the phase flow circulation values? Can we quantify the reconstruction accuracy as a function of turbulence strength, photons per frame, and number of data frames? These questions, along with other evolving issues, will require further investigation.

The technology developed here could have a substantial impact on the development of new space telescopes; such as the Next Generation Space Telescope(NGST) and its follow-on the Next NGST. Large Interferometric Systems of non-zero field, such as Planet Finder and Submillimeter Probe of the Evolution of Cosmic Structure, could benefit. These systems most likely will contain large, flexible optomechanical structures subject to dynamic disturbance. Furthermore, large systems for high resolution imaging of planets or Earth from space may also benefit. Such systems could include next generation Landsat systems or atmospheric sensors for dynamic imaging of individual, severe storms. Tactical and Strategic Defense systems will need to image very small targets as well and could benefit from the technology developed here.

We believe our technique offers improvement in the context of various system architectures. For large, space systems with flexible structures various control architectures will be applied. Control will most likely be distributed. The control subsystem goal is to improve a system with substantially aberrated imaging to diffraction-limited imaging. In the realm of the temporally varying disturbances our algorithm is expected to be the most effective. Indeed it is the hope that it can eliminate the need for any higher order aberration correction in the temporal domain and leave perhaps just a simple two-axis FSM. Post-processing using this algorithm will work at all but the lowest light levels. Realistic estimates of light-level limits on performance will be investigated. This algorithm could in the future be applied and the software written for a specific flight project.

This investigation may yield significant reduction in complexity, cost, and risk (quantitative and qualitative) of space-borne optical systems by overcoming dynamic disturbances. More robust systems almost certainly will be a result as well.

ACKNOWLEDGEMENT

We would like to acknowledge Michael K. Tilton's contributions in providing information and most particularly in developing the data and figures for this paper.

6. REFERENCES

1. A. Labeyrie, "Attainment of diffraction limited resolution in large telescopes by Fourier analyzing speckle patterns in star images," *Astron. Astrophys.* 6, 85-87 (1970).
2. M. C. Roggemann and B. Walsh, Imaging Through Turbulence, CRC Press, 124-125, 1996.
3. K. T. Knox and B. J. Thompson, "Recovery of images from atmospherically degraded short-exposure photographs," *Astron. J.* 193, L45-L48 (1974).
4. G.C. Dente, "Speckle Imaging and Hidden Phase," *Appl. Opt.* 39, 1480-1485 (2000).
5. D. L. Fried, "Branch point problem in adaptive optics," *J. Opt. Soc. Am.* 15, 2759-2768 (1998).
6. J. C. Fontanella and A. Seve, "Reconstruction of turbulence-degraded images using the Knox-Thompson algorithm," *J. Opt. Soc. Am.* 4, 438-448 (1987).
7. H. Takajo and T. Takahashi, "Least-squares phase estimation from the phase difference," *J. Opt. Soc. Am.* 5, 416-425 (1988).
8. W. W. Arrasmith, "Branch-point tolerant least-squares phase reconstructor," *J. Opt. Soc. Am. A* 16, 1864-1872 (1999).
9. E. Le Bigot and W. J. Wild, "Theory of branch-point detection and its implementation," *J. Opt. Soc. Am. A* 16, 1724-1729 (1999).

10. T. W. Lawrence, D. M. Goodman, E. M. Johansson and J. P. Fitch, "Speckle imaging of satellites at the U. S. Air Force Maui Optical Station," Appl. Opt. 31, 6307-6321 (1992).
11. A. Sommerfeld, "Mechanics of Deformable Bodies: Lectures on Theoretical Physics, Volume II", (Academic Press, New York, 1959), section IV.20.
12. W. H. Press, B. P. Flannery, S. A. Teukolsky and W. T. Vetterling, "Numerical Recipes in Fortran 77, Second Edition", (Cambridge University Press, 1992), page 116.

Speculation on Future Adaptive Optics Technology

Robert Q. Fugate
Air Force Research Laboratory/Starfire Optical Range

ABSTRACT

What advances can we expect in adaptive optics technology for ground based telescopes in the next 25-50 years? This paper presents some speculation on what we might like to see and what might be possible.

Wavefront Control Testbed Results

David Redding, Scott Basinger, Andrew Lowman, Fang Shi, Charles Bowers, Richard Burg, Laura Burns,
Pierre Bely, David Cohen, Pamela Davila , Bruce Dean, Todd Norton, Peter Petrone, Brendon Perkins and
Mark Wilson

JPL, NASA/Goddard Space Flight Center

ABSTRACT

By segmenting and folding the primary mirror, quite large telescopes can be packed into the nose cone of a rocket. Deployed after launch, initial optical performance can be quite poor, due to deployment errors, thermal deformation, fabrication errors and other causes. We describe an automatic control system for capturing, aligning, phasing, and deforming the optics of such a telescope, going from initial cm-level wavefront errors to diffraction-limited observatory operations. This system was developed for the Next Generation Space Telescope and is being tested on the NGST Wavefront Control Testbed. Results of recent work on the Wavefront Control Testbed will be presented.

Benchtop Phase Diverse Imaging Testbed

G. Solyar

University of Maryland Baltimore County, Center of Excellence in Space Data And Information Sciences,
NASA/Goddard Space Flight Center, Code 900.1,
Greenbelt, MD 20771

R. G. Lyon

NASA/Goddard Space Flight Center, Greenbelt, MD 20771

J. E. Dorband

NASA/Goddard Space Flight Center, Code 934, Greenbelt, MD 20771

J. M. Hollis

Goddard Space Flight Center, Code 930, Greenbelt, MD 20771

U. A. Ranawake

University of Maryland Baltimore County, Center of Excellence in Space Data And Information Sciences,
NASA/Goddard Space Flight Center, Code 900.1,
Greenbelt, MD 20771

ABSTRACT

The method of phase diversity is promising for wavefront sensing using extended sources for space applications. It is used when the object under observation is not known a priori. Phase retrieval techniques are employed to determine phase aberrations and misalignments of the optical system for known object. In order to study phase diversity and phase retrieval, to gain more familiarity with actual data, and to quantify its' accuracy, precision, dynamic range and robustness we have developed a unit magnification benchtop imaging system in a controlled laboratory environment. The system is based on a source module, 2 off-axis parabolas and a focal plane. The system is deliberately designed to be simple to allow for easy tracking of error sources to optimize the time required for algorithm development as opposed to system development. In this work we describe the system, calibration and imaging process; other works, in these proceedings, describe the algorithms and methods in more detail as well as show results.

I. INTRODUCTION

Different scientific and engineering groups have developed testbeds to measure misalignments of the optical systems. The Developmental Cryogenic Active Telescope Testbed ⁽¹⁾ is under development at Goddard Space Flight Center in collaboration with the Jet Propulsion Lab. This testbed combines an actively controlled telescope with hardware and software elements of a closed loop wavefront sensing and control system to achieve diffraction limited imaging. Groups from Lockheed Martin Missiles and Space, ERIM International and CARA at W.M. Keck Observatory ⁽²⁾ conducted an experiment and developed a technique to measure piston misalignment of segment on the primary mirror. In both cases phase retrieval ^(3,4,5,6) and phase diversity ^(2,7) were used as baseline methods. The main problems were due to dispersion, scintillation and exposure times longer than the atmospheric correlation times, leading to a mismatch between imaging model and the real-world conditions.

The primary emphasis of our work is on quantifying accuracy, precision, dynamic range and robustness of phase-retrieval, and phase diversity techniques with actual data. The main sources of noise are detector noise, quantization, vibration of mechanical elements, as well as stray and ambient light, etc. Our goal is to reduce the complexity of the system (Figs.1 and 2) and to minimize hardware.

A set of scenes (Fig.3) collected by the Hubble Space Telescope and Landsat-7 (Fig.4), is imaged onto Kodak TechPan high-resolution film and used as the set of input extended objects. A pinhole and computer generated variable diameter circular masks serve as point sources. We use a 16-bit CCD camera size with 9-micron pixel size as a detector. Film is illuminated by incandescent source.

In our design we reduced the effects of stray light and vibration. A special technique separated the film processing effects from the aberrations of the optical system. This was performed by including, in the set of input objects, a computer generated set of masks (Fig.5), which were also imaged onto film. The ghosting and internal reflections of the CCD camera were also problematic and are addressed.

We designed and implemented special image reduction techniques and collected over 3,000 images of different objects with varying exposure times and focal positions of the detector. Necessary for image reduction procedures, bias, dark, blank and flat fields were collected with the aid of scripts, written by us for the CCD camera.

II. INSTRUMENTATION

Our system is similar to an optical layout, introduced in 1864 by A. Toepler, which subsequently became known as the schliren method. Our optical system (Fig.1) consists of: a dual light source module, two mirrors, a detector module, a pupil focusing lens, all mounted on optical table.

The dual optical source (Fig.2) module was designed to serve two purposes: system alignment with a He-Ne laser and imaging with an incandescent source. A flipper mirror redirected the light beam between two light sources and the optical system. An incandescent source module contains a 20W QTH source from Oriel, which was modified in order to achieve spatially stable and uniform illumination, and, to reduce stray light. It also contains a He-Ne line interference filter. A set of diffusers, a set of neutral density filters, a pinhole, and a set of films were positioned in a double filter wheel, which made switching to different phases of the experiment easy and reliable. Diffusers and neutral density filters were included in the source module to achieve a uniform illumination of the object and optimal dynamic range of light intensity with exposure time.

Two mirrors M1, M2 are 6" parabolas with $F/\# = 6$, each was mounted on separate 3-axis stages. The focal plane detector array is a KAF-0400-0 CCD in a MCD 600S Spectrasource camera with 768x512 format and 9-micron pixels. The detector is mounted on a micrometer controlled 3-axis stage with 25mm traveling range along the axes of light beam propagation. The readout noise (RO) is 13 electrons RMS, optical fill factor 100% and 18% of quantum efficiency at 632 nm. The full-well capacity (E_{cap}) is 85,000 electrons and the signal is digitized to 16 bits. The camera head is thermo-electrically cooled. The test data was taken at cooler set temperature of less than 265 K. Camera was saturated (E_{sat}) at 65,535 digital counts (ADU). Bias and dark current tests showed 1,081 and 1,104 counts correspondingly. The cooling fan, which served as a secondary cooling stage for the hot side of the Peltier thermo-electric elements, was removed and replaced with cooling system where the air from a remote fan was delivered to the CCD by the air duct. This replacement eliminated the vibration introduced by rigid physical connection between the fan and camera and significantly improved the image quality of the system.

The dynamic range of the detector, in bits, is given by:

$$DR(bits) = \log_2(E_{sat} / n_e) = 12.7 \quad (1)$$

The conversion factor q [e/ADU]:

$$q = E_{cap} / E_{sat} = 1.3 \quad (2)$$

Considering the readout noise independent of position on CCD and representable as a simple Gaussian error distribution the signal-to-noise ratio is:

$$SNR = qX / (qX + RO^2)^{1/2} \quad (3)$$

where X is number of digital counts per pixel. For $X = E_{sat} = 65,535$ counts the calculated SNR is 291. The Poisson limit of SNR can be obtained by using:

$$SNR_p = (qX)^{1/2} \quad (4)$$

and is 291.5. The same calculation for counts for bias and dark levels resulted $qX=2000$ SNR=43 and SNR_p=44.7. As it can be seen from these calculations that the SNR for ranges from dark current up to saturation is nearly Poisson limited.

The images were captured with the aid of CCD detector, interface card and modified scripts, provided by Spectrasource. We ran scripts on a PC with 233 MHz processor and stored images on 12 GByte hard drive.

Installing an iris diaphragm on the M1 mirror defined the location of the entrance pupil. A F=50mm lens, in front of the detector, was used to image the entrance pupil onto the detector to map out the pupil geometry. The serrated shape of the iris diaphragm is clearly seen (Fig.6) on the imaged pupil. A 12-micrometer diameter pinhole was illuminated via the thermal source with a narrowband interference filter centered on 0.6328 microns. The pinhole was imaged, via the optical system at F/#=38, to obtain a point spread function (PSF). The size of the pinhole (D_p) was chosen to satisfy:

$$D_p \leq 1.22 * \lambda * F/\# = 27 \text{ microns} \quad (5)$$

Nyquist sampling for detector with 9-micron pixel width (h) required:

$$F/\# > 2 * h / \lambda = 30 \quad (6)$$

We adjusted the F/# by apodizing the size of the entrance pupil with an iris diaphragm to a diameter of 21mm.

One of the requirements was to maintain identical registration, in 3D, across the set of objects, in the filter wheel during the experiment, i.e., as we rotated the filter wheel, between different objects, we found that the objects were not in the same plane and were rotated. We found a simple solution, without adding high precision mechanical components, by placing fiducials and circular masks, which serve as point sources, on the scenes of the same film transparency. The set of circular masks (Fig.4) with the diameters from 10 to 100 microns was generated on a computer and overlaid on the images containing the scenes. The result was processed onto a Kodak film to obtain a film transparency.

The number of waves of defocus ($N \lambda$) for a traveling range of $\Delta z = 12$ mm of the detector, along the beam propagation axes, can be calculated by:

$$N \lambda = \Delta z / (8 * \lambda * (F/\#)^2) = 1.7 \quad (7)$$

Stray light and ambient light baffling included a series of screens, edges and tubes (not shown on a Fig.1).

III. IMAGING SEQUENCE AND DATA REDUCTION

We collected a total of 3000 frames, necessary for the data reduction process. These frames could be separated into two main groups: image frames and field frames. The image frame group contains images of the pinhole and object transparencies with different scenes and masks. Flat, blank, dark and bias fields comprise the field frame group. For each member of both groups we collected 30 frames to improve the SNR by a factor $\sqrt{30} = 5.4$. Also, this allows us to parameterize in terms of SNR. With the exception of bias and dark fields each member was imaged at 3 different focal positions with 6mm translations of the focal plane. The exposure time, for each sequence, was chosen to maximize the useable dynamic range of the detector.

The nature of the field frames is described below. Bias field is a function of detector capacitive and leakage effects only. It was collected with the CCD camera shutter closed and with no exposure time. Dark field is a function of capacitive and leakage effects and thermal photoelectron noise of the detector. It was collected with the CCD camera shutter closed with 1- minute exposure time. Blank field has dependence on ambient light in addition to the all of the effects associated with the dark field. We collected it by blocking the object light source and exposing for 1/3 of a minute. Flat field is a function of the light source, the ambient light, detector effects and field dependence of the optics and detector. This sequence of images was collected with open shutter and transparent object, placed into the filter wheel. The exposure time remained the same as for blank field. All of the aforementioned field frames represent different sources of error. We attempted to compensate for their effects by postprocessing of the image frames using combinations of the field frames. We summarize the relations between different field frames for one pixel in the following formulas ⁽⁸⁾:

$$\langle FLAT \rangle = \langle SOURCE \rangle * GAIN + \langle Ambient \rangle * GAIN + \langle DARK \rangle \quad (8)$$

$$\langle DARK \rangle = \langle BIAS \rangle + \langle Photo-electron-noise \rangle \quad (9)$$

$$\langle BLANK \rangle = \langle DARK \rangle + \langle Ambient \rangle * GAIN \quad (10)$$

$$\langle DATA \rangle = \langle OBJECT \rangle * \langle GAIN \rangle * (\langle SOURCE \rangle + \langle Ambient \rangle) + \langle DARK \rangle \quad (11)$$

Where (GAIN) gain is factor due to different quantum efficiencies for different pixels; a (SOURCE) – intensity of the light source; (Ambient)- ambient and stray light intensity; (OBJECT)- transmittance of film transparency; (DATA)- registered by the detector intensity.

As a next step we imaged the entrance pupil by inserting a lens, installed on a flipping stage, into beam in front of the detector. This was necessary because the iris diaphragm, that we placed in front of the mirror M1 to define the size of the entrance pupil, had a serrated rather than circular shape and caused diffraction spikes in the images.

After these steps we imaged the set of objects. The object set consisted of a Hubble Space Telescope Double Jet and a Landsat-7 Washington DC scene. The raw scenes are actually digitized computer files subsequently photo reduced onto film. Precision and controllability of different system elements dictated the following sequence for the experiment. We translated the detector to introduce the phase diversity. The detector was moved with a micrometer controlled translational stage in 6mm increments (limited by the maximum traveling range of the translation stage) through three focal positions with one selected object positioned in a filter wheel. Another object was selected and the procedure was repeated. The same three focal positions were used for the set of objects, to preserve the same phase diversity. At each position the exposure time was 20 seconds.

The image reduction technique ^(8,9) was based on scaling different frame types to their exposure times and from the formulas (8, 9,10, 11):

$$\langle OBJECT \rangle = \frac{\langle DATA \rangle * \mathbf{a} - \langle DARK \rangle}{\langle FLAT \rangle * \mathbf{b} - \langle DARK \rangle} \quad (12)$$

Where $\mathbf{a} = \frac{t_{dark}}{t_{data}}$ and $\mathbf{b} = \frac{t_{dark}}{t_{flat}}$ are scaling coefficients.

IV. FILM PROCESSING AND CALIBRATION

We used Gammatech Company in Albuquerque to produce black- and- white film transparencies from the computer generated set of patterns and computer images taken by the Hubble Space Telescope and Landsat 7.

The process used is described below. Agfa Matrix QCR-Z was used as a film recorder. Digital calibration was done with the aid of look up tables modified to produce maximum density range for film and processing.

In an optical setup the neutral density filter was removed in order minimize possible distortion, which result in single exposure pass through the clear aperture. Kodak Technical Pan Professional 2415 film was selected for fine grain. The final processing was done at 68F with Kodak D-76 developer in a small tank for 11 minutes. Agitation was performed at 30-second intervals. Fixing process occupied 10 minutes that followed by 20 minutes of washing and was air-dried afterwards.

Film and process chemistry were preferred over Ektachrome slide film due to finer grain, ability to adjust camera look-up tables for better control of image detail, better control of process variables and higher stability of the film base during drying process.

Such film processing obviously introduced new spatial and intensity aberrations into the image compared to the initial computer digital images. We obtained new "ground truth" digital images by scanning films with Minolta Dimage Scan Multi density meter at 2750 dpi under the assumption that distortions and aberrations, introduced by scanning process are negligible compared to ones of optical system.

These aberrations could be characterized by determining responsivity (Fig.7) and modulation transfer function (MTF) of film processing (Fig.8). To solve this problem, we computer generated a set of patterns (Fig.4) with linear changing intensity $I(i, j) = i * I_o(i, j)$ and chirped pattern $I(i, j) = I_o(i, j) * \cos(k * i^2)$, where $I(i, j)$ and $I_o(i, j)$ are two dimensional intensities, $k = \text{const}$; made film and scanned it with density meter. Transparencies, containing these patterns were processed together with the rest of transparencies containing different scenes.

V. CONCLUSIONS AND FUTURE PLANS

We have built a testbed, which allowed us to estimate the sources of error and their effects. Most of the difficulties were associated with varying ambient light intensity, nonparallelism of detector window, thermal noise of a detector and vibration. Nonparallelism of detector window resulted in ghosting in the image, which was difficult to isolate. When the single frame exposure time of detector was of the order of one minute or more, the thermal photoelectron noise in detector along with leakage effects degraded the dynamic range and image quality. The experiment consumed many hours, during which the ambient light and temperature were varying significantly. This made the standard data reduction technique very difficult to apply, and we are currently looking at other more robust approaches. The length of experiment and manual positioning of the mechanical component made it very hard to maintain the precision in positioning of the detector and sources and was very tedious process to collect all the data.

Our future plans include design and installation of motorized system containing telescopes in place of the parabolic mirrors. This will significantly reduce the experiment time and also achieve better baffling to reduce ambient and stray light, and thermal drift of CCD camera. Making the experiment computer controlled will also lead to improved accuracy due to elimination of human factor and better positioning of a detector. The repeatability is also expected to significantly increase.

REFERENCES

1. Lebeof, Davila, C., Redding, D.S., Coulter, D. R., Pacini, L., *Deployed Cryogenic Active Telescope Testbed for the Next Generation Space Telescope*, Proceedings of SPIE, Vol. 3356, March 1998
2. Lofdahl, M.G., Kendrick, R.L., Harwit, A., Mitchell, K.E., Duncan A.L., Seldin, J.H., Paxman, R.G., Acton, D.S., *A Phase Diversity Experiment to Measure Piston Misalignment on the Segmented Primary Mirror of the Keck II Telescope*, Proceedings of SPIE 3356, March 1998.
3. Gonsalves R.A. and Chidlaw, *Wavefront Sensing by Phase Retrieval. Applications of Digital Image Processing III*, A.G. Tescher, ed., proc. SPIE 207, pp.32-39, San Diego, CA, 1997.
4. Lyon R.G., Dorband J.E. Hollis J.M., *Hubble Space Telescope Phase Retrieval: A Parameter Estimation*, Proceedings of SPIE, Vol. 1567, July 1991
5. Grey L.G., Lyon R.G., *Correction of Misalignment Aberrations of the Hubble Space Telescope via Phase retrieval*, Proceedings of SPIE, Vol. 1168, August 1989.
6. Redding D., Dupont P., and J. Yu, *Hubble Space Telescope Prescription Retrieval*, *Applied Optics*, Vol.32, No. 10, April 1993.
7. Seldin J.H., Schultz, and Fienup, Joint estimation of object and aberrations by using phase diversity, *J. Opt. Soc. Am. A* 9, pp.1072-1085, 1992
8. Gullixson G.A. *Two-dimensional imagery*. Astronomical CCD Observing and Reduction Techniques ASP Conference Series, vol. 23, pp.130-158, 1992, Steve B. Howell, ed.
9. Abbott, T.M.C., and Opal, C.B. *Instrumentation for Ground-Based Optical Astronomy: Present and Future*, New York: Springer Verlag, p.380, 1988, L.B. Robinson, ed.

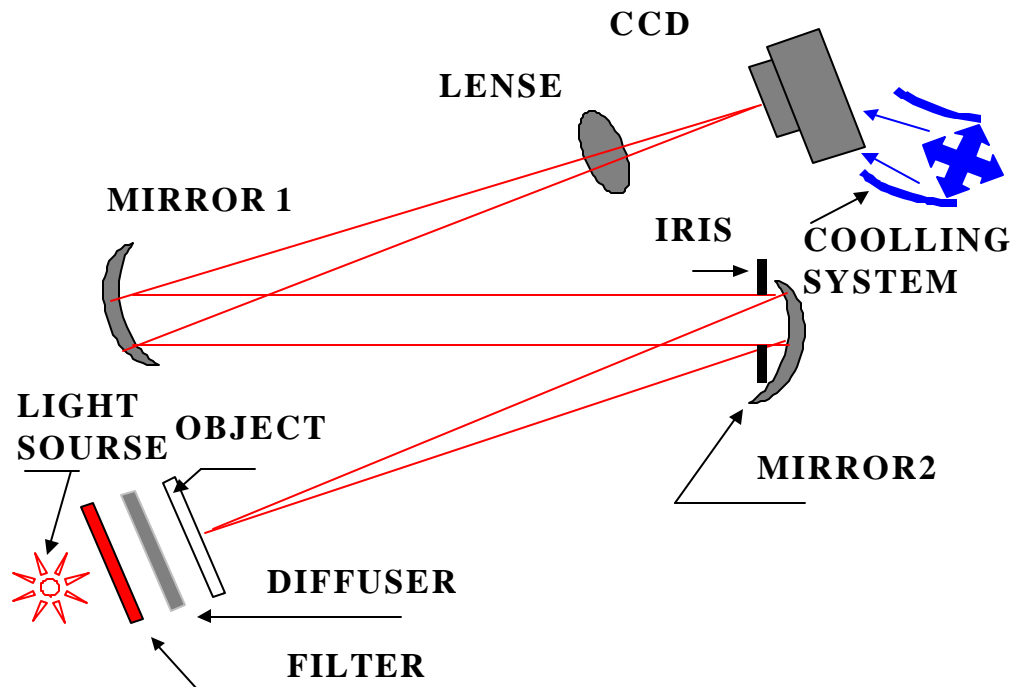


Fig.1 Optical System.

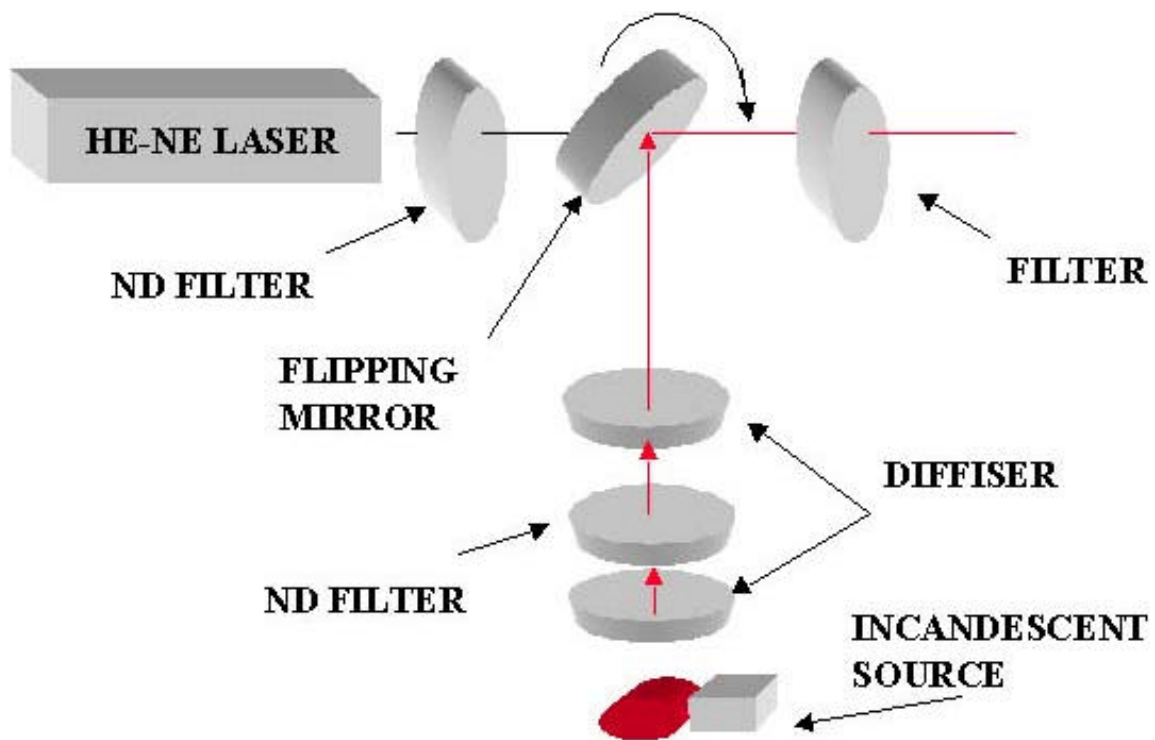


Fig.2 Dual light source module.



Fig.3 Double Jet imaged by Hubble Space Telescope.

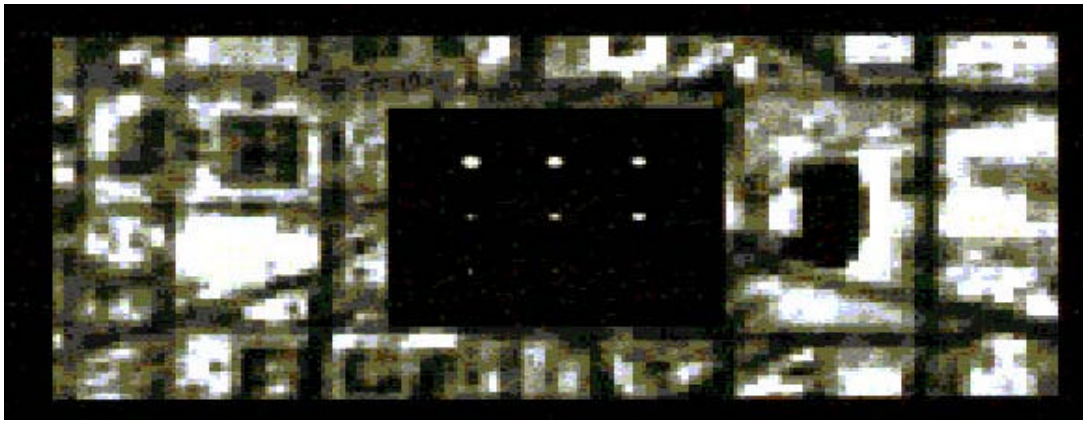


Fig.4. Washington DC fragment imaged by Landsat 7 with circular masks.

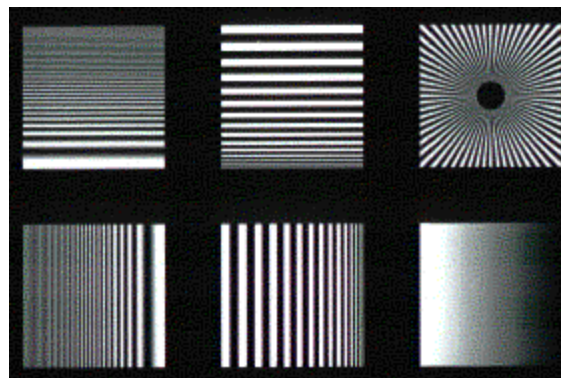


Fig. 5 Computer generated masks. From right low corner in clockwise direction:
1-linear intensity, 2, 5 and 6 –variable spatial frequency, 3 and 4 chirped patterns.

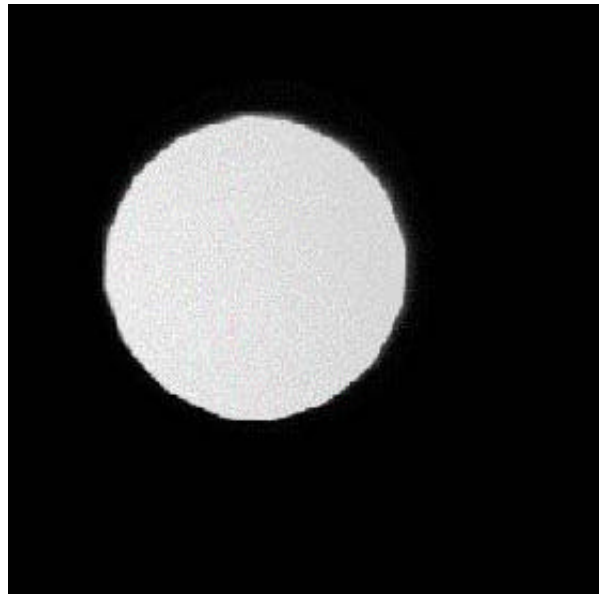


Fig.6. Imaged entrance pupil. *The serrated shape of iris diaphragm is clearly seen.*

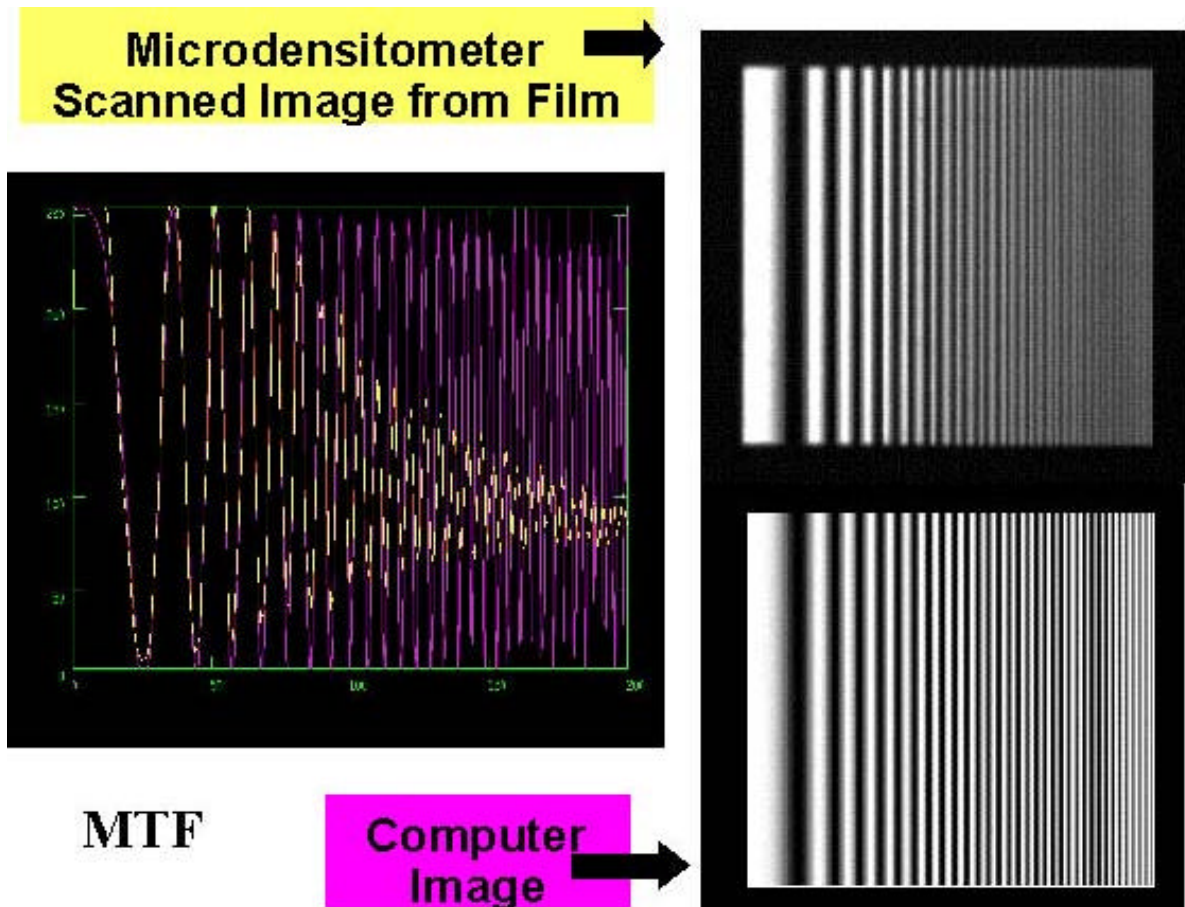


Fig.7 Film contrast (MTF). *Purple curve- computer generated, yellow- microdensitometer scanned.*

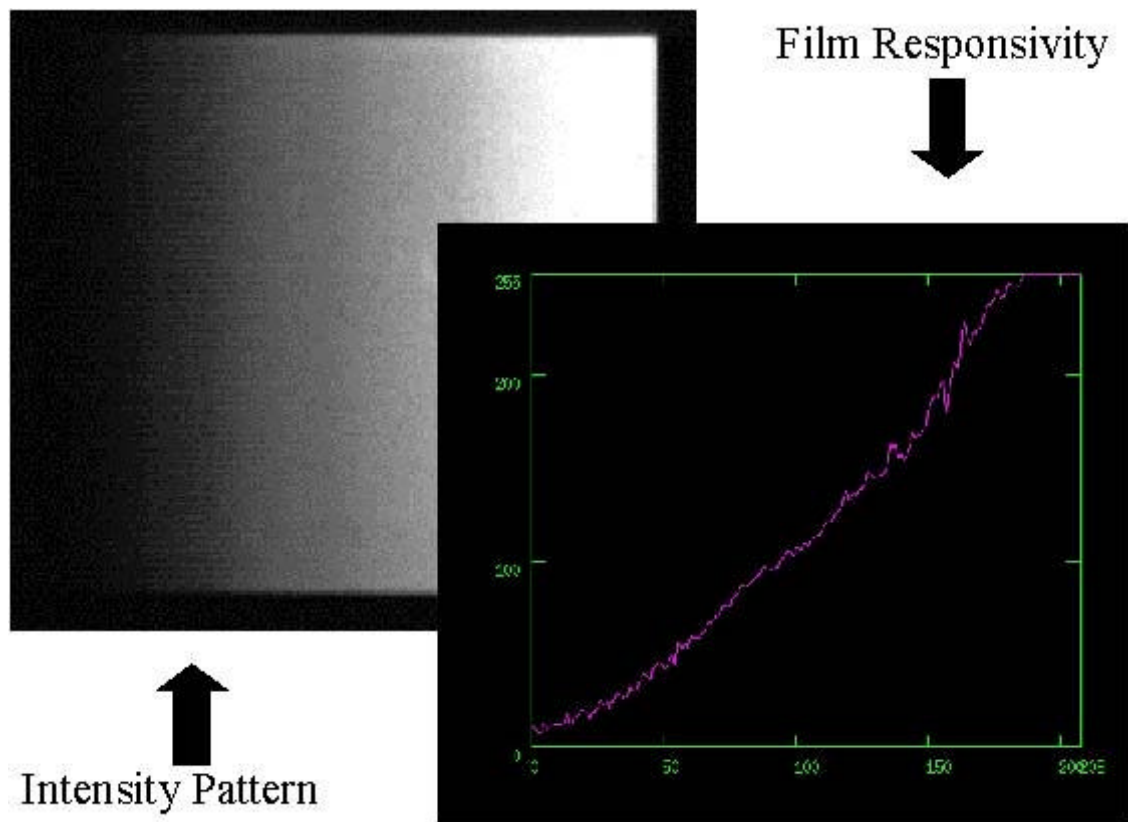


Fig. 8 Film responsivity.

Preliminary Phase Diverse Imaging Testbed Algorithms and Results

Richard Lyon
NASA - Goddard Space Flight Center
Greenbelt, MD 20771
lyon@jansky.gsfc.nasa.gov

Greg Solyar
University of Maryland Baltimore County, Center of Excellence in Space Data And Information Sciences,
NASA/Goddard Space Flight Center, Code 900.1,
Greenbelt, MD 20771

John Dorband,
NASA - Goddard Space Flight Center
Greenbelt, MD 20771

Udaya Ranawake
University of Maryland Baltimore County, Center of Excellence in Space Data And Information Sciences,
NASA/Goddard Space Flight Center, Code 900.1,
Greenbelt, MD 20771

ABSTRACT

We have developed a phase diversity testbed at NASA/Goddard Space Flight Center and conducted a series of experiments consisting of imaging a set of unresolved point sources and extended scenes images with differing diversities. We first discuss, and show results, using cross-validation of multiple phase retrieval methods to determine the diversities and estimate their accuracies. Following this we discuss the use of a modified iterative transform based phase diversity algorithm and show results of the algorithm with observed defocused and astigmatic extended scene images from the phase diversity testbed.

1. INTRODUCTION

In order to better understand and to further explore phase diverse imaging techniques as a potential technology for wavefront sensing and/or image deconvolution on future flight missions, NASA Goddard Space Flight Center has developed a low cost benchtop phase diverse imaging system. The purpose being to demonstrate "proof of principle", gain experience with "real" data, to complement simulation studies, and to validate models and algorithms.

The benchtop system, (as discussed in detail elsewhere in these proceedings, see G. Solyar et. al.) will be briefly reviewed here. It consists of a thermal source; a set of extended scenes on 35 mm film, 2 off-axis f/6 parabolas and a 16 bit thermoelectrically cooled CCD array with 9 micron pixels. A ~2 cm adjustable iris was placed at the primary mirror to define the entrance pupil. The system was nominally operated at f/38, giving approximately 1.3 times Nyquist sampling with respect to the spatial cutoff frequency of the modulation transfer function. The phase diversity (focus) was introduced by translation of the focal plane. The current system has a fixed amount of astigmatism. Figure 1 shows an optical schematic of the benchtop system. The system was deliberately designed to be as simple as possible, using commercial off-the-shelf hardware whenever possible. This was done to minimize the time and cost spent on hardware and minimal hardware implies lower complexity, thus, allowing us to separate the sources of error.

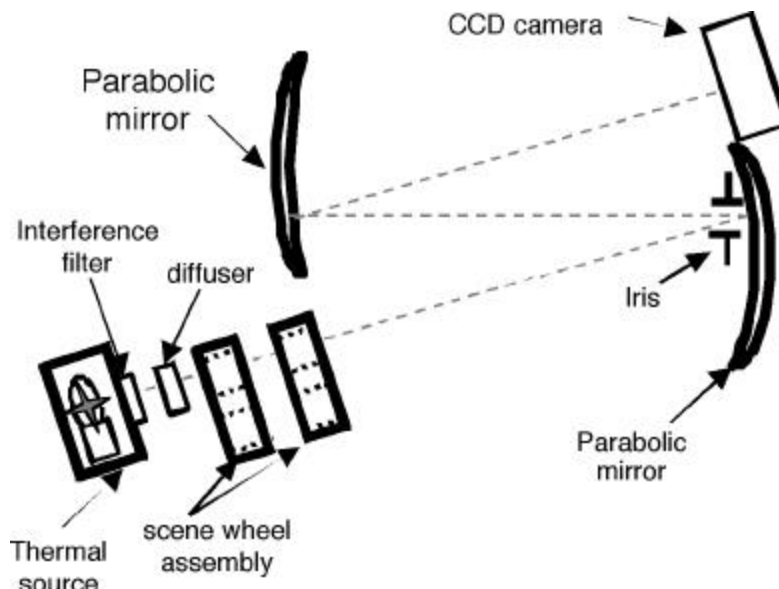


Figure 1
Optical Schematic

The CCD camera is mounted on a linear translation stage to introduce the focal diversity. The scene filter wheel contains a set of scenes, pinholes and calibration patterns on 35 mm film. The calibration patterns are radial and chirped modulation transfer (MTF) patterns to determine the transfer function of the film recording process. Also, a linear intensity sweep was used to determine the film linearity. The scene filter wheel is at the front focus of the first parabola. The combination of the 2 parabolas images the scene onto the CCD camera, with unit magnification. The extended scenes consist of a Hubble Space Telescope image and a Landsat-7 image. These were obtained in 8 bit grayscale computer files and transferred to film.

Figure 2 shows a simplified schematic of the data collection and data processing. Operationally data collection, preceded by bias, dark and flat field frames was collected at each of 3 focal positions. At each focal position: the scene filter wheel was rotated to a pinhole position and a set of 30 PSFs were collected, each with the same exposure time, set to maximize the detector dynamic range. Following this, the pinhole was rotated out and a scene rotated in; again 30 frames of the scene were collected. The focal plane was translated and the process repeated until all the data was collected.

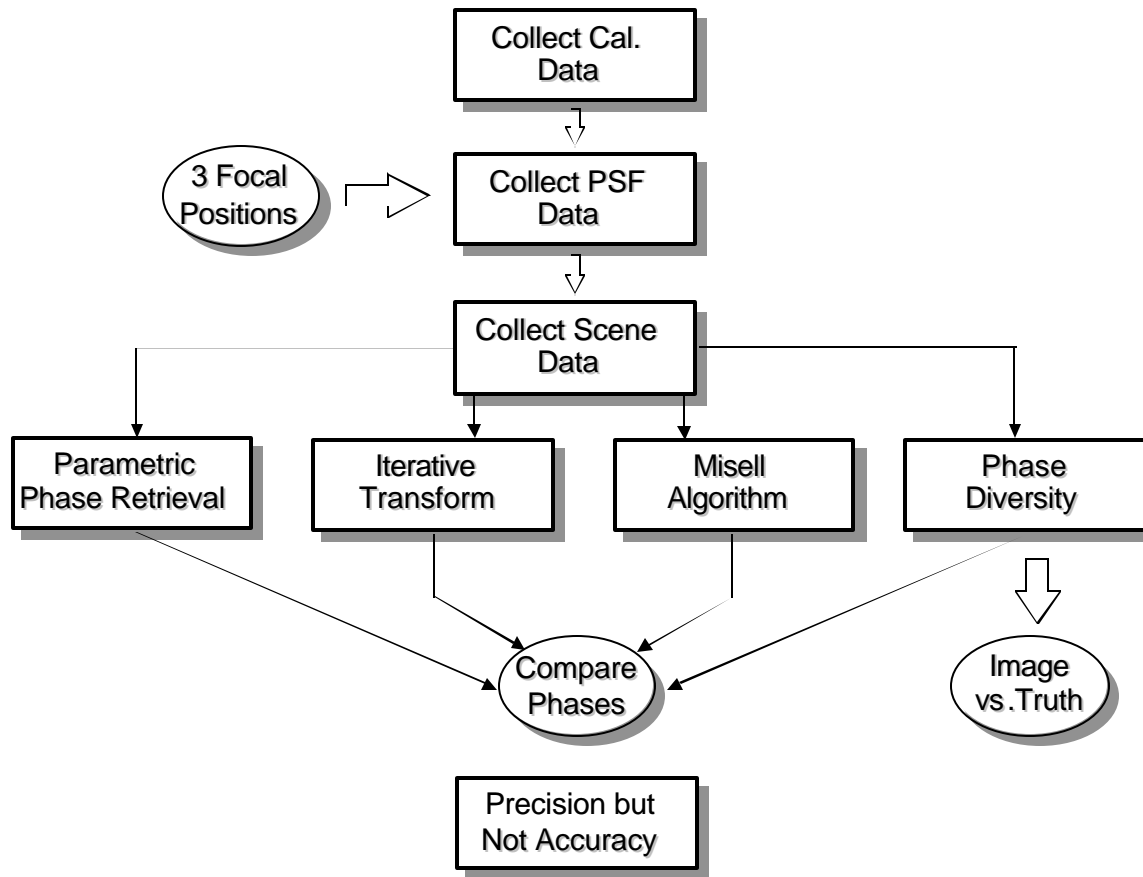


Figure 2
Cross Validation of Phase Retrieval and Phase Diversity Results

The individual sets of 30 frames, scenes and pinholes, were averaged and calibrated to obtain high signal to noise images. The averaged pinhole images were passed through a parametric phase retrieval algorithm and an iterative transform algorithm. To determine the diversity phases each of the two algorithms were run separately for each of 3 focal positions and the wavefront aberrations tabulated. The 3 focal position PSFs were also coupled together with the diversity information and input to a Misell algorithm to estimate the wavefront. Following this, the 3 extended scene images were passed through the phase diversity algorithm and both the object and the phase estimated. The phase retrieval and phase diversity methods as well as their results are reviewed and summarized below.

2. PHASE RETRIEVAL AND CROSS-VALIDATION

Phase retrieval is a method of determining the phase in an optical systems exit pupil from an image, or set of images, of an unresolved object. The phase is proportional to the wavefront error (aberrations) of the system. The wavefront error can come from design residuals, misalignments and deformations, polish marks and/or from an aberrating medium such as a turbulent atmosphere. Phase retrieval has conventionally been divided into two classes of algorithms, parametric and non-parametric. Herein we use both and cross-validate the results. The parametric algorithm is a Zernike fitting approach. It fits the phase in terms of a relatively low number of parameters. The non-parametric is an iterative transform algorithm, which treats every point in the pupil plane as an independent parameter. Thus a Zernike basis is not assumed a-priori.

2.1 PARAMETRIC PHASE RETRIEVAL

We used a parametric phase retrieval approach to estimate the phase at each of the 3 focal positions. In parametric phase retrieval the exit pupil phase is estimated in terms of a set of Zernike polynomials [1] and a set of background parameters. The method defines a maximum likelihood error metric based on: the

known noise statistics, the physical optics model and the detector model, and subsequently minimizes it with respect to the unknown parameters via a Levenberg-Marquardt (LM) optimization method [2]. The LM method is an iterative damped least squares approach, at each iteration the background (linear) parameters are solved for by a non-iterative Gauss-Jordan elimination. For the LM method, both the gradient and the Hessian are needed at each step of the algorithm. A minimum is reached when the gradient is zero and the sign of the second derivative (Hessian) is positive. The solution is independent of the Hessian value, which only affects the path through the parameter space. The LM method approximates the Hessian matrix by the outer product of the gradient of the model function. See ref [3] for the detailed mathematics of the algorithm used herein. The determination of the model function derivatives is not done using finite difference techniques but instead relies on calculation of the gradient via fast Fourier transform (FFT) techniques for each of the Zernike polynomials for each wavelength across the passband and averaging across the spectral weighting function.

Returned from the parametric method is a set of 4 background parameters and a set of Zernike coefficients for each input observed PSF. The background parameters represent the flux, a constant additive background and gradients in the background.

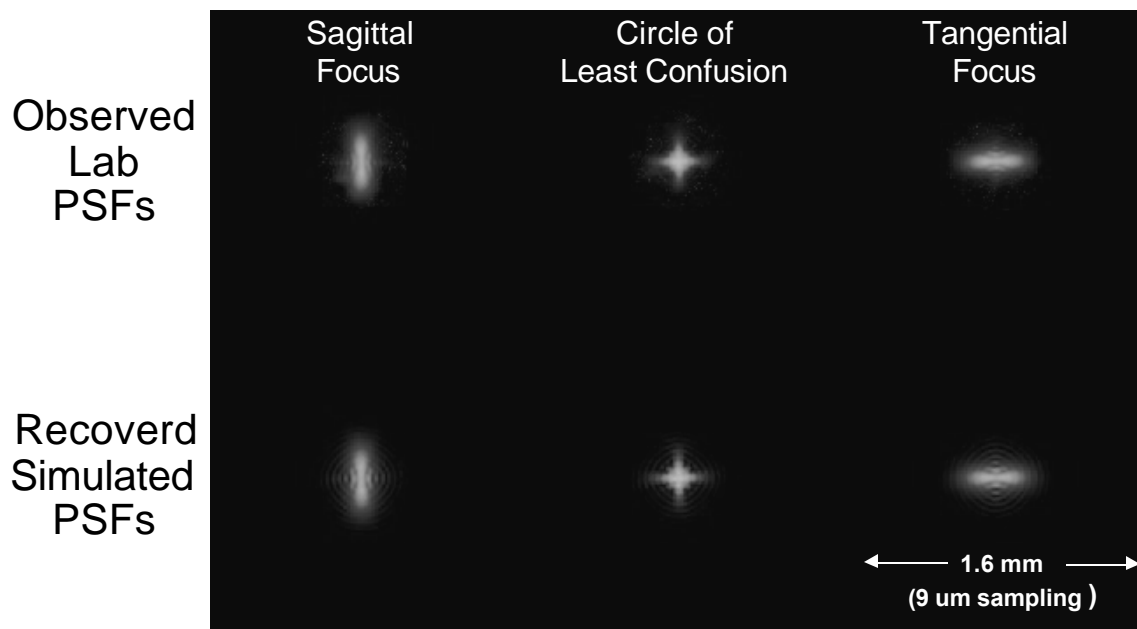


Figure 2
Observed and Simulated Optical Point Spread Functions

The top row of Figure 2 shows the set of observed PSFs at each of the 3 focal positions. Each image is the average of 30 frames. The sampling is 9 microns, $\lambda=0.633$ microns and the $F/\# = 38$. Thus, we are approximately 1.34 times Nyquist sampled. Astigmatism is the dominant aberration in the system; we show the PSFs at the sagittal, circle of least confusion and tangential foci. The bottom row of Figure 2 shows the simulated PSFs at each of these same positions. Figure 3 shows the parametrically recovered Zernike wavefronts at the sagittal, circle of least confusion and tangential foci, labeled 0,3 and 6 respectively. Table-1 summarizes the Zernike coefficients, at each of the 3 focal positions, in units of microns of zero-to-peak of wavefront error. The average X-Y astigmatism term is 0.241 microns of wavefront error. These results along with the iterative transform results were used to determine the diversities in the system.

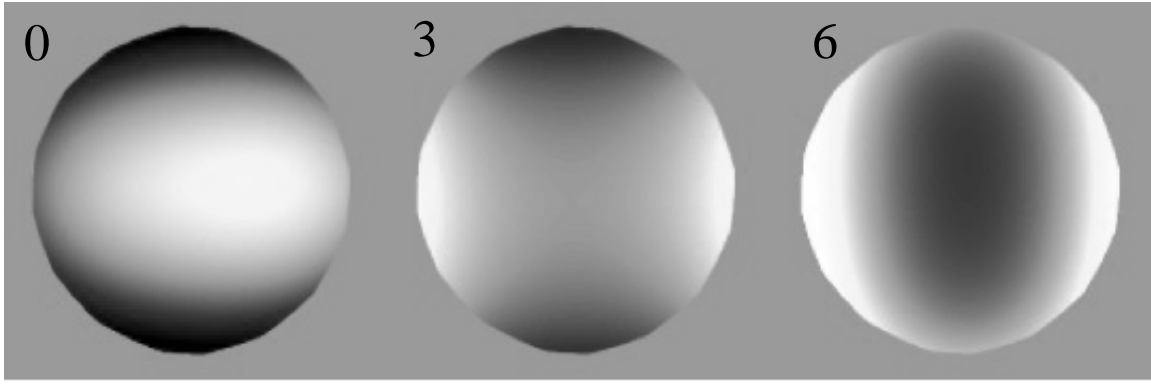


Figure 3
Parametric Recovered Wavefronts at 3 Focal Positions

Table 1 - Parametric Phase Retrieval Results

Term	0	3	6	Functional Form	Label
Z04	0.238	0.252	0.233	x^2x-y^2y	X-Y Astigmatism
Z05	-0.260	-0.004	0.241	2^*r^2-1	Focus
Z06	-0.009	-0.012	-0.007	2^*x^*y	45-degree Astigmatism
Z07	-0.005	-0.003	-0.004	$x^*(x^2-3^*y^2)$	Trefoil
Z08	-0.003	-0.003	-0.004	$x^*(3^*r^2-2)$	X-Coma
Z09	0.003	0.002	0.000	$y^*(3^*r^2-2)$	Y-Coma
Z10	-0.007	-0.004	-0.003	$y^*(3^*x^2-y^2)$	Trefoil
Z11	-0.008	-0.016	-0.015	$x^4+y^4-6^*x^2^*y^2$	Sphero-Astigmatism
Z12	-0.015	0.009	-0.013	$(2^*x^2-r^2)^*(4^*r^2-3)$	Sphero-Astigmatism
Z13	0.019	0.004	-0.016	$6^*r^4-6R^2+1$	Spherical Aberration
RMS-WFE	0.199	0.120	0.188		

2.2 ITERATIVE TRANSFORM PHASE RETRIEVAL ALGORITHM

The iterative transform algorithm method employed here (ITA) [4] is a non-parametric method of phase retrieval, which treats each point in the phase front as an independent parameter. Figure 4 is a pictorial representation of the ITA. The ITA defines a forward and a back propagator from the pupil to focal plane for the complex optical field and assumes an initial starting phase. The forward and back propagators are the Fourier transform kernel and its inverse implemented via FFT techniques. The complex pupil function is Fourier transformed to yield an estimate of the complex focal plane optical field. The focal plane amplitude is replaced with the convex sum of the observed amplitude, $(\sqrt{PSF(f)})$, and the amplitude for the Fourier transform, $(\tilde{P}_n(f))$, and the phase, $(\phi(f))$, is retained. The result is inverse transformed to yield an estimate of the complex pupil plane optical field. The pupil amplitude is replaced with the convex sum of known aperture mask, A_0 , and the amplitude of the inverse Fourier transform, $(P_n(x))$, and again the phase is retained. This process is cyclically iterated until the phase stabilizes.

Figure 5 shows the iterative transform wavefront results using the same set of PSFs from the top of Figure 2. A comparison of Figure 5 with Figure 3 shows qualitative agreement between the two sets of wavefronts recovered with the parametric and the non-parametric algorithms respectively. There is some noticeable higher frequency structure in the non-parametric results. Table 2 shows the non-parametric wavefronts expanded in terms of the same Zernike polynomials used for the parametric phase retrieval. The results agree to 2 significant figures.

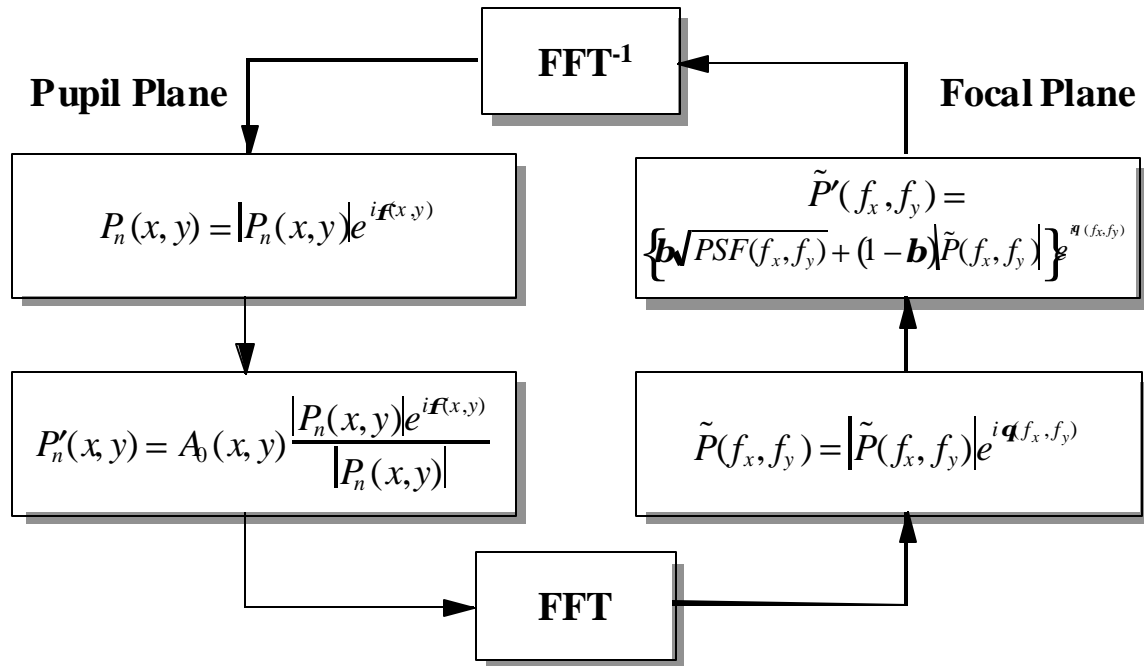


Figure 4
Iterative Transform Algorithm

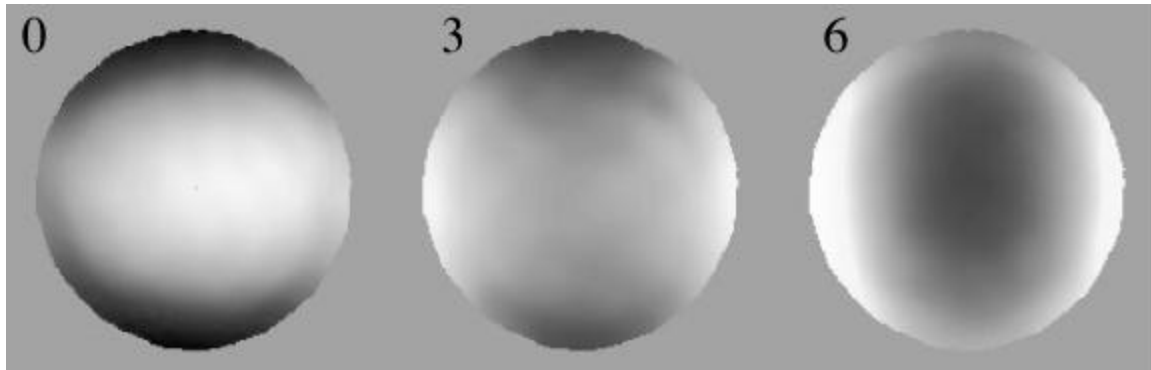


Figure 5
Iterative Transform Phase Retrieved Wavefronts

Table 2 - Iterative Transform Wavefronts Expanded in Zernike Polynomials

Term	0	3	6	Functional Form	Label
Z04	0.230	0.265	0.232	x^*x-y*y	X-Y Astigmatism
Z05	-0.247	0.004	0.227	$2*r^2-1$	Focus
Z06	-0.006	-0.011	-0.007	$2*x*y$	45-degree Astigmatism
Z07	-0.003	-0.008	-0.007	$x*(x^2-3*y^2)$	Trefoil
Z08	-0.007	-0.004	-0.007	$x*(3*r^2-2)$	X-Coma
Z09	-0.002	-0.006	0.000	$y*(3*r^2-2)$	Y-Coma
Z10	-0.002	0.000	-0.001	$y*(3*x^2-y^2)$	Trefoil
Z11	-0.010	-0.003	-0.009	$x^4+y^4-6*x^2*y^2$	Sphero-Astigmatism
Z12	-0.031	-0.021	-0.028	$(2*x^2-r^2)*(4*r^2-3)$	Sphero-Astigmatism
Z13	0.019	0.002	-0.024	$6*r^4-6R^2+1$	Spherical Aberration
RMS-WFE	0.186	0.114	0.172		

2.3 MISELL PHASE RETRIEVAL ALGORITHM

In sections 2.1 and 2.2 we used parametric and non-parametric phase retrieval to estimate the wavefronts at each of the 3 focal positions. We averaged the 2 recovered wavefronts (parametric and non-parametric) at each of the 3 focal positions and subtracted them from the nominal position (circle of least confusion). These estimates become our diversity wavefronts to be used in a Misell type phase retrieval algorithm and the extended scene phase diversity algorithm. Removing the focus from each of the 6 wavefronts and averaging the 6 residuals gave us a good starting point for both the Misell phase retrieval and the extended scene phase diversity.

Figure 6 shows the Misell algorithm used here. An initial random wavefront is used, the diversity wavefront added and each in parallel propagated to the focal plane. The simulated focal plane amplitude is replaced with the observed PSF's amplitude, i.e. square root of the data, and the focal plane phase is retained. This is equivalent to applying the constraints imposed by the data. Each focal field is then inverse propagated back to the pupil and the pupil plane phases are mixed to give an updated estimate of the phase. This process is cyclically iterated until convergence is reached. Figure 6 actually shows the algorithm for 4 PSFs whereas we used only 3 PSFs.

For a single input PSF the non-parametric approach (section 2.2) is not well constrained. In general for an infocus image the problem is ill-posed since the number of free parameters in the phase exceeds the number of valid intensity values in the input PSF, where the valid data points refers to points such that the local SNR is greater than 1. Since the problem is ill-posed any noise in an input variable, must map into multiple phase points, thus correlated noise cells, i.e. regions, are introduced into the phase map. One way to counter this problem is to deliberately introduce a known aberration into the optical path, i.e., a diversity function. This spreads the PSF in the focal plane, and, by integrating longer with the detector we can get many more points with SNR greater than 1. When the number of input data points exceeds the number of free parameters in the phase, the size of the noise cell drops to ~1 sample point in the phase, thus, the phase noise is decorrelated. Also, by utilizing multiple input PSFs the problem can be better posed. The focus diversity (Misell) [5] algorithm used here uses 3 PSFs, each at different focal positions.

Figure 7 shows our results using this Misell algorithm. The top row shows the recovered phases at the last iteration. The phases are recovered modulo 2π and must be unwrapped either prior to mixing or as part of the mixing process. The middle row shows the unwrapped phases and the left hand side of the bottom row shows the solution phase. The solution phase was expanded in terms of Zernike polynomials and the results listed in Table-3. The lower right hand side of Figure 7 shows the wavefront residual after expansion in terms of the Zernikes. The gray scale map has been enhanced to show the residual high frequency structure. The solution phase has an rms. wavefront error of 0.116 microns rms. and the residual phase an rms. of 0.006 microns rms. Thus the wavefront is well matched by the Zernike polynomials. Note that the X-Y astigmatism term is the dominant aberration. Now we have a good starting estimate for the wavefront

error and a good estimate for the diversity wavefronts at each of the 3 focal positions. This is enough information to perform the extended scene phase diversity algorithm.

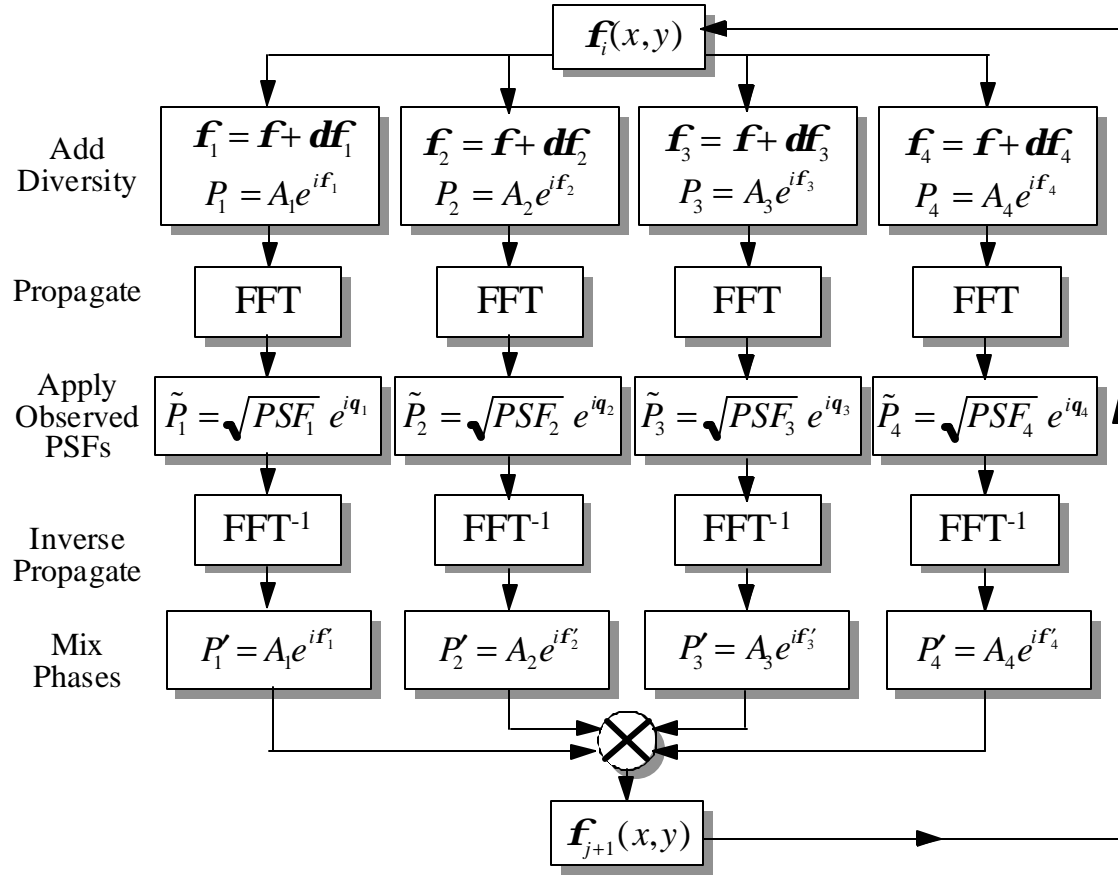


Figure 6
Misell Phase Retrieved Algorithm

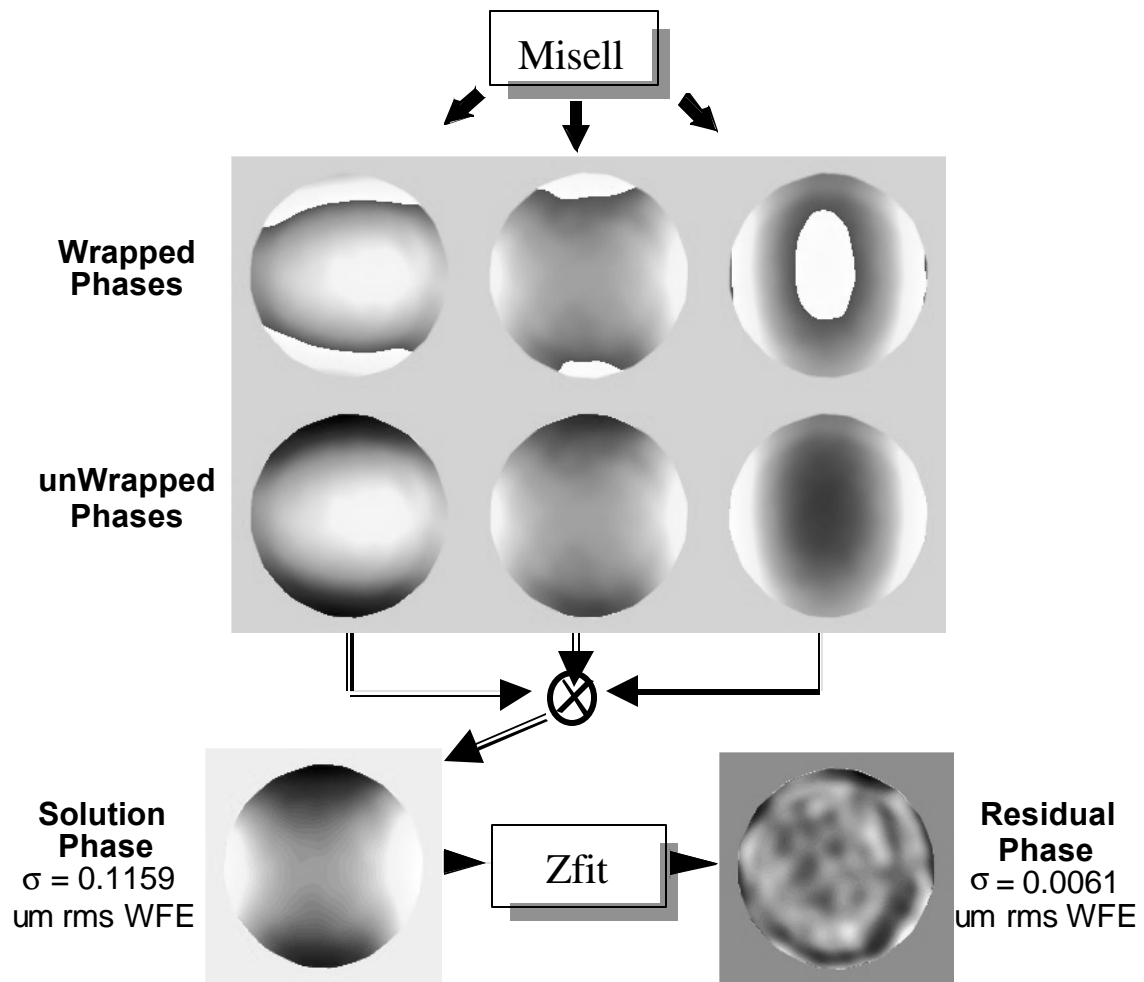


Figure 7
Misell Phase Retrieved Algorithm Wavefront Results

Table 3 - Misell Phase Retrieval Results

Term		Functional Form	Label
Z04	0.242	x^*x-y^*y	X-Y Astigmatism
Z05	-0.008	$2*r^2-1$	Focus
Z06	-0.009	$2*x*y$	45-degree Astigmatism
Z07	-0.006	$x^*(x^2-3*y^2)$	Trefoil
Z08	-0.007	$x^*(3*r^2-2)$	X-Coma
Z09	0.000	$y^*(3*r^2-2)$	Y-Coma
Z10	-0.003	$y^*(3*x^2-y^2)$	Trefoil
Z11	-0.013	$x^4+y^4-6*x^2*y^2$	Sphero-Astigmatism
Z12	-0.010	$(2*x^2-r^2)*(4*r^2-3)$	Sphero-Astigmatism
Z13	-0.002	$6*r^4-6R^2+1$	Spherical Aberration
σ -WFE	0.116		

3. PHASE DIVERSITY ALGORITHM

Phase Diversity is similar to phase retrieval in that it estimates the phase; however, the object is not known a-priori. In phase retrieval one assumes the object to be an unresolved point source. In phase diversity the object is not constrained, other than being positive. Phase diversity simultaneously estimates the phase and the object, hence, it is a joint estimation problem and generally less well-posed than phase retrieval with correspondingly less accuracy in the phase estimate. Also the phase estimate is a strong function of the contrast and spatial frequency structure in the scene.

In the phase diversity approach used herein [6] 3 extended scene images are collected, each at a different focal position. Focal error is accomplished via translation of the focal plane. The absolute focus is not known, however, the difference in focus (diversities) between the sets of channels was estimated using both the parametric and non-parametric phase retrieval methods. Each of the three channels “sees” the same aberrations, and object, except for the known difference in focus. Note, that the diversity aberration doesn’t have to be focus, it could be another aberration, or field dependence and/or wavelength, or even a coded aperture. With regards to Figure 8, the algorithm proceeds as follows, a “reasonable” estimate for the starting phase is chosen. “Reasonable” refers to using the phase recovered from the Misell algorithm from section 2.3. The closer the starting point to the solution the faster convergence is reached. The diversity functions are added to the starting phase for each of the channels and the pupil function constructed and propagated to the focal plane via Fast Fourier Transforms (FFT). An estimate of the object is made in the Fourier domain via a multiple channel Wiener filter. The object is inverse FFT’d and the constraint that the object must greater than or equal to zero is used. Any point in the object less than zero is set to zero. This is known as a projection operation. Then each of the PSFs are estimated via separate single channel Wiener filters and again if any PSF points are less than zero they are set to zero. An iterative transform algorithm is used to propagate from focal plane to pupil plane and the pupil functions are estimated. The pupil functions are mixed together and an updated estimate of the phase is returned. This is fed back at the top of Figure 8 and the process cyclically iterated until both the object and the phase estimates are no longer changing, i.e., convergence has been reached.

The top row of Figure 9 shows 3 collected and calibrated images of the Hubble Space Telescope double jet. The images are collected at the same focal positions as the PSFs were in sections 2.1, 2.2 and 2.3, i.e. the sagittal, circle of least confusion and tangential foci. Each image is the average of 30 frames of data to maximize the dynamic range. The lower left of Figure 9 is the object estimate output from the phase diversity algorithm. The lower right of Figure 9 is the original computer file image (8 bit) of the Hubble’s double jet. Qualitatively the object estimate “looks” sharper and has more contrast than the diversity images, however, it is not an exact match to the original computer file image. The left-hand side of Figure 10 shows the estimated wavefront with an rms. wavefront error of 0.101 microns. The middle of Figure 10 shows the estimated wavefront expanded in terms of Zernike polynomials and the right-hand side is the

residual after fitting. The residual after fitting is 0.029 microns rms. wavefront error, thus, the Zernike fitting did not account for 8% (in power) of the wavefront PSD. This is evident in the high frequency structure in the residual wavefront and series of correlated circular rings. Table 4 shows the Zernike coefficients in tabular form.

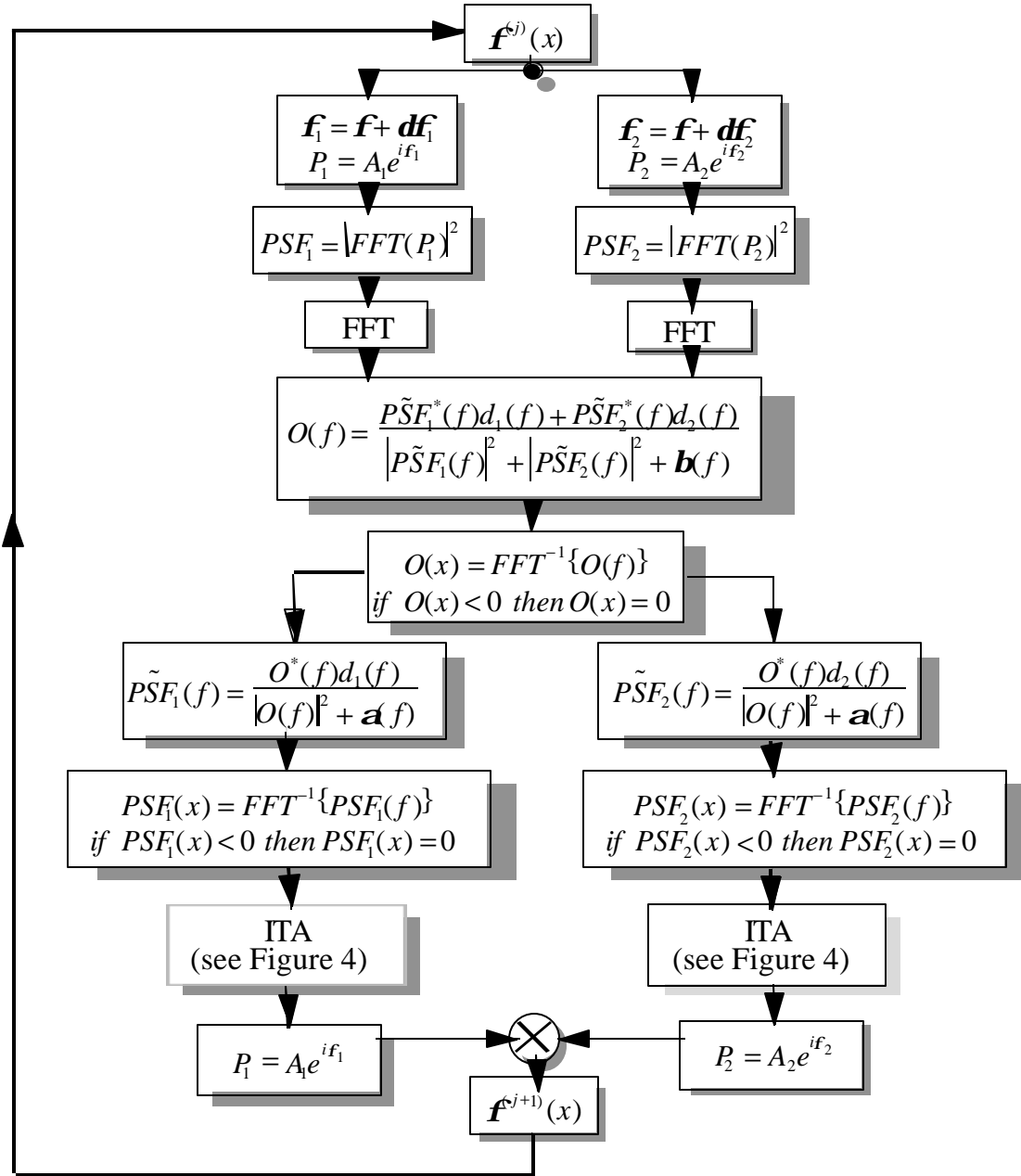


Figure 8
2 Channel Phase Diversity Algorithm

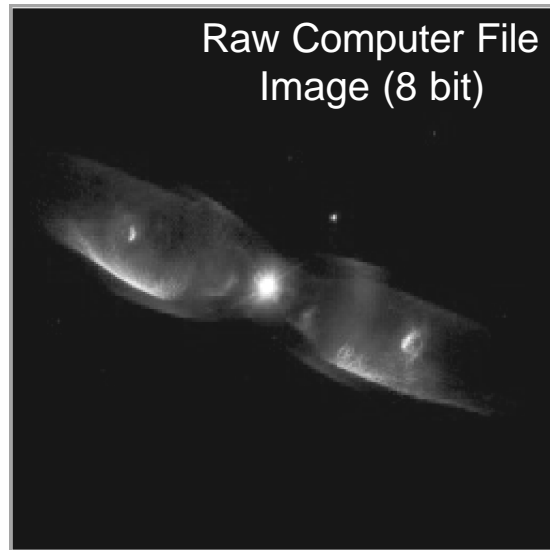
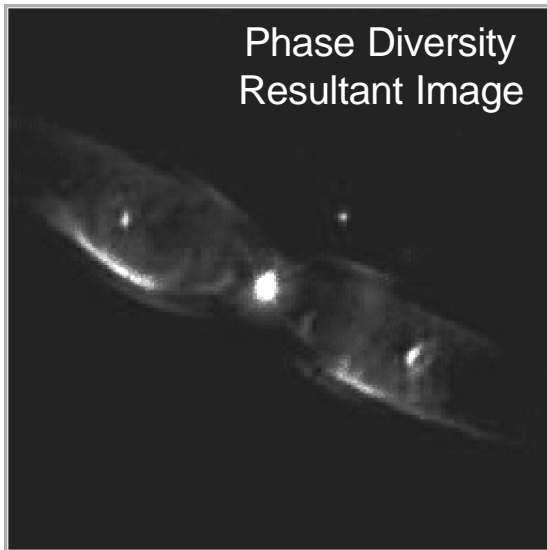
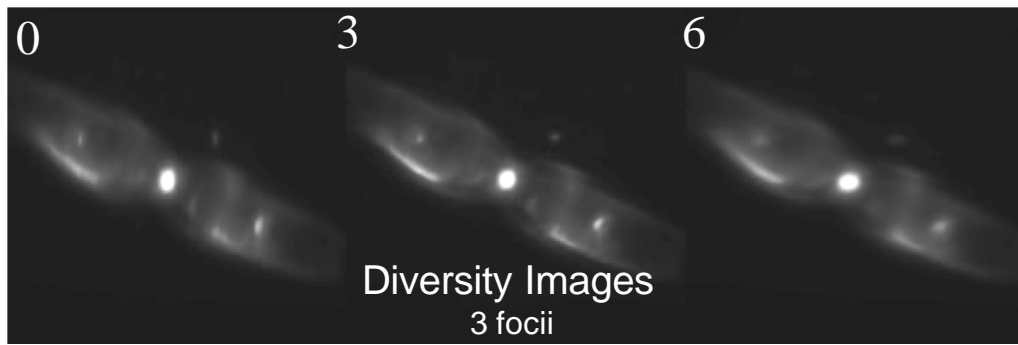


Figure 9
Phase Diversity Images

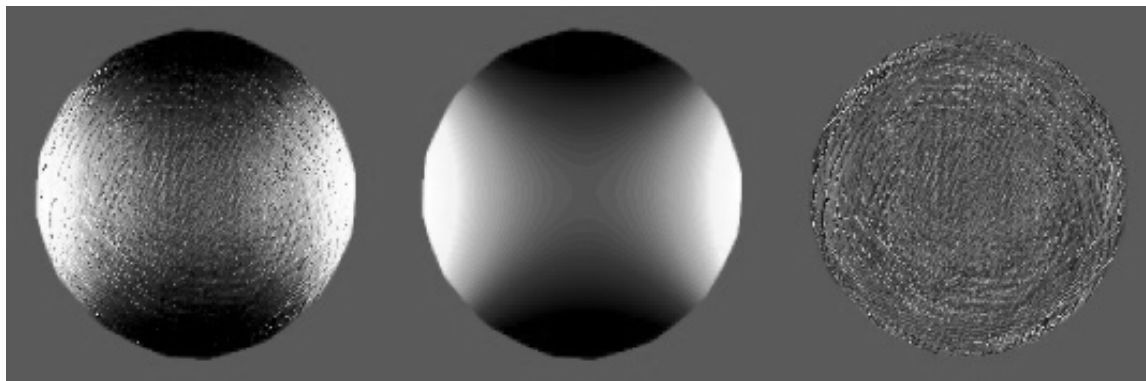


Figure 10

Phase Diverse Recovered Wavefront

Left - recovered wavefront, *Middle* - Zernike expansion of recovered wavefront, *Right* - Residual after Zernike expansion

Table 4 - Phase Diversity Results

Term		Functional Form	Label
Z04	0.235	x^2x-y^2y	X-Y Astigmatism
Z05	0.000	2^2r^2-1	Focus
Z06	0.000	2^2x^2y	45-degree Astigmatism
Z07	0.003	$x^2(x^2-3^2y^2)$	Trefoil
Z08	0.001	$x^2(3^2r^2-2)$	X-Coma
Z09	0.001	$y^2(3^2r^2-2)$	Y-Coma
Z10	0.002	$y^2(3^2x^2-y^2)$	Trefoil
Z11	-0.002	$x^4+y^4-6^2x^2y^2$	Sphero-Astigmatism
Z12	0.016	$(2^2x^2-r^2)^2(4^2r^2-3)$	Sphero-Astigmatism
Z13	0.000	$6^2r^4-6R^2+1$	Spherical Aberration
σ -WFE	0.101		

4. SUMMARY AND DISCUSSION

Table 5 is a summary of the phase retrieval and phase diversity results. The columns labeled 0,3, and 6 refer to the sagittal, circle of least confusion and tangential focal positions. These columns exist only for the Parametric and Iterative transform results since the Misell and Phase Diversity methods couple all 3 focal positions together. All units are in microns of zero to peak wavefront error. The dominant term is Z04 (X-Y astigmatism) and is 0.241 +/- 0.005 microns. This term is caused by deliberately misaligning the 2 parabolas in the system. All the others terms are small with the second most dominant term being Z12 (sphere-astigmatism).

We have successfully developed a benchtop phase diverse imaging system and have conducted a series of experiments and have estimated the phase using 4 different phase retrieval and/or phase diversity algorithms. We estimate the precision over the 8 recovered wavefront as better than 0.005 microns zero to peak over the set of images and the precision in a single wavefront recovery as ~0.012 microns zero to peak wavefront error. At this time we do not have an estimate of the accuracy since we did not have an independent verification of the "true" wavefront. Also we have not yet estimated the accuracy and precision as well spatial frequency content of the object recovery in the phase diversity algorithm.

All the computer codes are in "C" with Message Passing Interface for using parallel computer constructs. The codes were executed on NASA/Goddard Space Flight Center's HIVE computer, a Beowulf cluster of Pentium processors running the Linux operation system. All algorithms ran in less than 20 seconds.

Table 5 - Summary of All Results

Term	Parametric			Iterative Transform			Misell	Pdiv	AVE	SDEV	STD ERR
	0	3	6	0	3	6					
Z04	0.238	0.252	0.233	0.230	0.265	0.232	0.242	0.235	0.241	0.012	0.005
Z05	-0.260	-0.004	0.241	-0.247	0.004	0.227	-0.008	0.000	NA	NA	NA
Z06	-0.009	-0.012	-0.007	-0.006	-0.011	-0.007	-0.009	0.000	-0.008	0.004	0.001
Z07	-0.005	-0.003	-0.004	-0.003	-0.008	-0.007	-0.006	0.003	-0.004	0.004	0.001
Z08	-0.003	-0.003	-0.004	-0.007	-0.004	-0.007	-0.007	0.001	-0.004	0.003	0.001
Z09	0.003	0.002	0.000	-0.002	-0.006	0.000	0.000	0.001	0.000	0.003	0.001
Z10	-0.007	-0.004	-0.003	-0.002	0.000	-0.001	-0.003	0.002	-0.002	0.003	0.001
Z11	-0.008	-0.016	-0.015	-0.010	-0.003	-0.009	-0.013	-0.002	-0.010	0.005	0.002
Z12	-0.015	0.009	-0.013	-0.031	-0.021	-0.028	-0.010	0.016	-0.012	0.017	0.006
Z13	0.019	0.004	-0.016	0.019	0.002	-0.024	-0.002	0.000	0.000	0.015	0.006

Units are microns of zero to peak wavefront error.

5. REFERENCES

- [1] V.N. Mahajan, "*Zernike Annular Polynomials for Imaging Systems with Annular Pupils*", J. Opt. Soc. Am, Vol. 71, 75-85, 1981
- [2] W.H. Press, B.P. Flannery, S.A. Teukolsky, W.T. Vetterling, "Numerical Recipes in C", Cambridge University Press, first edition, 1988, pp. 541-545
- [3] Lyon, R. G., Dorband, J. E., Hollis, J. M., "*Hubble Space Telescope Faint Object Camera Calculated Point Spread Functions*", Applied Optics, Vol. 36, No. 8, March 10, 1997.
- [4] R.W. Gerchberg, W.O. Saxton, "*A Practical Algorithm for the Determination of Phase from Image and Diffraction Plane Pictures*", Optik, **35**, 237-246
- [5] Misell, "*A Method for the Solution of the Phase Problem in Electron Microscopy*", J. Phys. D, Vol. 6, L6-L9, 1973
- [6] Baba, H. Tomita, N. Miura, "*Iterative Reconstruction Method in Phase Diverse Imaging*", Applied Optics, **33**, No. 20, (1994)

A Performance Study of a Phase Diversity Program on NASA GSFC Hive Test Bed

Udaya A. Ranawake
UMBC/USRA CESDIS/NASA GSFC, Greenbelt, MD 20771, USA

Richard Lyon
NASA GSFC, Greenbelt, MD 20771, USA

John E. Dorband
NASA GSFC, Greenbelt, MD 20771, USA

ABSTRACT

We analyze and test the performance of a phase diversity program on the NASA GSFC Hive Computer. The Hive is a PC cluster consisting of up to 200 processors. A subcluster of the Hive consisting of dual pentium III gateway computers running at 500 MHz and interconnected by myrinet was used for this study. The phase diversity program originally written in the MPL programming language for the MasPar MP-2 computer was parallelized using domain decomposition and implemented using the C programming language and the MPICH communication library. The timing measurements on a 512 X 512 image shows that the message passing version of the phase diversity program runs as fast as the MasPar implementation using just eight processors of the Hive computer.

1. INTRODUCTION

Phase diversity is an important computational method used in space based imaging systems [1]. The phase diversity technique uses multiple observed imagery of an astronomical object with a high fidelity computer model to determine the mirror shapes and misalignments of an optical system and to boost the spatial frequency of an astronomical object. This technique can be combined with other wavefront sensing (WFS) methods and an active control system to determine the optimal mirror configuration on-orbit of segmented and sparse aperture telescopes that will form the heart of future space based imaging systems [2]. The ability to correct for errors caused by thermal/structural deformations, misalignments and other dynamic factors on-orbit by simply changing the configuration of the mirrors and some post-processing of the images will result in much larger and lower cost mirrors than permitted by the current monolithic mirror technology.

The algorithms for phase diversity are quite complex and require substantial computer resources. Until recently, the MasPar computer based on the single instruction multiple data (SIMD) architecture has been the preferred system for implementing image processing based applications. NASA GSFC currently has a large set of programs written in the native MPL[3] programming language for this system. However, the MasPar computer system has become obsolete with the advent of low cost PC clusters based on commodity hardware components and freely available software packages [4]. Due to their low cost, high performance, modular and simple design, these commodity clustered computers are also a good choice as the on-orbit computing engine of future space based imaging systems.

In this paper, we describe the porting of a phase diversity program from the MasPar to a commodity clustered computer called the Hive at NASA GSFC. We also study the scalability of the program on the Hive computer, identify performance bottlenecks and propose several changes to the code to improve performance.

2. THE HIVE COMPUTER

The Hive [5] is a heterogeneous PC cluster of two hundred processors built from commodity hardware components and freely available software packages. The nodes of the Hive consists of 64 dual Pentium PRO processors running at 200 MHz, 16 dual Pentium III Gateway computers running at 500 Mhz and 10 quad Pentium III Dell computers running at 500 Mhz. These nodes are interconnected by 100 MB/s fast ethernet. In addition, the gateway and the dell computer nodes are also interconnected by the myrinet [6]. Figure 2 shows the architecture of the Hive. The performance study of the phase diversity program was performed on the Gateway cluster using the myrinet.

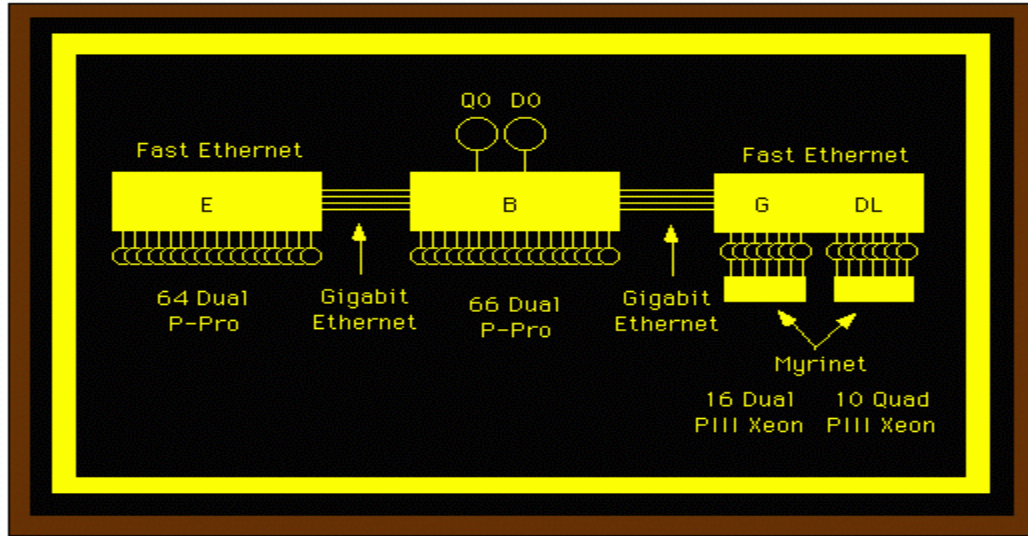


Fig. 1. Architecture of the Hive

3. Parallel Implementation

The message passing version of the phase diversity algorithm was implemented by using a simple block-oriented mapping scheme where the computational grid was divided into rectangular regions parallel to the y-axis and assigned to processors as shown in Figure 3. Converting the MPL version of the program to a

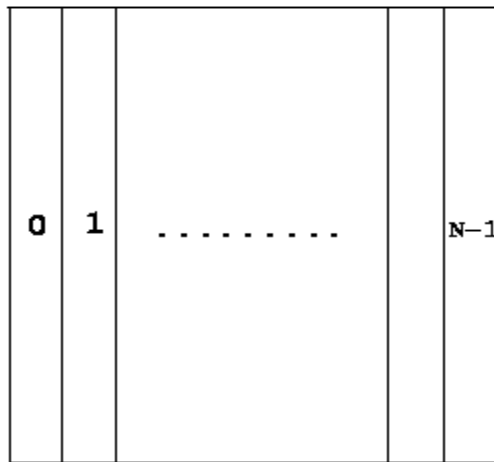


Fig. 2. Mapping of the Grid to Processors

C/MPICH [7], [8] program was quite easy and involved the following steps:

1. Replace declarations and references to virtual variables in MPL by array subscripts and implement a macro call to represent the forall operation in MPL that loops over elements of a virtual array.

2. Move global reduce operations embedded inside the forall blocks of the MPL program out of these blocks and implement functions for global reduce operations using MPI Allreduce routine.
3. Implement functions for shifting data parallel to the x and y axes. The phase diversity program uses a square grid with the data always shifted by half the grid size parallel to both axes several times during each iteration. Due to the simple partitioning scheme used, this shifting of data can be implemented easily and efficiently. For example, the shifting of data parallel to the y-axes is implemented as a memory copy and the shifting of data parallel to the x-axes is implemented as a exchange operation between pairs of processors.
4. Replace calls to Fast Fourier Transforms (ffts) to use the ones in the FFTW [9] software package.
5. Implement functions for providing input/output operations. The input data is read by process 0 and scattered to other processes using the MPI Scatter routine. Similarly, the output results are gathered by process 0 using MPI Gather routine and written to files that reside on the node process 0 is running.

4. Performance Analysis

We studied the performance of the phase diversity program on the Hive as a function of the number of processors. Figure 4 shows the execution time of the program for a 512 X 512 grid and 100 iterations. It can be observed that the

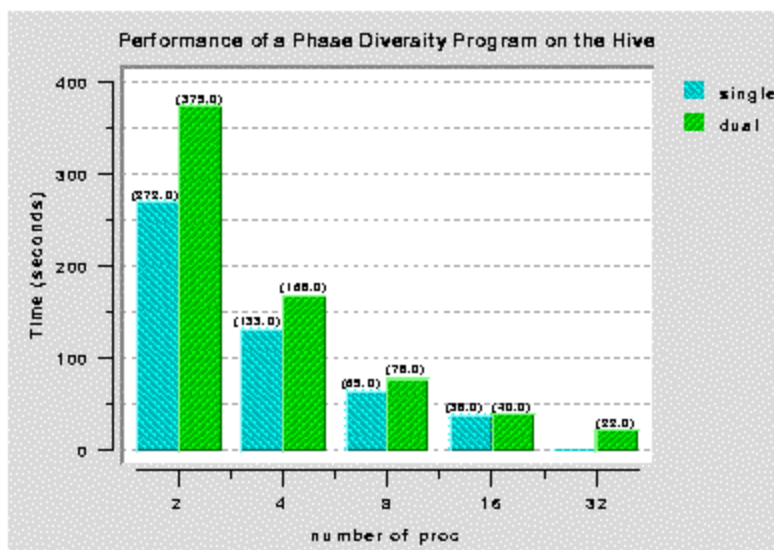


Fig. 3. Execution Times on the Hive

phase diversity program exhibits good scalability on up to 32 processors of the Hive. On two and four processors, the run times when using one processor per node is smaller than when using two processors per node due to decrease in performance caused by memory bottlenecks in the latter case. However, as the number of processors is increased the performance difference disappears due to better utilization of the cache. In Figure 4, we compare the execution times on the MasPar and the Hive. The message passing version of the phase diversity program runs as fast as the MasPar version when using just 8 processor of the Hive.

In order to identify the bottlenecks of the program and determine possible improvements to the code, we produced an execution profile of the program using the gprof profiling tool. This execution profile was generated using two processors for 100 iterations of the program on a 512 X 512 grid. Figure 4 shows the functions that utilize the most amount of time along with the percentage of time used by each part of those functions. We observe that the fft routine account

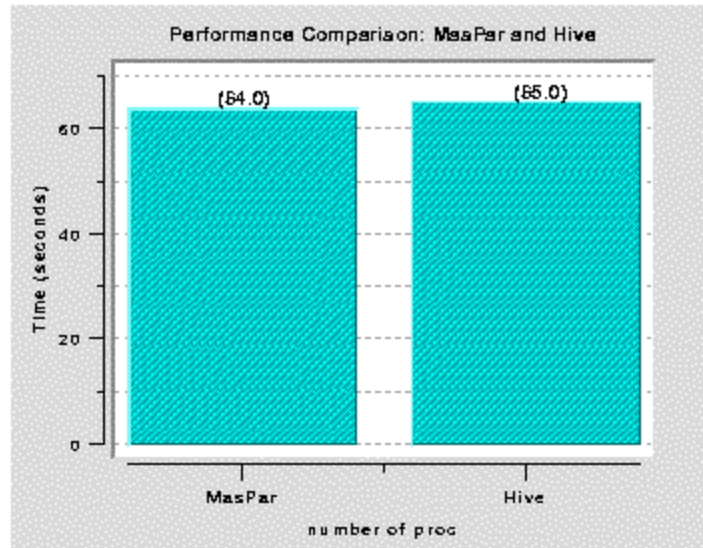


Fig. 4. Performance Comparison between MasPar and the Hive

for about 40 percent of the total time of the program. The fft computation is well known to be an extremely expensive operation in scientific programs. The phase diversity program uses nearly 10 fft computations per iteration. The C/MPICH implementation of the phase diversity program uses the FFTW package freely available from MIT. It can be seen from the execution profile that nearly 50 percent of the time of the fft computation is spent in the matrix transpose portion of the code in the two processor case. However, only 7 percent of the total time is spent in theacutalinter-processor communication and the rest is spent in performing the local transpose. We also observe that the phase diversity program spends considerable amount of time in computing an estimate for the object using the Wiener filter. The iterative portion of this function uses a global error estimate for convergence which requires about 10 global reduce operations per function call on the average. These reduce operations account for about 23 percent of the time of this function.

5. Concluding Remarks

In this paper, we have demonstrated that the phase diversity algorithm can be efficiently implemented on commodity clustered computers which would make

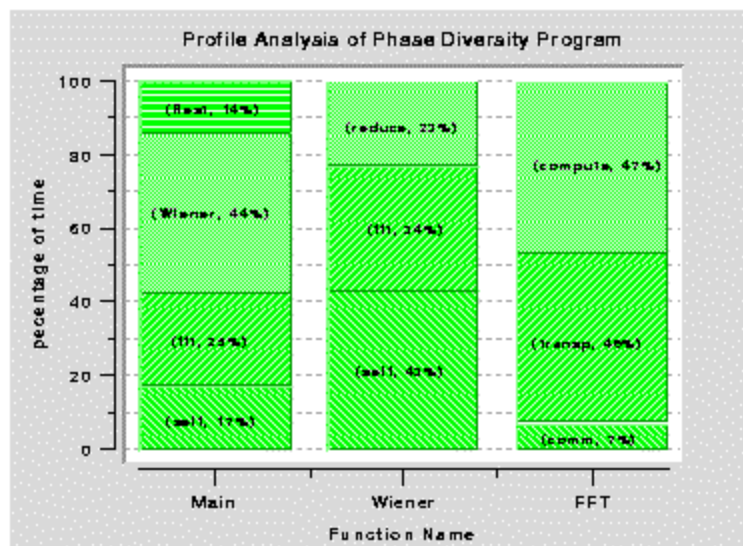


Fig. 5. Profile Analysis

these computers a good choice as the on-board computing engine of future space based imaging systems. We also have analyzed the bottlenecks of the program and identified the routines that needs to be optimized in order to further improve the performance of this code.

6. References

1. Richard Lyon, : OSCAR: Optical Systems Characterization and Analysis Research Project, Accessible on the Internet at World Wide Web URL <http://jansky.gsfc.nasa.gov/OSCAR/>
2. Richard Lyon, et al; Extrapolating HST Lessons to NGST, Optics and Photonics News, Vol9, No7 1998.
3. MasPar Computer Corporation, MPL (MasPar Programming Language) Manuals Document Part Number 9300-9034, July, 1992.
4. T. Sterling, et al., BEOWULF: A Parallel Workstation for Scientific Computation, Proc. of the 1995 International Conference on Parallel Processing, Milwaukee, Wisconsin, August 14-18, 1995.
5. J. Dorband and U. Ranawake, theHIVE: Highly-parallel Integrated Virtual Environment, Accessible on the Internet at World Wide Web URL <http://newton.gsfc.nasa.gov/thehive/>.
6. Nanette J. Boden, et al; Myrinet: A Gigabit per Second Local Area Network, IEEE Micro, Vol.15, No.1, February 1995, pp.29-36.
7. WGropp, ELusk, NDoss and A Skjellum, A high-performance, portable implementation of the MPI message passing interface standard, Parallel Computing vol22, No 6, Sep 1996, pp 789-828.
8. Myricom Inc; Myrinet Software and Documentation, Accessible on the Internet at World Wide Web URL <http://www.myricom.com/scs/index.html>.
9. M. Frigo and S. G. Johnson, FFTW: An Adaptive Software Architecture for the FFT, Proceeding of the ICASSP 1998, vol 3, p 1381.

Cramer-Rao Bounds for Focus Diverse Wavefront Sensing with Deformable Mirror “print-through” and Control Noise

Bruce H. Dean[†]; Richard G. Lyon[‡]

NASA Goddard Space Flight Center, Greenbelt, MD 20771

ABSTRACT

An estimation-theoretic analysis is presented for phase-diverse phase retrieval with additive deformable mirror “print-through” and control noise. The analysis is based on the imaging mode anticipated for NGST (Next Generation Space Telescope) and includes predictions for optimal focal settings and the effect of adding additional diversity images beyond two. Several test cases are discussed and modeled from experiments performed on the NGST Wavefront Sensing and Control Testbed (WCT).

1. INTRODUCTION

The ability to sense and control an optical wavefront for the purpose of removing unwanted residual or externally induced aberrations provides the operational basis for adaptive and active optical systems. The effectiveness of such a removal obviously depends upon the accuracy to which the system wavefront is known. As a result, the ultimate ability for these systems to provide aberration correction depends upon wavefront sensing accuracy, which in turn is influenced by noise and other degrading factors. In this paper we consider an estimation theoretic analysis of focus diverse phase retrieval to study the influence of a deformable mirror (DM) on the accuracy of aberration recovery. The point of the analysis is to demonstrate the utility of an estimation theoretic approach in providing engineering guidance for assessing system performance, and for finding optimal recovery configurations.

The DM is typically the “workhorse” of most adaptive optical systems. Its versatile range of control and intuitive means for correcting the optical wavefront have long been appreciated by the adaptive optics community (a good overview of the literature is given in (1)). The high frequency correction capability obtained from “many-actuator” membrane DM systems is also partly responsible for two effects introduced into the optical wavefront: (a) the residual bumpiness left over after flattening due to “print-through” and polish marks and (b) “control noise.” The residual bumpiness left over after flattening that is not due to print-through, but rather, a result of errors originating in the flattening procedure is termed here “control noise.” As a result, control noise is somewhat algorithm dependent. E.g., a DM flattening algorithm that is based on the minimization of the RMS wavefront error will result in mirror figures that are rather bumpy, but with correspondingly low RMS errors. An intuitive illustration of the additive DM residual is shown in Figure 1 (Zernike’s are in the Code V basis set).

Although the print-through and control noise effects are not often overly severe, both can be problematic for optical systems that incorporate actuator controlled membrane mirror DM’s. E.g., a discussion of 7% light scatter distributed about the PSF core due to actuator residuals from a Xinetics 349 channel DM is discussed in Ref. 2 based on data from the Goddard NGST/Nexus/Wavefront Sensing and Control Testbed (WCT). The questions we wish to address are thus – how is the aberration recovery effected by the additive DM residual in the imaging mode envisioned for NGST(?) - what are the consequences for the placement of focus diverse images from the nominal focal position(?) – and what advantages are gained (if any) in providing more than two focus diverse images? These questions may be addressed based on a calculation of the Cramer-Rao lower Bounds (CRB’s) which give a lower bound on the error bars associated with parameter estimation from noisy data. The issue of best focus has been previously addressed in the literature using the CRB analysis (Refs. 8-10). In this paper we consider an application of these earlier results to assess the influence of the DM surface residual.

[†] *Optics Branch: Design & Analysis Group; Code 551*

[‡] *Instrument Technology Center; Code 550*

The CRB's are a basic calculational tool of estimation theory and statistical signal processing , but have only recently been applied to digital image estimation. The calculations were first discussed with image recovery applications by Cederquist, et. al., specifically for the case of a shearing interferometer. The calculations were later applied to phase retrieval by Cederquist and Wackerman, and by Cederquist and Fienup, et. al. (6). The first application of the CRB's for assessing an optimal hardware configuration for aberration recovery was given by Fienup and Marron, et. al. (7). In this application, an optimal defocus setting for the Hubble Space Telescope was considered for the most accurate retrieval of spherical aberration. Expanding on this analysis, Fienup and Thelen, et. al. (8), have calculated the CRB's as a function of diversity defocus to assess the CR advantage of phase-diversity over curvature wavefront sensing. This trend of calculating the CRB's as a function of diversity defocus was further discussed by Lee and Roggemann, et. al. (9). In this latter paper the effect of splitting the available light among multiple diversity images was considered, as well as the aberration recovery for a known extended object (i.e., phase-diversity). The CR method for phase-diverse phase retrieval was also discussed by Sun (10) who compared the CR performance of a conventional diversity imaging system to that of a Hartmann sensor, and also for the case of a conventional imaging / Hartmann sensor combination.

To motivate the discussion, in Section 2 we show that the appearance of the WCT Testbed PSF's may be traced to the DM residual, and illustrate the PSF recovery with phase retrieval results using the Misell-Gerchberg-Saxton algorithm (11). In Section 3 we discuss the WCT Xinetics DM and in Section 4 we give a summary of the CR analysis used for the calculations.

2. TYPICAL TESTBED PSF'S

A typical sequence of defocused PSF data and exit pupil amplitude obtained from the WCT testbed are shown in Figure 2. The corresponding phase-retrieved PSF's are illustrated in Figure 3. In this case the wavefront has been intentionally aberrated with approximately 0.1 waves RMS of Y-Coma using the Itek simulator DM discussed in Section 3. The blemishes that are apparent near the center of the pupil (Figure 2) are remnants from dust specks and defects in the pupil imaging lens and are not measured in the PSF data. Therefore, the phase-retrieval results presented here do not incorporate the measured pupil irradiance in the phase-retrieval process, although for testing purposes we have utilized this data but have noted only minor changes in the results. For reference, the phase-retrieval method (11) is a focus diverse modified Misell-Gerchberg-Saxton algorithm. The core algorithm is based on the Gerchberg-Saxton (12) iterative transform method as discussed by Misell (13) (although there are slight differences). Roddier (14) utilized this method for analyzing the Hubble PSF's and the algorithm has also been discussed by Fienup and Marron, et. Al (15). An investigation of the algorithm's performance based on Monte Carlo and other simulation studies was given by Lyon (16) for the DCATT Testbed. The algorithm has been further utilized by Redding, et. Al (17), in combination with a Macos (18) ray trace model and applied to data from the DCATT and WCT testbeds.

The high SNR for this system is apparent from the integrated digital number counts (DNC's) listed below each image along with the corresponding average *detected* irradiance

$$I_{\text{detected}} = \frac{h c N_{\text{photons}}}{\lambda \Delta t A r} = \frac{h c N_{\text{DNCs}}}{\lambda \Delta t A} (\text{watts} / \text{m}^2), \quad (1)$$

where h is Planck's constant, c is the speed of light, λ is the wavelength ($= 6328 \text{ \AA}$), Δt is the integration time, A is the detector area and r is the conversion factor between electrons and DNC's. Calculations from the incident irradiance must be appropriately scaled via the quantum efficiency factor for the Photometrics CCD detector (19).

The "dimpling" that appears in the measured PSF's may be traced to the DM surface residual (see Figure 4 for a Zernike decomposition of this residual). To simulate this effect (see also Figure 1) we first generate a wavefront with approximately $S_{\text{Aber}} \approx 0.25$ waves (PV units) of Y-Coma and then Fourier propagate this phase map to the focal plane. After including an additive DM surface residual of

$S_{DM} \approx 0.045$ waves RMS, the PSF's are recalculated to simulate the measured PSF's. The result is shown in Figure 5.

3. THE XINETICS DM

The WCT testbed optical system (formerly known as DCATT (20) includes two DM's: a Xinetics 349 channel DM in combination with an 87 channel Itek Simulator DM. The Simulator DM is used to introduce known aberrations into the system while the Xinetics DM is configured to remove these aberrations based on the wavefront sensing and control system configured by Redding, et. Al (17). Optical design and other test results for this system are discussed in Ref's (20,2).

We have accumulated optical test data on the Xinetics DM based on early interferometric testing (21), and later from WCT phase retrieval studies (22). Early flattening results utilizing interferometer data are illustrated in Figure 6. Similar testing at JPL for the Simulator DM indicates that the high frequency wavefront dimpling that appears in the defocused PSF's is due primarily to the Xinetics DM residual. Both DM's contribute to this dimpling effect but the Simulator DM residual is of a much lower frequency and

4. CRAMER-RAO BOUNDS

Statistical Model

The CRB's are calculated from a statistical model relating the parameters being estimated to noise in the measured data. As a result, the CRB's are independent of the method used for parameter estimation and apply specifically to unbiased estimates of the parameters. For optical phase recovery, the governing statistics are given by the Poisson probability density function for photon limited images. The PDF is given by the product of individual event probabilities under the assumption that detected photon events are statistically independent (x are the detector elements):

$$\Pr[\Omega | \vec{a}] = \prod_x \frac{p(x, \vec{a})^{d(x)} e^{-p(x, \vec{a})}}{d(x)!}, \quad (2)$$

where Ω is the observed data set, p is the PSF, d are the detected photons, and \vec{a} is the aberration parameter vector being estimated. For phase-diversity, the PSF is replaced by the convolution of the PSF with the object irradiance distribution. Phase retrieval is therefore a special case of phase-diversity when the object irradiance is a delta function.

For convenience we choose the aberration parameters to be coefficients of a Zernike polynomial expansion of the wavefront error at the exit pupil:

$$\mathbf{j}(u, \vec{a}) = \sum_b a_b Z_b(u), \quad (3)$$

using Greek indices to denote components in the aberration parameter space. The complex pupil amplitude is therefore

$$g(u, \vec{a}) = A(u) \exp(2\pi i \mathbf{j}(u, \vec{a}) / \lambda), \quad (4)$$

where $A(u)$ is the binary aperture function and u denotes a 2-d spatial coordinate in the pupil plane. The complex amplitude of the electric field at the detector plane is the Fourier transform of (4):

$$G(x, \vec{a}) = \mathfrak{F}[g(u, \vec{a})], \quad (5)$$

where $\mathfrak{F}(\cdot)$ denotes the Fourier transform operator. We note for reference that the WCT testbed has the capability of taking pupil plane intensity measurements. This additional information can then be utilized by the retrieval algorithm as was originally intended by Gerchberg and Saxton. Utilizing the pupil plane intensity in the retrieval process has also been discussed by Fienup where further references can be found.

For the problem at hand, the phase map (3) is a linear combination of the aberration wavefront error, \mathbf{j}_{aber} , and the DM residual wavefront, \mathbf{j}_{DM} . For a circular pupil function this combination is conveniently expressed in terms of the Zernike polynomial basis:

$$\mathbf{j}(u, \vec{a}) = \mathbf{j}_{aber} + \mathbf{j}_{DM} = \sum_{b=1}^B a_b^{aber} Z_b(u) + \sum_{g=1}^{\Gamma} a_g^{DM} Z_g(u), \quad (6)$$

where typically $B \ll \Gamma$. For the analysis considered here, $B = 15$ is representative of the lower order phase errors while $\Gamma = 990$ (Zernike order 43) gives a reasonable approximation to the high frequency DM residual. E.g., in Figure 4 we illustrate an order 45 fit corresponding to $\Gamma = 1081$ terms. For simplicity in notation, equation (6) may be expressed using a single index under the assumption that $a_b^{aber} = 0$ for $b > B$:

$$\mathbf{j}(u, \vec{a}) = \sum_{b=1}^{\Gamma} (a_b^{aber} + a_b^{DM}) Z_b(u). \quad (7)$$

In a phase-diverse imaging system, multiple images are formed while varying one or more diversity parameters. Assuming that each member of a phase-diverse data set are statistically independent, the PDF for phase-diverse phase retrieval is given by

$$\Pr[\Omega | \vec{a}] = \prod_{m=1}^M \prod_x \frac{p_m(x, \vec{a})^{d_m(x)} e^{-p_m(x, \vec{a})}}{d_m(x)!}, \quad (8)$$

where M are the number of diversity channels. The log-likelihood function is thus

$$L = \ln(\Pr[d | \vec{a}]) = \sum_{m=1}^M \sum_x (\ln[p_m(x, \vec{a})^{d_m(x)} e^{-p_m(x, \vec{a})}] - \ln[d_m(x)!]). \quad (9)$$

The functional form of (7) suggests a number of alternative probability models. E.g., the probability model discussed above may be modified to include prior statistical information on a_b^{aber} , a_g^{DM} , or both. In this case the \vec{a} 's are no longer deterministic but are treated as random variables with known PDF's. For example, if one assumes that the DM control residual is not fixed but derived from a PDF=PDF(\vec{a}^{DM}) (i.e., based on a PDF modeled from say, a histogram of the coefficient data of Figure 4), the probability model in this instance takes the form

$$\Pr[\Omega, \vec{a}^{aber}, \vec{a}^{DM}] = \Pr[\Omega | \vec{a}^{aber}] \Pr(\vec{a}^{DM}). \quad (10)$$

Alternatively, the a_b^{aber} may be considered as deriving from some known PDF, or both. The inclusion of prior statistics into the model by assuming that the \vec{a} 's are random variables defines a Bayesian probability model (for instance, Hogg and Craig (3)). Analysis and discussion of the CRB in this context is given by Van Trees (3), p. 371-373. Image recovery applications are discussed by Thelen and Paxman, et. al. (24).

The CRB's are lowered by incorporating the statistical prior. However, the advantage gained by incorporating this information into the estimation process is minimized for high photon counts as illustrated below. Therefore, given the high photon counts for WCT (typically 4K to 60K counts/peak pixel), for simplicity we assume that a_b^{aber} and a_g^{DM} are both deterministic parameters and take

$$\Pr[\Omega, \vec{a}^{aber}, \vec{a}^{DM}] = \Pr[\Omega | (\vec{a}^{aber}, \vec{a}^{DM})]. \quad (11)$$

Cramer-Rao Theorem

The CR theorem states that

$$\text{Var}(\hat{a}_b) \equiv \mathbf{S}_{\hat{a}_b}^2 \geq F_{bb}^{-1}(\vec{a}), \quad (12)$$

where $\text{Var}(\cdot)$ is the variance and \hat{a}_b denotes an unbiased estimator for a_b . The Fisher information matrix, F_{ab} , is defined as the negative expectation of the log-likelihood Hessian matrix (using $\partial_a \equiv \partial / \partial a_a$, $\partial_{ab}^2 \equiv \partial^2 / \partial a_a \partial a_b$, etc.):

$$F_{ab} = -E \left[\partial_{ab}^2 L \right], \quad (13)$$

subject to the regularity condition, $E[\partial_a L] = 0$. $E[\cdot]$ denotes the ensemble average over both the observed data and a statistically meaningful sample of parameter realizations. The regularity condition states essentially that the order of differentiation and integration may be interchanged over the PDF – a condition that is not always satisfied (see Kay 3 p. 67). The CR theorem is derived in, typically by an application of the Schwarz inequality (25).

An intuitive understanding of the CR theorem is obtained by noting from inspection of (13) (and (12)) that the bounds are inversely proportional to the curvature of the log-likelihood function, i.e., to the sensitivity of L on the parameters being estimated. Therefore, it will be easier to produce more accurate estimates from data sets in which L is strongly influenced by the parameters. Conversely, for data corrupted by noise and other degrading factors, the functional dependence on the parameters will be reduced and therefore the bounds will be correspondingly higher according to (12).

Phase-Diverse Cramer-Rao Bounds

Substituting (9) into (13), it is straightforward to show that the deterministic Fisher matrix for phase-diverse phase retrieval with M diversity channels is given by

$$F_{ab} = F_{ab}^D = \sum_{m=1}^M \sum_x [\partial_a p_m(x, \vec{a})][\partial_b p_m(x, \vec{a})] / p_m(x, \vec{a}). \quad (14)$$

For completeness we note that by inclusion of the statistical prior one obtains

$$F_{ab} = F_{ab}^D + F_{ab}^P, \quad (15)$$

where F_{ab}^P is derived according to (13) from the *prior* log-likelihood function. The CRB's for this case have been discussed when the statistical prior is Gaussian (10) (and references therein). From (14) it is apparent that the deterministic Fisher matrix is proportional to the total integrated photon count, N_p , as discussed in (9) and (10). To illustrate the dependence of the CRB on light level, we calculate in units where the PSF is normalized to unity:

$$\int_x p_m(x, \vec{a}) = N_p \int_x P_m(x, \vec{a}) = N_p, \quad (16)$$

where P_m is the normalized PSF:

$$\int_x P_m(x, \vec{a}) = 1. \quad (17)$$

In terms of the normalized PSF, (14) is expressed

$$F_{ab} = F_{ab}^D = N_p \sum_{m=1}^M \sum_x (\partial_a P_m)(\partial_b P_m) / P_m, \quad (18)$$

and therefore, $\text{Var}(\hat{a}_b) \propto 1 / N_p$, which illustrates the CRB dependence on N_p . Furthermore, in cases where the prior is independent of N_p , (15) becomes

$$F_{ab} = N_p (F_{ab}^D + F_{ab}^P / N_p), \quad (19)$$

and therefore, the effect of the statistical prior on estimation accuracy is minimized.

Calculations and Analysis

An important distinction should be made regarding earlier calculations (e.g., Ref. 9) of the CRB as a function of N_p , and the calculations considered here. Specifically, this difference results from the fact that the WCT integration times are adjusted to produce approximately the same irradiance for each out of focus PSF – which is the imaging mode baselined for NGST. The numerical values for a typical data set are given in Figure 2. But typically, for systems that acquire multiple diversity images in parallel, N_p is divided among the total number of channels. As a result, there are limits on the estimation improvement that can be obtained by including an arbitrarily high number of diversity images due to reduced SNR's as discussed in Ref. 11. But for WCT this limitation does not exist since the integration times are adjusted to

approximate a constant irradiance as a discussed above. This method can lead to substantial improvements in estimation performance as more diversity images are added. However, an important disadvantage is that the integration times can be quite long (for WCT on the order of minutes per image), and therefore, optical stability over these long integration times is definitely a concern for large deployable mirror systems such as NGST where thermally induced jitter effects may exist. To minimize stability problems in the Lab, the WCT optical bench rests on a “seismic mass” in addition to being air isolated. The bench is also surrounded by baffles to minimize lab “seeing” effects.

We continue with the CR calculation by generating a series of zero mean Gaussian distributed aberration coefficients from a 12 term Zernike expansion of \mathbf{j}_{aber} (piston and tilt are ignored). The amplitudes are adjusted to produce an aberrated wavefront of approximately 0.13 waves RMS – which is typical for most WCT experiments to date. An additive DM residual of approximately 0.05 waves RMS is then added to produce the final noisy wavefront, $\mathbf{j} = \mathbf{j}_{aber} + \mathbf{j}_{dm}$. For convenience, the additive DM residual is fixed for each aberration realization. The defocused PSF's are then generated from each phase realization and used as input to (18). The resulting Fisher matrices are inverted, traced, and then divided by the number of estimated coefficients for each aberration case. A data point is then recorded as the ensemble average over the entire aberration set. For computational convenience we have found that 30 or so aberration cases give a reasonable sample (see Figure 7). For reference, in Ref. 9, 50 were averaged and in Ref. 10, 2000 aberration cases were generated. To summarize, the lower bounds we consider are averaged lower bounds taken from a statistical sample of Normally distributed random aberrations. The viewpoint adopted here is not to emphasize so much the numerical magnitude of these numerical values, but rather, to investigate and seek trends in the CR minima corresponding to optimal recovery configurations. Therefore, the averaged CRB is the appropriate quantity to consider for this work.

In Figure 7 the average bounds are displayed as a function of diversity defocus for a single defocused image. The Fisher matrix in this example is 12×12 . Similar plots have been discussed in Ref's 8, 9, & 10. Scattered data points correspond to individual aberration realizations generated at a given focus position while the average values at each position are plotted using circles. A minima in the bounds appear at a defocus setting of approximately one quadratic curvature wave of defocus (in peak to valley units) which is consistent with that discussed in earlier work Ref. 8. By including two symmetrically placed diversity images it is apparent that a definite improvement can be made in (potential) estimation accuracy as shown in Figure 8. Including four images results in an order of magnitude improvement. But note that such gains in (potential) estimation performance are due mainly to the available light levels for individual PSF's - which is specific to the NGST imaging mode. As discussed above, in imaging applications where diversity images are acquired simultaneously, the available light must be divided among the total number of diversity images - thus reducing the SNR and therefore the potential estimation performance (Ref. 9).

As the DM residual is added to the system, the recovery of these bumpy phase maps places a greater demand on recovery performance since many more coefficients must be estimated (as evidenced by the Zernike fit in Figure 4). To properly calculate this effect using the CRB's, the Fisher matrix size must increase accordingly. Figure 9 shows a summary of these results - the lower curve corresponds to the 12×12 case. Higher order calculations are shown successively for Fisher array sizes of 190^2 , 231^2 , 300^2 , and 350^2 . For computational convenience, the calculations are presented for a single phase-diverse image. The results illustrate the expected increase in lower bounds as the estimation demand increases and also a decreased sensitivity to focal position. If one assumes for simplicity that the optimal focal position scales linearly with the Fisher array size (the slope is approximately 6×10^{-3} waves / per unit # of Zernike terms), the optimal focal positions can be extrapolated from lower order results to avoid $\approx 10^3 \times 10^3$ Fisher array size calculations. Extrapolating these results to 1000 Zernike terms results in a prediction of about 6 waves at the outer defocus positions. Scaling these results to account for the effect of including four symmetrically placed images results in a prediction of approximately

$$a_{defocus} = \pm 12 \text{ quadratic curvature waves ,} \quad (20)$$

for the outermost images. The deviations from paraxial focus predicted for WCT are thus

$$\mathbf{d}_z = 8\mathbf{I}(f_{\#})^2 a_{defocus} \Big|_{a=(\pm 12, \pm 6) \text{ waves}} \quad (21)$$

$$\Rightarrow [17, 8.5, -8.5, -17] \text{ mm},$$

assuming that $f_{\#} = 16.6$ and $\mathbf{I} = 6328 \text{ \AA}$. For comparison, the current WCT testbed typically collects four diversity images corresponding to ± 18 and ± 9 quadratic curvature waves, respectively, at camera defocus positions, $[25, 12.5, -12.5, -25] \text{ mm}$ (assuming best focus at 0 mm).

5. SUMMARY AND DISCUSSION

In this workshop we have considered an information theoretic analysis of focus diverse phase-retrieval in the imaging mode anticipated for NGST. We have also calculated the bounds including the DM residual. As illustrated by the above results, two interesting effects are apparent as the number of diversity images are increased – the optimal focal positions shift outward as additional diversity images are included, and the bounds are less sensitive to the location of focal positions. The shift in optimal focal position that occurs when going from one to four symmetrically placed images is given approximately by a factor of 2 (i.e., to the ratio of the outer to innermost image positions), and the curve is much flatter with four images compared to two or one. The physical reasoning for this effect is given by noting that the aberration information is coupled in varying amounts to the PSF as a function of diversity defocus. I.e., the low order aberrations are more strongly coupled to the PSF at smaller diversity defocus settings, and therefore averaging this information over a larger range of focus settings (in our case $\times 2$) results in a reduced sensitivity in recovery accuracy as a function of diversity defocus. As a result, the CRB exhibits less “curvature” about the optimal defocus position as illustrated in Figure 8. The latter effect of the defocus position shifting outward by approximately $\times 2$ is a result of a “compromise” between the inner and outer defocus pairs on the recovery.

As the DM residual is added to the system, the recovery of these high frequency phase maps places a greater demand on estimation performance since many more coefficients must be estimated. As a result, the optimal defocus position is pushed outward even further and there is a reduced dependence on recovery accuracy as a function of diversity defocus (i.e., the curve flattens out). The first effect is due to the fact that the higher frequency aberration content is more strongly coupled to the PSF at larger defocus settings - making larger defocus more desirable for high frequency aberration recovery. The secondary effect may be understood by noting that at large defocus settings, the PSF structure changes very little as one perturbs the diversity defocus position, and therefore, one should expect a minimal change in recovery accuracy as the defocus setting is shifted about a large diversity value. This is manifested in the CRB results as a flattening of the curves as a function of defocus.

In conclusion, one consequence of including a DM in the wavefront sensing and control system is that the camera stage must be pushed outward to enhance the high frequency structure in the PSF (sampling notwithstanding – WCT data is undersampled by nearly a factor of two at $\mathbf{I} = 6328 \text{ \AA}$). But as pointed out earlier in Ref 8, there are negative consequences for arbitrarily increasing the diversity defocus value since the MTF develops zeros at higher spatial frequencies resulting in reduced contrast in the measured PSF's. A further analysis of this effect should be considered for the SNR's and aberration cases likely to be encountered for NGST since the available light levels and integration times are expected to be reduced compared to those for the testbed.

For biased algorithm performance, no meaningful comparison can be made to the CRB results. Therefore, we have made no attempt to correlate the CRB numerical values with the estimation performance of the modified Misell-Gerchberg-Saxton algorithm. Before meaningful results can be obtained from such a comparison, careful studies of algorithm bias must be performed, similar to the analysis considered in (26). A study of jitter induced bias for the Misell-Gerchberg-Saxton algorithm was discussed earlier by Roddier (14).

6. ACKNOWLEDGMENTS

We thank Brian Thelen (ERIM) and Tim Schulz (Michigan Technological University) for helpful discussion on the technical content. We also acknowledge many stimulating discussions with Chuck Bowers and Pam Davila. From JPL we thank Dave Redding, Scott Basinger, Andrew Lowman and Fang Shi. From Goddard we thank Bernie Seery, Richard Burg, Mike Fitzmaurice, Todd Norton, Brendon Perkins, Pete Petrone, Ladd Wheeler, Laura Burns, and Mark Wilson.

7. FIGURE CAPTIONS

Figure 1. (a) Simulated Wavefront: Tetrafoil + DM residuals, (b) Exit Pupil Phase Map from the Nexus/WCT Testbed with DM “Print-Through” and Control Noise.

Figure 2. WCT PSF’s (and Pupil) with Artificial Coma Introduced through the Itek Simulator DM.

Figure 3. Comparison of measured PSF data to recovered PSF’s.

Figure 4. Zernike Decomposition of the DM Residual.

Figure 5. (a) Comparison of Measured PSF’s (with arbitrary Coma) to (b) Simulated PSF’s with pure Coma, and then with (c) Pure Coma + DM residuals.

Figure 6. Xinetics DM Before and After Flattening.

Figure 7. Single Image Cramer-Rao Bounds as a Function of Diversity Defocus (12×12 Fisher matrix; Dots are Individual Aberration Realizations; Circles are Averages).

Figure 8. Cramer-Rao Bounds as a Function of Diversity Defocus for 1, 2, and 4 Image Data Sets (circles are averages).

Figure 9. Single Image Cramer-Rao Bounds as a function of Diversity Defocus including DM Residual and for Varying Fisher Array Size.

8. REFERENCES

- 1) P. W. Milonni, *Resource Letter: Adaptive Optics for Astronomy*, Am. J. Phys. 67, 476-485 (1999).
- 2) C. Bowers, P. Davila, B. Dean, B. Perkins, M. Wilson, D. Redding, S. Basinger, D. Cohen, A. Lowman, F. Shi, L. Burns, M. Fitzmaurice, T. Norton, P. Petrone, L. Wheeler, *Initial test results from the Next Generation Space Telescope (NGST) wavefront sensing and control testbed (WCT)*, Proceedings of SPIE Volume 4013: Astronomical Telescopes and Instrumentation, Munich, Germany (2000).
- 3) Harry L. Van Trees, *Detection, Estimation, and Modulation Theory*, New York, Wiley, 1968.
- 4) Anthony D. Whalen, *Detection of Signals in Noise*, New York, Academic Press, 1971.
- 5) Steven M. Kay, *Fundamentals of Statistical Signal Processing*, Englewood Cliffs, N.J., Prentice-Hall, 1993.
- 6) Robert V. Hogg and Allen T. Craig, *Introduction to Mathematical Statistics*, 4th edn., New York, Macmillan, 1978.
- 7) J.N. Cederquist, S.R. Robinson, D. Kryskowski, D., J.R. Fienup, C.C. Wackerman, *Cramer-Rao lower bound on wavefront sensor error*, Opt. Eng., 25, 586-592 (1986).
- 8) J. N. Cederquist, C.C. Wackerman, *Phase-Retrieval Error: A Lower Bound*, J. Opt. Soc. Am. A, 4, 1788-1792 (1987).
- 9) J.N. Cederquist, J.R. Fienup, C.C. Wackerman, S.R. Robinson, D. Kryskowski, *Wavefront estimation from Fourier intensity measurements*, J. Opt. Soc. Am. A, 6, 1020-1026 (1989).
- 10) J.R. Fienup, J.C. Marron, T.J. Schulz, J. H. Seldin, *Hubble Space Telescope characterized by using phase-retrieval algorithms*, Appl. Opt., 32, 1747-1767, 1993.
- 11) J.R. Fienup, B. J. Thelen, R. G. Paxman, D.A. Carrara, *Comparison of Phase Diversity and Curvature Wavefront Sensing*, in Adaptive Optical System Technologies, Proc. SPIE Vol. 3353, 930-940 (1998).
- 12) D. J. Lee, M.C. Roggemann, B.M. Welsh, *Cramer-Rao Analysis of Phase Diverse Wavefront Sensing*, J. Opt. Soc. Am. A, 16, 1005-1015 (1999).
- 13) Wei Sun, *Cramer-Rao Lower Bound Analysis on Estimation Accuracy for Phase Retrieval*, M.S. Thesis, Michigan Technological University, 1998 (Directed by T. Schulz).
- 14) the analysis presented in this paper is based on Cramer-Rao and phase-retrieval software developed for the testbed by B. Dean. The primary software implemented on the WCT Testbed has been developed by Redding, et. al. (Refs. [Error! Bookmark not defined.]).
- 15) R.W. Gerchberg and W.O. Saxton, *A Practical Algorithm for the Determination of Phase from Image and Diffraction Plane Pictures*, OPTIK, Vol. 35, 237-246 (1972).
- 16) W.O. Saxton, *Computer Techniques for Image Processing in Electron Microscopy*, Academic, NY (1978).
- 17) D.L. Misell, *A method for the solution of the phase problem in electron microscopy*, J Phys. D, 6, L6-L9 (1973).
- 18) C. Roddier, F. Roddier, *Reconstruction of Hubble Space Telescope Wavefront Distortion from Stellar Images Taken at Various Focal Positions*, Final Report – JPL Contract 958893 on HST OTA Analysis, May 1991, pp. 2-3.

- 19) J.R. Fienup, J.C. Marron, R. G. Paxman, T.J. Schulz, J. H. Seldin, B. Thelen, *Image Inversion Analysis of the Hubble Space Telescope*, Final Report – JPL Contract 958892 on HST OTA Analysis, August 1991.
- 20) R. G. Lyon, *DCATT Comparative Wavefront Sensing and Optical Control Study - Final Report*, Feb. 22, 1999. <http://jansky.gsfc.nasa.gov/OSCAR/>
- 21) D. Redding, S. Basinger, A. Lowman, Fang Shi, C. Bowers, L. Burns, P. Davila, B. Dean, M. Fitzmaurice, J. Hagopian, C. LeBoeuf, G. Mosier, B. Perkins, P. Petrone, T. Norton, M. Wilson, L. Wheeler *Wavefront Sensing and Control for a next Generation Space Telescope*, Proceedings of SPIE: Space Telescopes and Instruments V, Kona, Hawaii, p. 727 (1998).
- 22) D. Redding, S. Basinger, A. Lowman, Fang Shi, C. Bowers, L. Burns, P. Davila, B. Dean, M. Fitzmaurice, B. Perkins, P. Petrone, T. Norton, M. Wilson, L. Wheeler *Performance of the NGST wavefront control system as tested on DCATT*, NGST Science and Technology Exposition, Not Woods Hole, MA (1999).
- 23) Scott Basinger, D. Redding, A. Lowman, Fang Shi, C. Bowers, L. Burns, P. Davila, B. Dean, M. Fitzmaurice, J. Hagopian, C. LeBoeuf, G. Mosier, B. Perkins, P. Petrone, T. Norton, M. Wilson, L. Wheeler *Controlling the DCATT/NEXCAT hardware*, NGST Science and Technology Exposition, Not Woods Hole, MA (1999).
- 24) D. Redding, S. Basinger, A. Lowman, Fang Shi, C. Bowers, L. Burns, P. Davila, B. Dean, M. Fitzmaurice, G. Mosier, B. Perkins, P. Petrone, T. Norton, M. Wilson, L. Wheeler *Wavefront Control for a deployable space telescope*, Proceedings of SPIE Volume 4013: Astronomical Telescopes and Instrumentation, Munich, Germany (2000).
- 25) S. Basinger, D. Redding, A. Lowman, *Performance of wavefront sensing and control algorithms on a segmented telescope testbed*, Proceedings of SPIE Volume 4013: Astronomical Telescopes and Instrumentation, Munich, Germany (2000).
- 26) Macos Manual, California Institute of Technology, Jet Propulsion Laboratory, copyright 1992-1999.
- 27) Photometrics CCD; <http://www.roperscientific.com/pdfs/datasheets/series300/4200.pdf>
- 28) P. S. Davila, A. Lowman, Mark Wilson, et. al., *Optical Design of the Developmental Cryogenic Active Telescope Testbed*, Proceedings of SPIE: Space Telescopes and Instruments V, Kona, Hawaii, (1998).
- 29) P.S. Davila, R.A. Boucarut, C.W. Bowers, B. H. Dean, M.W. Fitzmaurice, J.G. Hagopian, A.E. Lowman, T.A. Norton, P. Petrone III, D.C. Redding, M.E. Wilson, *Looking at NGST through the eyes of DCATT*, Proceedings of SPIE Volume 4013: Astronomical Telescopes and Instrumentation, Munich, Germany (2000).
- 30) B. Dean, R. Boucarut, *Deformable Mirror Optical Calibration and Test Results*, NGST Science and Technology Exposition, Not Woods Hole, MA (1999).
- 31) B. Perkins B. Dean, *JPL Wavefront Sensing and Control Workshop*, April 2000.
- 32) J. R. Fienup, *Phase Retrieval Algorithms: A Comparison*, Applied Optics, 21, 2758-2769 (1982).
- 33) B. J. Thelen, R. Paxman, D. Carrara, J. Seldin, *Maximum a posteriori estimation of fixed aberrations, dynamic aberrations, and the object from phase-diverse speckle data*, J. Opt. Soc. Am. A, 16, 1016-1025 (1999).
- 34) S. G. Krantz, *Real Analysis and Foundations*, CRC Press, Boca Raton, 1991, p. 254.

- 35) R. Lyon, J. Dorband, J. Hollis, *Hubble Space Telescope Faint Object Camera Calculated Point-Spread Functions*, Applied Optics, 36, 1752-1775, (1997).

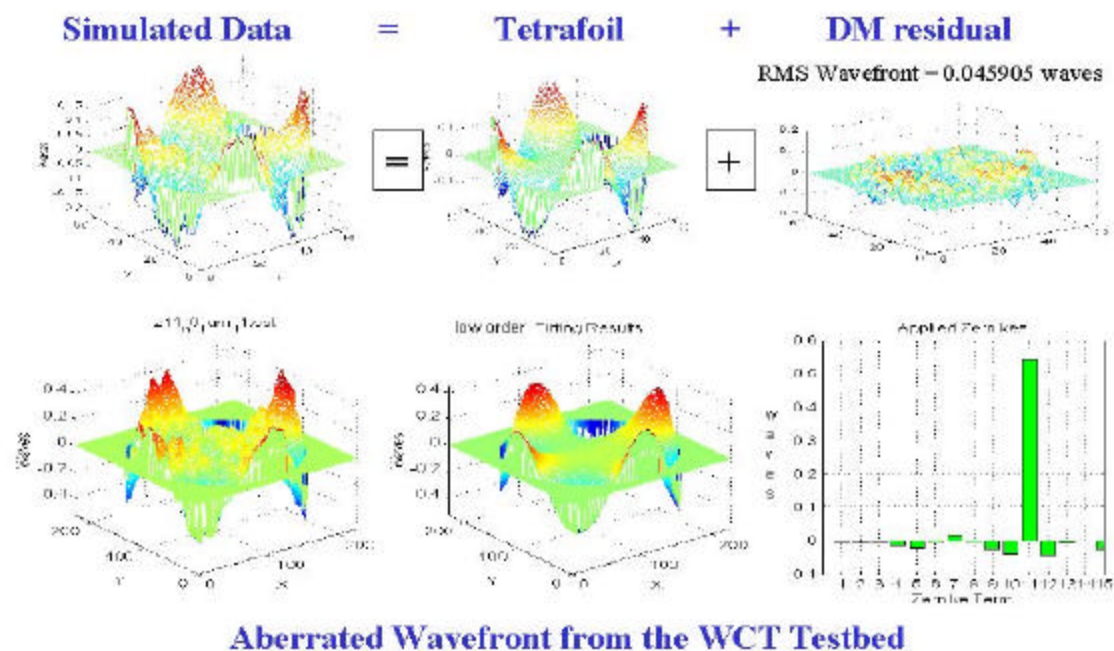


Figure 1. (a) Simulated Wavefront, (b) Exit Pupil Phase Map from the Nexus/WCT Testbed with DM "Print-Through" and Control Noise.

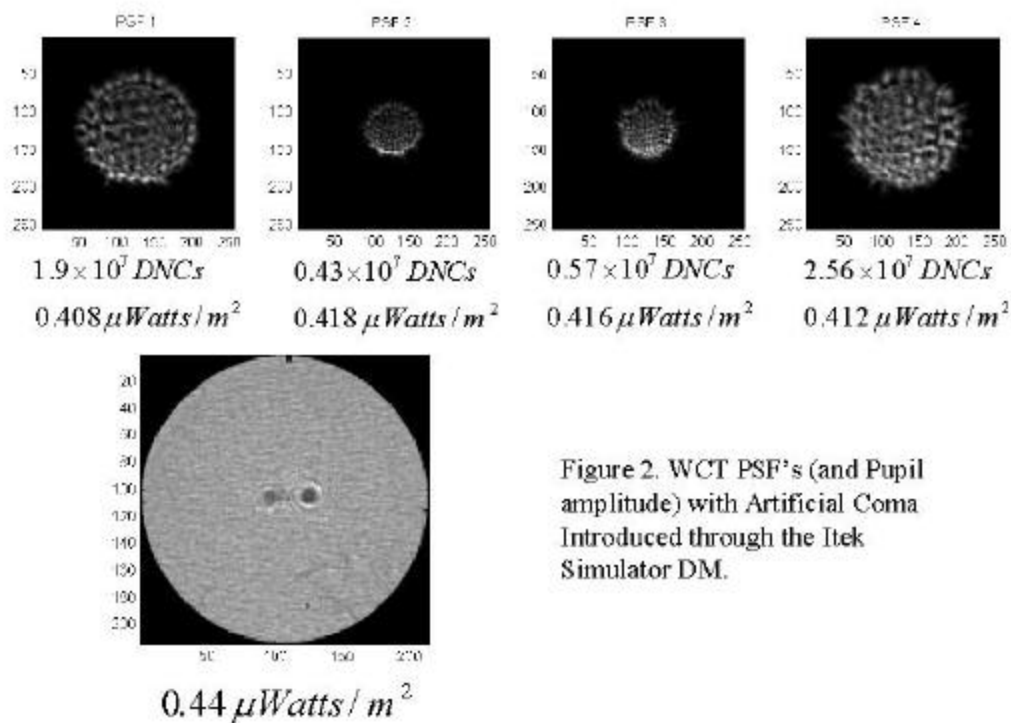


Figure 2. WCT PSF's (and Pupil amplitude) with Artificial Coma Introduced through the Itek Simulator DM.

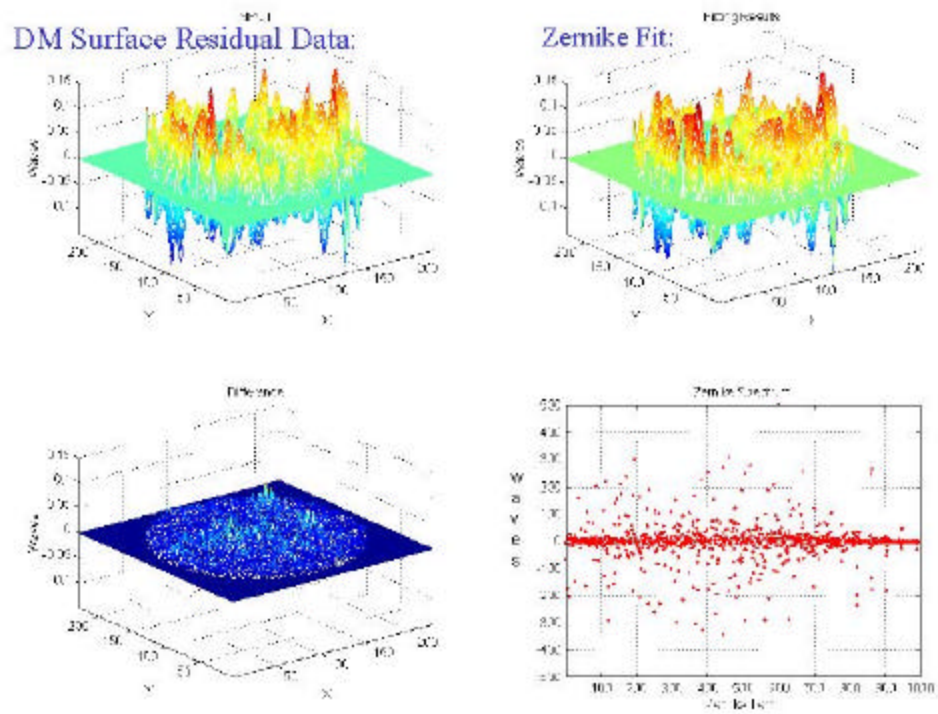
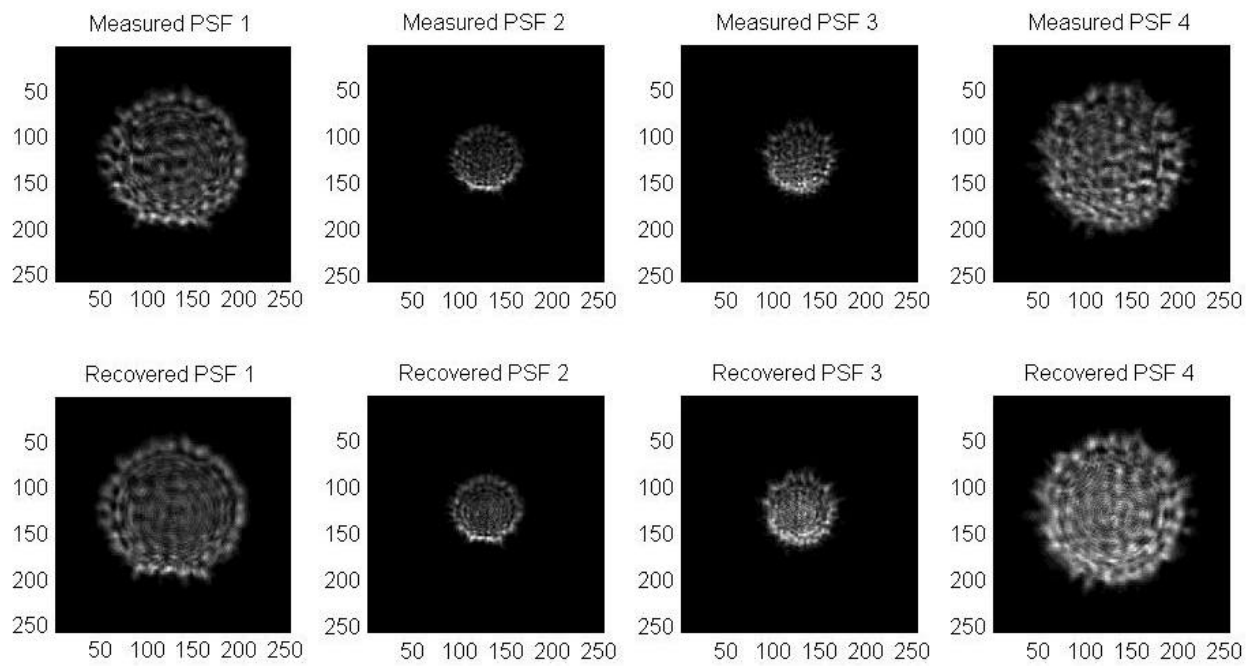


Figure 4. Zernike Decomposition of the DM Residual

DM Residual in the PSF's:

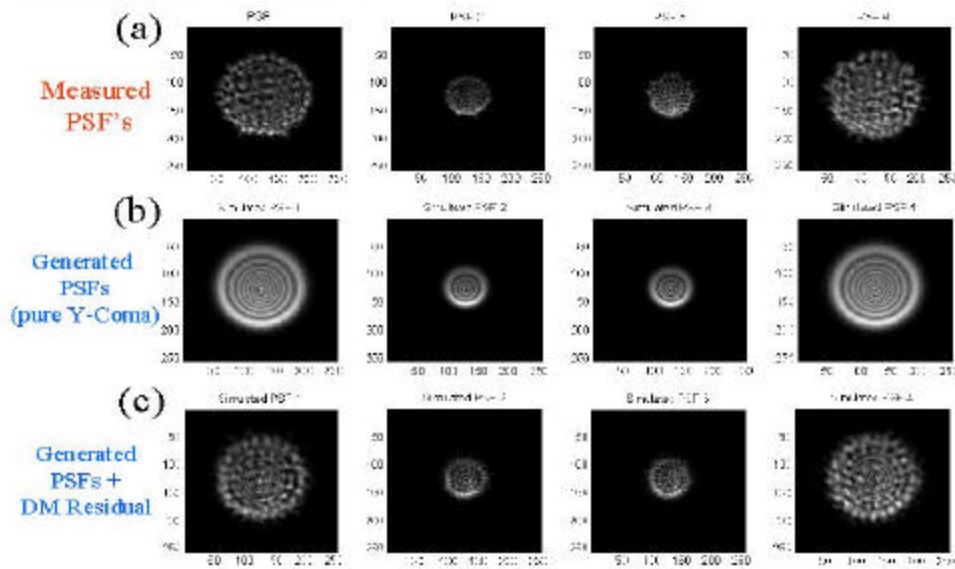


Figure 5. (a) Comparison of Measured PSF's (with arbitrary Coma) to (b) Simulated PSF's with pure Coma, and then with (c) Pure Coma + DM residuals.

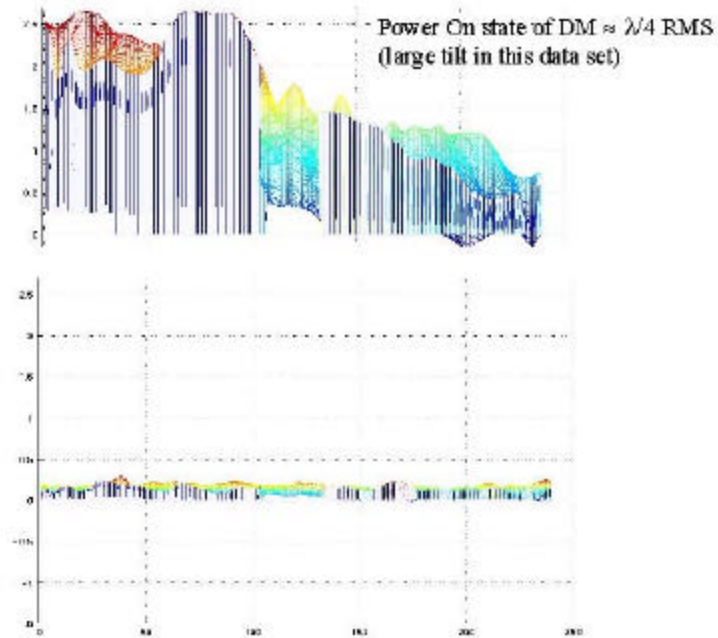


Figure 6. Cross Section of the Kinetics 349 Channel DM Before and After Flattening

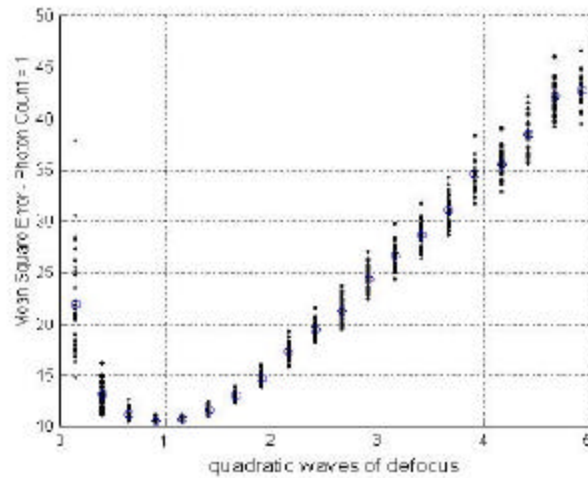


Figure 7. Single Image Cramer-Rao Bounds as a Function of Diversity Defocus (12×12 Fisher matrix; Dots are Individual Aberration Realizations; Circles are Averages).

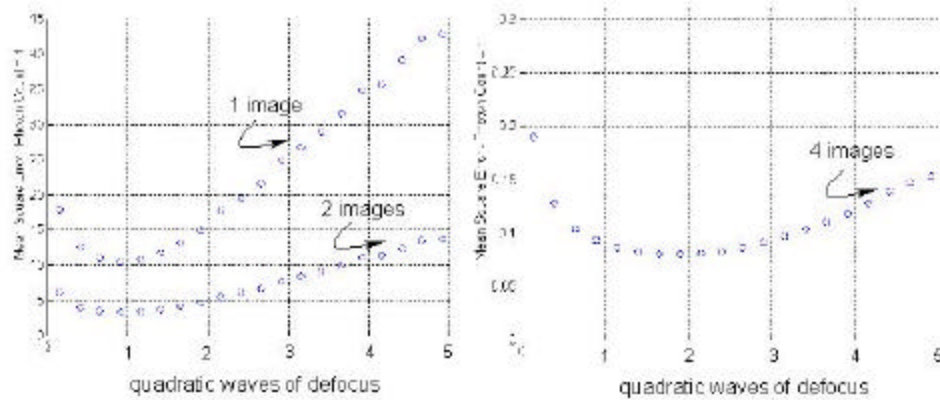


Figure 8. Cramer-Rao Bounds as a Function of Diversity Defocus for 1, 2, and 4 Image Data Sets (Circles are Averages).

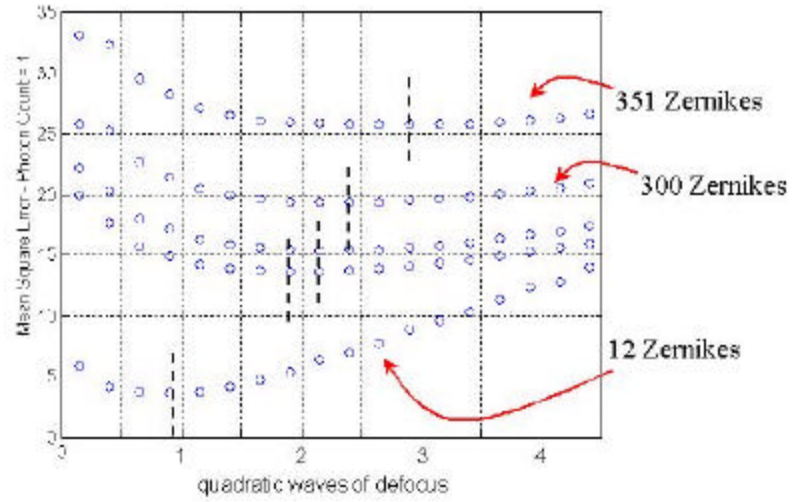


Figure 9. Single Image Cramer-Rao Bounds as a function of Diversity Defocus including DM Residual for Varying Fisher Array Size.

Fast Algorithms for phase diversity and phase retrieval

Russell Luke
Department of Applied Mathematics
Box 352420
University of Washington
Seattle, WA 98195
EMAIL: russell@amath.washington.edu

James V. Burke
Department of Mathematics
University of Washington

and

Richard Lyon
NASA Goddard Space Flight Center
Greenbelt MD 20771

Abstract

In this paper we develop the mathematical foundation of, and numerical solution techniques for the problem of deconvolution and wavefront reconstruction. This problem is fundamentally ill-posed. Following the work of previous investigators, this issue is addressed by solving an approximation problem using regularized least-squares and Fourier transform techniques. We show that steepest descent optimization methods applied to a least-squares objective is equivalent to a specific implementation of an iterative transform algorithm. The convergence properties of the method can be derived from standard results in the optimization literature. Convergence is accelerated by using limited memory techniques with trust-regions. CPU time for the method is reduced by using multi-resolution techniques. Numerical experiments on simulated data suggest that the method is both efficient and robust.

1. Introduction

In this paper we develop numerical methods for the problem of non-parametric deconvolution and wavefront reconstruction. This problem is fundamentally ill-posed. Following the work of previous investigators, this issue is addressed by solving an approximate regularized problem using least-squares and Fourier transform techniques. An algorithmic approach based on limited memory, trust-region, and multiresolution techniques is proposed. The convergence properties of the method can be derived from standard results in the optimization literature. The results of numerical experimentation on simulated data suggest that the method is both efficient and robust. Phase reconstruction and deconvolution problems arise in diverse fields such as microscopy, optical design, crystallography, and astronomy. The physical setting is that of a wave generated from an incoherent, monochromatic, far-field source depicted in figure (1). The wave passes through a diffraction grating and is focused with a thin lens onto an array of receptors that measure intensity in a plane parallel to the diffraction grating. The plane in which the receptors lie is referred to as the image plane and the plane in which the diffraction grating lies is referred

to as the pupil plane. The intensity mapping resulting from a point source is the Green's function or the point spread function of the optical system. What is often referred to as the phase retrieval problem involves recovering the phase of an electromagnetic wave from intensity measurements alone when the source is a point source. If the image plane lies within a certain region relative to the focal point of the lens, to first order (i.e. in the Franco .ER approximation), the intensity mapping is the modulus squared of the Fourier transform of the wavefront on the support of the diffraction grating [14]. In this case, the problem of phase retrieval is one of determining the phase of the wavefront from amplitude measurements in the spatial and Fourier domains. The problem is greatly complicated when the wave source is an unknown extended object rather than a point source. This situation often arises in earth-based optical astronomy where the atmosphere causes aberrations in the wavefront. In this situation one wishes to find both the unknown source and the wavefront aberration *simultaneously*.

Until the 1970's the problem of phase retrieval was thought to be hopeless for a number of reasons. In particular, in one dimension the discrete problem has a multitude of solutions. Indeed there are as many solutions to the problem as there are grid points. To address this problem a number of researchers have proposed the addition of constraints to narrow the number of potential solutions [21,16,24]. In 1972 Gerchberg and Saxton [12] proposed a particularly simple and successful projection algorithm for solving phase retrieval problems in two dimensions, though it's convergence properties are not well understood. In 1981 Hayes [15] showed that the solution to the two dimensional phase retrieval problem, if it exists, is almost surely unique up to rotations and linear shifts. One year later Fienup [11] generalized the Gerchberg-Saxton algorithm and analyzed many of it's convergence properties, showing, in particular, that the directions of the projections in the Gerchberg-Saxton algorithm are similar to directions of steepest descent for a least squares performance measure. We show below that the steepest descent direction is *equivalent* to an averaged, simultaneous projection algorithm. Also in 1982, Gonsalves [13] proposed a stable solution for the more general problem of simultaneous phase reconstruction and deconvolution which involved finding the least squares solution for several *diversity* measurements. The solution to the deconvolution problem over several measurements is the phase diversity solution. Since the introduction of the Gerchberg-Saxton algorithm and phase diversity numerous papers have been published on both of these problems, too many to provide a comprehensive list here. With a few notable exceptions, e.g. [10], all of the methods for solving the wavefront reconstruction and (simultaneous) deconvolution

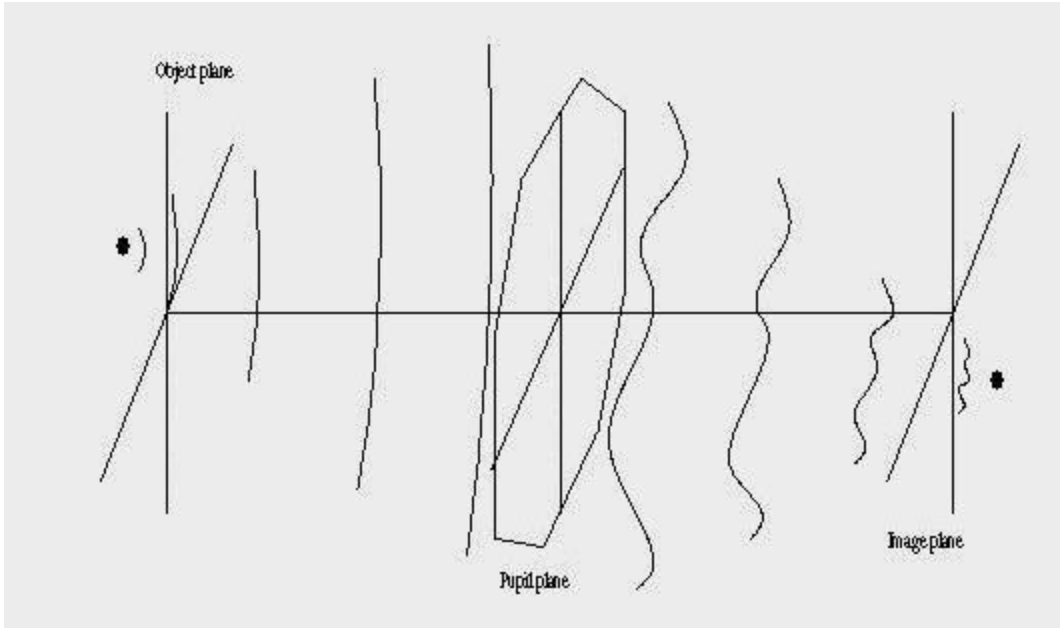


Figure 1: Model optical System

problems have at their core the Gerchberg Saxton algorithm and phase diversity. Showing convergence of these algorithms has proven to be notoriously difficult. In particular, with regard to projection algorithms, the nonconvexity of the underlying sets is a fundamental limitation. What are often referred to as convergence results for projection algorithms are statements that the error between iterations will not increase. To date, mathematical convergence for the nonconvex case with convergence rates has not been shown. In what follows we provide a heuristic foundation for stronger, global convergence results for a class of non-convex projection algorithms. A detailed convergence proof is beyond the scope of this paper, but can be found in [18]. Our main focus is on algorithms and implementation.

In section 2 we derive the mathematical model for diffraction imaging. In the same section we formulate the abstract optimization problem associated with image recovery. To place our algorithm in the context of previous work we detail the specific optimization problem for the least squares performance measure. Other performance measures, however, are possible. Paxman et al [23] have noted that the stochastic model implied by the least squares formulation is not appropriate for all situations. The algorithmic approach we study in this paper is not dependent on the performance measure and therefore can be applied to other statistical models and other performance measures. In Section 3 we detail the limited memory algorithm and the incorporation of trust regions. Section 4 details the performance of the algorithm on simulated data.

2. Mathematical formulation

2.1 Mathematical Model of Diffraction Imaging

What follows is a development of the formalism necessary for a precise discussion of the mathematical model. For ease of exposition we formulate the problem in the continuum leaving discretization until the very end. We represent the wavefront as a complex phasor, fe^{iq} , with amplitude f and phase q . We limit our discussion to ordered pairs $(f, \theta) \in S$ where $S \subset (L^1 \cap L^2)[\mathbb{R}^2, \mathbb{R}] \times (L^1 \cap L^2)[\mathbb{R}^2, \mathbb{R}]$. We denote the source by the function $\varphi : \mathbb{R}^2 \rightarrow \mathbb{R}$ and the image by the function $\psi : \mathbb{R}^2 \rightarrow \mathbb{R}$. For reasons that will

become clear below, we restrict our attention to sources $\varphi \in U \subset (L^1 \cap L^2)(\mathbb{R}^2, \mathbb{R})$. We show that the images therefore belong to $(L^1 \cap L^2)(\mathbb{R}^2, \mathbb{R})$.

The optical system we model includes all of space from the pupil plane to the image plane. In the perfect imaging system of figure (1) we assume that the true wavefront is planar and that any deviations from this are aberrations in the optical system. Perturbations in the wavefront are reflected in the phase term, and may occur at any point along the axis of propagation. To first order, the data recorded in the image plane is a geometric projection along the axis of propagation. Thus the locations of the aberrations along this axis are not important. Accordingly, we consider the phase of the wavefront to be the phase or aberration of the *generalized pupil function* $P : \mathbb{R}^2 \rightarrow \mathbb{C}$, $P(\underline{x}) = f(\underline{x})e^{i\theta(\underline{x})}$, lying in the pupil plane (see figure 1). The support of f describes the geometry of the aperture in the pupil plane, and q describes imperfections in the optics that cause changes in the optical path length. For a thorough treatment of the physics see [4, 14]. A simple example of an aberration is defocus. Defocus is often added to the optical system to stabilize numerical schemes.

The ideal optical system of figure (1) is modeled as a convolution operator. The image ψ resulting from a source φ emitting an incoherent, monochromatic, planar, optical wave is given by a Fredholm integral equation of the first kind:

$$\mathcal{K}[f, \theta]\varphi = \psi. \quad (1)$$

Here $\mathcal{K}[f, \theta]$ is a convolution operator whose kernel, $|\kappa[f, \theta]|^2$, is parameterized by f and θ :

$$\mathcal{K}[f, \theta]\varphi \equiv |\kappa[f, \theta]|^2 * \varphi, \quad (2)$$

where

$$\kappa[f, \theta] = (f e^{i\theta})^\wedge. \quad (3)$$

The kernel of the convolution operator is the *pointspread function* of the optical system. We denote convolution by $*$. The symbols $^\wedge$ and $^\vee$ denote the Fourier transform and its inverse respectively. Since we have limited our discussion to functions on $(L^1 \cap L^2)(\mathbb{R}^2, \mathbb{R})$ we can define the Fourier transform in the usual sense:

$$u^\wedge(\xi) \equiv \int_{\mathbb{R}^n} u(\underline{x}) e^{-2\pi i \underline{x} \cdot \xi} d\underline{x}.$$

The Fourier transform is an isomorphism. Consequently,

$$\kappa \in (L^1 \cap L^2)(\mathbb{R}^2, \mathbb{C})$$

and

$$\mathcal{K} : (L^1 \cap L^2)(\mathbb{R}^2, \mathbb{R}) \rightarrow (L^1 \cap L^2)(\mathbb{R}^2, \mathbb{R}).$$

Thus we require $\psi \in (L^1 \cap L^2)(\mathbb{R}^2, \mathbb{R})$. The problem of recovering φ as well as θ from data ψ and the magnitude of the wavefront, $f = \mathcal{A}$, is an ill-posed inverse problem, linear in φ (deconvolution),

and nonlinear in θ (wavefront reconstruction). Phase retrieval is a specialization of (1) to the case where $\varphi = \delta$, the Dirac delta function.

In phase diversity several data sets, ψ_j , $j = 1, \dots, m$, are collected with the goal of finding the unknown phase common to all. The data sets are called *diversity* images. The diversity images are generated by adding known phase aberrations, ϕ_j , $j = 1, \dots, m$, to the unknown phase aberration on the support of the pupil:

$$|\kappa[(\mathcal{X}f, \theta + \phi_j)]|^2 * \varphi = \psi_j, \quad (4)$$

where the indicator function \mathcal{X} denotes the support of the pupil. We formulate the diversity problem as a system of operator equations

$$\underline{\mathcal{K}}[f, \theta]\varphi = \underline{\psi}, \quad (5)$$

where $\underline{\mathcal{K}}[f, \theta] : (L^1 \cap L^2)[\mathbb{R}^2, \mathbb{R}] \rightarrow (L^1 \cap L^2)^m[\mathbb{R}^2, \mathbb{R}]$ and $\underline{\psi} \in (L^1 \cap L^2)^m[\mathbb{R}^2, \mathbb{R}]$. Here $\underline{\mathcal{K}}[f, \theta]$ is a linear operator parameterized by the functions f and θ , and defined by

$$\begin{aligned} \underline{\mathcal{K}}[f, \theta] &= (\mathcal{K}_1[f, \theta], \dots, \mathcal{K}_m[f, \theta]) \\ &\equiv (\mathcal{K}[(\mathcal{X}f, \theta + \phi_1)], \dots, \mathcal{K}[(\mathcal{X}f, \theta + \phi_m)]). \end{aligned} \quad (6)$$

Thus $\underline{\mathcal{K}}\varphi = (\mathcal{K}_1\varphi, \dots, \mathcal{K}_m\varphi)$. The space $(L^1 \cap L^2)^m[\mathbb{R}^2, \mathbb{R}]$ inherits the usual product space topology.

One must regularize the problem in order to obtain numerical stability since (5) is a Fredholm integral equation of the first kind. We achieve this by perturbing (5) to a “nearby” Fredholm integral equation of the *second* kind. For small $\alpha > 0$,

$$(\underline{\mathcal{K}}[f, \theta] + \alpha \underline{\mathcal{N}}[f, \theta])\varphi = \underline{\psi} \quad (7)$$

where the zero function is the only function contained in the null space of the components of both $\underline{\mathcal{K}}$ and $\underline{\mathcal{N}}$. This is a slightly different way of arriving at some of the more common regularization techniques, among which is the well known Tikhonov regularization. Regularization is a rich topic in and of itself, but we will not touch on it here. For our purposes we require the operator $\underline{\mathcal{N}}$ to be a convolution operator with a real valued kernel satisfying

$$\text{null} [(\underline{\mathcal{K}}[f, \theta] + \alpha \underline{\mathcal{N}}[f, \theta])^* (\underline{\mathcal{K}}[f, \theta] + \alpha \underline{\mathcal{N}}[f, \theta])] = \{0\},$$

where $(\cdot)^*$ denotes the adjoint. The kernel of the j th component of $\underline{\mathcal{N}}$, $\nu_j \in L^1 \cap L^2[\mathbb{R}^2, \mathbb{R}]$, is parameterized by the functions f and θ :

$$\mathcal{N}_j[f, \theta]\varphi = \nu_j[f, \theta] * \varphi.$$

Problem (5) is still ill-posed, even with regularization. We must therefore seek the best object estimate, φ_* , and the best wavefront estimate, $f_* e^{i\theta_*}$, for a given performance measure, ρ :

$$\begin{aligned} (\mathcal{P}) \quad & \text{minimize} \quad \rho[\psi, (\underline{\mathcal{K}}[f, \theta] + \underline{\mathcal{N}}[f, \theta])\varphi] \\ & \text{over} \quad \varphi \in U, (f, \theta) \in S, \end{aligned}$$

where ϕ_j , and ψ_j ($j = 1, 2, \dots, m$) are given and $U \subset (L^1 \cap L^2)[\mathbb{R}^2, \mathbb{R}]$ and $S \subset (L^1 \cap L^2)^2[\mathbb{R}^2, \mathbb{R}]$. If in addition the amplitude f is assumed known, problem (P) is the phase diversity problem.

We diagonalize the system of equations (7) by transforming the equation to its Fourier dual. We define the *Fourier dual* to a functional equation as the Fourier transform of both sides of the equation. For example, by the convolution theorem any convolution operator, \mathcal{G} , with kernel $g \in L^1$, is associated with a dual multiplication operator G , with “kernel” g^\wedge , defined by the Fourier dual to the corresponding operator equation:

$$\mathcal{G}\varphi \equiv g * \varphi = \psi \quad \xleftrightarrow{\mathcal{F}} \quad G\varphi^\wedge \equiv (g^\wedge) (\varphi^\wedge) = \psi^\wedge.$$

Given that $\underline{\mathcal{K}} + \alpha \underline{\mathcal{N}}$ is a convolution operator with real kernel, we can apply the convolution theorem to define a dual operator that is diagonal with a Hermitian kernel. By *Hermitian* we mean a function $u : \mathbb{R}^n \rightarrow \mathbb{C}$ satisfying $u(\underline{x}) = \overline{u(-\underline{x})}$. Equivalently, u is Hermitian if and only if u^\wedge is a real valued function. As we will see below, this will greatly simplify calculations of the gradient of the objective. As a simple example, let $\nu = \delta$, the Dirac delta function, then \mathcal{N} is the identity operator. Alternatively, if we define $\nu = (1 - \mathcal{X}_\Omega)^\vee$, where \mathcal{X}_Ω is the indicator function of the support, Ω , of $[\kappa[f, \theta]]^\wedge$, then $\mathcal{N}[f, \theta]$ is the projection onto the null space of $\mathcal{K}[f, \theta]$.

From equations (2) and (3) it is clear that kernel of the convolution operator \mathcal{K} is the modulus squared of the Fourier transform of the generalized pupil functional, $|\kappa[f, \theta]|^2 = (fe^{i\theta})^\wedge (\overline{fe^{i\theta}})^\wedge$. Using the identity $u^{\wedge\wedge} = u(-\underline{x}) = u^{\vee\vee}$, it is straight forward to verify that, for any complex valued scalar functions $u, v \in L^1 \cap L^2[\mathbb{R}^n, \mathbb{C}]$, one has

$$((u^\wedge) (v^\vee))^\wedge = u \star v, \quad (8)$$

where \star is the correlation operator defined by

$$u \star v(\underline{x}) \equiv \int_{\mathbb{R}^n} u(\underline{x}') v(\underline{x} + \underline{x}') d\underline{x}'. \quad (9)$$

Thus

$$[|\kappa[f, \theta]|^2]^\wedge = (fe^{i\theta}) \star (\overline{fe^{i\theta}}). \quad (10)$$

We denote the Fourier dual of $\underline{\mathcal{K}}$ by \underline{K} where

$$\begin{aligned} \underline{K}[f, \theta]\varphi^\wedge &= \left(\left[(\mathcal{X} f e^{i\theta + \phi_1}) \star (\overline{\mathcal{X} f e^{i\theta + \phi_1}}) \right], \dots, \left[(\mathcal{X} f e^{i\theta + \phi_m}) \star (\overline{\mathcal{X} f e^{i\theta + \phi_m}}) \right] \right) \varphi^\wedge \\ &= \left(\left[(\mathcal{X} f e^{i\theta + \phi_1}) \star (\overline{\mathcal{X} f e^{i\theta + \phi_1}}) \right] \varphi^\wedge, \dots, \left[(\mathcal{X} f e^{i\theta + \phi_m}) \star (\overline{\mathcal{X} f e^{i\theta + \phi_m}}) \right] \varphi^\wedge \right). \end{aligned} \quad (11)$$

Similarly, the Fourier dual to $\underline{\mathcal{N}}$ is a multiplication operator denoted by \underline{N} with

$$\underline{N}[f, \theta]\varphi^\wedge = ((\nu_1[\mathcal{X} f, \theta + \phi_1])^\wedge, \dots, (\nu_1[\mathcal{X} f, \theta + \phi_m])^\wedge) \varphi^\wedge.$$

We can thus write the Fourier dual of (7) as

$$(\underline{K} + \alpha \underline{N}) \varphi^\wedge = \underline{\psi}^\wedge. \quad (12)$$

The diagonalization of the convolution operator is a crucial property for numerical solutions and the reason for choosing \mathcal{N} to be a convolution operator. Note also that the kernel of $\underline{K} + \alpha \underline{N}$ is Hermetian.

Using the Fourier dual representation we can also write the pointspread function as a quadratic in the dual function $\tilde{f} \in S^\wedge \subset (L^1 \cap L^2)[\mathbb{R}^2, \mathbb{R}]$ where $\tilde{f}e^{i\tilde{\theta}}$ is the Fourier dual of the wavefront $f e^{i\theta}$:

$$|\kappa|^2 = \tilde{f}^2. \quad (13)$$

It is useful to interpret the functions $\tilde{f}e^{i\tilde{\theta}}$ in terms of wave propagation. In geometric optics $\tilde{f}e^{i\tilde{\theta}}$ represents the distribution of *ray* components, *i.e.* the directions of propagation, of the wave $f e^{i\theta}$. In studies of wave propagation in which the Wigner distribution plays a role, the domain of interest is the product space including the physical domain and the frequency domain. The wavefront exists in the physical domain and the distribution of rays exists in the frequency domain. This product space is called *phase space*. Analogously we can formulate problem (\mathcal{P}) in phase-space,

$$\begin{aligned} (\mathcal{P}') \quad & \text{minimize} \quad \rho \left[\psi, \underline{\mathcal{K}}[f, \theta] \varphi, \tilde{\mathcal{K}}[\tilde{f}, \tilde{\theta}] \varphi \right] \\ & \text{subject to} \quad (f e^{i\theta})^\wedge = \tilde{f} e^{i\tilde{\theta}} \\ & \quad (f, \theta) \in S, \quad (\tilde{f}, \tilde{\theta}) \in S^\wedge \\ & \quad \varphi \in U \end{aligned}$$

Here $\tilde{\mathcal{K}}[\tilde{f}, \tilde{\theta}] : (L^1 \cap L^2)[\mathbb{R}^2, \mathbb{R}] \rightarrow (L^1 \cap L^2)^m[\mathbb{R}^2, \mathbb{R}]$ is a convolution operator defined by

$$\tilde{\mathcal{K}}[\tilde{f}, \tilde{\theta}] \varphi = \left(\left| \left[\mathcal{X} e^{i\phi_1} (\tilde{f} e^{i\tilde{\theta}})^\vee \right]^\wedge \right|^2 * \varphi, \dots, \left| \left[\mathcal{X} e^{i\phi_m} (\tilde{f} e^{i\tilde{\theta}})^\vee \right]^\wedge \right|^2 * \varphi \right). \quad (14)$$

For a general review of this theory see [1, 2].

2.2 Least Squares Minimization

The system of equations (7) is linear in φ and nonlinear in (f, θ) . This structure allows us to split the corresponding optimization problem using a Benders decomposition [3]. Benders decompositions are common techniques for splitting large-scale optimization problems such as (\mathcal{P}) into smaller problems which can be solved independently of one another in sequence. The least squares performance measure admits a particularly simple way to split the problem. This was first recognized by Gonsalves [13] and later generalized by Paxman *et al* [23].

A common assumption in adaptive optics is that the amplitude of the wavefront across the support of the pupil is constant with unit magnitude. We add this constraint as a penalty in the objective function. Using the least squares performance measure, the problem (\mathcal{P}) becomes

$$\begin{aligned} (\mathcal{P}_{LS}) \quad & \text{minimize} \quad J_{LS} = \frac{1}{2} \|(\underline{\mathcal{K}}[f, \theta] + \alpha \underline{\mathcal{N}}[f, \theta]) \varphi - \underline{\psi}\|^2 + \frac{1}{2} \|f^2 - \mathcal{X}^2\|^2 \\ & \text{over} \quad \varphi \in U, \quad (f, \theta) \in S, \end{aligned}$$

Benders decomposition involves first obtaining φ_* by optimizing over φ for fixed f and θ . Next we optimize over f and θ holding φ_* fixed. The process is repeated until the iterates exceed some tolerance. Let $(\mathcal{P}_{LS})_{(f, \theta)}$ denote the least squares problem (\mathcal{P}) with (f, θ) fixed. For the least

squares performance measure, the optimal solution φ_* to $(\mathcal{P}_{LS})_{(f,\theta)}$ can be written in closed form. We obtain this by considering the Fourier dual to $(\mathcal{P}_{LS})_{(f,\theta)}$

$$\begin{aligned} (\mathcal{P}_{\widehat{LS}})_{(f,\theta)} \quad & \text{minimize} \quad J_{LS}^\wedge = \frac{1}{2} \|(\underline{K}[f, \theta] + \alpha \underline{N}[f, \theta]) \varphi^\wedge - \underline{\psi}^\wedge\|^2 + \frac{1}{2} \|f^2 - \mathcal{X}^2\|^2. \\ & \text{over} \quad \varphi^\wedge \in U \end{aligned}$$

Assume that \mathcal{N} has been chosen so that it's Fourier dual satisfies

$$\text{null}[(\underline{K}[f, \theta] + \underline{N}[f, \theta])^* (\underline{K}[f, \theta] + \underline{N}[f, \theta])] = \{0\}.$$

The optimal dual object estimate, denoted φ_*^\wedge , is the solution to the normal equations:

$$\varphi_*^\wedge = [(\underline{K} + \alpha \underline{N})^* (\underline{K} + \alpha \underline{N})]^{-1} (\underline{K} + \alpha \underline{N})^* \underline{\psi}^\wedge, \quad (15)$$

By Parseval's relation the optimal values of $(\mathcal{P}_{\widehat{LS}})_{(f,\theta)}$ and $(\mathcal{P}_{LS})_{(f,\theta)}$ are equivalent. The optimal solution to (\mathcal{P}_{LS}) is thus $\varphi_* \equiv [\varphi_*^\wedge]^\vee$. The first step of Benders decomposition can therefore be executed implicitly by substituting $[\varphi_*^\wedge]^\vee$ directly into (\mathcal{P}_{LS}) and optimizing over f and θ alone. Expression (15) is a generalized Wiener filter for diffraction limited systems. The regularization reflects the diffraction limits of the optical system.

If J_{LS} is Fréchet differentiable and the feasible set $U \cap S$ is nonempty and compact then a solution to (\mathcal{P}_{LS}) exists. The analytic properties of the objective are detailed in a forthcoming paper [19]. For our purposes we assume that a solution exists and that the objective is uniformly differentiable with uniformly continuous derivative.

2.3 Phase Retrieval

Projection algorithms, among which are iterative transform methods, are central to current numerical techniques for solving the phase retrieval problem [5, 8, 11, 12, 17, 20, 29, 28]. In this section we derive the minimization problem that these projection algorithms attempt to solve. Before we do this, however, we show the relationship between the phase retrieval problem as it is commonly posed and (\mathcal{P}_{LS}) .

When $\varphi = \delta$, the Dirac delta function, the objective J_{LS} in (\mathcal{P}_{LS}) , minus the magnitude constraint, simplifies to

$$\frac{1}{2} \|(\underline{K}[f, \theta] + \alpha \underline{N}[f, \theta]) \delta - \underline{\psi}\|^2 = \frac{1}{2} \sum_{j=1}^m \left\| |\kappa_j|^2 + \alpha \nu_j - \psi_j \right\|^2.$$

Here $\kappa_j = \kappa[\mathcal{X}f, \theta + \phi_j]$. Regularization of the linear convolution problem is no longer necessary, so we take $\alpha = 0$. It has been noted, however, that the linearized least squares phase retrieval problem is in some sense still ill-posed. To address this a Tikhonov regularization strategy has been suggested. The regularization is critical to theoretical convergence results, though its effect on numerical performance is not always crucial. For details see [10].

The norm squared and modulus squared make the objective effectively a quartic in the unknowns which will tend to flatten out the objective and slow convergence. We therefore consider the following quadratic objective

$$\tilde{J} = \frac{1}{2} \sum_{j=1}^m \left\| |\kappa_j| - \psi_j^{1/2} \right\|^2. \quad (16)$$

We know ahead of time that the data ψ is non-negative, so the square root is not problematic. Adding to \tilde{J} a quadratic constraint on the amplitude yields the sum of set distance errors:

$$J_{sde} = \frac{1}{2} \sum_{j=1}^m \left\| |\kappa_j| - \psi_j^{1/2} \right\|^2 + \frac{1}{2} \|f - \mathcal{X}\|^2. \quad (17)$$

The phase retrieval problem is posed as finding the minimum of the set distance error J_{sde} :

$$\begin{aligned} (\mathcal{P}_{sde}) \quad & \text{minimize} \quad J_{sde}[f, \theta] \\ & \text{over} \quad (f, \theta) \in S. \end{aligned}$$

The objective J_{sde} is not differentiable in the usual sense. What is needed is a less restrictive notion of differentiation. Variational analysis [25] provides just such tools, however this is beyond the scope of this paper. For our purposes it suffices to perturb the problem (\mathcal{P}_{sde}) to a nearby optimization problem with an objective function which is differentiable. The gradient is well defined for the perturbed objective function J_{sde}^ϵ :

$$J_{sde}^\epsilon = \frac{1}{2} \sum_{j=1}^m \left\| \frac{|\kappa_j|^2}{|\kappa_j| + \epsilon} - \psi_j^{1/2} \right\|^2 + \frac{1}{2} \left\| \frac{f^2}{f + \epsilon} - \mathcal{X} \right\|^2. \quad (18)$$

We solve the optimization problem

$$\begin{aligned} (\mathcal{P}_{sde}^\epsilon) \quad & \text{minimize} \quad J_{sde}^\epsilon[f, \theta] \\ & \text{over} \quad (f, \theta) \in S. \end{aligned}$$

As with the regularization suggested in [10], while the regularization above is necessary for theoretical purposes it does not have dramatic numerical effect.

3 Numerical Methods

3.1 Limited Memory BFGS with Trust regions

In this section we briefly review limited memory techniques with trust regions for solving the equation $\nabla J[f_*, \theta_*] = 0$. An optimal solution (f_*, θ_*) to (\mathcal{P}'_{LS}) or (\mathcal{P}_{sde}) , if it exists, will satisfy $\nabla J[f_*, \theta_*] = 0$. The objective functions J_{LS} and J_{sde}^ϵ are not convex in f and θ . Therefore all that can be said of the point (f_*, θ_*) is that it is a critical point. This is fundamental to the theory of optimization and is covered at length in [18]. For the purposes of this paper we will be satisfied with solving the equation $\nabla J[f, \theta] = 0$, recognizing, however, that the solution to this equation is not necessarily a solution to the corresponding optimization problem.

The method we propose uses as much information about the objective function as possible while preserving the non-parametric nature of the formulation. Newton's method is an efficient iterative algorithm for solving equations and is based on the first two terms of the Taylor series expansion. For ∇J this can be written formally as

$$\nabla J[(f, \theta) + \underline{d}] \approx \nabla J[f, \theta](\underline{d}) + \nabla^2 J[f, \theta](\underline{d}, \underline{d}). \quad (19)$$

Near a solution Newton iterates converge quadratically, *i.e.* if at step i the value of the function is 10^{-2} , the value of the function at the next iterate will be 10^{-4} ; the following iterate will yield a function value of 10^{-8} and so forth. The Hessian, $\nabla^2 J[f, \theta; \underline{d}]$, of a function $J : \mathbb{R}^n \rightarrow \mathbb{R}$ is an $n \times n$ matrix; thus for large systems it is not feasible to represent the Hessian explicitly in a computer. The approach we follow involves a discretization in terms of pixels. A 512×512 image, for example, yields an optimization problem with 2^{10} variables (recall that we treat *both* the phase θ and amplitude f as unknowns so we have 2×2^9 unknowns). The corresponding Hessian, assuming it exists, is a $2^{10} \times 2^{10}$ matrix. Limited memory methods provide an efficient way to use approximate Hessian information without explicitly forming the matrix. These techniques are derived from quasi-Newton, or matrix secant methods. Quasi-Newton methods are two step quadratic methods that approximate the Hessian by divided differences of the gradients. Newton and Newton-like methods, however, cannot be expected to converge for starting guesses far from the solution or when the curvature is nearly zero. These methods are made robust with the introduction of trust regions. For a thorough treatment of matrix secant and trust region methods see [9].

We denote the discretized unknown functions (f, θ) by $u \in \mathbb{R}^n$. Matrix secant iterates are generated by

$$u_{k+1} = u_k - (\lambda_k M_k)^{-1} \nabla J(u_k) \quad (20)$$

where $\lambda_k \in \mathbb{R}$ is a scaling factor for the step length and $M_k \in \mathbb{R}^{n \times n}$ is an approximation to $\nabla^2 J[f, \theta; \underline{d}]$ satisfying the quasi-Newton equation:

$$M_k(u_{k-1} - u_k) = \nabla J(u_{k-1}) - \nabla J(u_k). \quad (21)$$

Equation (21) is a system of n equations in n^2 unknowns, thus infinitely many solutions are possible. Broyden's update, symmetric rank one (SR1) matrices, and the Broyden-Fletcher-Goldfarb-Shanno (BFGS) update are common choices for the matrix secant M_k . The BFGS update has been shown empirically to be superior in many cases. We will review the limited memory techniques for BFGS matrices, however similar methods for alternative updates are possible.

The BFGS approximation to the true Hessian is given by

$$M_k = M_{k-1} + \frac{y_k y_k^T}{y_k^T s_k} - \frac{M_{k-1} s_k s_k^T M_{k-1}}{s_k^T M_{k-1} s_k}, \quad k = 1, 2, \dots \quad (22)$$

where

$$y_k \equiv \nabla J(u_{k+1}) - \nabla J(u_k), \quad s_k \equiv u_{k+1} - u_k.$$

The BFGS approximation is symmetric positive definite as long as $s_k^T y_k > 0$.

In [7] Byrd *et al* derive compact representations of the BFGS approximation. Just as with conjugate gradients, these representations allow one to compute the product $M_k^{-1} \nabla J(u_k)$ without actually forming the matrix M_k^{-1} . Let $S_k \equiv [s_{k-m}, \dots, s_{k-1}] \in \mathbb{R}^{n \times m}$ denote a matrix of steps from previous iterations. Similarly we store previous gradient differences, $Y_k \equiv [y_{k-m}, \dots, y_{k-1}] \in \mathbb{R}^{n \times m}$. Limited memory techniques amount to generating *at each iteration* the BFGS matrix from the m most recent of the pairs $\{y_i, s_i\}_{i=1}^{k-1}$ and the generating matrix $M_k^{(0)}$. Typically $m \in [5, 10]$. The choice of $M_k^{(0)}$ that is often used is $M_k^{(0)} = \lambda_k I$ where I is the identity matrix and λ_k is some scaling (see [26]). With this generating matrix limited memory BFGS is equivalent to doing m steps of

conjugate gradients at each iteration. Using limited memory BFGS, denoted L-BFGS, it can be shown that the complexity of calculating (20) is on the order of $mn + m^3$. See [7] for details.

Before accepting the step to the next iterate one usually checks the accuracy of the quadratic approximation

$$\tilde{J}(u_{k+1}) = J(u_k) + \nabla J(u_k)^T \cdot s_k + \frac{1}{2} s_k^T M_k s_k \quad (23)$$

against the true function value $J(u_{k+1})$. Usually what is computed is the ratio of the actual change in the function value between iterates u_k and u_{k+1} and the predicted change, *i.e.*

$$r(s_k) = \frac{\text{predicted change}_k}{\text{actual change}_k}. \quad (24)$$

If the ratio is below some tolerance, the quadratic model is constrained by a *trust region*, *i.e.* a ball around the current iterate u_k that contains the largest “trustworthy” step length to the next iterate given the unreliable quadratic model. The trust region subproblem with trust region radius Δ is given by

$$\begin{aligned} TR(\Delta) \quad & \text{minimize} \quad \nabla J(u_k)^T s + \frac{1}{2} s^T M_k s. \\ & \|s\| \leq \Delta \end{aligned}$$

The Lagrangian of $TR(\Delta)$ yields the following unconstrained, *implicit* trust region subproblem

$$\begin{aligned} TR'(\mu) \quad & \text{minimize} \quad \nabla J(u_k)^T s + \frac{1}{2} s^T (M_k + \mu I) s. \\ & s \in \mathbb{R}^n \end{aligned}$$

A solution, $s_*(\mu)$, to $TR'(\mu)$ corresponds to a solution to $TR(\Delta)$ with $\Delta = \|s_*(\mu)\|$. The larger μ the smaller the trust region radius Δ .

In [6] Burke and Wiegmann derive a compact representation of the inverse of the matrix $\mu I + M_k$ for solving the trust region subproblem. This inverse can be computed with the same computational complexity as the computation of M_k^{-1} . The basic assumption of the trust region step is that the step s_k is at least as effective as the step obtained by moving in the direction of steepest descent. Thus the strategy is “global” in the sense that far from the solution the method will perform at least as well as gradient descent while near a solution the second order information will accelerate convergence.

3.2 Algorithms and Implementation

As noted in [6], for the proper scaling, λ_k , the trust region is required only a small fraction of the time. This scaling is key to the success of the algorithm. There are many definitions for the optimal scaling λ_k [22]. We follow the scaling suggested by Shanno and Phua [26]

$$\lambda_k = \frac{y_{k-1}^T y_{k-1}}{s_{k-1}^T y_{k-1}}. \quad (25)$$

In our implementations we default to the unconstrained L-BFGS method, *i.e.* by default $\mu = 0$ in $TR'(\mu)$ at the beginning of each iteration. The trust region is invoked only if the ratio $r(s_k)$ falls below a given tolerance, indicating that the quadratic model (23) is not reliable, *i.e.* $r(s_k) < \text{tol}_{TR}$.

Numerical experiments indicate, however, that when a step does not give sufficient decrease in the objective value, or even causes an *increase* in the objective, it is worthwhile to keep that step direction and use it to update the L-BFGS matrix, even though the step is not taken. The rational behind this is that bad steps still contain curvature information that is useful in approximations to the Hessian of the objective.

Algorithm 3.1 (Limited Memory Trust Region BFGS) For $k \geq 1$, given the vectors $u_{k-1} \in \mathbb{R}^n$, $\nabla J(u_{k-1})$, the scalars $J(u_{k-1})$, $\|\nabla J(u_{k-1})\|_2^2$, $\bar{m} \in \{1, 2, \dots, n\}$, and the tolerance tol_{MS} :

0. Set $S_{k-2} = Y_{k-2} = [\]$, the empty matrix, and $m = 0$. Use some line search method (e.g. line search with backtracking) to find a direction of descent to the point u_k . Calculate the vectors s_{k-1} , y_{k-1} , $\nabla J(u_k)$, and the scalar $\|\nabla J(u_k)\|_2^2$.
1. If $s_{k-1}^T y_{k-1} \leq 0$, goto step 0.; otherwise set $m = \min\{m + 1, \bar{m}\}$, $\lambda_k = y_{k-1}^T y_{k-1} / (s_{k-1}^T y_{k-1})$ and update S_{k-1} , Y_{k-1} , $Y_{k-1}^T Y_{k-1}$, and $S_{k-1}^T Y_{k-1}$ (see algorithm 3.1 of [7]).
2. If $r(s_k) < tol_{TR}$ restrict trust region Δ and solve the trust region subproblem (see [6]); otherwise calculate $\nabla J(u_{k+1})$, $\|\nabla J(u_{k+1})\|_2^2$, and update S_k , Y_k and the limited matrix BFGS matrix (see [7]).
3. If $\|\nabla J(u_{k+1})\|_2^2 < tol_{MS}$, end; otherwise calculate the actual change, the predicted change, $r(s_k)$ via (24), set $k = k + 1$ and return to 1.

3.3 Gradients

In the appendix we outline the derivation for the formal derivative of J_{LS} in the direction $\underline{d} = (\delta f, \delta \theta, \delta \varphi)$. For a regularization operator \mathcal{N} that is independent of (f, θ) we have:

$$\nabla J_{LS}[f, \theta, \varphi](\underline{d}) = \left\langle \underline{d}, 2Re \left[\sum_{j=1}^m \underline{g}_j \right] \right\rangle + \left\langle \underline{d}, 2f \cdot r_{\mathcal{X}} \begin{pmatrix} 1 \\ 0 \end{pmatrix} \right\rangle \quad (26)$$

where

$$\underline{g}_j = \left(\mathcal{X} e^{-i(\theta+\phi_j)} \left[(\varphi^\vee r_j^\wedge) \star (\mathcal{X} f e^{i(\theta+\phi_j)}) \right], -i \mathcal{X} f e^{-i(\theta+\phi_j)} \left[(\varphi^\vee r_j^\wedge) \star (\mathcal{X} f e^{i(\theta+\phi_j)}) \right], \frac{1}{2} \tilde{\kappa}_j \star r_j \right) \quad (27)$$

and

$$r_j \equiv (|\kappa_j|^2 + \alpha \mathcal{N}) \star \varphi - \psi_j, \quad r_{\mathcal{X}} \equiv f^2 - \mathcal{X}, \quad \tilde{\kappa}_j = |\kappa_j|^2 + \alpha \mathcal{N}. \quad (28)$$

Solving for φ in terms of f and θ via (15), the directional derivative $\nabla J_{LS}[f, \theta](\underline{d})$ for $\underline{d} = (\delta f, \delta \theta)$ takes the form

$$\nabla J_{LS}[f, \theta](\underline{d}) = \left\langle \underline{d}, 2Re \left[\sum_{j=1}^m \tilde{g}_j \right] \right\rangle + \left\langle \underline{d}, 2f \cdot r_{\mathcal{X}} \begin{pmatrix} 1 \\ 0 \end{pmatrix} \right\rangle \quad (29)$$

where

$$\tilde{g}_j \equiv \mathcal{X} e^{-i(\phi_j + \theta)} \left[(\varphi_*^\vee r_j^\wedge) \star (\mathcal{X} f e^{i(\theta + \phi_j)}) \right] \begin{pmatrix} 1 \\ -if \end{pmatrix}. \quad (30)$$

A Cartesian representation of the wavefront yields a simpler expression than (30). Let $w + iz = f e^{i\theta}$. The directional derivative of J_{LS} with respect to w and z is

$$\begin{aligned} \nabla J_{LS}[w, z](\underline{d}) &= \left\langle \underline{d}, 2\text{Re} \left[\sum_{j=1}^m \mathcal{X} e^{-i\phi_j} \left[(\varphi_*^\vee r_j^\wedge) \star (\mathcal{X} e^{i\phi_j}(w + iz)) \right] \begin{pmatrix} 1 \\ -i \end{pmatrix} \right] \right\rangle \\ &\quad + \left\langle \underline{d}, 2\text{Re} \left[(w + iz) \cdot r_{\mathcal{X}} \begin{pmatrix} 1 \\ -i \end{pmatrix} \right] \right\rangle. \end{aligned} \quad (31)$$

Note that the components of the gradient with respect to w and z are the real and imaginary parts of

$$2 \sum_{j=1}^m \mathcal{X} e^{-i\phi_j} \left[(\varphi_*^\vee r_j^\wedge) \star (\mathcal{X} e^{i\phi_j}(w + iz)) \right] + 2(w + iz) \cdot r_{\mathcal{X}}$$

respectively. Expression (31) is more efficient to calculate and does not suffer from 2π ambiguities in the phase.

The gradient of the set distance error objective J_{sde}^ϵ , also derived in the appendix, is formally

$$\begin{aligned} \nabla J_{sde}^\epsilon[f, \theta](\underline{d}) &= \left\langle \underline{d}, \text{Re} \left[\sum_{j=1}^m \mathcal{X} e^{-i(\theta + \phi_j)} \left[\left(\frac{|\kappa_j| + 2\epsilon}{(|\kappa_j| + \epsilon)^2} \right) \kappa_j \cdot r_j \right]^\vee \begin{pmatrix} 1 \\ -if \end{pmatrix} \right] \right\rangle \\ &\quad + \left\langle \underline{d}, \left(\frac{f + 2\epsilon}{(f + \epsilon)^2} \right) f \cdot r_{\mathcal{X}} \begin{pmatrix} 1 \\ 0 \end{pmatrix} \right\rangle. \end{aligned} \quad (32)$$

where $r_j = \frac{|\kappa_j|^2}{|\kappa_j| + \epsilon} - \psi^{1/2}$ and $r_{\mathcal{X}} = \frac{f^2}{f + \epsilon} - \mathcal{X}$. In the limit as $\epsilon \rightarrow 0$ this expression formally becomes

$$\nabla J_{sde}[f, \theta](\underline{d}) = \left\langle \underline{d}, \text{Re} \left[\sum_{j=1}^m \mathcal{X} e^{-i(\theta + \phi_j)} \left[\frac{\kappa_j}{|\kappa_j|} r_j \right]^\vee \begin{pmatrix} 1 \\ -if \end{pmatrix} \right] + r_{\mathcal{X}} \begin{pmatrix} 1 \\ 0 \end{pmatrix} \right\rangle. \quad (33)$$

Note that if $\kappa_j(\underline{x}) > 0$ for all \underline{x} , then (33) is simply the sum of the *simultaneous* projections onto all the magnitude constraints. Thus, at least heuristically, a gradient descent method for this objective can be viewed as a particular case of a projection method. Convergence results for projection methods applied to this problem do not exist since the problem is non-convex. Convergence results for gradient descent algorithms, however, can be derived from standard results in the optimization literature.

4 Results

In this section we report the performance of the algorithm described in section (3.2) on simulated data. We discretize the functions above into a pixel basis. Thus for a 512×512 image the

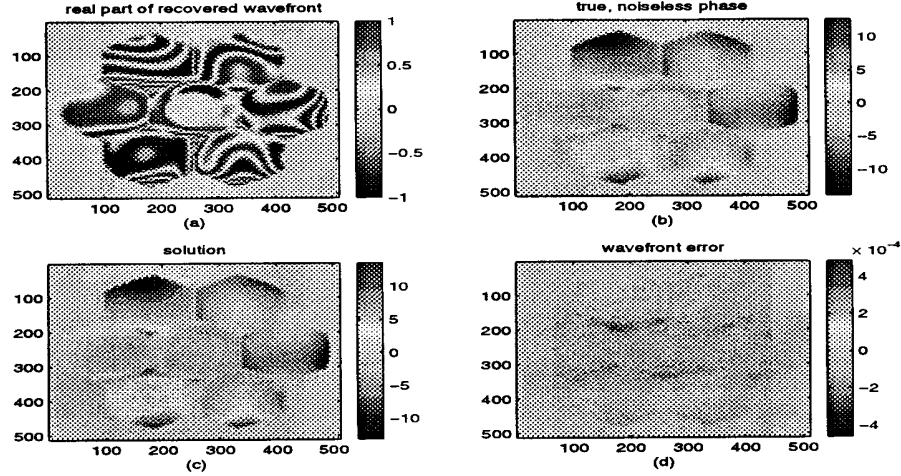


Figure 2: Seven paneled, segmented aperture with phase aberrations.

optimization problem (\mathcal{P}_{LS}) involves 786432 variables. In all simulations we used little or no regularization. We begin with the simplest problem, phase retrieval.

The first example shows the performance of the limited memory algorithm with the objective J_{sde}^ϵ against a common iterative transform algorithm called the Misell algorithm [5, 20]. The Misell algorithm projects between several diversity images in a sequential manner. The same information, two out of focus images and one in focus image, is available to the Misell algorithm that is available to the limited memory algorithm. We take the parameter ϵ in J_{sde}^ϵ to be machine precision, 10^{-16} . With this small regularization, a steepest descent algorithm applied to J_{sde}^ϵ is practically the same as a simultaneous, weighted projection algorithm. Given the connection between the gradient (33) and evenly weighted, simultaneous projections, the difference between the two algorithms is the weighting of the projections, and, in the case of limited memory, the use of previous iterations for acceleration. Figure (3a) shows the performance of the two algorithms on a single panel of the aperture shown in figure (2b). Figure (3b) shows the performance of the algorithms on the full segmented pupil with a resolution of 512×512 pixels. The limited memory algorithm has trouble finding a descent direction in the middle iterations, but converges rapidly toward the end. The Misell algorithm has trouble resolving the boundaries of the pupil. This test was terminated after 1000 iterations, at which point the Misell algorithm had made no further progress than it had in the first 200 iterations.

Figure (4) shows the performance of various implementations of the limited memory algorithm. In all examples the given test problem was the full segmented aperture shown in figure(2b) at 512×512 resolution. In figure(4a) limited memory with the objective function J_{LS} is compared to limited memory with the objective J_{sde}^ϵ . Both examples started from the same zero phase initial guess. The polar wavefront representation was used with f fixed. For random initial guesses the Cartesian representation outperformed all other formulations on average, though performance is comparable.

Figure (4b) illustrates the “flat” spot in the objective J_{sde} . In the middle iterations the gradient

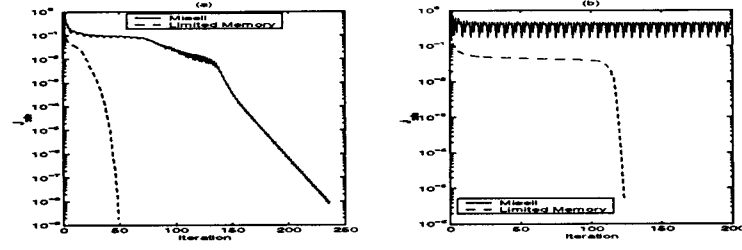


Figure 3: Comparison of the Misell algorithm with limited memory.

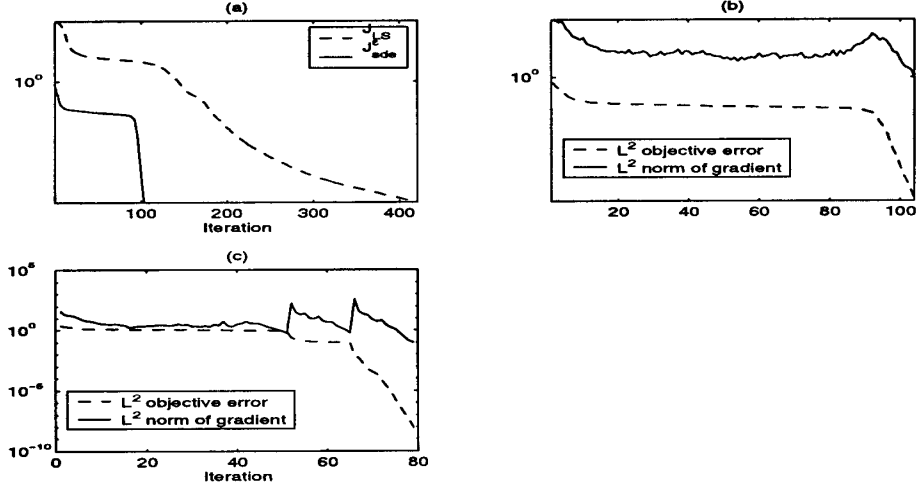


Figure 4: Comparison of limited memory implementations.

becomes very small, indicating that a strong direction of descent is not being found. Lacking better curvature information, we make use of a multi-resolution strategy that ensures that the “hard” work of the middle iterations is performed at low resolutions where the computations are inexpensive. The more expensive, higher resolution computations are only executed after the low resolution images have converged. This is shown in figure (4c).

The multi-resolution strategy is implemented by iterating only on the center pixels of the data image ψ_j and expanding the portion included pixels by factors of 2 to allow for fullest use of the fast Fourier transform. The solution at resolution 2^n is used as the first guess for the problem at resolution 2^{n+l} . The solution to the multiresolution example is shown in figure(2). In figure (4c) we started with the center 32×32 pixels of ψ_j . We used the solution at this resolution as the initial guess for the problem at resolution 128×128 . Once a solution at 128×128 was found, we used this solution as the initial guess for the full resolution problem. The jumps in the gradient indicate where the resolution has changed. At resolutions of 128×128 and 512×512 less than 15 iterations were necessary to achieve the desired tolerance. At the tolerance shown in figure (4c) the maximum per

pixel wavefront error is less than 10^{-3} wavelengths, well below the tolerance of most operational systems (see figure (2d)). The computation time for the multi-resolution implementation from random initial guesses is on average 3.5 minutes using Matlab on a dec alpha workstation.

Figure (5) shows the numerical solution to the phase diversity problem. The method successfully converges to a diffraction limited solution, however, the rate of convergence is extremely slow, as is indicated by the performance with the J_{LS} objective in figure (4a). It has been noted that the BFGS approximation to second order information is not a competitive substitute for true second order information [27]. A method for incorporating second order information has been proposed by Dobson [10]. This is an active area of research.

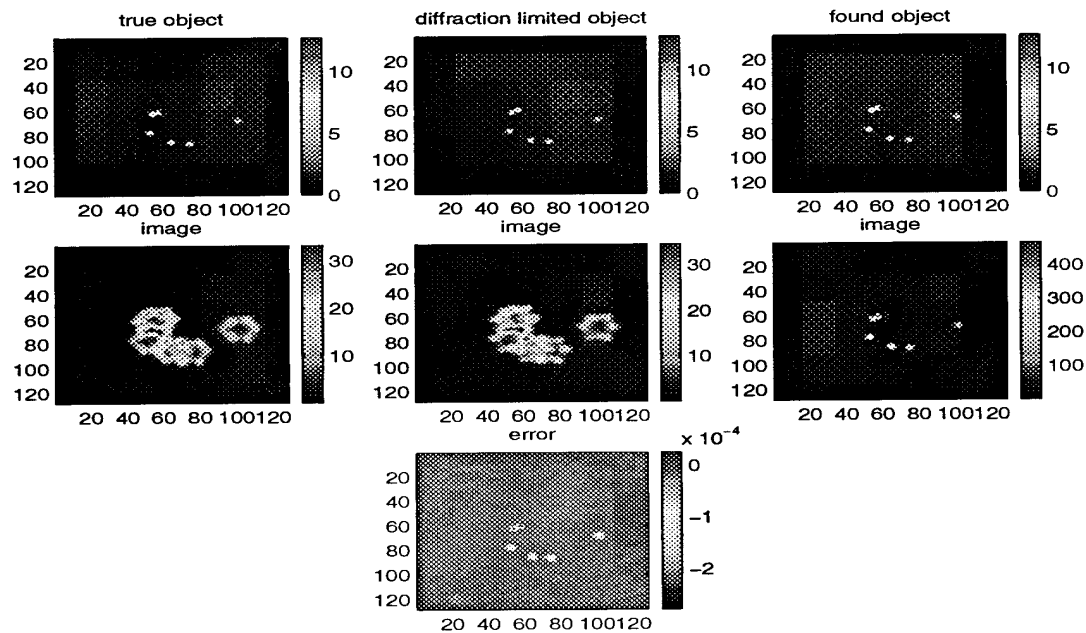


Figure 5: Phase diversity.

5 Conclusion

The phase retrieval and phase diversity problems are fundamentally ill-posed. Not only is the mathematical model ill-posed, but the underlying functions are not differentiable. A precise mathematical framework is necessary for a thorough treatment of these issues. The proposed regularization strategy for the phase diversity algorithm involves perturbing the original ill-posed problem to a nearby, numerically stable problem. Similarly, the non-differentiability of the set distance error used in phase retrieval is addressed by perturbing the objective to a nearby differentiable function which is asymptotically consistent with the original problem. Dobson [10] shows that the gradient of the J_{LS} objective is a compact operator. This introduces instabilities into the linearized problem which

necessitates further regularization. The non-parametric approach we take here allows researchers the freedom to choose a regularization that is physically justified. More work on regularization is necessary not only for theoretical results, but for faster algorithms.

Prototype test examples indicate that limited memory methods with trust regions are more robust than iterative transform methods and have faster rates of convergence. The performance measure is crucial to fast convergence. One critical advantage of the trust region limited memory techniques over iterative transform methods is in the careful scaling of the step size (25). This in conjunction with multi-resolution implementations decrease cpu time dramatically. Further speed up in run time is possible by processing the expressions for the gradients (31) and (32) in parallel. The limited memory BFGS algorithm with trust regions converges to diffraction limited solutions for the phase diversity problem, though convergence is slow. More work is needed to find efficient algorithms that make use of second order information.

A Gradient Calculations

The formulas for the gradients follow from tedious, though elementary vector calculus. Wherever possible we detail the operations in general, leaving the particulars of the specific operators for the reader. The reader will not, therefore, find complete explicit formulations in what follows. Where there is no chance for confusion, we omit the arguments from the operators.

- **Convolution and Correlation identities:** Define the convolution operator, \ast , by

$$u \ast v(\underline{x}) \equiv \int_{\mathbb{R}^n} u(\underline{x}')v(\underline{x} - \underline{x}')d\underline{x}'. \quad (34)$$

Define the correlation operator, \star , by

$$u \star v(\underline{x}) \equiv \int_{\mathbb{R}^n} u(\underline{x}')v(\underline{x} + \underline{x}')d\underline{x}'. \quad (35)$$

We define the inner product to be $\langle u, v \rangle \equiv \int_{\mathbb{R}^n} u(\underline{x})\bar{v}(\underline{x})d\underline{x}$. It is elementary to verify the following identities.

$$u \star v = u^{\wedge\wedge} \ast v; \quad (36)$$

$$u \ast v = [u^{\wedge} \cdot v^{\wedge}]^{\vee} = [u^{\vee} \cdot v^{\vee}]^{\wedge}; \quad (37)$$

$$u \star v = [u^{\vee} \cdot v^{\wedge}]^{\vee} = [u^{\wedge} \cdot v^{\vee}]^{\wedge}; \quad (38)$$

$$\langle u \ast v, h \rangle = \langle v, \bar{u} \star h \rangle; \quad (39)$$

$$\langle u \star v, h \rangle = \langle \bar{h} \star v, \bar{u} \rangle; \quad (40)$$

$$\text{if } h^{\vee} \text{ is real then } \langle v \star u, h \rangle = \langle h \star v, \bar{u} \rangle. \quad (41)$$

- **Least squares gradient:** For $\underline{p} \in [L^2[\mathbb{R}^n, \mathbb{C}]]^m$, an m -vector of complex valued, Fréchet differentiable functionals $p_j : \mathcal{S} \rightarrow L^2[\mathbb{R}^n, \mathbb{C}]$ ($j = 1, \dots, m$), where $\mathcal{S} \subset [L^2[\mathbb{R}^n, \mathbb{R}]]^m$, the variational derivative of $\frac{1}{2} \|\underline{p}[\underline{u}]\|^2$ at $\underline{u} \in \mathcal{S}$ in the direction $\underline{d} \in \mathcal{S}$ is given by

$$\begin{aligned} \left[\nabla \frac{1}{2} \|\underline{p}[\underline{u}]\|^2 \right] (\underline{d}) &= \sum_{j=1}^m \text{Re} \langle \nabla p_j[\underline{u}](\underline{d}), p_j[\underline{u}] \rangle \\ &= \sum_{j=1}^m \langle \underline{d}, \text{Re} [\nabla p_j[\underline{u}]]^* (p_j[\underline{u}]) \rangle \\ &= \left\langle \underline{d}, \text{Re} \sum_{j=1}^m [\nabla p_j[\underline{u}]]^* (p_j[\underline{u}]) \right\rangle \end{aligned} \quad (42)$$

- **Convolution adjoints:** Let $p, q \in L^2[\mathbb{R}^n, \mathbb{C}]$, and given $\mathcal{S} \subset [L^2[\mathbb{R}^n, \mathbb{R}]]^m$ let $g : \mathcal{S} \rightarrow L^2[\mathbb{R}^n, \mathbb{C}]$ be the Fréchet differentiable kernel of the convolution operator \mathcal{G} . The directional derivative of \mathcal{G} at $[\underline{u}]$ in the direction \underline{d} , where $[\underline{u}], \underline{d} \in \mathcal{S}$ is given by $(\nabla \mathcal{G}(\underline{d}))p = [\nabla g[\underline{u}](\underline{d})] \ast p$. Applying Tonelli's theorem we define the adjoint with respect to \underline{d} by

$$\begin{aligned} \langle [\nabla \mathcal{G}[\underline{u}](\underline{d})] p, q \rangle &\equiv \langle \nabla g[\underline{u}](\underline{d}) \ast p, q \rangle \\ &= \langle \nabla g[\underline{u}](\underline{d}), \bar{p} \star q \rangle \\ &= \langle \underline{d}, [\nabla g[\underline{u}]]^* (\bar{p} \star q) \rangle. \end{aligned} \quad (43)$$

Thus we define

$$[\nabla G p]^* (q) \equiv [\nabla g[\underline{u}]]^* (\bar{p} \star q). \quad (44)$$

Note that while $(\nabla G(\underline{d})) p \in L^2[\mathbb{R}^n, \mathbb{C}]$, the adjoint $[\nabla g[\underline{u}]]^* (\bar{p} \star q) \in [L^2[\mathbb{R}^n, \mathbb{C}]]^m$.

- **Multiplicative adjoints:** Let $p, q \in L^2[\mathbb{R}^n, \mathbb{C}]$, and let $g : \mathcal{S} \rightarrow L^2[\mathbb{R}^n, \mathbb{C}]$, where $\mathcal{S} \subset [L^2[\mathbb{R}^n, \mathbb{R}]]^m$, be a Fréchet differentiable “kernel” of the multiplication operator G . The directional derivative of the multiplication operator at $[\underline{u}]$ in the direction \underline{d} , where $[\underline{u}], \underline{d} \in \mathcal{S}$ is given by $(\nabla G(\underline{d})) p = [\nabla g[\underline{u}](\underline{d})] p$. The adjoint with respect to \underline{d} is defined by

$$\begin{aligned} \langle [\nabla G[\underline{u}](\underline{d})] p, q \rangle &\equiv \langle [\nabla g[\underline{u}](\underline{d})] p, q \rangle \\ &= \langle \nabla g[\underline{u}](\underline{d}), \bar{p} q \rangle \\ &= \langle \underline{d}, [\nabla g[\underline{u}]]^* (\bar{p} q) \rangle. \end{aligned} \quad (45)$$

Thus we define

$$[\nabla G p]^* (q) \equiv [\nabla g[\underline{u}]]^* (\bar{p} q). \quad (46)$$

Again, note that while $(\nabla G(\underline{d})) p \in L^2[\mathbb{R}^n, \mathbb{C}]$, the adjoint $[\nabla g[\underline{u}]]^* (\bar{p} q) \in [L^n[\mathbb{R}^2, \mathbb{C}]]^m$.

- **The Lebesgue dominated convergence theorem and it's consequences:** The formulas for the gradient given by (26), (29), (32), and (33) assume that the generalized pupil function $f e^{i\theta}$ satisfies $|f(\underline{x})| \rightarrow 0$ as $|\underline{x}| \rightarrow \infty$. In the case of the Cartesian representation this condition is $|w(\underline{x}) + iz(\underline{x})| \rightarrow 0$ as $|\underline{x}| \rightarrow \infty$. The Lebesgue dominated convergence theorem then implies that the variational directional derivative commutes with the Fourier transform, i.e. that $\nabla_{w,z}[(w + iz)^\wedge](\underline{d}) = [\nabla_{w,z}[w + iz](\underline{d})]^\wedge$ where $\nabla_{w,z}[\cdot](\underline{d})$ is defined as the variation with respect to the functions w and z in the direction \underline{d} .

References

- [1] M. J. Bastiaans. The wigner distribution function and hamilton's characteristics of a geometric-optical system. *Optics Communications*, 30(3):321–326, 1979.
- [2] M. J. Bastiaans. Application of the wigner distribution function to partially coherent light. *J.Opt.Soc.Am.A*, 3(8):1227–1238, 1986.
- [3] J. F. Benders. Partitioning procedures fro solving mixed variables programming problems. *Numerische Mathematik*, 4:238–252, 1962.
- [4] M. Born and E. Wolf. *Principles of Optics*. 6 edition, 1980.
- [5] R. H. Boucher. Convergence of algorithms for phase retrieval from two intensity measurements. *SPIE*, 231:130–141, 1980.
- [6] J. V. Burke and A. Wiegmann. Low-dimensional quasi-newton updating strategies for large-scale unconstrained optimization. Submitted to the SIAM Journal on Optimization, July 1996.

- [7] R. H. Byrd, J. Nocedal, and R. B. Schnabel. Representations of quasi-newton matrices and their use in limited memory methods. *Math. Prog.*, 63:129–156, 1994.
- [8] J. Dainty and J. Fienup. Phase retrieval and image reconstruction for astronomy. In H. Stark, editor, *Image Recovery: Theory and Application*. Academic Press, 1987.
- [9] J. E. Dennis and R. Schnabel. *Numerical Methods for Unconstrained Optimization and Non-linear Equations*. Prentice Hall, 1983.
- [10] D. C. Dobson. Phase reconstruction via nonlinear least squares. *Inverse Problems*, 8:541–557, 1992.
- [11] J. Fienup. Phase retrieval algorithms: a comparison. *Appl. Opt.*, 21(5):2758–2768, 1982.
- [12] R. Gerchberg and W. Saxton. A practical algorithm for the determination of phase from image and diffraction plane pictures. *Optik*, 35:237–246, 1972.
- [13] R. Gonsalves. Phase retrieval and diversity in adaptive optics. *Opt. Eng.*, 21(5):829–832, 1982.
- [14] J. Goodman. *Introduction to Fourier Optics*. McGraw-Hill, 1968.
- [15] M. H. Hayes. *Signal Reconstruction from Phase or Magnitude*. PhD thesis, Massachusetts Institute of Technology, 1981.
- [16] M. H. Hayes and A. V. Oppenheim. Signal reconstruction from phase or magnitude. *IEEE Trans. Acc. Sp. and Sig. Proc.*, 1980.
- [17] A. Levi and H. Stark. Image restoration by the method of generalized projections with application to restoration from magnitude. *J. Opt. Soc. Am. A*, 1(9):932–943, 1984.
- [18] D. R. Luke. PhD thesis, University of Washington, in preparation.
- [19] D. R. Luke and J. V. Burke. Non-parametric phase retrieval and diversity. in preparation.
- [20] D. L. Misell. An examination of an iterative method for the solution of the phase problem in optics and electron optics i. test calculations. *J. Phys. D.*, 1973.
- [21] A. V. Oppenheim and R. W. Schaffer. *Digital Signal Processing*. Prentice-Hall, 1975.
- [22] S. S. Oren and E. Spedicato. Optimal conditioning of self-scaling variable metric algorithms. *Math. Prog.*, 10:70–90, 1976.
- [23] R. Paxman, T. Schultz, and J. Fienup. Joint estimation of object and aberrations by using phase diversity. *J. Opt. Soc. Am. A*, 9(7):1072–1085, 1992.
- [24] T. Quatieri and A. V. Oppenheim. Iterative techniques for minimum phase signal reconstruction from phase or magnitude. *IEEE Trans. on Acc., Sp. and Sig. Proc.*, ASSP-29(6):1187–1193, Dec. 1981.
- [25] R. T. Rockafellar and R. J. Wetts. *Variational Analysis*. Springer, 1998.
- [26] D. F. Shanno and K. Phua. Matrix conditioning and nonlinear optimization. *Math. Prog.*, 14:149–160, 1978.

- [27] C. R. Vogel, T. Chan, and R Plemmons. Fast algorithms for phase diversity-based blind deconvolution. Technical report, Department of Mathematical Sciences, Montana State University, 1999.
- [28] D. C. Youla. Mathematical theory of image restoration by the method of convex projections. In H. Stark, editor, *Image Recovery: Theory and Applications*, pages 29–77. Academic Press, 1987.
- [29] D. C. Youla and H. Web. Image restoration by the method of convex projections: Part i - theory. *IEEE Trans Med. Im.*, MI-1(2):81–94, Oct. 1982.

Sparse Matrix Approximation Method for Phase Retrieval Based Active Optical Control System

Timothy P. Murphy
NASA Goddard Space Flight Center
murphy@albert.gsfc.nasa.gov

Richard G. Lyon
NASA Goddard Space Flight Center

John E. Dorband
NASA Goddard Space Flight Center

Jan M. Hollis
NASA Goddard Space Flight Center

ABSTRACT

We develop a sparse matrix approximation method to decompose a wavefront into a basis set of actuator influence functions for an active optical system consisting of a deformable mirror and a segmented primary mirror. The wavefront used is constructed by Zernike polynomials to simulate the output of a phase retrieval algorithm. Results of a Monte-Carlo simulation of the optical control loop are compared to the standard, non-sparse approach in terms of accuracy and precision, as well as computational speed and memory. The sparse matrix approximation method can yield more than a 50-fold increase in the speed and a 20-fold reduction in matrix size, and commensurate decrease in required memory, with a less than 10% degradation in solution accuracy. We show that the method developed herein is a viable alternative to using the full control matrix in a phase retrieval based active optical control system. We show that the method developed herein is a viable alternative to using the full control matrix in a phase retrieval based active optical control system.

1. INTRODUCTION

Wavefront sensing in an active optical system may be achieved by Shack-Hartmann sensing [1], interferometry [2], curvature sensing [3], or phase retrieval methods [4, 5, 6, 7]. Each of these wavefront sensing methods attempts to determine either the wavefront error or the gradient of the wavefront error. After determining the wavefront error, actuators move or deform optical elements to minimize an error metric and improve the quality of imaging. This wavefront correction process may have to be iteratively repeated for at least three cases: (1) the wavefront is time dependent, (2) imprecise knowledge of the wavefront response to actuator motion, and, (3) errors in the wavefront sensing process itself.

The Shack-Hartmann sensor typically provides the gradient of the wavefront error at several hundred sample points. In contrast, phase retrieval techniques provide the wavefront error on the order of tens of thousands of points. Shack-Hartmann sensors have been preferred in time sensitive applications, because they provide the wavefront data faster, due to lower computational complexity, than phase retrieval. Phase retrieval is an iterative algorithm that uses images of unresolved point sources, together with knowledge of the system, to determine the wavefront error. Major advantages of phase retrieval are that no separate wavefront sensor hardware is required and that all data are collected with a standard focal plane camera.

Herein we address the phase retrieval case, since typically the resultant wavefront provides tens of thousands of spatial sample points in the system exit pupil, thereby providing higher spatial frequency content. Correction of the wavefront at high spatial frequencies requires a large number of actuators and, therefore, a correspondingly large system control matrix. The control loop computation time and memory size both scale with the system control matrix size. Hence, we are motivated to find a fast, lower memory control method. For a system with a segmented primary and an active deformable mirror (DM), we demonstrate the viability of a sparse matrix approximation approach as a solution for minimizing the squared

error of a phase retrieved wavefront. We specify the matrix size, calculation time and wavefront error of this approach and compare it to that of the standard full matrix technique.

2. DESCRIPTION OF ACTIVE OPTICAL SYSTEM

Figure 1 is a schematic of an optical system consisting of a segmented primary mirror, a secondary mirror, two off-axis parabolas for collimating and focusing, a DM, and a focal plane detector. A segmented primary may be required in a system with a very large aperture, so that the weight and size of a single element remains manageable. The demagnified pupil is imaged onto the DM. The actuators of the DM are moved such that an error metric of the wavefront is minimized. The output wavefront of the phase retrieval algorithm is Nyquist sampled such that the number of samples across one dimension times the sample spacing is twice the pupil diameter (figures 2a and 2b).

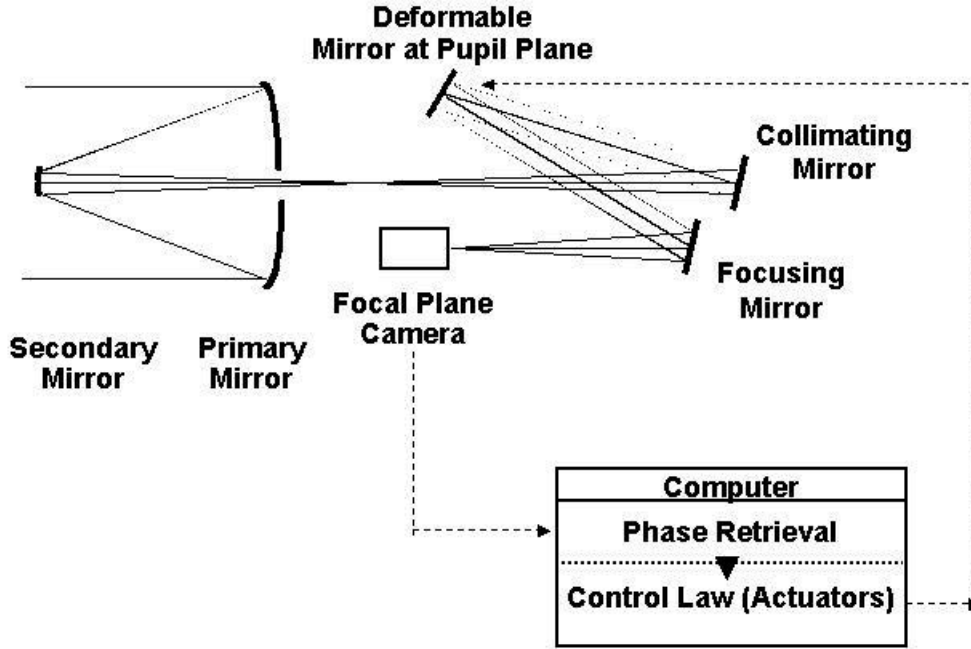


Figure 1. Active Optical System. Images detected at the focal plane camera are processed by the phase retrieval algorithm to form a wavefront. The wavefront is processed by the control software to provide commands for the DM actuators.

In our model of the system, we consider the two-dimensional wavefront lexicographically reordered as a one-dimensional m -vector, \mathbf{w} , m is initially 512×512 in our example. This reordering has no effect on the physical interpretation of the system and is done to simplify the notation. In equation (1) we assume a linear model for the influence of the DM actuators on the wavefront, i.e., the actual shape of the surface of the DM is a linear superposition of all the actuator influence functions. Applying approximation methods for a deformable plate [8], the influence on the wavefront of 349-actuator deformable mirror is modeled as follows:

$$\mathbf{r}_j = \exp(-\mathbf{a}\|\mathbf{x} - \mathbf{x}_j\|) \sin(\mathbf{a}\|\mathbf{x} - \mathbf{x}_j\| + \mathbf{p}/4) \quad (1)$$

\mathbf{r}_j is the m -vector, also known as influence function, of the j th actuator; \mathbf{x}_j is the location of the j th actuator in the pupil plane; $\|\mathbf{x} - \mathbf{x}_j\| \equiv \sqrt{(x - x_j) \cdot (x - x_j)}$ is the distance in m -space from the j th actuator location to the

point \mathbf{x} ; and α is a constant in units of inverse distance. The influence function of equation (1) is typical of a Xinetics-type [9, 10] DM. Such a DM has an α of 256 m^{-1} and physical spacing of 7 mm between each of 349 actuators. Thus, the influence of an actuator drops to ~9% of its peak value at a neighboring actuator. The actuators are spaced on a square grid with 21 actuators across the pupil. The optical system images the pupil onto the DM so that the edge of the pupil is approximately at the center of the outermost actuators.

The wavefront, $\mathbf{w}^{(k)}$, after the k th iteration of correction by the DM, is modeled:

$$\mathbf{w}^{(k)} = \mathbf{w}^{(k-1)} + \mathbf{R}\mathbf{a}^{(k)} \quad (2)$$

where \mathbf{R} is the $m \times n$ response matrix and $\mathbf{a}^{(k)}$ is the n -vector ($n=349$) of the k th iteration of actuator excursions. The response matrix, \mathbf{R} , consists of n columns of the influence functions, \mathbf{r}_j , $j \in \{0, \dots, n-1\}$, described previously. Equation (2) is based on the assumption that the DM influence on the wavefront is a linear superposition of the influence of each actuator. We assume the initial actuator positions, $\mathbf{a}^{(0)}$, are set to zero.

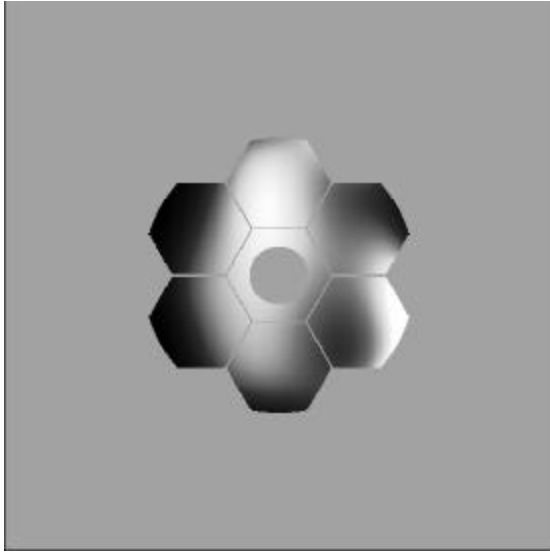


Figure 2a

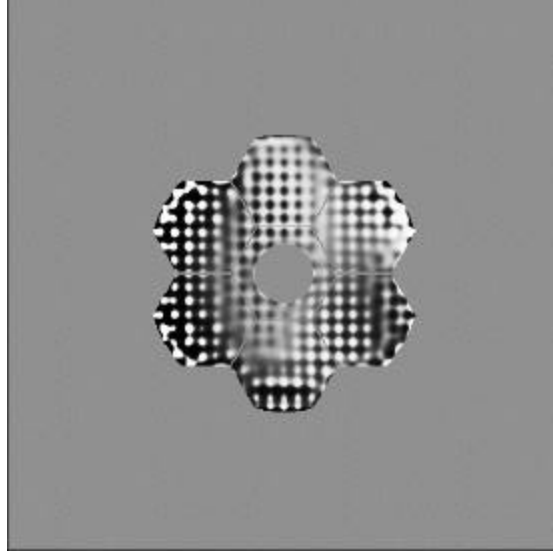


Figure 2b.

(a) Example of wavefront before correction. (b) Example of wavefront after correction. The contrast in (b) is enhanced to show the influence of the actuators

Method of Solution

In order to solve equation (2), we wish to find the vector, \mathbf{a} , that minimizes the variance of the wavefront, $\|\mathbf{w}\|^2$. The mean of the wavefront, $\bar{\mathbf{w}}$, can be arbitrarily set to zero without loss of information. Throughout this work we refer to the relative wavefront error at the k th iteration of the control loop, \mathbf{e}_w , which we define as:

$$\mathbf{e}_w = \frac{\|\mathbf{w}^{(k)}\|}{\|\mathbf{w}^{(0)}\|} \quad (3)$$

The solution of a least-squared error linear system is known as the normal equations [14]. We refer to the application of the normal equations to the active optical system as the actuator fitting process. For an active optical system the linear least-squared solution is:

$$\mathbf{a}^{(k)} = \mathbf{a}^{(k-1)} - (\mathbf{R}^T \mathbf{R})^{-1} \mathbf{R}^T \mathbf{w}^{(k-1)} \quad (4)$$

where we define, $\mathbf{S} \equiv (\mathbf{R}^T \mathbf{R})^{-1} \mathbf{R}^T$. Thus,

$$\mathbf{a}^{(k)} = \mathbf{a}^{(k-1)} - \mathbf{S} \mathbf{w}^{(k-1)} \quad (5)$$

where \mathbf{S} is the $n \times m$ solution matrix and the wavefront has 512×512 points. For a deformable mirror with 349 actuators, \mathbf{S} has over 91 million elements. If stored in 64-bit floating-point format, \mathbf{S} occupies 698 MB. Manipulating a data array the size of \mathbf{S} poses practical memory and storage problems. If \mathbf{S} is stored on disk, then the disk reading process will take several seconds even on the fastest systems. If stored in memory, the price of that memory will be substantial, particularly for a space-based or high-reliability system. Even as an array stored in memory, the time required to read \mathbf{S} and execute the product $\mathbf{S} \mathbf{w}$ can be substantial. We will show a method for efficiently using only the larger magnitude elements of \mathbf{S} and ignoring the remainder.

3. SPARSE MATRIX APPROXIMATION METHOD

In this section we describe an algorithm for creating a sparse approximation of \mathbf{S} .

The first step to reducing the size of matrices \mathbf{R} and \mathbf{S} is to remove the region around the pupil, which has the value zero for all wavefronts. The zero-valued region around the pupil exists to avoid aliasing in the phase retrieval process. For example, if the phase retrieval algorithm produces a 512×512 sampled wavefront, the pupil extends only over the central 256×256 region (figure 2a). The reduction of approximately four fold in the wavefront size is not counted toward the gains afforded by the algorithm. We used the central 260×260 points of the wavefront. Of these 67,600 points, many are still outside the pupil, either in the central obscuration or outside the primary mirror segments. The total number of points in the pupil is 40,928, for our example. In our example, the matrix dimension, m , is reduced from 262,144 to 67,600 by removing those elements outside the central region. Because of the large size of the full solution matrix, \mathbf{S} , we created and stored it on a multi-processor, parallel computer [12].

For the creation of a sparse matrix, we define the fraction of matrix elements to be retained as the density parameter, \mathbf{x} , where $1 \geq \mathbf{x} > 0$. The sparseness is defined as $1-\mathbf{x}$. A row of \mathbf{S} is made sparse by removing the $1-\mathbf{x}$ fraction of matrix elements smaller than a certain threshold. In the algorithm, a pair of thresholds, one each for positive and negative values, is found for each row, such that $m\mathbf{x}$ elements remain in that row. The distribution of element values in a row varies from one row to another, so use of a single pair of thresholds for all the rows would remove a different number of elements from each row. Such an approach concentrates the algorithmic errors in certain actuators. In particular, those rows of \mathbf{S} corresponding to actuators near the edge of the pupil have a distribution of values quite different from those rows corresponding to actuators at or near center of a pupil segment. The product of a row of \mathbf{S} with the corresponding column of \mathbf{R} is unity. Thus, introducing error into the rows of \mathbf{S} with the smallest magnitude elements will introduce error into those actuators corresponding to the columns of \mathbf{R} with the greatest magnitude elements.

Once the thresholds for each row are determined the algorithm must extract the row elements outside the threshold bounds. Besides the value of a row element, the algorithm must account for the location of the element in the original row. Rather than storing one location for each extracted element, the algorithm stores the locations of strings of consecutive elements outside the threshold. The lengths of these strings are stored as well. For example, if elements 3 through 210 of a row are outside the threshold, the algorithm stores 3 and 207 as the location and length of the string of elements. For each row the extracted elements, string locations, and string lengths are stored. To facilitate reading this structure, the total number of extracted elements and total number of strings are also stored in the structure for each row.

An actuator fitting program that uses the sparse approximation matrix was developed. This program executes equation (5) using the sparse approximation matrix, $\hat{\mathbf{S}}$, in place of the full solution matrix, \mathbf{S} . For each actuator element, the program reads the data structure for the corresponding row of $\hat{\mathbf{S}}$ from storage. The product of the wavefront with the sparse row data is executed to yield updated actuator data.

The algorithm removes those row elements of smallest absolute values, such that the sum of the elements removed was as close as possible to zero. Thus, two thresholds, one for positive and one for negative elements, were used to remove row elements. In the algorithm it is assumed that at least one element of every row of \mathbf{S} is equal to zero. Let $U_{i,j}$ be the reordered elements of row i of \mathbf{S} , such that:

$$U_{i,j} = S_{i,k} \quad k \in \{0, \dots, m-1\} \quad (6)$$

$$U_{i,l+1} \leq U_{i,l} \quad l \in \{0, \dots, m-2\} \quad (7)$$

A positive threshold index, pt_i , and a negative threshold index, nt_i , are initially valued such that:

$$U_{i,nt_i} < 0 \quad \text{and} \quad U_{i,nt_i-1} = 0 \quad (8)$$

$$U_{i,pt_i} > 0 \quad \text{and} \quad U_{i,pt_i+1} = 0 \quad (9)$$

The bias, B_i , defined as the sum of the elements removed from the row i , is calculated:

$$B_i = \sum_{k=pt_i+1}^{nt_i-1} U_{i,k} \quad (10)$$

The algorithm proceeds by either incrementing nt_i upward or pt_i downward at each step according to the following rule:

$$\text{if } B_i < 0, \quad pt_i \longrightarrow pt_i - 1 \quad (11)$$

$$\text{if } B_i > 0, \quad nt_i \longrightarrow nt_i + 1 \quad (12)$$

$$\text{if } B_i = 0, \quad nt_i \longrightarrow nt_i + 1 \text{ and } pt_i \longrightarrow pt_i - 1 \quad (13)$$

The incrementing process continues until the target number of elements outside the thresholds is reached, i.e., $\text{int}(m\alpha) = m+1+pt_i-nt_i$. In cases where either threshold index is incremented to the limiting values, $m-1$ for nt_i and 0 for pt_i , respectively, the algorithm then ignores B_i and continues by incrementing only the threshold index not at the limiting value. Once the final values for the threshold indices are established, the sparse approximation matrix is created as follows:

$$\hat{S}_{i,j} = \begin{cases} S_{i,j} & \text{if } S_{i,j} \leq U_{i,nt_i} \text{ or } U_{i,pt_i} \leq S_{i,j} \\ 0 & \text{otherwise} \end{cases} \quad (14)$$

The matrix, $\hat{\mathbf{S}}$, is stored and used as the solution matrix in the control loop actuator fitting algorithm.

4. MONTE CARLO SIMULATION

A Monte Carlo simulation was conducted to estimate the error introduced by the algorithm and to determine the speed. One hundred initial wavefront cases were applied to a simulated optical control loop (figure 3) consisting of a wavefront simulator and an actuator fitting program. The cases were generated by assigning random numbers to each of the coefficients of Zernike polynomials [15] fitted across the circular pupil spanning the aperture. Twenty-nine Zernike polynomials (Z3 through Z32) were used. The first term, Z0, which represents piston, was not used because wavefront piston is not relevant. Terms Z1 and Z2, representing tip and tilt, were not used because these terms depend on the placement of the point source in the images used for phase retrieval. The bounds of the uniform distribution were such that the initial wavefront error for the 100 cases ranged from 0.1 to 0.6 waves rms.

The simulated optical control loop ran for 4 iterations for each initial wavefront with density parameter values of 1.0, 0.3, 0.25, 0.2, 0.15, 0.1, 0.05, 0.02, 0.01 and 0.005. Each iteration (figure 3) consists of a wavefront generation and an actuator fitting. The rms wavefront error at each iteration was recorded. The wavefront piston was ignored in the wavefront error calculation. In a practical system, care must be taken to assure that an arbitrary constant bias, due to the algorithm, does not accumulate in the actuator vector over several iterations. All actuator values and the time to compute equation (5) were recorded.

5. RESULTS

Five desired characteristics of the sparse matrix approximation were identified:

1. Small increase in error compared to the full matrix case.
2. Stability, i.e., monotonic decrease in error with control loop iteration.
3. Smaller storage size.
4. Higher computational speed.
5. Monotonic decrease in error with decreasing sparseness

The results for the sparse matrices show monotonic increase in relative wavefront error with increasing number of elements removed (figures 4 and 5). Note that the error decreased monotonically with increasing iterations through the simulated control loop. The performance of the algorithm is stable with respect to choice of sparseness level and with respect to iteration number. After one iteration, the mean relative error rises from 0.067, for the full matrix, to 0.072, for the 0.05 sparse matrix, an increase of only ~8% in error for a ~95% decrease in matrix element count. After two iterations, the mean relative error rises from 0.062, for the full matrix, to 0.064 for the 0.02 sparse matrix, an increase of ~4%.

These results show that an adaptive optical system as described above can benefit from a 20-fold decrease in memory usage by using this sparse technique with little error penalty. If two iterations through the control loop are used, the memory usage benefit is 50 fold.

TIMING RESULTS

System software timing calls were used to determine the time to execute the matrix-vector multiply (equation 5). The time to read the stored data from disk was not included. For all cases, there is uncertainty associated with the timing results because the values returned by timing calls depend on other loads on the operating system. The timing call returns values in 0.01 s increments. Thus, the timing results have large relative errors for mean values less than 0.1 s ($x \leq 0.02$). The computation time results for the sparse calculations scale linearly with x (figure 6). For the full matrix calculation the matrix is broken up on a row basis, with 21 or 22 rows handled at each processor. It was suspected apriori that the overhead of reading the sparse data string locations and lengths would lead to the full matrix calculation time being lower than the sparse matrix times extrapolated to density parameter $x=1.0$. The opposite proved true, however. The mean time for the full calculation was 5.1 s, while the $x=0.3$ time was 0.68 s. Thus the sparse calculation time extrapolates to 2.3 s for the full case. One possible explanation for this is that the smaller rows of the sparse matrix fit into the 512 KB level-2 cache of the processors, while the full rows (541 KB each) do not. For $x=0.05$, the mean calculation time was 0.092 seconds, less than one-fiftieth of the full matrix calculation time.

MATRIX SIZE RESULTS

The sparse approximation matrix sizes are shown in figure 7. The figure shows the total matrix size and, for the sparse matrices, the overhead storage associated with the data location and length. Overhead storage size is defined as the sparse matrix size minus the product of x with the full matrix size. The overhead storage decreases with x ; but at a rate slower than the total matrix size. For x greater than 0.05, overhead is less than 10% of the total size.

6. CONCLUSIONS

We have designed, developed, coded and Monte-Carlo simulated a method of using a sparse matrix approximation to the solution of a least-squared wavefront error based actuator fitting algorithm. For a single iteration through the control loop, a matrix size reduction of 20 fold and a speed advantage of 50 fold can be realized at the cost of less than 10% loss of accuracy. Simulations show that the control loop using this method is stable and that the relative wavefront error decreases monotonically as more elements are added to the matrix. This can be of great utility in a space-based mission, where memory use is at a premium, or a ground-based system, where speed is at a premium.

T .P. M., R. G. L. and J. E. D. acknowledge the support of the NASA Remote Exploration and Experimentation Project and High Performance Computing and Communication Program for this work. J. M. H. received support from NASA RTOP 344-02-03-01.

REFERENCES

- 1) B. L. Ellerbroek, B. J. Thelen, D. J. Lee, D. A. Carrara, and R. G. Paxman, "Comparison of Shack-Hartmann wavefront sensing and phase-diverse phase retrieval," in *Adaptive Optics and Applications*, R. K. Tyson and R. Q. Fugate, ed., Proc SPIE **3126**, 307-320 (1997).
- 2) P. Hariharan, *Optical Interferometry* (Academic Press, Sydney, Australia, 1985)
- 3) L. Salas, "Variable separation in curvature sensing: fast method for solving the irradiance transport equation in the context of optical telescopes," Appl. Opt. **35**, 1593-1596 (1996).
- 4) R. W. Gerchberg and W. O. Saxton, "A practical algorithm for the determination of phase from image **35**, 237-246 (1972).
- 5) R. A. Gonsalves, "Phase retrieval and diversity in adaptive optics," Opt. Eng. **21**, 829-832 (1982).
- 6) R. G. Lyon, J. E. Dorband, and J. M. Hollis, "Hubble Space Telescope Faint Object Camera calculated **36**, 1752-1765 (1997).
- 7) J. R. Fienup, "Phase-retrieval algorithms for a complicated optical system," Appl Opt. **32**, 1728-1736 (1993).
- 8) S. Timoshenko and S. Woinowsky-Krieger, *Theory of Plates and Shells* 2nd Ed. (McGraw-Hill, New York, 1959).
- 9) Xinetics Inc., 37 MacArthur Ave., Devens, MA 01432. <http://www.tiac.net/users/xinetics>.
- 10) M. A. Ealey and J. A. Wellman, "Xinetics Low Cost Deformable Mirrors with Actuator Replacement Cartridges," in *Adaptive Optics in Astronomy*, M. A. Ealey and F. Merkle, ed., Proc. SPIE **2201**, 680-687 (1994).
- 11) G. Strang, *Linear Algebra and Its Applications* (Academic Press, New York, 1976).
- 12) <http://newton.gsfc.nasa.gov/thehive/>
- 13) R. Noll, "Zernike polynomials and atmospheric turbulence," J. Opt. Soc. Am. **66**, 207-211 (1976).

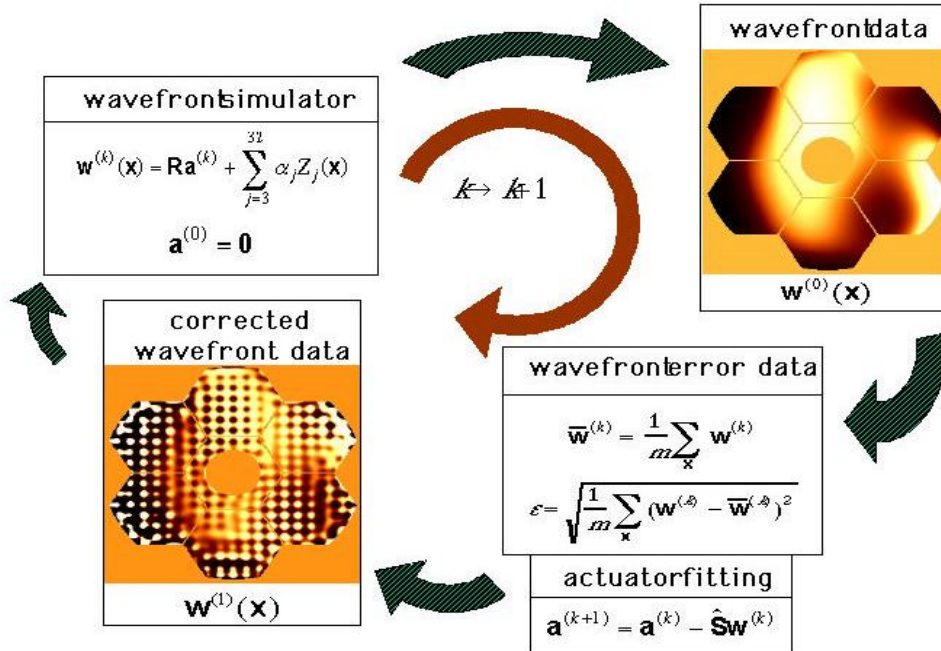


Figure 3. Simulated optical control loop. Initial wavefronts are generated from Zernike polynomials. Wavefront error is assessed. Actuators are fit by equation (5).

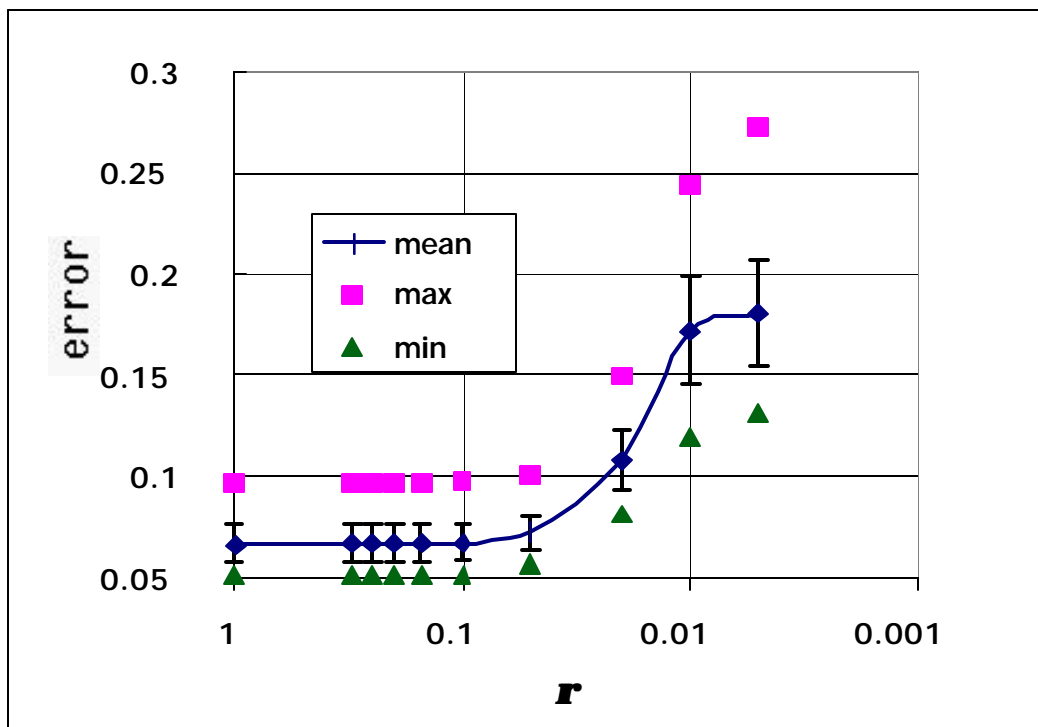


Figure 4. Wavefront relative error

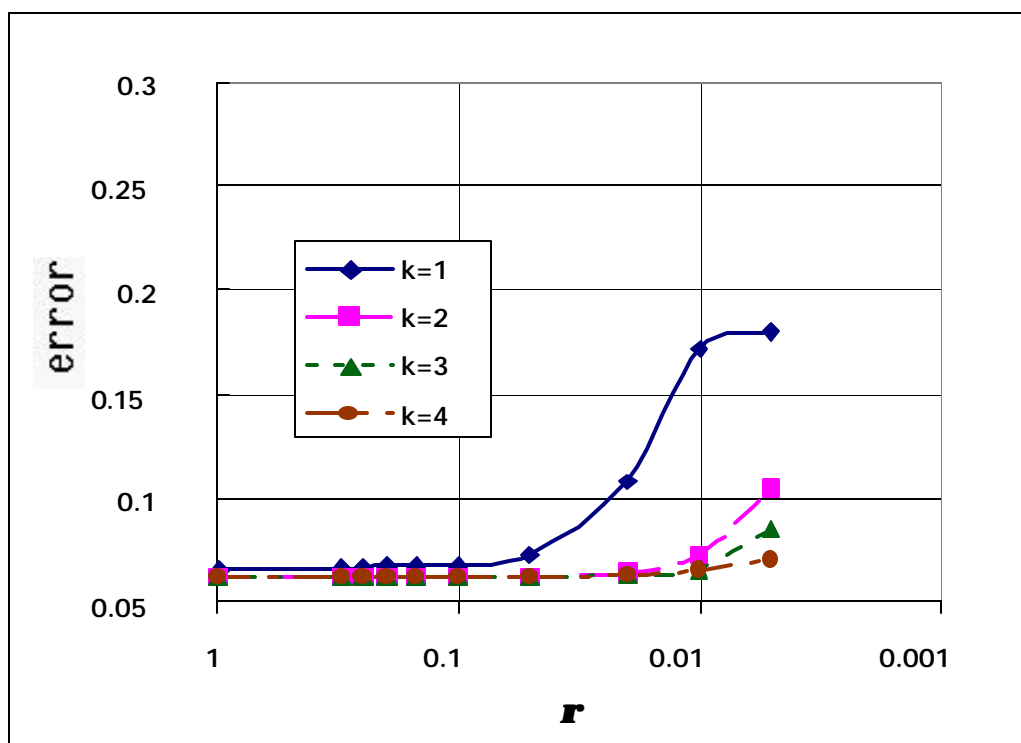


Figure 5. Mean wavefront relative error for 4 iterations.

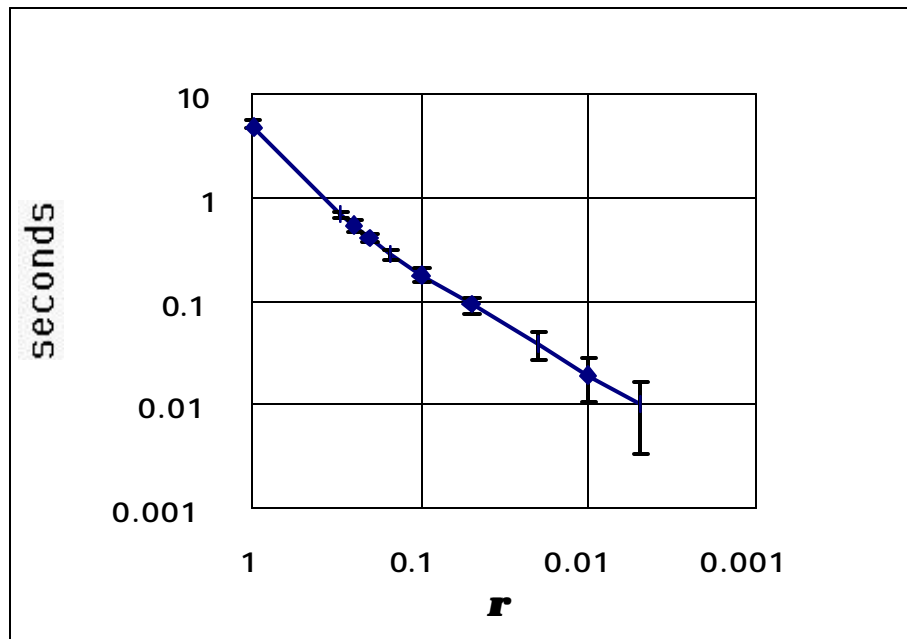


Figure 6. Calculation time.

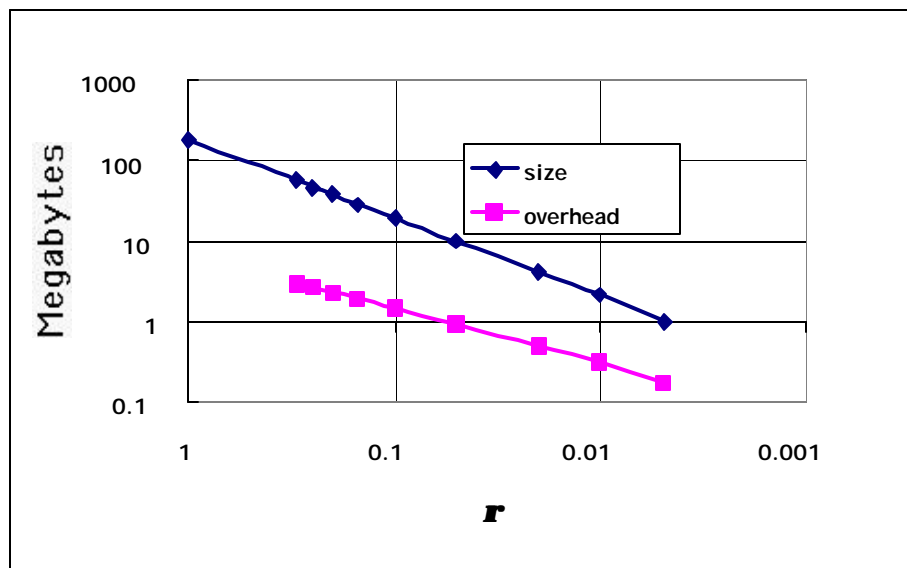


Figure 7. Matrix sizes and overhead.

The Application of Radio Astronomy Algorithms to Imaging Interferometry for SPECS, SPIRIT, and WIIT

Xiaolei Zhang (Raytheon ITSS / NASA GSFC)
Lee Mundy and Peter Teuben (University of Maryland)

ABSTRACT

In this paper, we survey the mosaic image reconstruction algorithms commonly used in radio astronomy. We discuss possible extensions of these techniques for applications in the planned SPECS (the Submillimeter Probe of the Evolution of Cosmic Structure) and SPIRIT (the SPace InfraRed Interferometric Telescope) missions. We outline the specific revisions that need to be made to the existing astronomical software packages in order to process the data acquired in the Wide Field Imaging Interferometry Testbed (WIIT), and to prepare us for the eventual processing of the data acquired from the space far-infrared interferometry missions.

INTRODUCTION

The technique of linear and nonlinear mosaic reconstruction of interferometry images has evolved from the practice of radio astronomy during the past two decades. In the recent effort to develop next generation space interferometry missions in the far infrared and submillimeter, i.e. SPECS and SPIRIT (Mather et al. 2000), which will be used for the study of the formation and evolution of galaxies and structures in the early universe, it is recognized that the heritage of the image reconstruction techniques developed in radio astronomy can be put to good use, and thus give us a head start in arriving at algorithms which can meet the specific requirements of space interferometry.

In what follows, we will first review image reconstruction principles and techniques. We then discuss the image reconstruction routines in existing astronomical software packages, and their possible extension for application to the SPECS and SPIRIT missions. The WIIT testbed (Leisawitz et al. 1999, Zhang 1999) under construction at Goddard will be used for the development and testing of many of the algorithms and routines intended for the eventual space interferometry applications.

MOSAIC IMAGE RECONSTRUCTION IN RADIO ASTRONOMY

For a source confined to a small region of the sky surrounding coordinate center (0,0), the source intensity distribution $I(l,m)$ near (0,0) and the visibility function $V(u,v)$ measured by a Michelson interferometer with pointing and phase reference center both at (0,0) satisfy a two-dimensional Fourier transform relation

$$A(l,m) \cdot I(l,m) = \int_{-\infty}^{\infty} \int_{-\infty}^{\infty} V(u,v) e^{2\pi i(ul+vm)} du dv \quad (1)$$

where $A(l,m)$ is the primary beam response of the single antenna/collector mirror. In the above expressions l,m are coordinates on the sky, and u,v are the coordinates in spatial frequencies. A detailed description of the definition of the above coordinate system as well as the derivation of the Fourier transform relation can be found in Clark (1989).

A two-element interferometer of baseline separation B in principle can measure spatial frequencies in the range of $(B-D, B+D)$, where D is the diameter of the single antenna dish. However, for a single pointing observation, the spatial frequency obtained by a two-element interferometer is only that corresponding to baseline B . As shown in Ekers and Rots (1979), if one observes instead a series of pointings (l_0, m_0) , and stamps the measured visibility by both the pointing and baseline coordinates, i.e. $V = V(u, v; l_0, m_0)$, then in principle one can recover the u, v in the entire range $(B-D, B+D)$, through the use of the following Fourier transform relation with respect to the pointings (l_0, m_0) :

$$\int_{-\infty}^{\infty} \int_{-\infty}^{\infty} V(u_0, v_0, l_0, m_0) \cdot e^{-2\pi i(u l_0 + v m_0)} dl_0 dm_0 \quad (2)$$

$$= FT(A)(u_0, v_0) FT(I)(u_0 + u, v_0 + v),$$

where $FT(A)(u_0; v_0)$; $FT(I)(u_0; v_0)$ are the Fourier transform of $A(l, m)$ and $I(l, m)$, respectively, and where $V(u_0; v_0; l_0; m_0)$ is defined through the familiar relation between sky brightness and visibility, with the relevant quantities stamped by the pointing location of the primary beam

$$V(u_0, v_0, l_0, m_0) \equiv \int_{-\infty}^{\infty} \int_{-\infty}^{\infty} A(l, m, l_0, m_0) I(l, m) \cdot e^{-2\pi i(u_0 l + v_0 m)} dl dm. \quad (3)$$

In the measurement defined above, the visibility is measured with the interferometer having delay and phase reference center (0,0), and primary beam pointing center (l_0, m_0) . In practice, scanning for the continuous pointing range is not required, because the Fourier transform of the primary beam is band-limited. The Nyquist criterion tells us that $V(u, v, l_0, m_0)$ is fully specified by its values sampled on a regular grid in l_0, m_0 with the grid spacing equal to $\lambda=2D$. In the applications for SPECS, SPIRIT and WIIT, the multiple pointings are equivalently accomplished by a Nyquist-spaced large-format detector array on the focal plane.

The above scheme due to Ekers and Rots (1979) for a two element interferometer is often replaced in practice by the following alternative mosaic joint-deconvolution scheme for measurements using an interferometer array (Cornwell 1989). In this approach we maximize the entropy

$$H = -\sum_k I_k \ln \frac{I_k}{M_k e} \quad (4)$$

subject to the constraint of χ^2 :

$$\chi^2 = \sum_r \frac{|V(u_r, v_r, l_{0r}, m_{0r}) - \hat{V}(u_r, v_r, l_{0r}, m_{0r})|^2}{\sigma_{V(u_r, v_r, l_{0r}, m_{0r})}^2} \quad (5)$$

where I_k represents the model image, M_k represents the default image incorporating one's best prior knowledge of the recovered image, e is the base of the natural logarithm, $V(u_r, v_r, l_{0r}, m_{0r})$ is the observed visibility function at the baseline location u_r, v_r and sky location l_{0r}, m_{0r} , $\hat{V}(u_r, v_r, l_{0r}, m_{0r})$ is the model visibility distribution, and $\sigma_{V(u_r, v_r, l_{0r}, m_{0r})}$ is the rms noise of the measurement.

In this scheme, deconvolution is performed simultaneously with the untangling of information available at the various spatial frequencies. Since the required deconvolution is nonlinear, this approach yields better results especially for image points located near the overlapping boundaries of the different pointing positions. over the image field, as well as the addition of zero spatial frequency information.

EXISTING ASTRONOMICAL SOFTWARE

The maximum entropy (MEM) joint deconvolution approach presented above is implemented in the astronomical software package AIPS (which stands for Astronomical Image Processing Software) as one variation of the task VM. It is a nonlinear mosaic procedure which combines the measured visibility data *during* the deconvolution phase. Another variation of the non-linear joint deconvolution approach is developed by Sault et al. (1996). This approach combines the dirty images *before* the deconvolution process, and the subsequent deconvolution can be performed using either the maximum entropy or the CLEAN algorithm. This approach is implemented in the astronomical software package MIRIAD (which stands for Multi-channel Image Reconstruction, Image Analysis and Display) as the tasks MOSMEM (the version using MEM) and MOSSDI (the version using CLEAN). A third variation of the deconvolution approach is a linear mosaic procedure, implemented as the MIRIAD task LINMOS. In this approach the clean images are combined after

they are individually deconvolved using either CLEAN or MEM. Single dish data can be added using the task IMMERGE. Each of the above mosaicing algorithms can yield relatively superior result depending on the characteristics of the imaged object, as well as on our knowledge of the observing instrument such as pointing stability and the primary beam shape. The applicability of each algorithm to the space interferometer observation of different types of objects under different configurations therefore need to be further investigated.

When the existing radio astronomy packages and routines are applied to WIIT, SPIRIT and SPECS, changes are expected especially in the area of input format and spectral data processing. This is so because the existing packages all assume a receiver/correlator combination, whereas the above three Michelson interferometers will use the delay line/direct detector combination. Significant modeling capabilities also need to be added into the existing software packages. Widefield Imaging Interferometry Testbed is designed to facilitate experimentation with the approaches to beam combination, signal detection, as well as algorithm development for data analysis. By carefully modeling the testbed as an integrated system we expect to learn where the significant error sources lie, how to achieve the best possible synthesized image quality, and ultimately, how to design the SPIRIT and SPECS space instruments.

REFERENCES

- Clark, B.G. 1989, "Coherence in Radio Astronomy", in Synthesis Imaging in Radio Astronomy, ASP Conf. Ser. vol. 6, eds. R.A. Perley, F.R. Schwab, & A.H. Bridle, p.1
- Cornwell, T.J. 1989, "Wide Field Imaging III: Mosaicing" , in Synthesis Imaging in Radio Astronomy, ASP Conf. Ser. vol. 6, eds. R.A. Perley, F.R. Schwab, & A.H. Bridle, p.277
- Ekers, R.D., & Rots, A.H. 1979, "Short Spacing Synthesis from a Primary Beam Scanned Interferometer," Proc. IAU Coll. 49, Image Formation from Coherence Functions in Astronomy, C. van Schooneveld, Ed., D. Reidel (Dordrecht, Holland), p. 61
- Leisawitz, D. et al. 1999, "Wide Field Imaging Interferometry", NASA proposal NRA-99-01-SPA-020.
- Mather, J., Moseley, S. H., Leisawitz, D., Dwek, E., Harwit, M., Mundy, L. G., Mushotzky, R. F., Neufeld, D., Spergel, D., Wright, E. L., & Zhang, X. 2000, "The Submillimeter Probe of the Evolution of Cosmic Structure", submitted to the Review of Scientific Instruments.
- Sault, R.J., Staveley-Smith, L. & Brouw, W.N. 1996, "An approach to interferometric mosaicing", A&A, 120, 375
- Zhang, X. 1999, "Preliminary Design Considerations for the Wide-Field Imaging Interferometry Testbed (WIIT)", SPECS technical memo.

A Two-dimensional Mathematical Formulation of Inhomogeneous Electromagnetic Waves in Photorefractive Polymer

Shahram Shiri, Murray Loew, Richard Lyon, Wasyl Wasylkiwskyj
(George Washington University, Washington, DC, 20037)(ML, George Washington University, Washington, DC, 20037)(RL, Goddard Space Flight Center, Greenbelt, MD 20771)(WW, George Washington University, Washington, DC, 20037)

ABSTRACT

The photorefractive polymer based holographic memories provide the alternative of achieving terabytes of digital data storage with gigabits per seconds of transfer. The stored information in the medium is in the form of electromagnetic distribution and it is governed by the second order inhomogeneous Helmholtz equations with no known exact solution. A numerical approximation using finite element method is employed to model the wave propagation in the inhomogeneous material of photorefractive polymer. The initial results from the mathematical formulation conform to the theoretical expectation of coupled-wave theory in the non-conducting and non-magnetic materials. The model is used to simulate electromagnetic wave propagation through a two-dimensionally varying index of refraction poly (N-vinylcarbazol) (PVK) polymer. The transmissive waves are computed at various angles of incidents. A hundred percent diffraction efficiency was achieved through the simulation process by changing the coupling coefficient between the writing beams.

Keywords: Volume Holographic Storage, Finite Element, Numerical Simulation, and Inhomogeneous Medium

INTRODUCTION

The information age has brought with it an ever-increasing demand for storage devices with high capacity, fast data-transfer rate, and short access time. The optical memories already play an important role in the existing commercial systems such as magneto-optical, CDROM, and multi-layer optical-disk-based storage. However, this technology falls short of providing terabytes of data storage capacity with gigabits per second of data transfer rate. As an alternative to above, the volume holographic optical memories with advances in the spatial-light-modulator (SLM) and charge-coupled-devices (CCD) have made it possible to demonstrate this concept of high capacity storage using photorefractive polymers with fast transfer rate by means of parallel access, and short access time by means of non-mechanical scanning.

The volume holographic recording is accomplished by combining an image bearing light beam and a reference beam in the form of interference patterns in the recording medium (Figure 1).

Holographic Optical Storage System Read/Write Process Diagram

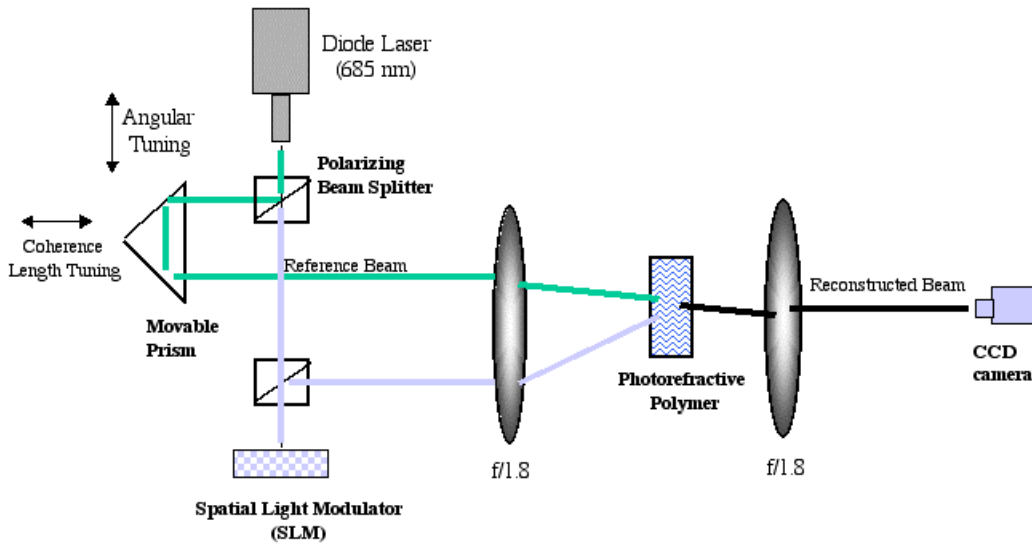


Figure 1: A holographic optical storage system consists of a diode laser, beam splitter, movable prism, spatial light modulator (SLM), lenses to focus the beam into/out of recording medium, and a CCD camera.

volume. In the photorefractive medium the charges are excited from impurity regions in the presence of light and subsequently trapped. The resulting space-charge field causes modulation in the index of refraction through the electro-optic effect. When the medium is exposed to a reference beam identical to the original one used in the recording, the light will diffract to reproduce the original image-bearing wavefront. In this technique, the digital data are converted to optical signal using the SLM. A hologram corresponding to one data-page of SLM is recorded in a photorefractive medium. Multiple holograms are written in the medium using various multiplexing approaches such as angular multiplexing corresponding to each data-page. Readout of the stored data-page involves illuminating the medium with appropriate reference beam and imaging the diffracted optical signal onto a CCD array, which converts the optical signal back to a digital data. With parallel read-out of CCD array all pixels in a stored data page are reconstructed and fast data transfer rates can be achieved.

The main criteria used in evaluating the performance of a holographic storage system are 1) capacity, 2) data transfer rate, 3) access time, 4) and bit-error rate. In this evaluation, the data transfer rate and access time are limited by the supporting technologies such as CCD array and beam steerers while the medium capacity and the bit-error-rate are determined by the presence of contributing noise sources to the overall system design ¹. With the increase of stored holograms, the diffraction efficiency of medium falls proportionally. As the diffraction efficiency drops the signal-to-noise ratio (SNR) decreases due to light beam scattering in the medium. Therefore, the number of stored holograms is determined by the minimum acceptable SNR. The optical hologram memories based on photorefractive effects have the potential to become the large capacity, high throughput, low powered and small volume devices that could become commercially available and/or used in various medical projects. In order to achieve a viable holographic storage system which supersedes the current technologies, the capacity of storage device should be in the terabytes of data, the data transfer rate should reach the gigabits per seconds, with minimal access time and bit-error-rate of less than 10^{-12} .

REVIEW OF APPROACHES

A review of the literature shows that for the past several years holographic data storage has been an active field of research. In a number of investigations, a variety of address-multiplexing schemes such as wavelength², angle³, phase⁴, shift, and peristrophic⁵ multiplexing have been used.

Since holographic storage system offer multi-dimensional access to the addressed data, it is possible to hybridize multiplexing approaches to take advantage of the positive aspects each method may have to offer. In hybridization, two or more pure multiplexing approaches are utilized. For example, the shift and/or the peristrophic multiplexing actually is composed of angle and phase multiplexing with additional use of some limited spatial multiplexing.

Until recently, the most commonly utilized recording medium in the investigations was the inorganic photorefractive crystals such as Sodium Niobate (LiNbO₃). Some of the attractive properties of the crystals are their reversibility, erasability, potentially useful response time, sensitivity, and dynamic range. Some of the undesirable properties are difficulty in the production of high optical quality crystals, fast hologram decay in the dark, the reversibility in a sense that it leads to erasure of stored information during subsequent writing and reading of data. However, improvements in the diffraction efficiencies of organic photorefractive polymer composites such as poly-vinyl carbazole: 40% 3-fluoro-4-N,N diethylamino-methyl Beta nitrostyrene: 0.2% C60 (PVK: FDEAMNST:C60) has made them more advantageous than the inorganic crystals. The composites are more easily fabricated, can be formed into large area films, and are significantly less expensive to manufacture⁶. In addition they can also be modified to permit optimization for a given application. In these high performance materials the different functionality required for photorefractivity such as the photoinduced carrier generation, photoconductivity, and electro-optic effect, are provided by different molecular components that are mixed together (Figure 2).

Despite all the advancements in the inorganic crystals, the polymers require totally different wavelengths and geometries for recording and readout of holograms. The research in the photorefractive polymer is still in its infancy and a lot of issues and practical limitations have to be resolved before a commercial system becomes available. Some of these limitations are due to cross-talk effects, beam depletion and material heating absorption effects, recording medium dynamic range, and multiplexing approaches. Resolving these limitations requires repetitive experiments with the goal of analyzing and determining an accepted range for each optical component involved in the process and its contribution to the overall system error. In practice, undertaking such experiments is costly and time consuming⁷.

PHOTOREFRACTIVE EFFECT

The photorefractive effect was accidentally discovered in 1966 in Sodium Niobate (LiNbO₃) as detrimental optically induced refractive index inhomogeneities. It was referred to as 'optical damage' because it caused a degradation of the performance of nonlinear optical devices based on these materials. A few years later, holographic optical storage was demonstrated in LiNbO₃ using newly discovered effect. The term photorefractive, which literally means light induced change of the refractive index, was introduced later on and since then has been reserved for this particular mechanism. In figure2, the basic mechanism is explained. The photorefractive effect is observed in materials that are both electrooptic and photoconducting. If such a sample is illuminated with a nonuniform light intensity pattern resulting from the interference of two mutually coherent beams, charge generation will take place at the bright areas of the fringes. These photogenerated charges will migrate and eventually get trapped at the dark areas, a process, which can take place through several circles of photogeneration, diffusion, and trapping. The resulting charge redistribution creates an internal electric field, the space charge field, which changes the refractive index via electrooptic effect. The space charge field forces the charges to drift in the opposite direction than diffusion and a dynamic equilibrium is reached when it has grown strong enough to cause a drift current which totally compensates the diffusion current. Application of an external electric field assists charge separation through drift and generally a higher space charge field can be produced in this way⁸.

Photorefractive Effect

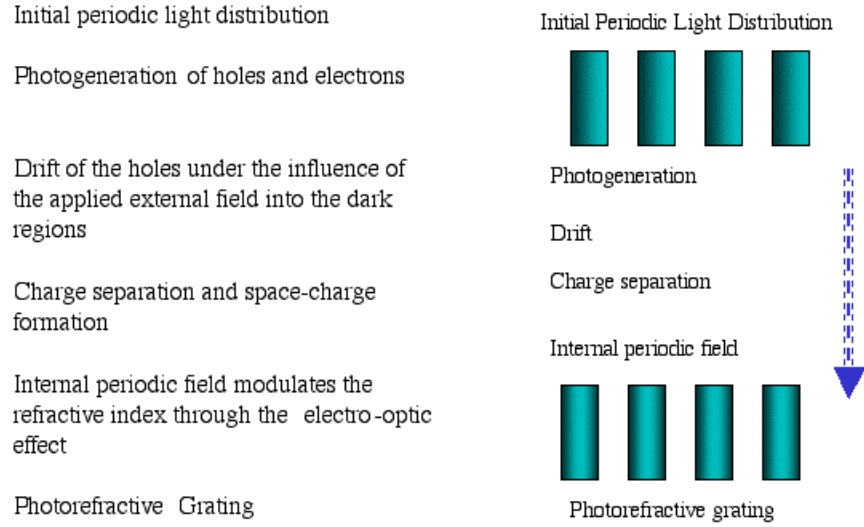


Figure 2: The photorefractive effect process from initial period light distribution, photogeneration, drift, charge separation, internal periodic field and creation of photorefractive grating.

When a photorefractive polymer is illuminated by an interference of two sinusoidal writing beams, the refractive index of the material is changed by the spatial variation of the light intensity given by $I = 2 I_0 [1 + m \cos(k_g \cdot r)]$, where I_0 stands for the intensity of the writing beams, k_g , for the grating wave vector, and m for the intensity modulation depth. The resulted refractive index grating is given by, $n(r) = n_0 + \Delta n(r)$, where n_0 is the equilibrium refractive index and $\Delta n(r) = \Delta n \cos(k_g \cdot r - \mathbf{j})$. The phase \mathbf{j} is the phase shift between the light interference and the refractive index gratings.

THE FORMULATION OF ELECTROMAGNETIC FIELD IN THE PHOTOREFRACTIVE POLYMER

The electromagnetic field in the polymer is an electrodynamic process, which is governed by Helmholtz equation in an inhomogeneous medium with spatially varying index of refraction in three dimensions. The electric field distribution in the medium can be represented by $\nabla^2 \vec{E}(\vec{r}) + k_0^2 \epsilon(\vec{r}) \vec{E}(\vec{r}) = \nabla(\nabla \ln \epsilon(\vec{r}) \cdot \vec{E}(\vec{r}))$, where $\epsilon(\vec{r})$ is the permittivity of photorefractive polymer, and k_0^2 is the wave vector. The above equation describes the field distribution which has already reached a steady-state or equilibrium state and hence it is independent of time factor. In addition, the right hand side represents the coupling of the fields in the inhomogeneous medium.

Geometry of Two-dimensional Problem

The electromagnetic field distribution in the medium can be modeled in terms of a spatially varying two-dimensional permittivity $\epsilon(x, y)$. The permeability, μ , in the medium is assumed to be constant. Figure 3 depicts the geometry of electric field propagation into the medium,

Geometry of Two-Dimensional Problem

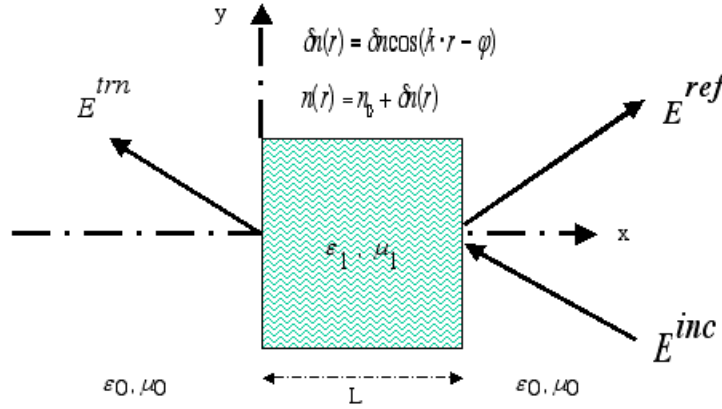


Figure3: Geometry of two-dimensional problem, The incident field is a polarized electric field plane wave perpendicular to the propagation direction on the right side of the medium.

In this geometry the incident field is a polarized field plane wave perpendicular to the propagation direction on the right side of the medium. Index of refraction is varying in two dimensions. Also, in this formulation it is assumed that the index of refraction changes are small such that, $\nabla(\nabla \ln \epsilon(\vec{r}) \cdot \vec{E}(\vec{r})) = 0$.

Finite Element Formulation of Electromagnetic Problem

In order to compute the field propagation in the medium, finite element of Rayleigh-Ritz method in two-dimension is employed⁹. For this purpose, the problem is subdivided into two regions, 1) field in the dielectric medium and 2) fields in the open space (right side of the medium representing the reflective/incident fields and left side of the medium representing the transmissive field). The incident wave is represented by an electrically polarized plane wave perpendicular to the propagation direction,

$$E_z^{inc}(x, y) = E_0 e^{-jk_0(-x \cos(\theta) + y \sin(\theta))}.$$

The scalar Helmholtz equation governing the electric field in the medium can be written as,

$$\frac{\partial}{\partial x} \left(\frac{1}{\mu_r} \frac{\partial E_z}{\partial x} \right) + \frac{\partial}{\partial y} \left(\frac{1}{\mu_r} \frac{\partial E_z}{\partial y} \right) + k_0^2 \epsilon_r(x, y) E_z = 0 \quad \text{Equation (1)}$$

Where μ_r is constant through out the medium and $\epsilon_r(x, y)$ is a scalar changing in x and y direction.

In order to solve the problem, the evaluated Helmholtz equation governing the fields in the right side and left side of the medium is used as boundary condition for the medium. Once the field in the medium is computed, its propagation on the two sides of the geometry derives the reflective and transmissive fields.

NUMERICAL VERIFICATION AND RESULTS

In order to validate the model, an electric field is propagated through the medium where the following scenarios are investigated and validated,

- 1) Propagation through a homogeneous medium with index of refraction close to the equilibrium index of refraction of photorefractive polymer (PVK, $n=1.7$).
- 2) Angular propagation (-45 to 45 degrees) of incident beam into the medium.

- 3) Propagation through an inhomogeneous medium with index of refraction varying in either x or y direction.
- 4) Propagation of the beam through an aperture with width smaller than the wavelength of the incident light to width greater than the wavelength of the light.
- 5) Propagating through a dielectric slab with zero input reflection coefficient.

Figure 4 shows the Zero Input Reflection Coefficient when the medium is assumed to be a dielectric slab of $n=1.7$. Figures 5 shows the distribution of electric field through the medium where the index of refraction changes only in the horizontal direction. Figures 6 shows the field distribution through the polymer when the index of refraction changes only in the vertical direction. Figure 7 shows the distribution when the permittivity changes in both x and y direction. In all the simulations, an equilibrium index of refraction of 1.7 was selected to match the PVK polymer base index of refraction. No constraints were imposed on the upper and lower boundaries of the medium. Figure 8 shows the electric field propagation through the medium assuming the existence of aperture on the right side.

Dielectric Slab: Zero Input Reflection Coefficient

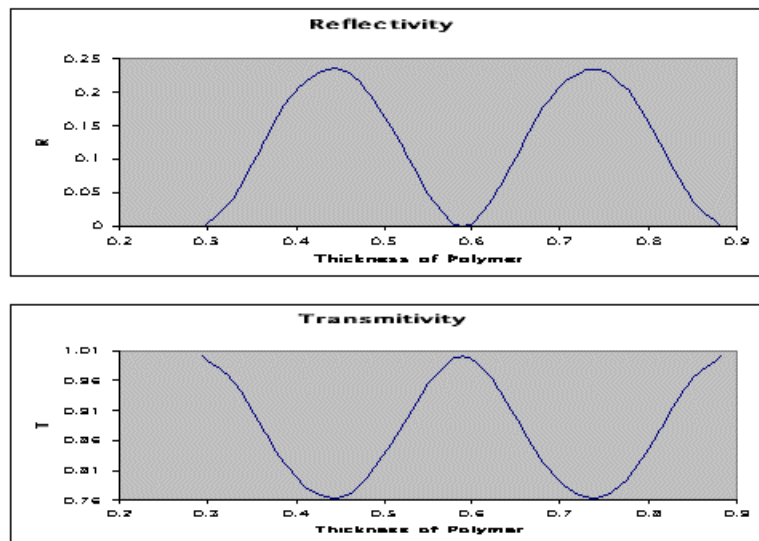


Figure 4: A beam propagating to recording medium with index of refraction = 1.7, the reflectivity coefficient is zero at $d = \frac{\pi\lambda}{2}, d = \frac{3\lambda}{2}$. The transmittivity coefficient for the above geometry is 1.0 when reflectivity is zero.

Electric Field Propagation Through Recording Medium with Index of Refraction Changing in x Direction

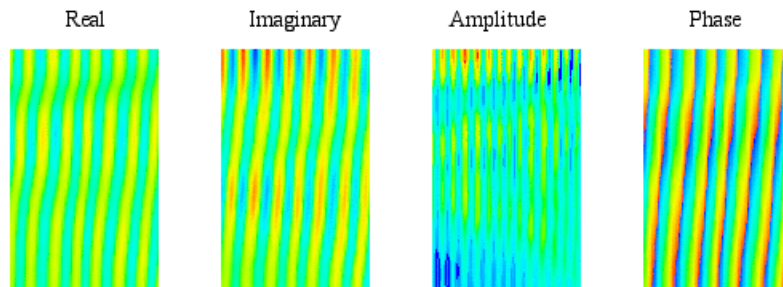


Figure 5: Simulation of electric field distribution through photorefractive polymer with index of refraction changing in only x-direction. The angle of incident is 15 degrees. The beam has wavelength of 500 nm. The medium thickness is 4 times the wavelength. The equilibrium index of refraction for the medium is 1.7.

Electric Field Propagation Through Recording Medium with Index of Refraction Changing in y Direction

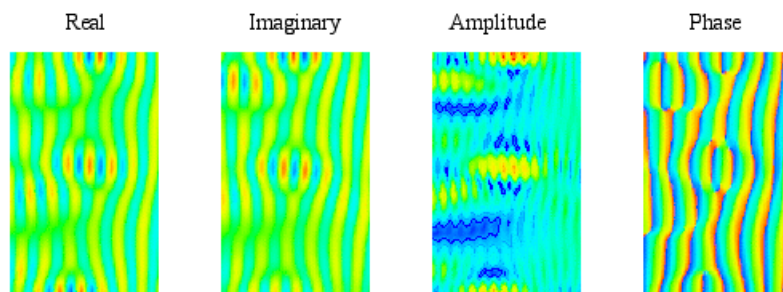


Figure 6: Simulation of electric field distribution through photorefractive polymer with index of refraction changing in only y-direction. The angle of incident is 15 degrees. The beam has wavelength of 500 nm. The medium thickness is 4 times the wavelength. The equilibrium index of refraction for the medium is 1.7.

Electric Field Propagation Through Recording Medium with Index of Refraction Changing in x & y Direction

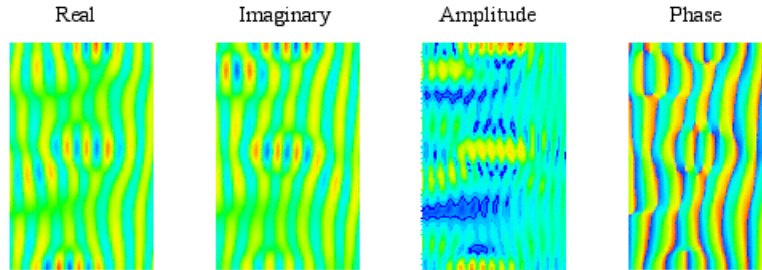


Figure 7: Simulation of electric field distribution through photorefractive polymer with index of refraction changing in only x & y direction. The angle of incident is 15 degrees. The beam has wavelength of 500 nm. The medium thickness is 4 times the wavelength. The equilibrium index of refraction for the medium is 1.7.

Electric Field Propagation Through An Aperture on the Right Side of Recording Medium with Index of Refraction 1.7

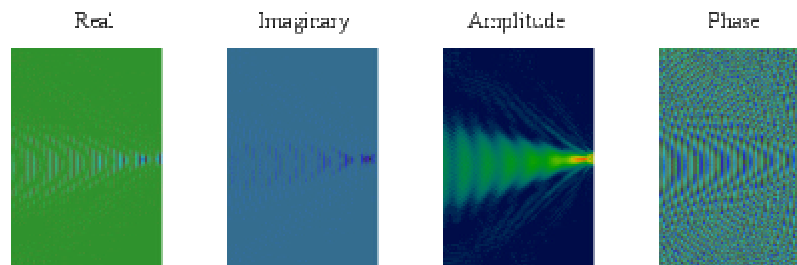


Figure 8 Simulation of electric field distribution through an aperture on the right side of photorefractive polymer with index of refraction 1.7. The beam has wavelength of 500nm

ACKNOWLEDGEMENTS

This work was supported in part by a grant from NASA, Goddard Space Flight Center, Code 930, Greenbelt, MD 20771. The numerical simulation was performed on HIVES parallel computer under direction of Dr. John E. Dorband.

CONCLUSION

In this study we have mathematically formulated the propagation of the electromagnetic field (specifically electric field) in the photorefractive polymer and numerically simulated such propagation in two-dimensionally spatial-varying index of refraction. The reflective field and transmissive field surrounding the medium have been computed and the results agree with the theoretical expectation of coupled-wave theory. On continuation of this study we plan to include the coupling of beams such that the variation is not slow and then continue the simulation effort to more realistic scenario of three-dimensional spatial-varying index of refraction.

REFERENCES

1. S. Jutamulia and George M. Storti, "Three-dimensional optical storage", *Optical Storage and Retrieval: Memory, Neural Networks, and Fractals*, F. T. U. Yu, S. Jutamulia, pp. 109-139, 1996.
2. G. A. Rakuljic, V. Leyva, and A. Yariv, "Optical data Storage by using orthogonal wavelength multiplexed volume holograms", *Optics Letters*, **17**, pp. 1471-1473, 1992.
3. S. Campbell, X. Yi, and P. Yeh, "Hybrid sparse-wavelength angularly multiplexed optical data storage", *Optics Letters*, **19**, pp. 2161-2163, 1994.
4. J. Lembcke, C. Denz, T. Tschudi, "General formalism for angular and phase-encoded multiplexing in", *Optics Letters*, **4**, pp. 428-432, 1995.
5. A. Pu, G. Barbestathis, M. Levene, and D. Psaltis, "Shift multiplexed holographic 3-D disk", *Optical Computing Technical Digest*, (Optical Society of America, Washington, DC., 1995), **10**, pp. 219-221, 1995.
6. M. E. Orczyk, J. Zieba, and P. N. Prasad, "Holographic diffraction in polymeric thin films: Influence of slanted grating experimental geometry", *Nonlinear Optics*, **12**, pp. 153-163, 1995.
7. P. M. Lundquist, C. Poga, R. G. DeVoe, Y. Jia, and W. E. Moerner, "Holographic digital data storage in", *Optics Letters*, **21**, No. 12, pp. 890-892, 1996.
8. A. M. Glass, "The photorefractive effect", *Optical Engineering*, **17**, No. 5, pp. 470-479, 1978.
9. J. Jin, *The Finite Element Method in Electromagnetics*, pp. 72-135, John Wiley & Sons, Inc., 1993.

Superresolution Using Laplace Filter on Isophote Ridges

David Maker
Teledyne Brown Engineering
david.maker@tbe.com

The mathematical problem is to extract PSF centers X_i, Y_i and amplitudes k_i from one single (noncoherent) intensity function for a circular aperture. Thus the functions $k_i(J_i(R_i)/R_i)^2$ must be disentangled from:

$$I(x, y) = \sum_{M=1}^N k_i \left(\frac{J_i(R_i)}{R_i} \right)^2, \text{ with } R_i = \sqrt{(X_i - x)^2 + (Y_i - y)^2 + (Z_i - z)^2} \quad (1)$$

given some noise. So we must somehow solve for X_i and Y_i and k_i . Specifically we are concerned here with PSFs that are closer than the Rayleigh limit, the problem of superresolution.

In this regard we start by writing down derivatives of an individual PSF in $I(x, y)$:

$$\begin{aligned} I_i(x, y) &= k_i \left(\frac{J_i(R_i)}{R_i} \right)^2 = k_i (J'_i(R_i) + J_2(R_i))^2 = \\ &= \left(\frac{1}{2} k_i (J_o(R_i) - J_2(R_i)) + J_2(R_i) \right)^2 = k_i \left(\frac{1}{2} (J_o(R_i) + J_2(R_i)) \right)^2 \end{aligned} \quad (2)$$

So,

$$\begin{aligned} \frac{dI_i(x, y)}{dR} &= k_i \left(\frac{2}{2} (J'_o(R_i) + J'_2(R_i)) (J_o(R_i) + J_2(R_i)) \right) = \\ &= k_i \left(\frac{2}{2} \left(-J_1(R_i) + \frac{1}{2} (J_1(R_i) - J_3(R_i)) \right) (J_o(R_i) + J_2(R_i)) \right) \\ &= k_i \left(-\frac{1}{2} (J_1(R_i) + J_3(R_i)) (J_o(R_i) + J_2(R_i)) \right) = \text{first derivative.} \end{aligned} \quad (3)$$

But $J_1(R_i) \& J_3(R_i) = 0$ at $R=0$ so at $R=0$ we have $I'(x, y) = 0$. To get the second derivative: $I''(x, y) =$

$$I''(x, y) = k_i \left(-\frac{1}{2} (J'_1(R_i) + J'_3(R_i)) (J_o(R_i) + J_2(R_i)) + (J_1(R_i) + J_3(R_i)) (J'_o(R_i) + J'_2(R_i)) \right) \quad (4)$$

(not writing the R dependence so the our expressions can be written more succinctly)

$$\begin{aligned} k_i \left(-\frac{1}{2} ((J_0 - J_2) + (J_2 - J_4)) (J_0 + J_2) + (J_1 + J_3) \left(-J_1 + \frac{1}{2} (J_1 - J_3) \right) \right) = \\ k_i \left(-\frac{1}{2} ((J_0 - J_4)) (J_0 + J_2) - \frac{1}{2} (J_1 + J_3)^2 \right) = \end{aligned} \quad (5)$$

(At $R=0$ $J_4=0, J_2=0, J_1=0, J_3=0$) $= -\frac{1}{2} k_i J_0^2 = \text{second derivative}$

So the modulus of the second derivative is maximum at $R=0$ since J_0 is maximum there. Again at $R=0$ the first derivative $= 0$ and $|\text{second derivative}| = \text{maximum}$. And you can characterize a function by its derivatives (as in a Taylor expansion).

We **conjecture** here that the above derivative results for a single PSF near $R=0$ survive as orthogonal partial derivatives even when several PSFs are very close together. This we claim is the solution to the superresolution problem.

There are many deconvolution algorithms (using Fourier transforms for example) that allow us to calculate k_i and R_i given the imaged values of $I(x_i, y_i)$. The problem arises when the psf's are closer than a Rayleigh length: the number of artifact images (false images) available for a deconvolution algorithm to stumble onto is then very large. Thus the probability of a false deconvolved image is very large. This is the ambiguous image problem first identified by Toraldo di Francia(1955).

In that regard we identify three regions and associate with each of these regions the probability density of a deconvolution resulting in an artifact (or false) image. $P_1(x_1, y_1)$ let's say is the probability density inside regions (or set of points) of small tangential derivatives $\{x_1, y_1\}$. Thus we take our tangential derivative:

$$dI(x, y)/d\phi = 0, \quad (6)$$

which is the first derivative taken tangentially to a circle around the point of highest intensity in a given imaged blob (in practice we find the minimums of this derivative on the circle). This gives us the set $\{x_1, y_1\}$ which become "ridges" on the isophote presentation of the image. We parameterize these ridge line $\{x_1, y_1\}$ regions with a distance parameter we call "s". But also along "s" we have regions $\{x_2, y_2\}$ of largest Laplace filter return, i.e., have largest modulus of the second derivatives. The probability density of artifacts here let's say is $P_2(x_2, y_2)$. So let:

$$|\nabla^2 I(x, y)| = |\partial^2 I(x, y)/\partial s^2| \quad (7)$$

be the modulus of the partial second derivative along those $\{x_1, y_1\}$ ridge lines and so it is taken orthogonal to the direction the first derivative is taken (implied by our conjecture). And let the Actual region where the PSFs centers are located be $\{x_A, y_A\}$. The probability density of artifacts (i.e., $P_A(x_A, y_A)$) here of course is zero. The probability density of artifact images outside these three regions let's say is $P_o(x_o, y_o)$ and is very high inside the Rayleigh region. The total probability for deconvolved false artifact solutions is then:

$$\int P(x, y) dA = \int P_o(x_o, y_o) dA + \int P_1(x_1, y_1) dA + \int P_2(x_2, y_2) dA. \quad (8)$$

(counting overlap regions only once and taking maximum P in overlap region)

But according to our above conjecture (concerning the PSF derivatives) the regions of highest Laplace filter return and smallest tangential first derivative (each being orthogonal to the other) intersect at the PSF points i.e., $\{x_1, y_1\} \cap \{x_2, y_2\} = \{x_A, y_A\}$. Note this excludes the second derivative high points on the circular diffraction pattern outside the central blobby Airy PSF region which would be a problem if we only used the Laplace filter. But the probability for an artifact: $\int P(x, y) dA > \int P_A(x_A, y_A) dA$ and $P_A(x_A, y_A) = 0$ so we Decrease the probability of getting such an artifact a great deal by restricting our deconvolution to the $\{x_1, y_1, z_1\} \cap \{x_2, y_2\}$ region which is the intersection of the $\{x_1, y_1\}$ and $\{x_2, y_2\}$ regions. In this way we solve the ambiguous image problem.

We then use numerical relaxation deconvolution (which we prove below to be equivalent to a least squares deconvolution) on the region intersecting the Laplace filter maxima and the small tangential derivatives to solve for the respective k_i s and further delineate the boundaries of the $\{x_A, y_A\}$ region since they appear fuzzy due to noise. The noise problem is also addressed by "smoothing" once.

Numerical Relaxation and Least Squares

Let $\bar{I}(X_i, Y_i) = \sum_{j=1}^N k_j \left(\frac{J_1(R_{ij})}{R_{ij}} \right)^2$ where $\bar{I}(X_i, Y_i)$ is the measured data intensity at the point

(X_i, Y_i) and $I(X_i, Y_i)$ will be the intensity that we will get from the result of our deconvolution (ie.,3).

The square of the error \mathbf{h} using equation (2) is written as:

$$\sum_{a=1}^N (I(X_a, Y_a) - \bar{I}(X_a, Y_a))^2 = \mathbf{h}^2 \quad (9)$$

and the least squares algorithm is done by taking the extrema of \mathbf{h}^2 with respect to the est choices of PX and PY in equation (1). \bar{I} is not minimized with respect to PX and PY since it is pure data and "l(x,y)" is an unknown function of PX and PY. To find l(x,y) it is necessary to take derivatives with respect to PX and PY:

$$\frac{\mathcal{I}}{\mathcal{I}(PX)} \left(\sum_{a=1}^N (I(X_a, Y_a) - \bar{I}(X_a, Y_a))^2 \right) = 0 \quad (10)$$

$$\sum_{a=1}^N 2 \left(\frac{\mathcal{I}}{\mathcal{I}(PX)} I(X_a, Y_a) \right) (I(X_a, Y_a) - \bar{I}(X_a, Y_a)) = 0 \quad (11)$$

$$\text{and } \frac{\mathcal{I}}{\mathcal{I}(PY)} \left(\sum_{a=1}^N (I(X_a, Y_a) - \bar{I}(X_a, Y_a))^2 \right) = 0 \quad \text{so,} \quad (12)$$

$$\sum_{a=1}^N 2 \left(\frac{\mathcal{I}}{\mathcal{I}(PY)} I(X_a, Y_a) \right) (I(X_a, Y_a) - \bar{I}(X_a, Y_a)) = 0 \quad (13)$$

with one solution being:

$$\frac{\mathcal{I}}{\mathcal{I}(PY)} I(X_a, Y_a) = 0 \quad (14)$$

Since $\bar{I}(X_a, Y_a)$ is just our data then $I(X_a, Y_a)$ is the function minimized with respect to PX, PY. If the X_a, Y_a is the same as the associated PX, PY then in a random test on the fuzzy region close to the

$[\{x_1, y_1\} \cap \{x_2, y_2\}]$ region (this is used in the computer code because of noise) we have that:

$\left(\frac{J_1(R_{ij})}{R_{ij}} \right)^2 = 1$ so that we have a square matrix of a repeated list of k_i s. So when the function:

$$I(x_i, y_i) = \sum_{j=1}^N k_j \left(\frac{J_1(R_{ij})}{R_{ij}} \right)^2 = \sum_{j=1}^N k_j (1) = F \quad (15)$$

is put back into equation 4 we see that it is minimized (relaxed) with respect to the test PX, PY points, we not only have the correct (PX, PY) positions but also the correct k_i s for the point sources. In this way, the locations of the correct PSF source locations and intensities are found using ‘numerical relaxation’.

Standard deconvolution algorithms unfortunately would have included $\int P_o(x_o, y_o) dA$ for example and so have a much higher artifact return. And the CLEAN algorithm (which also uses numerical relaxation) manages to catch only part of this $\{x_A, y_A\}$ region since it only goes a short distance down the ridges and it catches more and more non ridge areas some of the more points are transferred over (thus adding in some $\int P_o(x_o, y_o) dA$), thus increasing the probability of getting image artifacts.

WE HAVE EXPLICITLY TRIED TO CAPTURE ALL OF THIS $\{x_A, y_A\}$ REGION WITH THIS METHOD using our conjecture (on the PSF derivatives) as our guide.

I put the above algorithm (i.e., that Laplace filter on isophote ridge lines) into a 2,000 line Fortran code and also built a working superresolution telescope which used CCD imaging. I found that it was necessary that it be a Herschel (i.e., off axis telescope) to eliminate diffraction effects of secondary mirror supports. Did many experiments to verify that this superresolution method works.

If this method had been used on a Herschel version of the Hubble it would have yielded a 5 fold increase in resolution (on “blobby” bright objects).

Notes:

We are not “getting something for nothing” if there is a high SNR. Also recall that the second derivative of $I(x, y)$ at $R=0$ is $-.5k_i J_0^2$. So to get a larger dynamic range for this superresolution method we should replace $|\partial^2 I(x, y) / \partial s^2|$ in our algorithm with $|\partial^2 I(x, y) / \partial s^2| / I(x, y)$ to normalize the laplacian in the intensity k_i and so give low intensity PSF contributions equal weight.

Apodization doesn’t improve the superresolution here. Could use highest local curvature on smoothed isophotes (in contour plot representation) to identify ridges in general case.

Given the SNR requirements found here one can use the rule of thumb that says that any “blob” that gives at least two clearly observable concentric diffraction rings (above background noise) will allow this superresolution method to be used on it. A magnified image must be made of just this region with the “Airy Disk” diameter at least half of the CCD focal plane smallest dimension. Method would have lower SNR requirements with concentric circle CCD pixel arrangement.